

Synthesis of P-Block Metals and Cobalt Polyphthalocyanines Supported on Multi-Walled Carbon Nanotubes for the Electrochemical Carbon Dioxide Reduction Reaction

Thesis submitted to the University of Nottingham for the degree of

Doctor of Philosophy

Ethan Norman MSci
14288020
Supervisors: Jesum Alves Fernandes, Darren Walsh

May, 2025

Contents

Units and Symbols **4**

Symbols **5**

Constants **8**

List of Abbreviations **9**

Chemical Abbreviations **12**

1 Introduction **17**
1.1 Climate change and CO_2 . . . 17
1.2 CO_2 valorisation by the electrochemical Carbon Dioxide Reduction Reaction 17
1.3 The Carbon Dioxide Reduction Reaction for Methanol Production . . . 19
1.4 Carbon Dioxide Reduction Reaction for Formate Production . . . 21

2 Electrochemical and Analytical Methods for the Analysis of Electrocatalysts **27**
2.1 Electrochemical Theory . . . 27
2.1.1 Introduction to electrochemical reactions . . . 27
2.1.2 Electrochemical kinetics . . . 30
2.2 Electrochemical Techniques . . . 33
2.2.1 Voltammetry . . . 33
2.2.2 The Diffusion Layer . . . 38
2.2.3 Diffusion in Nanoparticle Modified Electrodes . . . 40
2.2.4 Electrical Double Layer and Non-Faradaic Current . . . 44
2.2.5 Chrono- techniques . . . 47
2.3 CO_2 Electrocatalysis . . . 48
2.3.1 Basics . . . 48
2.3.2 Role of the Electrolyte . . . 50
2.3.3 Inapplicability of Tafel Analysis for this work . . . 53
2.3.4 Practical Considerations for Electrocatalysis . . . 57
2.4 Experimental Techniques . . . 62
2.4.1 Thermo-Gravimetric Analysis . . . 62

2.4.2 Transmission electron microscopy 64

3 Multi-Walled Carbon Nanotubes as supports for the electrochemical CO_2 reduction reaction 73
3.1 Structure and Properties of Single-Walled Carbon Nanotubes 73
3.1.1 Carbon Nanotube Structure 73
3.1.2 Electronic Properties of Carbon Nanotubes 76
3.1.3 Multi-Walled Carbon Nanotubes 77
3.1.4 Multi-Walled Carbon Nanotubes as electrocatalyst supports 79
3.1.5 Electrochemistry 79

4 Cobalt Phthalocyanines on Multi-Walled Carbon Nanotubes for the electrochemical Carbon Dioxide Reduction Reaction 85
4.1 Background 85
4.1.1 Cobalt Phthalocyanine for CH_3OH production 87
4.1.2 Polyphthalocyanines on Multi-Walled Carbon Nanotubes 90
4.1.3 Copper as a co-catalyst for the electrochemical Carbon Dioxide Reduction Reaction 92
4.2 Cobalt Polyphthalocyanine on Multi-Walled Carbon Nanotubes 93
4.2.1 Synthesis 93
4.2.2 Characterisation 98
4.2.3 Electrochemistry 101
4.2.4 Electrocatalysis 103
4.3 Copper Polyphthalocyanine on Multi-Walled Carbon Nanotubes 105
4.3.1 Synthesis 105
4.3.2 Characterisation 106
4.3.3 Electrochemistry 107
4.3.4 Electrocatalysis 109
4.4 Copper on Cobalt Polyphthalocyanine on Multi-Walled Carbon Nanotubes 111
4.4.1 Synthesis 111
4.4.2 Characterisation 111
4.4.3 Electrochemistry 117
4.4.4 Electrocatalysis 128
4.4.5 Conclusions 131

5 P-Block Metals on MWNTs for the electrochemical CO_2 reduction reaction 139
5.1 Background 139
5.1.1 Lead for the CO_2RR 139
5.1.2 Bismuth for the CO_2RR 141
5.1.3 Indium for the CO_2RR 144
5.2 Pb/MWNTs 146
5.2.1 Synthesis 146

5.2.2 Characterisation . . . 148
5.2.3 Electrochemistry . . . 161
5.2.4 Electrocatalysis . . . 166
5.3 Bi/MWNTs . . . 167
5.3.1 Synthesis . . . 167
5.3.2 Characterisation . . . 167
5.3.3 Electrochemistry . . . 175
5.3.4 Electrocatalysis . . . 180
5.4 In/MWNTs . . . 182
5.4.1 Synthesis . . . 182
5.4.2 Characterisation . . . 183
5.4.3 Electrochemistry . . . 195
5.4.4 Electrocatalysis . . . 204
5.5 Conclusions . . . 206

6 Conclusions and Future Work **214**
6.1 Polyphthalocyanines on Multi-Walled Carbon Nanotubes . . . 214
6.2 P-Block Metals on Multi-Walled Carbon Nanotubes . . . 215

Appendices **216**
I Kapusta and Hackerman[1] . . . 217
II Experimental . . . 217
II.1 Chapter 4 Experimental . . . 217
II.2 Chapter 5 Experimental . . . 221

Units

Name	Symbol	Definition
Amperes	A	Unit of electrical current, defined as $1\,C\,s^{-1}$
Coulombs	C	Unit of electric charge, defined as the quantity of electricity delivered by $1\,A\,s^{-1}$
Degrees Celsius	°C	Temperature in Celsius
Molarity or Molar Concentration	M	Concentration in mol dm^{-3}
Parts per Million	ppm	Dimensionless quantity-per-quantity measure in which the total quantity is divided into 10^6 parts
Standard Cubic Centimetres per Minute	sccm	Flow of gas in $cm^3\,min^{-1}$. Gas is assumed ideal, at 1 atm, and 0 °C
Volts	V	Unit of Electric Potential
Watts	W	Power, defined as $1\,J\,s^{-1}$

Symbols

Name	Symbol	Definition
π-orbital misalignment	ϕ	Misalignment of the π-orbital of the atoms that compose a Nanotube (NT)
Cell potential	E_{cell}	Cell potential in V
Change in Gibbs Free Energy	ΔG	Change in Gibbs free energy, with positive and negative values denoting non-spontaneous and spontaneous reactions respectively
Charge	Q	Charge in C
Current	i	Current in A
Current density	j	Current measured per unit area of electrode, typically in mA cm^{-2}
Electron transfer coefficient	α	Constant between 0 and 1 (typically approximated to be 0.5) representing the fraction of interfacial potential at an electrode involved in the lowering of ΔG for a given electron transfer reaction

Name	Symbol	Definition
Exchange current density	$j_\circ$	Current density when no overall net current is flowing and at 0 applied potential
Graphene lattice vector	a_n	lattice vectors of the graphene primitive unit cell used to describe roll-up vector R
Nanotube chiral indices	m, n	Indices describing the chiral vector of a Single-Walled Carbon Nanotube (SWNT)
Nanotube Diameter	D_{NT}	Diameter of Carbon Nanotube (CNT) measured from outer wall to outer wall
Number of electrons	z	Integer number of electrons
Overpotential	η	Difference between the standard electrode potential of a redox reaction and the experimentally applied potential
Oxidation potential	E_{ox}	Oxidation Potential in V
Pertaining to reduction or oxidation	$X_{red/ox}$	Quantity or feature X is associated with a reduction (X_{red}) or oxidation (X_{ox}) process
Potential	E	Potential in V
Pyramidalisation angle	θ	Angle of the sp^2 orbitals of the C atoms in a CNT
Reduction potential	E_{red}	Reduction Potential in V
Roll-up vector	R	Vector upon which a sheet of graphene would be rolled to produce a SWNT. Described by the lattice vectors of the graphene primitive unit cell

Name	Symbol	Definition
Rotations per minute	rpm	Number of complete revolutions made per minute
Scan rate	v	Scan rate in V s^{-1}

Constants

Name	Symbol	Value
Avogadro constant	N_A	6.022×10^{23} mol^{-1}
Electron Volts	eV	1.602×10^{-19} J
Faraday's Constant	F	96485 C mol^{-1}
Ideal Gas Constant	R	8.3145 J mol^{-1} K^{-1}

List of Abbreviations

Abbreviation	Full Name
CO_2RR	Carbon Dioxide Reduction Reaction
AC-STEM	Aberration corrected-scanning transmission electron microscopy
AC-TEM	Aberration corrected-transmission electron microscopy
ATR-IR	Attenuated Total Reflectance Infra-red Spectroscopy
BET	Brunauer-Emmett-Teller surface area analysis
BF	Bright-field
BF-TEM	Bright-Field Transmission Electron Microscopy
CV	Cyclic Voltammetry
DF	Dark-field
DF-TEM	Dark-Field Transmission Electron Microscopy
ECSA	Electrochemical Surface Area
EDS	Energy Dispersive X-ray spectroscopy
EDX	Energy Dispersive X-ray
EELS	Electron Energy Loss Spectroscopy
EELS-SI	Electron Energy Loss Spectroscopy Spectral Imaging
EIS	Electrochemical Impedance Spectroscopy
FE	Faradaic efficiency

Abbreviation	Full Name
FT-IR	Fourier Transform Infra-red Spectroscopy
GC	Gas Chromatography
GCE	Glassy carbon electrode
HAADF	High-Angle Annular Dark Field
HER	Hydrogen Evolution Reaction
HOMO	Highest Occupied Molecular Orbital
HR-TEM	High Resolution-Transmission Electron Microscopy
IR	Infra-red
LCAO	Linear Combination of Atomic Orbitals
LSV	Linear Sweep Voltammetry
LUMO	Lowest Unoccupied Molecular Orbital
MO	Molecular Orbital
NMR	Nuclear Magnetic Resonance
OCP	Open Circuit Potential
PCET	Proton Coupled Electron Transfer
RDE	Rotating Disk Electrode
RDS	Rate-Determining Step
RHE	Reversible Hydrogen Electrode
RRDE	Rotating Ring Disk Electrode
SCE	Saturated Calomel Electrode
SHE	Standard Hydrogen Electrode
STEM	Scanning transmission electron microscopy
TEM	Transmission electron microscopy

Abbreviation	Full Name
TGA	Thermo-Gravimetric Analysis
XPS	X-ray Photoelectron Spectroscopy
XRD	X-ray Diffraction Spectroscopy

Chemical Abbreviations

Abbreviation	Full Name
Bi/MWNT	Bismuth on Multi-Walled Carbon Nanotubes
CNT	Carbon Nanotube
COF	Covalent Organic Framework
CoPc	Cobalt Phthalocyanine
CoPc/MWNT	Cobalt Phthalocyanine on Multi-Walled Carbon Nanotubes
CoPPc	Cobalt Polyphthalocyanine
CoPPc/MWNT	Cobalt Polyphthalocyanine on Multi-Walled Carbon Nanotubes
Cu/CoPPc	Copper on Cobalt Polyphthalocyanine
Cu/CoPPc/MWNT	Copper on Cobalt Polyphthalocyanine on Multi-Walled Carbon Nanotubes
CuPc	Copper Phthalocyanine
CuPPc	Copper Polyphthalocyanine
CuPPc/MWNT	Copper Polyphthalocyanine on Multi-Walled Carbon Nanotubes
DBU	1,8 – diazobicyclo(5.4.0) undec – 7-ene
DWNT	Double-Walled Carbon Nanotube
GNF	Graphitic Nanofibre
HOPG	Highly-Ordered Pyrolytic Graphite

Abbreviation	Full Name
In/MWNT	Indium on Multi-Walled Carbon Nanotubes
ITO	Indium Tin Oxide
MPPc/MWNT	Metal Polyphthalocyanine on Multi-Walled Carbon Nanotubes
MWNT	Multi-Walled Carbon Nanotube
NiPc	Nickel Phthalocyanine
NT	Nanotube
Pb/MWNT	Lead on Multi-Walled Carbon Nanotubes
PPc	Polyphthalocyanine
PPc/MWNT	Polyphthalocyanine on Multi-Walled Carbon Nanotubes
PTFE	Polytetrafluoroethylene
SWNT	Single-Walled Carbon Nanotube
TCB	1,2,4,5 – tetracyanobenzene
THF	Tetrahydrofuran
$PbNO_3$/MWNT	Lead Nitrate on Multi-Walled Carbon Nanotubes

Abstract

The electroreduction of CO_2 to value added products presents a promising step forward towards a net-zero carbon cycle, where produced CO_2 can be captured and then recycled into products such as methanol or formic acid via means of renewable energy sources. However, selectivity and activity of CO_2 electrocatalysts pose a significant challenge towards viability, owing to the intrinsic stability of the CO_2 molecule and the multi-stepped reduction pathway with many potential products capable of formation.

In this body of work, Multi-Walled Carbon Nanotubes (MWNTs) were investigated as highly conductive and high surface area supports for two distinct types of CO_2 electrocatalyst systems: polyphthalocyanines, and p-block metals (Pb, Bi, and In), in which a correlative approach combining electrochemical analysis and electron microscopy techniques was utilised to gain a hollistic understanding of the structure-electrochemical function relationship of said materials in aims of optimising electrocatalytic activity.

The polyphthalocyanine section of this work investigates Cobalt Polyphthalocyanine on Multi-Walled Carbon Nanotubes (CoPPc/MWNT) for the electrocatalytic conversion of CO_2 to methanol in which the first production of methanol using CoPPc/MWNT is observed. From this, a novel bimetallic system, Copper on Cobalt Polyphthalocyanine on Multi-Walled Carbon Nanotubes (Cu/CoPPc/MWNT), is produced via the magnetron sputtering of Cu onto the CoPPc/MWNT, and it is found that the system undergoes an electrochemically driven metal displacement reaction of the Co by the Cu at negative potentials, and is enabled by the close proximity and single-atom level dispersion of the Cu atoms on the polyphthalocyanine surface as confirmed by Aberration corrected-scanning transmission electron microscopy (AC-STEM) and novel single-atom resolution Electron Energy Loss Spectroscopy Spectral Imaging (EELS-SI).

The p-block metal section of this work investigates the use of MWNTs as supports for the p-block metal nanoparticles of Pb, Bi, and In at various weight loadings and synthetic conditions and the resulting impact on the electrocatalytic activity towards formic acid/formate production from CO_2. By utilising both electrochemical analysis and electron microscopy to iterate and guide the synthesis, the production of a $\sim 100\%$ selective Indium on Multi-Walled Carbon Nanotubes (In/MWNT) catalyst is achieved, with a partial current density j_{HCOO^-} of 15.5 mA cm^{-2} making it the highest performing indium based catalyst in literature to the best of the authors knowledge.

Acknowledgements

Firstly, thank you to my supervisors, Jesum Alves Fernandes and Darren Walsh for providing their assistance and support in my research.

I am incredibly grateful for the invitation Jesum extended to me to join his group, and from there the incredible amount of support, advice, and understanding he gave to me throughout my work. My time in his group was instrumental for gaining my confidence as a researcher and I wouldn't have been able to get this done without him.

Darren's input and advice was monumental in helping me develop my expertise and confidence as an electrochemist. Through our discussions I was able both refine and improve my approach to electrochemistry, and was able to finally understand concepts that just wouldn't click after years of working in the field, and I am incredibly grateful for his help.

Throughout my PhD I worked alongside some incredible people who gave their support to me throughout my research, and I would like to thank (in alphabetical order): Benjamin Weare, Bradley Flinn, Ian Cardillo-Zallo, Kayleigh Fung, Michael Fay, Ryan Whitehead, Tara LeMercier, Tom Burwell, and William Cull. I couldn't have made it through without you all. You have made my time as a PhD student the best time of my life, and I will forever miss chatting at lunch, playing cards and chess, hanging out both at and outside of uni, and working alongside you all.

I would also also like to thank the members of the Nottingham Nanocarbon Group and the JAF-Lanterna Group for providing support, assistance, and accomodation for my research work: Andreas, Emmerson, Ben, Tom, Rob, Matt, Sean, and Toby.

A massive thank you to my Masters student: Arshpreet Kaur, who contributed heavily to the p-block metals project found in chapter 5. Arsh contributed a large amount of synthesis and electrochemical analysis to the project, and also offered incredibly helpful insight and worked with me to shape the overall project. I am incredibly lucky to have supervised and worked with such a talented masters student, and without her contributions and effort to the p-block metals project, it would have likely not seen completion.

Thank you to the MASI project, for providing magnetron sputtering, collaboration opportunities, support, and funding for my research. For their direct contributions to my work, I would like to thank: Gazi Aliev for providing AC-STEM imaging, and Luke Norman, Emmerson Kohlrausch, and Matthew Young for conducting magnetron sputtering of my polyphthalocyanine samples.

Thank you to the nmRC for providing the facilities to conduct TEM and EDX analysis, and the assistance of the staff in conducting said techniques.

Thank you to Quentin Ramasse and the Daresbury SuperSTEM laboratory for providing

the single atom resolution EELS found in this work.

Outside of my academic research, I would firstly thank my parents: Elizabeth and David Norman for their encouragement, support, and financial assistance during my self-funded period and my write-up. I hope I have made you proud with what I have accomplished, and know that I am forever grateful to you both. Thank you to my siblings: Zak Norman, Will Saunders, and Sarah Hayes, and also my extended family: Sue Moorman, Michael Hunt, and Karen Kelsall for their encouragement and support throughout.

I would like to give special thanks to my fiancée: Molly McConnell, for her unwaivering support, encouragement, and love during my PhD. Despite working so incredibly hard in your journey to becoming midwife, I knew you were always there for me when I needed you. I wouldn't have made it through without you and I am incredibly lucky to be able to spend the rest of my life with you.

Lastly, I would like to thank William Clark and Andrew Bacon for their enduring friendship throughout my PhD, and their patience with me when timezone differences result in difficulty keeping in touch. I am incredibly grateful to have had you guys to keep me entertained and give me company whenever I needed it, and also making sure I was reminded that I am bald.

Chapter 1

Introduction

1.1 Climate change and CO_2

The emission of CO_2 by anthropogenic activity remains one of the most pressing issues society faces today, as further increasing greenhouse gas emissions result in a dire need to reduce our carbon footprint.[1,2] CO_2 has had the largest effect on the earths climate compared to other greenhouse gases due its ever increasing rate of production from sources ranging from concrete production to fossil fuel consumption. These effects result in, on average, higher temperatures globally due to increasing the radiation retention of the atmosphere,[3] with these higher temperatures having a knock-on effect to almost every facet of the environment, including loss of marine life, decreased crop yields and weather pattern changes which will continue to worsen as CO_2 levels rise.[2]

1.2 CO_2 valorisation by the electrochemical Carbon Dioxide Reduction Reaction

Methods to utilise CO_2 into useful value added products presents itself as an attractive solution to the emissions problem, allowing produced CO_2 to be recycled back into energy dense materials, given a renewable CO_2 energy source is used for the conversion such as solar energy.[4,5] The electrochemical Carbon Dioxide Reduction Reaction (CO_2RR) allows for the conversion of CO_2 into value added products and presents a promising pathway to a zero emissions carbon cycle, and has been a target of research due to the requiring no increased temperatures or pressures.[4,6,7]

There are many possible reduction products that can be produced from the CO_2RR,[8,9] and to illustrate economic feasibility, the relationship between the market value of the product, the energy density of the product, and the market value of the energy required must all be considered when screening for a target product, with this relationship being

demonstrated below Fig. 1.1.

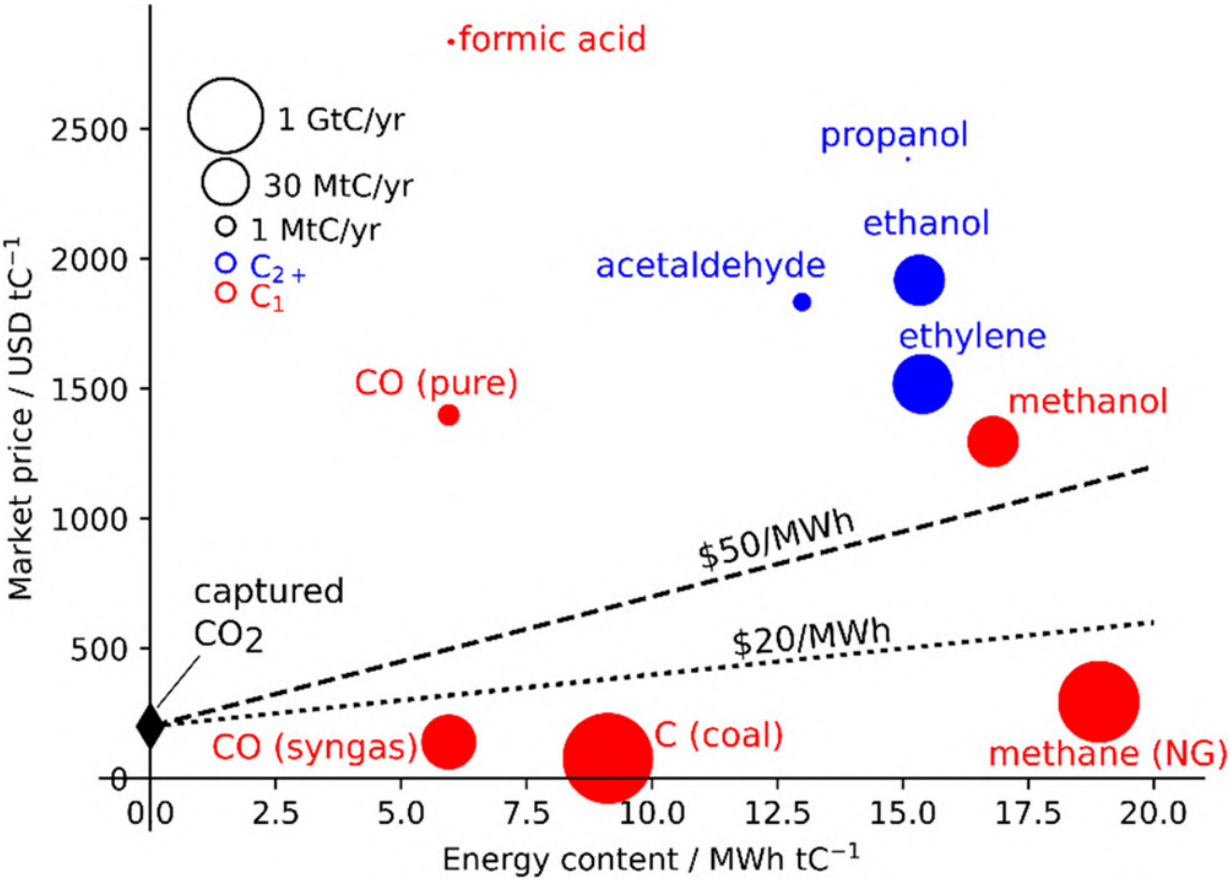


Figure 1.1: Market price of CO_2 reduction products as a function of energy content. Market price is given in USD per ton of carbon (USD $t_c{}^{-1}$) of CO_2RR products. Energy content per ton of carbon is given in megawatt hours per ton of carbon ($MWh\ t_c{}^{-1}$). Marker size indicates the logarithmic size of the global market. The notation C_1 and C_2 refer to the number of carbon atoms in the reduction product. The dashed and dotted lines represent the minimum cost of production given a captured CO_2 price of \$200 t_c^{-1} at \$50 MWh^{-1} or \$20 MWh^{-1}. \$200 t_c^{-1} is a representative price for carbon captured from a power plant. \$50 MWh^{-1} and \$20 MWh^{-1} represent energy costs of recent solar installations and the record low costs of solar installations respectively. Adapted from Nitopi *et al*[9]

From Fig. 1.1, a region of economic feasibility can be inferred from the area above the dashed line, as chemicals above this line introduces a net profit of production. Speciality chemicals such as formic acid and propanol for example, are economically viable, but aren't as impactful in reducing a large amount of CO_2 emissions due to the market size compared to products such as ethylene, methanol or methane.[9] C_{2+} chemicals such as ethanol and ethylene represent the highest economic values whilst also having a market large enough to have an appreciable effect on CO_2 emissions, however Cu and Cu based materials remain the only catalysts to be able to electrochemically produce C_{2+} materials with appreciable efficiency, however, Cu catalysts notoriously also struggle with selectivity due to the wide range of possible products they are able to produce.[9,10] This leaves the C_1 products HCOOH and CH_3OH as viable targets for the catalyst

development within this work. CO was not chosen as a target product as at this point in CO_2RR research, as CO electrocatalysts are numerically vast and have decades of research resulting in numerous high activity, stability, and selectivity catalysts with low overpotentials and already present themselves as candidates for future potential scale-up and commercial applications.[9]

1.3 The Carbon Dioxide Reduction Reaction for Methanol Production

Methanol is a valuable target product from the electrochemical CO_2RR due to its uses as a primary feedstock, intermediate for various chemical products, and potential use as a fuel source in methanol fuel cells.[11] Currently, methanol is produced industrially by catalytic thermal hydrogenation of syngas (CO and H_2 gas)[12] and requires high temperatures and pressures, and which results in large CO_2 emissions from both the energy demand and the sourcing of hydrogen from fossil fuels. Due to this, the electrochemical CO_2RR could provide a promising alternative, as it can be performed at room temperature and pressure. Additionally, given the energy required to drive the electrochemical reaction is sourced sustainably, the process potentially can could approach CO_2 neutrality given the CO_2 conversion efficiency is high enough.

Currently, there have been many electrocatalysts as of the time of writing that have shown to produce methanol as the primary reduction product,[13] however none have shown commercial viability owing to large overpotentials and issues pertaining to selectivity.[13] The reduction to CH_3OH from CO_2 requires an overall $6e^-$ reduction, and involves multiple intermediate steps in the mechanism. During the reduction to CH_3OH, it is typical that lesser reduced products found along the reduction pathway such as CO form more favourably than CH_3OH (see Section 2.3 for further discussion), and more than often result in either appreciable activity or selectivity for a given CH_3OH electrocatalyst, rather than both.

The highest selectivity for methanol from an CO_2RR electrocatalyst recorded to date was achieved by Canfield *et al*[14] using an n-doped GaAs-crystal with the As (111) crystal face, which achieved a near 100% Faradaic efficiency (FE) towards methanol at an η of -1.20 - -1.40 V vs Saturated Calomel Electrode (SCE) in 0.2 M Na_2SO_4 electrolyte.[14] Whilst the GaAs catalyst showed an unprecedented selectivity towards methanol, it suffers from a j_{CH_3OH} of only 0.2 mA cm^{-2} and a intricate, multi-stepped synthesis, which results in scarce potential for commercial viability.

The highest methanol activity reported to date was achieved by Li *et al*[15] with a $Ag, S \cdot Cu_2O/Cu$ catalyst, and achieved an unprecedented j_{CH_3OH} of 122.7 mA cm^{-2} with an appreciable FE of 67%.[15] Unfortunately, whilst the selectivity is moderate, the minor products of this catalyst include HCOOH,[15] greatly hindering it's viability on

scale-up due to the requirement of liquid-liquid separation. Moreover, this activity was achieved in ionic liquid electrolyte which provides further difficulties to commercial viability due to the lack of commercial scale ionic liquid availability.[15]

The two previously explored catalysts exemplify the "one or the other" problem between activity and selectivity present in methanol producing electrocatalysts, therefore it is evident that research efforts should be directed towards either: (A): An electrocatalyst that can either achieve near uniform selectivity with an appreciable activity, or (B): An electrocatalyst with high activity in which methanol is the sole liquid product so that product collection is viable at scale. Furthermore, electrocatalysts should be capable of being produced without specialised or overly difficult syntheses, regardless of selectivity goals.

A promising electrocatalyst that may potentially meet the second criteria (B) can be found with Cobalt Phthalocyanine on Multi-Walled Carbon Nanotubes (CoPc/MWNT) derived catalysts,[16] which have recently been found to produce methanol at appreciable efficiency and activity, with only gaseous side products being produced.[16,17] Additionally, due to the recency of research into the methanol production capabilities of CoPc/MWNT, there is potential for improvement of already promising efficiency and activity figures, whilst allowing further optimisations such as reductions in overpotential. Further exploration of the current research into CoPc/MWNT is explored in Chapter 4, however relevant to this section is the potential for further development into CoPc/MWNTs, specifically, focussing on improvement of the efficiency and stability of these catalysts is a worthwhile endeavour as CoPc/MWNT has already been shown to be compatible with scaled-up flow catalyst systems.[18]

The stability issues CoPc/MWNTs based catalysts currently face are due to reductive deactivation of the catalysts,[17] which result in activity for methanol over periods of around $1-2$ hours before deactivation as of time of writing. A potential solution for this could be found in the polymerisation of the catalyst to give Cobalt Polyphthalocyanine on Multi-Walled Carbon Nanotubes (CoPPc/MWNT), which could both increase the resilience of the catalyst to reductive deactivation, but also potentially increase activity whilst keeping additional complexity in the synthesis to a minimum.[19] Furthermore, as discussed in relation to the the works of Canfield *et al*[14] and Li *et al*,[15] it can be assumed that selectivity and activity increases in methanol catalysts are associated with dual metal systems, however in CoPc/MWNT there are complications in introducing a co-catalytic metal to the catalyst. Specifically, introducing another metal to the CoPPc/MWNT will result in either disruption of the phthalocyanine binding, encapsulation of the added metal into the Multi-Walled Carbon Nanotube (MWNT) , or requires demetalation of the Co due to the high binding strength of the Co to the phthalocyanine ring.[20] Unfortunately, synthesising a mixed metal polyphthalocyanine by utilising another metal in addition to Co during the polymer synthesis is not a practical solution to creating a mixed metal polymer, as the binding strength of Co and tendency of the polymer to aggregate on

the MWNT surface will result in near zero control of the placement of the co-metal. A solution to these practical limitations may potentially be found via utilising magnetron sputtering to deposit an additional metal on the surface of the CoPc/MWNT catalyst in a solvent-free "dry" synthesis. In this work this technique was utilised, allowing for the initial characterisation of a novel bimetallic Polyphthalocyanine on Multi-Walled Carbon Nanotubes (PPc/MWNT) catalyst.

These twin motivations of methanol production with CoPc/MWNT with improved stability and synthesis of novel dual-metal CoPc/MWNT catalysts led to the research conducted in Chapter 4 on CoPPc/MWNT and Copper on Cobalt Polyphthalocyanine on Multi-Walled Carbon Nanotubes (Cu/CoPPc/MWNT).

1.4 Carbon Dioxide Reduction Reaction for Formate Production

Formic acid, referred to commonly as its conjugate base formate, is another high value target product from the electrochemical CO_2RR due to its multiple applications including use as a feedstock chemical in industry and also as a means of hydrogen storage.[21] Currently, formic acid is produced industrially via hydrolysis of methyl formate or formamide and oxidation of biomass,[22] and compared to these current methods, production of formate by the electrochemical CO_2RR can reduce the cost of formate production from $\$0.8 - 1.2$ to $\sim \$0.34$[23] given 100% FE_{HCOO^-} and a catalyst stability of 4.45 years.[21,23] Additionally, added benefits can be ascribed to the electrochemical production of formate from the possibility of a net zero carbon cycle given renewable energy is used for the production of formate given that no elevated temperatures or pressures are required.[21]

Currently, the most promising catalysts for formate production are p-block metal based catalysts (Sn, In, Bi, Pb), due to a shared intrinsically high selectivity towards formate,[24] with catalysts utilising each of these metals being shown to have achieved selectivities $> 95\%$.[25] The largest share of research interest belongs to Sn based catalysts,[24,26] and this attention is largely due to the seminal works by Hori *et al*,[27,28] in which Sn achieved the highest FE_{HCOO^-} out of the range of metals tested, and also was the most cost effective metal in the study.[29]

As research has continued to present, the other p-block metals (In, Bi, Pb) have generally shown themselves to be more promising catalysts than Sn towards formate, achieving selectivities approaching or equalling 100% with appropriate nano-structuring,[25,26] and all but Pb having demonstrating lower on average Overpotential for formate production than Sn.[25] Each of the p-block metals aforementioned whilst similar in function, require different considerations for optimising selectivity due to the larger amount of mechanistic routes CO_2 can take to reduce to formate,[30,31] and these considerations are explored in greater depth in Chapter 5 with specific literature reviews for Pb, Bi, and In (Section 5.1).

Consequently, this remainder of this section will comment on the general trends in p-block metal catalyst design shared amongst its highest performing catalysts.

What is evident amongst the highest performing p-block catalysts is the shared use of a conductive carbon supports such as CNTs, graphene/graphene oxide, or Graphitic Nanofibres (GNFs).[32–35] The use of conductive supports allows nano-structuring of metal catalysts by allowing electron delivery to the catalysts without reliance on bulk conductivity, which has also been shown to decrease overpotential.[32–35] Additionally, catalyst morphology can be influenced via the support, with an example being given by Burwell *et al*[36] who demonstrated that GNFs step-edges stabilise nanoparticles in-situ and increase activity.[36] The research efforts into formate electrocatalysts have resulted in multiple high selectivity and activity catalysts using the aforementioned p-block metal catalysts,[21,25,34] there has been little attention paid to the scalability of the catalysts, specifically in terms of synthesis of the catalyst materials, with the current state of the art continuous formate electrolysers utilising p-block metal plates.[37] The current highest performing In, Bi, and Pb catalysts make use of either intricate syntheses to achieve the desirable near 100% selectivity,[38] or syntheses more suitable for scalability which sacrifice ideal selectivity, for example by utilising single step thermal decompositions.[39,40]

Despite the large amount of research into supported p-block metal catalysts, there is a surprising lack of research on p-block metal nanoparticles supported on MWNTs in a potentially scalable catalyst system. As of the time of writing, only Lead on Multi-Walled Carbon Nanotubes (Pb/MWNT)[34] has been investigated in literature, however the synthesis requires a three-step process including additional reagents such as chitosan and acetic acid.[34]

When taking the previously discussed points into consideration, it is evident that it is worthwhile to screen and develop a feasibly scalable supported p-block metal nanoparticle catalyst with the highest selectivity possible whilst keeping the synthesis relatively facile. Thus, the research conducted in Chapter 5 utilises a two-component metal-support synthesis with only water as a solvent in efforts to evaluate and develop a Pb/MWNT, Bismuth on Multi-Walled Carbon Nanotubes (Bi/MWNT), and Indium on Multi-Walled Carbon Nanotubes (In/MWNT) catalyst. Furthermore, the only modification to the synthesis made, that being the use of ethylene glycol Section 5.4, resulted in a significantly increased selectivity whilst not introducing any additional synthetic techniques to be used.

Chapter 1 Bibliography

(1) S. Solomon, G. K. Plattner, R. Knutti and P. Friedlingstein, "Irreversible climate change due to carbon dioxide emissions", *Proceedings of the National Academy of Sciences of the United States of America*, 2009, **106**, 1704–1709.

(2) I. E. Agency, "Global Energy Review: CO2 Emissions in 2021", *Global Energy Review: CO2 Emissions in 2021*, 2022.

(3) G. Myhre, E. J. Highwood, K. P. Shine and F. Stordal, "New estimates of radiative forcing due to well mixed greenhouse gases", *Geophysical Research Letters*, 1998, **25**, 2715–2718.

(4) X. Liu, B. Q. Li, B. Ni, L. Wang and H. J. Peng, "A perspective on the electrocatalytic conversion of carbon dioxide to methanol with metallomacrocyclic catalysts", *Journal of Energy Chemistry*, 2021, **64**, 263–275.

(5) N. Han, Y. Wang, L. Ma, J. Wen, J. Li, H. Zheng, K. Nie, X. Wang, F. Zhao, Y. Li, J. Fan, J. Zhong, T. Wu, D. J. Miller, J. Lu, S. T. Lee and Y. Li, "Supported Cobalt Polyphthalocyanine for High-Performance Electrocatalytic CO2 Reduction", *Chem*, 2017, **3**, 652–664.

(6) Q. Lu and F. Jiao, "Electrochemical CO2 reduction: Electrocatalyst, reaction mechanism, and process engineering", *Nano Energy*, 2016, **29**, 439–456.

(7) J. Qiao, Y. Liu, F. Hong and J. Zhang, "A review of catalysts for the electroreduction of carbon dioxide to produce low-carbon fuels", *Chemical Society Reviews*, 2014, **43**, 631–675.

(8) H. Ishida, in *Carbon Dioxide Chemistry, Capture and Oil Recovery*, ed. I. Karamé, J. Shaya and H. Srour, InTech, 2018, ch. 2.

(9) S. Nitopi, E. Bertheussen, S. B. Scott, X. Liu, A. K. Engstfeld, S. Horch, B. Seger, I. E. Stephens, K. Chan, C. Hahn, J. K. Nørskov, T. F. Jaramillo and I. Chorkendorff, "Progress and Perspectives of Electrochemical CO2 Reduction on Copper in Aqueous Electrolyte", *Chemical Reviews*, 2019, **119**, 7610–7672.

(10) J. Gao, H. Zhang, X. Guo, J. Luo, S. M. Zakeeruddin, D. Ren and M. Grätzel, "Selective C-C Coupling in Carbon Dioxide Electroreduction via Efficient Spillover of Intermediates As Supported by Operando Raman Spectroscopy", *Journal of the American Chemical Society*, 2019, **141**, 18704–18714.

(11) Z. Tian, Y. Wang, X. Zhen and Z. Liu, "The effect of methanol production and application in internal combustion engines on emissions in the context of carbon neutrality: A review", *Fuel*, 2022, **320**, 123902.
(12) G. Leonzio, "Methanol synthesis: Optimal solution for a better efficiency of the process", *Processes*, 2018, **6**, 20.
(13) K. Wiranarongkorn, K. Eamsiri, Y. S. Chen and A. Arpornwichanop, "A comprehensive review of electrochemical reduction of CO2 to methanol: Technical and design aspects", *Journal of CO2 Utilization*, 2023, **71**, 102477.
(14) D. Canfield and K. W. Frese, "Reduction of Carbon Dioxide to Methanol on n - and p - GaAs and p - InP . Effect of Crystal Face, Electrolyte and Current Density", *Journal of The Electrochemical Society*, 1983, **130**, 1772–1773.
(15) P. Li, J. Bi, J. Liu, Q. Zhu, C. Chen, X. Sun, J. Zhang and B. Han, "In situ dual doping for constructing efficient CO2-to-methanol electrocatalysts", *Nature Communications*, 2022, **13**, 1965.
(16) E. Boutin, M. Wang, J. C. Lin, M. Mesnage, D. Mendoza, B. Lassalle-Kaiser, C. Hahn, T. F. Jaramillo and M. Robert, "Aqueous Electrochemical Reduction of Carbon Dioxide and Carbon Monoxide into Methanol with Cobalt Phthalocyanine", *Angewandte Chemie - International Edition*, 2019, **58**, 16172–16176.
(17) Y. Wu, Z. Jiang, X. Lu, Y. Liang and H. Wang, "Domino electroreduction of CO2 to methanol on a molecular catalyst", *Nature*, 2019, **575**, 639–642.
(18) C. Sun, Y. Hou, N. Lüdi, H. Hu, M. de Jesús Gálvez-Vázquez, M. Liechti, Y. Kong, M. Liu, R. Erni, A. V. Rudnev and P. Broekmann, "Improving the lifetime of hybrid CoPc@MWCNT catalysts for selective electrochemical CO2-to-CO conversion", *Journal of Catalysis*, 2022, **407**, 198–205.
(19) J. Chen, J. Li, W. Liu, X. Ma, J. Xu, M. Zhu and Y. F. Han, "Facile synthesis of polymerized cobalt phthalocyanines for highly efficient CO2 reduction", *Green Chemistry*, 2019, **21**, 6056–6061.
(20) M. S. Liao and S. Scheiner, "Electronic structure and bonding in metal phthalocyanines, metal=Fe, Co, Ni, Cu, Zn, Mg", *Journal of Chemical Physics*, 2001, **114**, 9780–9791.
(21) S. A. Al-Tamreh, M. H. Ibrahim, M. H. El-Naas, J. Vaes, D. Pant, A. Benamor and A. Amhamed, "Electroreduction of Carbon Dioxide into Formate: A Comprehensive Review", *ChemElectroChem*, 2021, **8**, 3207–3220.
(22) A. Álvarez, A. Bansode, A. Urakawa, A. V. Bavykina, T. A. Wezendonk, M. Makkee, J. Gascon and F. Kapteijn, "Challenges in the Greener Production of Formates/-Formic Acid, Methanol, and DME by Heterogeneously Catalyzed CO2 Hydrogenation Processes", *Chemical Reviews*, 2017, **117**, 9804–9838.
(23) M. Rumayor, A. Dominguez-Ramos, P. Perez and A. Irabien, "A techno-economic evaluation approach to the electrochemical reduction of CO2 for formic acid manufacture", *Journal of CO2 Utilization*, 2019, **34**, 490–499.

(24) Z. Yang, F. E. Oropeza and K. H. Zhang, "P-block metal-based (Sn, In, Bi, Pb) electrocatalysts for selective reduction of CO2to formate", *APL Materials*, 2020, **8**, 60901.
(25) S. Li, Y. Liu, D. Xu and H.-g. Wang, "Conjugated polycopper phthalocyanine as the anode-active material with high specific capacity for lithium-organic batteries", *Materials Letters*, 2023, **333**, 133682.
(26) M. F. Philips, G. J. M. Gruter, M. T. Koper and K. J. P. Schouten, "Optimizing the Electrochemical Reduction of CO2to Formate: A State-of-the-Art Analysis", *ACS Sustainable Chemistry and Engineering*, 2020, **8**, 15430–15444.
(27) Y. Hori, A. Murata and R. Takahashi, "Formation of hydrocarbons in the electrochemical reduction of carbon dioxide at a copper electrode in aqueous solution", *Journal of the Chemical Society, Faraday Transactions 1: Physical Chemistry in Condensed Phases*, 1989, **85**, 2309–2326.
(28) Y. Hori, H. Wakebe, T. Tsukamoto and O. Koga, "Electrocatalytic process of CO selectivity in electrochemical reduction of CO2 at metal electrodes in aqueous media", *Electrochimica Acta*, 1994, **39**, 1833–1839.
(29) Federal Institute for Geosciences and Natural Resources, *Preismonitor (Report)*, tech. rep., Federal Institute for Geosciences and Natural Resources, 2020, p. 3.
(30) C. X. Zhao, Y. F. Bu, W. Gao and Q. Jiang, "CO2 Reduction Mechanism on the Pb(111) Surface: Effect of Solvent and Cations", *Journal of Physical Chemistry C*, 2017, **121**, 19767–19773.
(31) D. Ewis, M. Arsalan, M. Khaled, D. Pant, M. M. Ba-Abbad, A. Amhamed and M. H. El-Naas, "Electrochemical reduction of CO2 into formate/formic acid: A review of cell design and operation", *Separation and Purification Technology*, 2023, **316**, 123811.
(32) K. Mou, Z. Chen, S. Yao and L. Liu, "Enhanced electrochemical reduction of carbon dioxide to formate with in-situ grown indium-based catalysts in an aqueous electrolyte", *Electrochimica Acta*, 2018, **289**, 65–71.
(33) S. Liu, X. F. Lu, J. Xiao, X. Wang and X. W. Lou, "Bi2O3 Nanosheets Grown on Multi-Channel Carbon Matrix to Catalyze Efficient CO2 Electroreduction to HCOOH", *Angewandte Chemie - International Edition*, 2019, **58**, 13828–13833.
(34) Y. Xing, M. Cui, P. Fan, J. Ren, C. Zhang, N. Li, X. Wen and X. Ji, "Efficient and selective electrochemical reduction of CO2 to formate on 3D porous structured multi-walled carbon nanotubes supported Pb nanoparticles", *Materials Chemistry and Physics*, 2019, **237**, 121826.
(35) T. Burwell, M. Thangamuthu, E. Besley, Y. Chen, J. Pyer, J. Alves Fernandes, A. E. Lanterna, P. Licence, G. N. Aliev, W. Theis and A. N. Khlobystov, "In Situ Transformation of Tin Microparticles to Nanoparticles on Nanotextured Carbon Support Boosts the Efficiency of the Electrochemical CO2 Reduction", *ACS Applied Energy Materials*, 2025, DOI: 10.1021/acsaem.4c02830.
(36) T. Burwell, M. Thangamuthu, G. N. Aliev, S. Ghaderzadeh, E. C. Kohlrausch, Y. Chen, W. Theis, L. T. Norman, J. A. Fernandes, E. Besley, P. Licence and A. N. Khlobystov, "Direct formation of copper nanoparticles from atoms at graphitic

step edges lowers overpotential and improves selectivity of electrocatalytic CO2 reduction", *Communications Chemistry*, 2024, **7**, 140.

(37) K. Fernández-Caso, G. Díaz-Sainz, M. Alvarez-Guerra and A. Irabien, "Electroreduction of CO2: Advances in the Continuous Production of Formic Acid and Formate", *ACS Energy Letters*, 2023, **8**, 1992–2024.

(38) S. Kim, W. J. Dong, S. Gim, W. Sohn, J. Y. Park, C. J. Yoo, H. W. Jang and J. L. Lee, "Shape-controlled bismuth nanoflakes as highly selective catalysts for electrochemical carbon dioxide reduction to formate", *Nano Energy*, 2017, **39**, 44–52.

(39) Z. M. Detweiler, J. L. White, S. L. Bernasek and A. B. Bocarsly, "Anodized indium metal electrodes for enhanced carbon dioxide reduction in aqueous electrolyte", *Langmuir*, 2014, **30**, 7593–7600.

(40) Z. Duan, W. Guo, Z. Fang, G. Xie, G. Mei, X. Lang, D. Liu, Y. Zhai and X. Lu, "Indium Metal Oxide Tandem Ag Catalyst toward Highly Selective CO2 Electroreduction to CO over a Wide Potential Window", *ACS Sustainable Chemistry and Engineering*, 2024, **12**, 9231–9238.

Chapter 2

Electrochemical and Analytical Methods for the Analysis of Electrocatalysts

2.1 Electrochemical Theory

2.1.1 Introduction to electrochemical reactions

Electrochemistry at its core is focussed on the relationship between an applied electrical potential and chemical processes. An electrode reaction is the transfer of electrons to or from a surface. This electrode reaction may be anodic process corresponding to a species being oxidised, or cathodic corresponding to the reduction of a species. Electrode reactions are typically half reactions, *i.e.*:

$$\mathrm{A}^{\mathrm{n}+} + \mathrm{ne}^- \rightleftharpoons \mathrm{A} \tag{2.1}$$

where at the electrode surface, species A^{n+} and A are in dynamic equilibrium with each other due to the need to maintain an overall charge balance.[1] Additionally, as the reaction involves electron transfer, the equilibrium is described by an equilibrium potential (E_e).[1,2]

In practice, a lone half-reactions cannot be dealt with experimentally, as it will remain in equilibrium. Therefore, the introduction of another half-reaction can allow the an electrode reaction to proceed, and this gives the full redox reaction shown in Eq. (2.2).

$$\mathrm{A}^{n+} + \mathrm{ne}^- \rightleftharpoons \mathrm{A} \tag{2.2a}$$

$$\mathrm{B} \rightleftharpoons \mathrm{B}^{m+} + \mathrm{me}^- \tag{2.2b}$$

$$\mathrm{mA}^{n+} + \mathrm{nB} \longrightarrow \mathrm{nB}^{n+} + \mathrm{mA} \tag{2.2c}$$

The introduction of another half reaction consequently results in the addition of another

electrode for said reaction to take place, and with this a corresponding equilibrium potential for the new half reaction. Therefore the overall favourability for the redox reaction can be described by the Gibbs free energy change:

$$\Delta G = -nF(E_e^C - E_e^A) \tag{2.3}$$

where the difference between the equilibrium potentials of the cathode (E_e^C) and anode (E_e^A) determine if the reaction is spontaneous.[1,2] If said redox reaction occurs spontaneously, the movement of electrons can be facilitated via the connection of the cathode and anode via a wire, and charge balancing can be facilitated by having the electrodes in contact with an electrolyte containing mobile ions (which has the added benefit of being able to act as a solvent for the reactants). The result of this experimental set up is known as a galvanic cell, and acts as the simplest description of an electrochemical cell (Fig. 2.1).

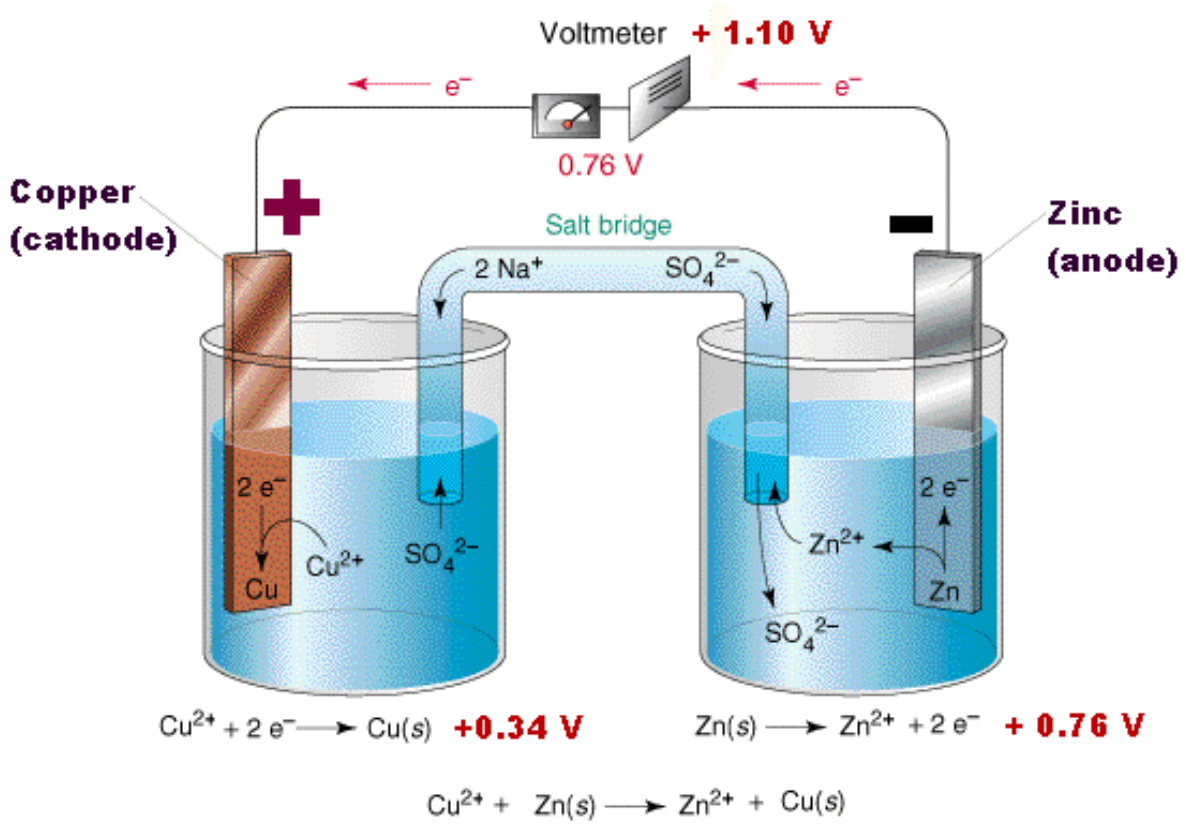


Figure 2.1: Galvanic cell constructed from the Cu^{2+}/Cu and Zn/Zn^{2+} cell. Reproduced from the Georgia Institute of Technology Biological Principles webpage[3]

Galvanic cells are constructed from redox processes that occur spontaneously, *i.e.*:

$$\Delta G < 0 = -nFE_{cell} \tag{2.4}$$

However, most redox processes of analytical interest are non-spontaneous redox processes, *i.e.*:

$$\Delta G > 0 = -nFE_{cell} \tag{2.5}$$

therefore, to facilitate non-spontaneous reactions we must apply an external potential across the cathode and anode greater than $(E_e^C - E_e^A)$ to have the reaction proceed.[1,2]

Regardless of spontaneity, the rate of the electrochemical reaction, *i.e.* the current i, depends on the kinetics of the two electrode reactions, and for the ions to move through solution in the electrolyte energy must be supplied, thus the overall cell voltage (V) to have a reaction to proceed is given by:

$$V = (E_e^C - E_e^A) - |\eta_A| - |\eta_C| - iR \tag{2.6}$$

where R is the resistance of the electrolyte solution and η is the overpotential, defined as deviation of the potential from the equilibrium value (more simply thought of in this case as the potential being applied to to the electrode for a given reaction).[1,2] From Eq. (2.6) we can see it is necessary to both minimise the solution resistance iR to obtain information about the system. Additionally, in a two electrode cell both overpotential terms will vary, meaning the experimentally derived V and i will have little value.[1] Therefore, it is necessary to design the experimental set up so that the V and i data collected corresponds to one electrode only, which can be achieved via the addition of a third reference electrode to the cell, of which the potential of the electrode of interest can be controlled against.[1,2]

Finally, combining all of these elements together results in a three electrode cell capable of analytical electrochemistry.[1,2] This cell is composed of:

- A potentiostat - An external, controllable source of applied voltage capable of measuring current
- The working electrode - the electrode where current is measured.
- The reference electrode - an electrode with an invariate potential to measure the working electrode against.
- The counter electrode - an electrode that can facilitate an electrode reaction via charge balancing from the facilitation of an opposing half reaction.

By varying the potential at the working electrode, it is possible to analyse reaction processes taking place at the working electrode.[1,2] As previously discussed, the applied potential is analogous to the energy required to drive a reaction, so therefore the observed current that results is analogous to electrochemical rate.[1,2] This is because electron transfer to the analyte is accompanied by the movement of ions in solution and electrons through the external circuit as a measurable current, so therefore the amount of current i passed from the working to the counter electrode in an amount of time t can be equated to the number of electrons z transferred to the moles of starting material n, given by the charge Q as described by Faraday's law[1,2]:

$$Q = \int_0^t idt = nzF \tag{2.7}$$

Lastly, it is more useful to have i account for the electrode area, as the current is always dependant on it in the examples given in this work, therefore current i can be converted into current density j by simply dividing it by the electrode area A.[1,2]

$$j = \frac{i}{A} \tag{2.8}$$

Additionally current density j is more meaningful for electrocatalytic analysis as it normalises the activity of electrodes with large variances in surface area.

2.1.2 Electrochemical kinetics

To further understand the information obtained from the analytical electrochemistry, we must first further explore the electrochemical kinetics of an electron transfer reaction at an electrode.

Consider a two-electrode cell containing a redox active species in which the counter electrode has a invariate potential of 0 V, and which no current is flowing through the cell and the potential of the working electrode is given by the Nernst Equation (Eq. (2.9)).[1,2]

$$E_e = E_e^\circ + \frac{RT}{nF} ln \frac{[Ox]^\sigma}{[Red]^\sigma} \tag{2.9}$$

Where E_e is the equillibrium potential, and is related to the E_e° standard potential of the couple Ox/Red, $[Ox]^\sigma$ and $[Red]^\sigma$ are the concentrations of the oxidised and reduced analyte at the electrode surface (concentrations are used as activities are assumed unity),

F is Faraday's Constant, n is the number of electrons, T is the temperature, and R is the ideal gas constant.[1,2,4]

From Eq. (2.9) it can be seen that the standard potential E_e° is the equillibrium potential E_e when the surface concentrations of Ox and Red are equal ($\ln 1 = 0$). As no current is flowing through the cell, the surface concentrations of $[Ox]^\sigma$ and $[Red]^\sigma$ must be equal to the bulk concentrations $[Ox]^\infty$ and $[Red]^\infty$, therefore the difference between the cathode and anode potentials E_{cell} can be given by (Eq. (2.10)).[1,2]

$$E_{cell} = E_e^\circ + \frac{RT}{nF} ln \frac{[Ox]^\infty}{[Red]^\infty} \tag{2.10}$$

Whilst no net current is flowing there is no chemical change, meaning the concentrations of Ox and Red are in equillibrium, meaning that the oxidation and reduction of Ox and Red are at equal rates and therefore an associated current will exist for each process, but there is no net current flow (Eq. (2.11)).[1,2]

$$-j_{red} = j_{ox} = j^\circ \tag{2.11}$$

Where j^o is the exchange current density, and $j_{ox/red}$ is the partial current density of the oxidation and reduction reactions with the negative sign being the cathodic current by convention.[1,2] The exchange current density is the current at zero potential and with no net chemical process occurring,[1,2] and is more conveniently thought of for future explanation as the baseline current that is modified by electrochemical parameters to give the net current flow. If the applied potential to the working electrode results in the E_{cell} being more negative than the standard potential E_e° determined by bulk concentrations of Ox and Red in Eq. (2.10), then equilibrium can only be restored when the surface concentrations have changed to satisfy Eq. (2.9) at the applied potential.[1,2] This results in a required change to the ratio of $[Ox]^\sigma/[Red]^\sigma$ which can only be achieved via the conversion of Ox to Red via the passage of cathodic current and vice versa for anodic current.

This explains the why electrochemical reactions proceed thermodynamically under an applied potential, but does not provide information on the magnitude of current, only whether it would be positive or negative. The determining factor for current magnitude are the electron transfer kinetics associated with a given electrode reaction.[1,2] Firstly, the net current can be thought of as the summation of all electron transfers happening at any potential[1,2]:

$$j = j_{red} + j_{ox} \tag{2.12}$$

and each of the partial current densities (analogous to electrochemical rate) $j_{ox/red}$ depends on a rate constant and the concentration of the redox active species at the site of electron transfer via Eqs. (2.13) and (2.14)

$$j_{red} = -nFk_{red}[Ox]^{\sigma} \tag{2.13}$$
$$j_{ox} = nFk_{ox}[Red]^{\sigma} \tag{2.14}$$

with the rate constant $k_{ox/red}$ being dependant on the potential at the electrode surface during electrode transfer, as given by Eqs. (2.15) and (2.16)

$$k_{red} = k^{\circ}_{red} \exp\left(-\frac{\alpha_C nF}{RT}E\right) \tag{2.15}$$
$$k_{ox} = k^{\circ}_{ox} \exp\left(\frac{\alpha_A nF}{RT}E\right) \tag{2.16}$$

where $k^{\circ}_{ox/red}$ is the rate constant at 0 V and $\alpha_{C/A}$ is the charge transfer coefficient for the cathodic or anodic reaction.[1,2] $\alpha_{C/A}$ is the fraction of the infacial potential at the electrode-electrolyte interface that lowers the free energy barrier of an electrochemical reaction in a given direction. It can also be thought of as the fractional charge on the reacting ion in the transition state.[5] Defining overpotential as $\eta = E - E_e$ and noting that at $\eta = 0$ there is no net chemical change occurring, *i.e.* the current density j is the exchange current density $j_{\circ}$ (Eq. (2.11)), meaning Eqs. (2.13) to (2.16) can be manipulated into to give an overarching equation governing electrode transfer kinetics known as the Butler-Volmer equation (Eq. (2.17)).[1,2,6]

$$j = j^{\circ}\left[\exp\left(\frac{\alpha_A nF}{RT}\eta\right)\right] - \left[\exp\left(\frac{\alpha_C nF}{RT}\eta\right)\right] \tag{2.17}$$

The Butler-Volmer equation is essentially the basis for electrode kinetics governed by electron transfer, the concepts and derivation of which being fundamental in understanding the experimental work conducted in this thesis (Section 2.2.1). The Butler-Volmer equation shows how the current density (j) depends on exchange current density ($j_{\circ}$), applied potential (η), and charge transfer coefficients (α), with α and $j_{\circ}$ being parameters that by themselves can characterise the kinetics of an electrode reaction in it's entirety.[1,2]

However, as will be explored in Section 2.3.3 the determination of these parameters in practice is requires specific conditions to be met, and is potentially inapplicable for certain electrode reactions.

2.2 Electrochemical Techniques

2.2.1 Voltammetry

Voltammetry is a series of electrochemical techniques in which an applied potential is varied and the resulting current is recorded. The measured current is a result of both the capacitive current from the double layer charging, and redox reactions in the solution or at the electrode surface.[2,4] The voltammetric techniques in this work can be distinguished into two types: Cyclic Voltammetry (CV) and Linear Sweep Voltammetry (LSV). In LSV, an applied potential is linearly increased positively (anodic) or negatively (cathodic) at a constant Scan rate from a starting potential E_0 to a final potential E_1, with current increases (in an anodic sweep) and decreases (in a cathodic sweep) taking the form of peaks and correspond to oxidation or reduction reactions of the analyte at the electrode respectively.

In CV, The potential is linearly swept at a constant scan rate v from a starting potential E_0 to a potential E_1 and then the scan is reversed until reaching potential E_2. Following which the scan will either end or reverse again until reaching an end point potential. As in LSV, the peaks in the voltammogram corresponding to either oxidation or reduction reactions of the analyte, with anodic and cathodic peaks able to be coupled to each other as the corresponding inverse processes due to the voltammogram potentially encompassing both.[1,2,4]

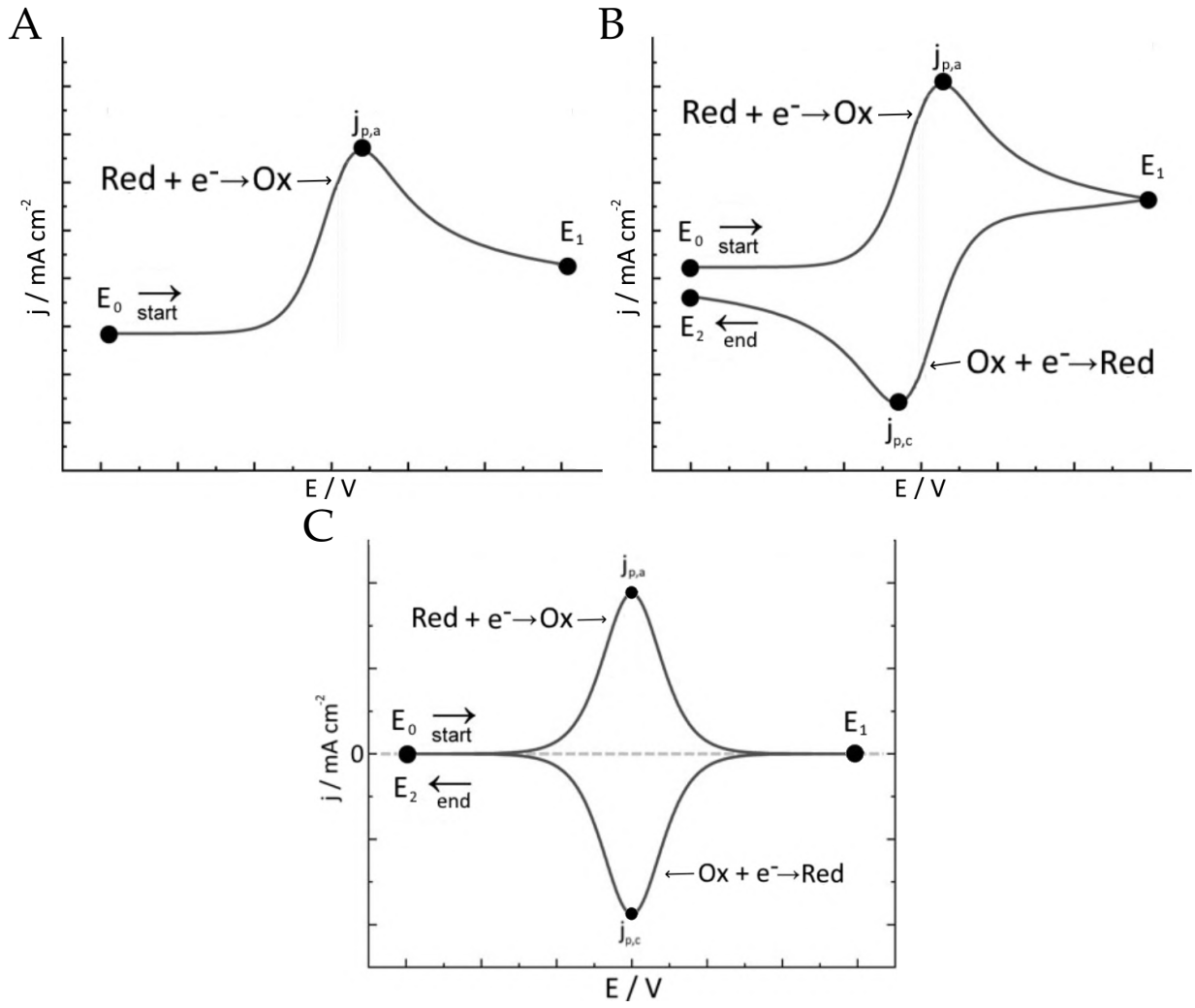


Figure 2.2: (A) Example LSV of an anodic scan in which solvated species *Red* is oxidised to species *Ox* via the loss of an electron, in which the starting potential E_0, end potential E_1, and peak anodic current $j_{p,a}$ are labelled; (B) Example CV in which solvated species *Red* is oxidised to species *Ox* on the anodic scan, and reduced back to species *Red* on the cathodic scan, in which the starting potential E_0, turn around potential E_1, second turn around potential (and end point) E_2, and peak anodic $j_{p,a}$ and cathodic $j_{p,c}$ current are labelled; (C) Example CV in which the surface confined species *Red* is oxidised to species *Ox* on the anodic scan, and reduced back to species *Red* on the cathodic scan, with the baseline highlighted by a gray dashed line with other notable points labelled as they were in (B). All figures reproduced from Yamada *et al*[7] and then modified to suit the explanation in this work.

The peak shape in voltammetry which corresponds to either a reduction or oxidation processes during the potential sweep arises for different reasons depending on whether the analyte is in solution or is confined to the surface of the electrode, and understanding these differing reasons is relevant for this work as it is the rationale why the voltammetry peaks observed in this body of work can be definitively assigned to the surface confined electrocatalysts.

To explain the origin of the peak shape in voltammetry, consider the oxidation reaction:

$$\text{Red} + \text{e}^- \longrightarrow \text{Ox}$$

occurring at the electrode surface. The equations Eq. (2.14) and Eq. (2.16) (Section 2.1.2) govern the electrochemical rate *i.e.* current and the associated rate constant of this oxidation reaction.

$$j_{ox} = nFk_{ox}[Red]^{\sigma} \tag{2.14}$$

$$k_{ox} = k_{ox}^{\circ} \exp\left(\frac{\alpha_A nF}{RT}E\right) \tag{2.16}$$

In voltammetry, once the applied potential E is sufficient for the oxidation to proceed, the recorded current will increase via Eq. (2.14) in the voltammogram. This is associated with a shift in the equilibrium of Ox $\rightleftharpoons$ Red at the surface of the electrode predicted by the Nernst Equation (Eq. (2.9)) resulting in a decrease in $[Red]^{\sigma}$.

As E is further swept forward and increased, the recorded current j_{ox} continues to increase, despite the now lowered concentration of Red at the electrode surface. This is due to the exponential dependency of k_{ox} on E, making the decrease in $[Red]^{\sigma}$ negligible with respect to the overall recorded current associated with the oxidation j_{ox}. Therefore the recorded current j_{ox} continues to increase and $[Red]^{\sigma}$ continues to decrease as the potential is increased until all of the electroactive material at the surface is depleted ($[Red]^{\sigma} = 0$) and the anodic peak current $j_{p,a}$ is reached. The electrochemical rate j_{ox} is now no longer kinetically limited by the rate of electron transfer, but instead has become mass transport limited as the delivery of further *Red* to the surface of the electrode is much slower than the rate of electron transfer. Once the peak current $j_{p,a}$ has been reached and the applied potential continues to increase, it is necessary to distinct whether or not the analyte *Red* exists solely as surface confined analyte, or was in solution phase where there exists a bulk concentration of the reactant $[Red]^{\infty}$ in the electrolyte, as these will dictate the current response beyond $j_{p,a}$.

In the case of a solution phase analyte, diffusion of *Red* to the surface from the bulk concentration of analyte $[Red]^{\infty}$ becomes the rate determining factor, as the rate of electron transfer to the analyte is much faster by comparison. This diffusion limited rate is therefore dependant on the flux of analyte to the electrode and thus is governed by Fick's laws of diffusion (Eqs. (2.18) and (2.19))[1,2]

$$\text{Flux} = -D_a \frac{d[a]}{dx} \tag{2.18}$$

$$\frac{\partial[a]}{\partial t} = D_a \frac{\partial^2[a]}{\partial x^2} \tag{2.19}$$

in which the first law (Eq. (2.18)) describes the flux of species a at distance x through a plane parallel to the electrode surface (assuming the electrode is a one-dimensional plane) and the second law (Eq. (2.19)) describes the change in concentration of species a with respect to time due to diffusion where D_a is the diffusion coefficient.[1,2]

Application of Ficks Laws with boundary conditions describing this particular experiment give Eqs. (2.20) and (2.21).[1,2]

$$\frac{j}{nF} = -D_{Red} \left(\frac{d[Red]}{dx} \right)_{x=0} \tag{2.20}$$

$$\frac{\partial[Red]}{\partial t} = D_{Red} \left(\frac{\partial^2[Red]}{\partial x^2} \right)_{x=0} \tag{2.21}$$

Practically, Eq. (2.20) states that the steeper the concentration gradient of *Red* between the bulk concentration and electrode surface (x=0), the greater the rate of diffusion of *Red* and hence, the greater the current response. Additionally, Eq. (2.21) states that the concentration gradient of *Red* will decrease over time as diffusion is naturally acting to minimise said gradient, therefore the current response will also decrease. In terms of the voltammetric response, this means that after the peak current $j_{p,a}$ has been reached, the current response, now limited by diffusion, will decrease as time increases. Since in voltammetry the potential is swept incrementally over time, this means that the current response in the voltammogram will decrease, but crucially never reach zero as there is flux of *Red* continually to the electrode as the potential to reduce *Red* has been reached. The solutions to Eqs. (2.20) and (2.21) for a single potential step is given by the Cottrell equation (Eq. (2.22)), whilst the solution for a potential sweep experiment is given by the Randles-Sevcik equation (Eq. (2.23)).

$$j = \frac{nF\sqrt{D}[Red]^{\infty}}{\sqrt{\pi}\sqrt{t}} \tag{2.22}$$

$$j_{peak} = 0.4463nFAC\frac{nFvD}{RT}^{\frac{1}{2}} \tag{2.23}$$

It is important to note that for electrode processes that are diffusion limited, introducing convection as a mode of mass transport via stirring or use of an Rotating Disk Electrode (RDE) would result with no decrease in current being observed. This is due to the fact that the concentration *Red* at the electrode surface would never reach zero, and thus the current would continue to increase before reaching a current plateau dictated by the rate of mass transport (with this property being the basis of hydrodynamic voltammetry techniques).[1,2]

In the case of a surface confined analyte, defined here as an analyte in which the electrochemical process does not involve any solution phase reactants, diffusion limitations do not apply as there is no further *Red* to be delivered from the bulk as all of the *Red* exists on the surface of the electrode. In terms of voltammetric response, after reaching the peak current $j_{p,a}$, all of the *Red* will have been converted into Ox and as a result the recorded current j will fall back to 0 regardless of mass transport effects, assuming the analyte is catalytically inactive to species in the electrolyte. Practically, this means that if a electrolyte solution is experiencing convection (stirring), a peak shape will still arise if it is a surface confined analyte.

Due to the fact there is a fixed amount of *Red* on the surface, the voltammogram peaks of surface confined peaks will ideally be sharp, the oxidation and reduction peaks tend to be symmetrical and of equal peak height and width with little to no peak to peak separation (See Fig. 2.2C). Caution must be taken however, as these characteristics do not always arise, particularly in this work, largely due to energy barriers associated with electron transfer from the surface to the adsorbed species and also due to incomplete conversion of a species into its reduced/oxidised form due to chemical transformations after the redox reaction (CO_2 binding for example). The peak current density j_{pc} for a one electron reversible surface confined process can be given in a general form by Eq. (2.24)

$$j_{pc} = \frac{n^2F^2\Gamma_{Red}}{4RT}v \tag{2.24}$$

where Γ_{Red} is the surface excess of *Red* before application of potential and is given by

$$\Gamma_{Red} = \left|\frac{Q}{nF}\right| \tag{2.25}$$

where Q is the charge associated with the oxidation of *Red*. Notably, Eq. (2.24) reveals that the current is linearly proportional to the scan rate $i \propto v$, unlike the case for solution phase voltammetry where the current is proportional to the inverse square of the scan rate $i \propto \sqrt{v}$ (as shown by Eq. (2.22)).

Further theory associated with surface confined equations quickly becomes too broad in scope to warrant further discussion in this work given the variety of adsorption isotherms and electrochemical processes that can occur and influence the electrode reaction, so further discussion will be left to literature.[8,9]

Taking all of this into consideration, it is possible to determine criteria for whether a given redox peak can be attributed to a surface confined or solution phase process, with these criteria being:

1. The current returns to the baseline current from prior to the redox event
2. Peak shapes pertaining to surface confined analytes are still present whilst the solution is being stirred
3. Current will be linearly proportional to the scan rate $i \propto \#$ rather than to the square root of scan rate $i \propto \sqrt{v}$)

Whilst all of the above criteria will be indictive of a surface confined process, the criterion that will always be true regardless of specific cases is the point of stirring, *i.e.* a surface confined processes will not depend on mass transport. The baseline current point can be impacted by catalytic processes, which is particularly relevant for this work as there will be continued electrochemical processes after and sometimes before a surface confined peak. Additionally, the presence of electrocatalysis can likely convolute determining the scan rate proportionality, as electrocatalytic processes, particularly CO_2RR are diffusion controlled and result in a current response. Therefore, the simplest way to ensure a voltammetric peak response has arisen from a surface confined electrocatalyst is to introduce convection to the cell, which was achieved in this work by conducting voltammetry with an RDE at a constant, large rotation rate sufficient to introduce a large amount of convection so that solution phase processes will only have an associated current rise and not a characteristic peak shape (See Section 2.3.4.2).

2.2.2 The Diffusion Layer

As previously discussed in Section 2.2.1, the current of an electrode process in which an analyte exists within the solution (e.g. CO_2RR) will be limited by diffusion once the concentration of analyte at the surfaces reaches zero. The diffusion gradient between the bulk and the electrolyte results in a zone known as the diffusion layer, where the electrolyte concentration differs its bulk value. A simplified Nernst model of the diffusion layer is shown below in Fig. 2.3.

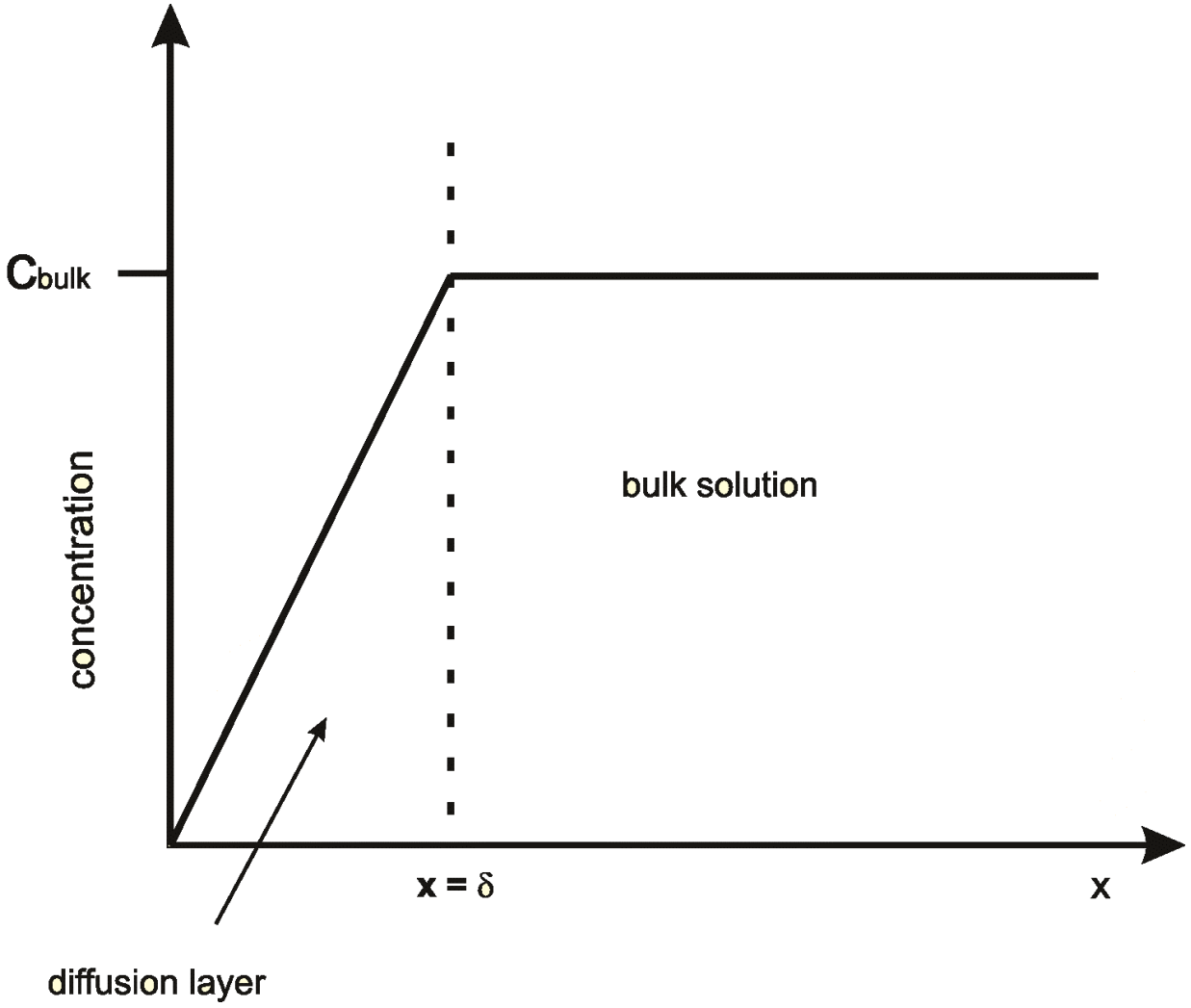


Figure 2.3: Nernst model of the diffusion layer

At distances between $x = 0$ and $x = \sigma$, natural convection is lessened and diffusion is the dominant mass transport regime for the analyte, resulting in the concentration changes of analyte being described solely by Fick's laws (Eqs. (2.20) and (2.21)), with the current being limited by the rate of diffusion *i.e.* the concentration gradient. The thickness of the diffusion layer will directly impact the limiting current, with smaller diffusion layers providing steeper gradients and therefore higher rates of diffusion. The Cottrell equation (Eq. (2.22)) and Randles-Sevcik equation (Eq. (2.23)) can therefore describe the diffusion layer thickness in terms of the parameters D and $\sqrt{v}$. Experimentally, this results in changes in scan rate changing the size of the diffusion gradient, with smaller scan rates having a larger gradient and therefore lower current and higher scan rates resulting in a smaller gradient and therefore higher current.

2.2.3 Diffusion in Nanoparticle Modified Electrodes

The diffusion behaviour of a nanoparticle modified electrode is distinct to the previously discussed flat one-dimensional electrode assumed in Section 2.2.1, as electrochemical reactions will occur at a nanoparticle surface, adding additional complexity with regards to the diffusion behaviour at the electrode. Consider a planar nanoparticle-modified electrode in which electrochemical reactions occur exclusively at the nanoparticle surface and the nanoparticles are randomly distributed on the electrode surface. For modelling this system, the nanoparticles can either be spherical or hemispherical and are shown in Fig. 2.4.

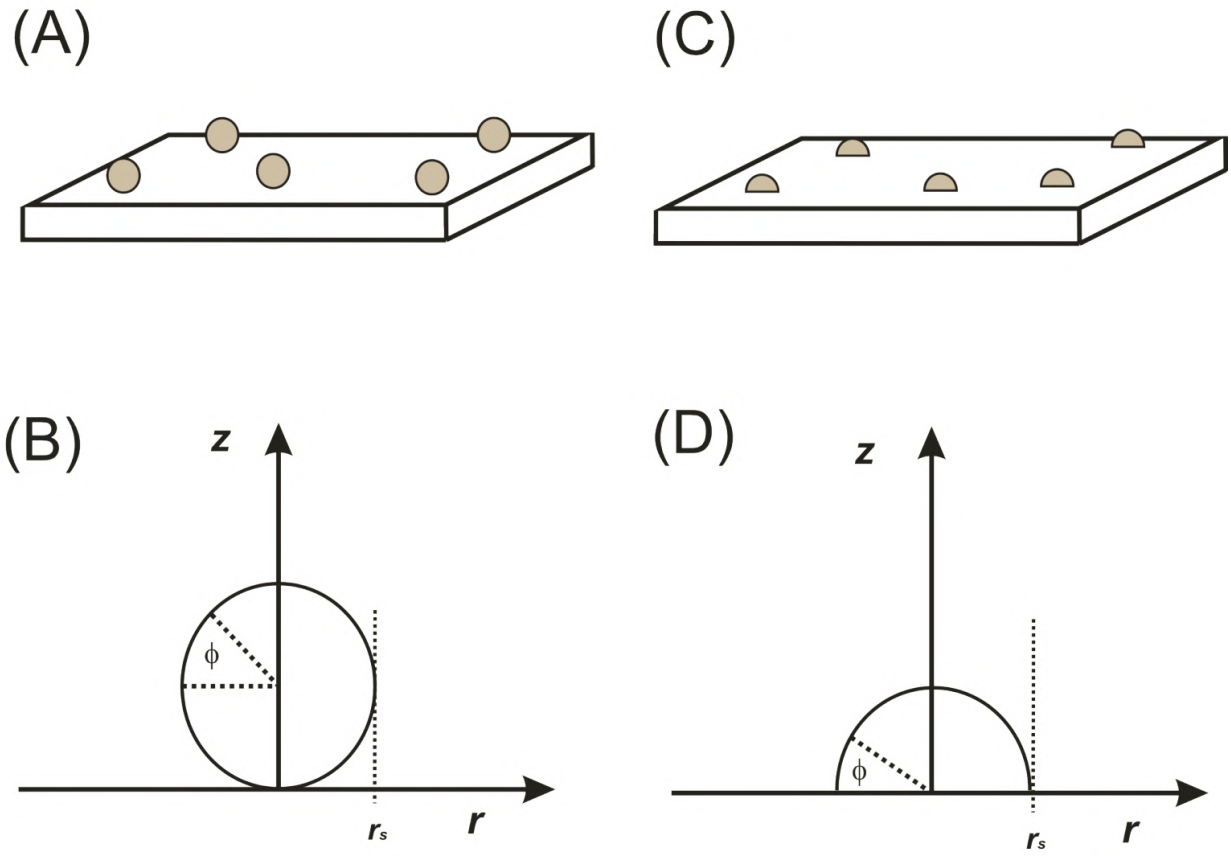


Figure 2.4: (A) Spherical nanoparticle-modified planar electrode; (B) single spherical nanoparticle; (C) hemispherical nanoparticle-modified planar electrode; (D) single hemispherical nanoparticle. Reproduced from Streeter *et al.*[10]

The diffusion limited current for a single spherical nanoparticle can be found by solving Fick's second law of diffusion (Eq. (2.21)) in cylindrical polar coordinates, and is given for a spherical and hemispherical nanoparticle in Eq. (2.26) and Eq. (2.27) respectively.

$$i_{lim} = -8.71nFDr_s[A]_{bulk} \tag{2.26}$$

$$i_{lim} = -2\pi nFDr_s[A]_{bulk} \tag{2.27}$$

Where i_{lim} is the diffusion limited current, D is the diffusion coeffeicient, r_s is the radius of the nanoparticle, and $[A]_{bulk}$ is the concentration of the analyte in the bulk solution. The derivations of these equations are beyond the scope of this work, and originate from Brookes *et al*[11] who initially modelled these systems. The current as described by Eq. (2.26) and Eq. (2.27) is dependant on the nanoparticle radius, rather than area as is the case for planar electrodes, indicating a convergent diffusion around the nanoparticle.[10] As will be seen in later results chapters, the nanoparticles in this work are not perfectly spherical, and therefore the limiting current will be given by Eq. (2.28).

$$i_{lim} = -JnFD[A]_{bulk}\sqrt{\frac{a^2 + b^2}{2}} \tag{2.28}$$

Where J is the flux density of the analyte, and a and b are the equatorial and polar radius of the nanoparticle.[10] For any shape of nanoparticle, as the scan rate increases, the diffusion layer will become increasingly compressed around the nanoparticle, increasing not only the current, but the uniformity of the local current density as a function of the angle around the nanoparticle. This is demonstrated in Fig. 2.5 below.

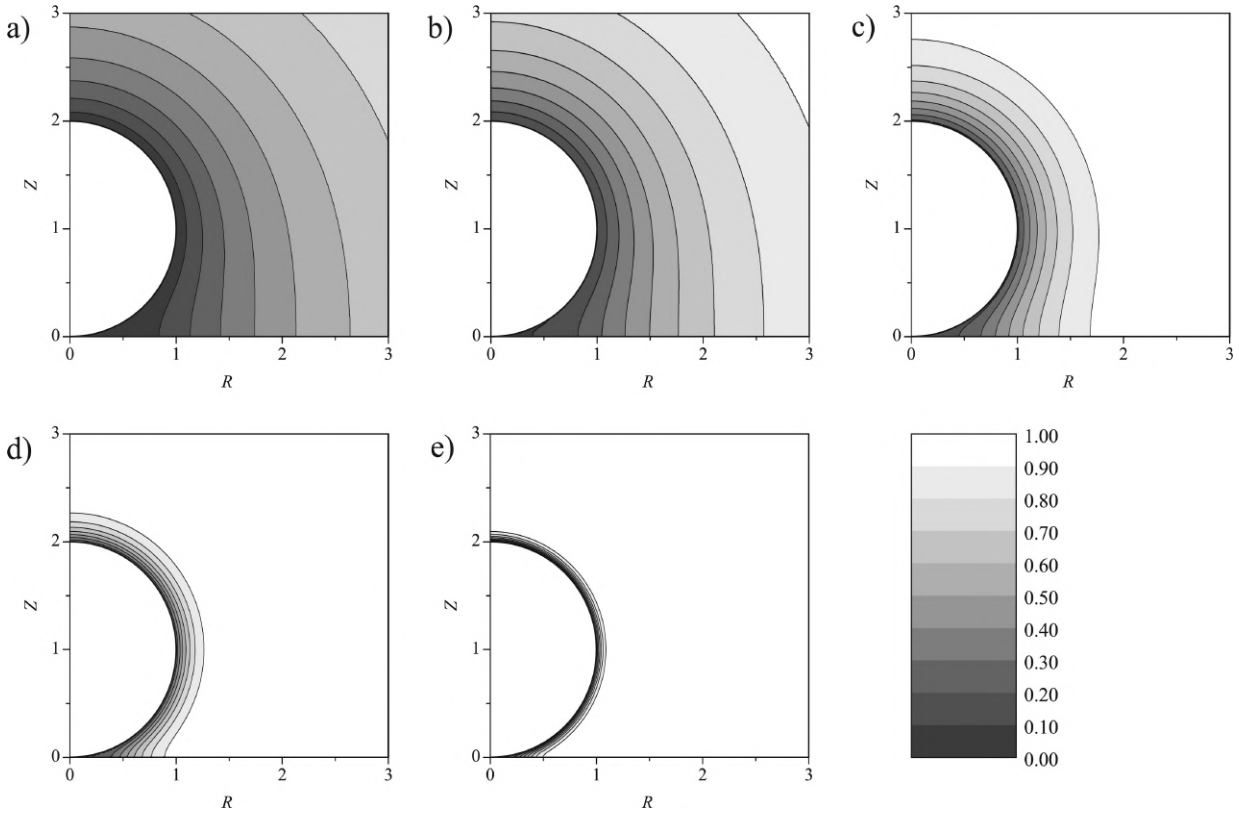


Figure 2.5: Simulated concentration profile of analyte around a spherical nanoparticle with increasing dimensionless scan rate σ: (a) $\sigma = 0.1$; (b) $\sigma = 1$; (c) $\sigma = 10$; (d) $\sigma = 100$; (e) $\sigma = 1000$. Adapted from Streeter *et al*.[10]

This change in the concentration profile around a nanoparticle results in the voltammetry significantly differing at various scan rates, with higher scan rates having planar diffusion behaviour, and lower scan rates having a near steady-state profile, akin to the profile of a planar electrode under convection (Fig. 2.6).

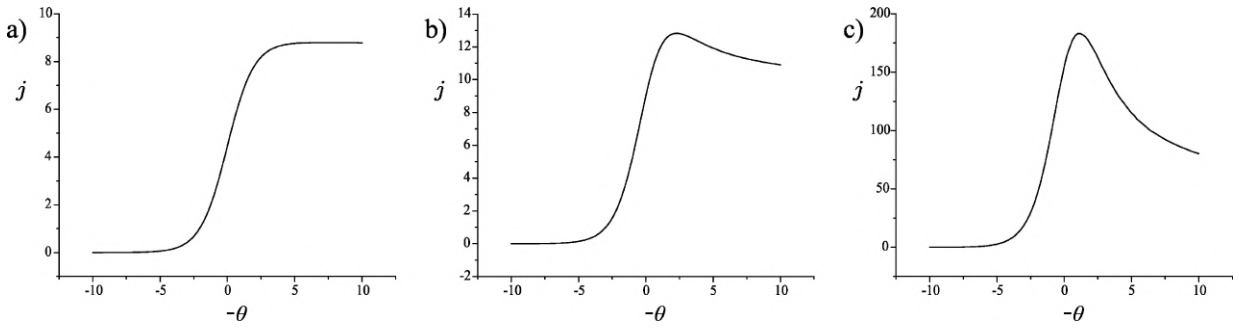


Figure 2.6: simulated voltammetry for a reversible electron transfer at a spherical nanoparticle with dimensionless scan rates of: (a) $\sigma = 10^{-3}$; (b) $\sigma = 1$; (c) $\sigma = 1000$. Adapted from Streeter *et al*.[10]

Typically, it is usually the case in electrocatalytic studies that an electrode is not comprised of a single adsorbed nanoparticle, but rather multiple nanoparticles randomly distruted in a nanoparticle array. When an electrode has sufficient coverage of nanoparticles such

that their diffusion layers can interact, the current per nanoparticle is less than that which would be predicted for a single isolated nanoparticle. As outlined by Davies *et al*,[12] there are four cases of diffusion that can impact voltammetry based off of the positioning of the nanoparticles on the electrode. The four cases are shown in Fig. 2.7

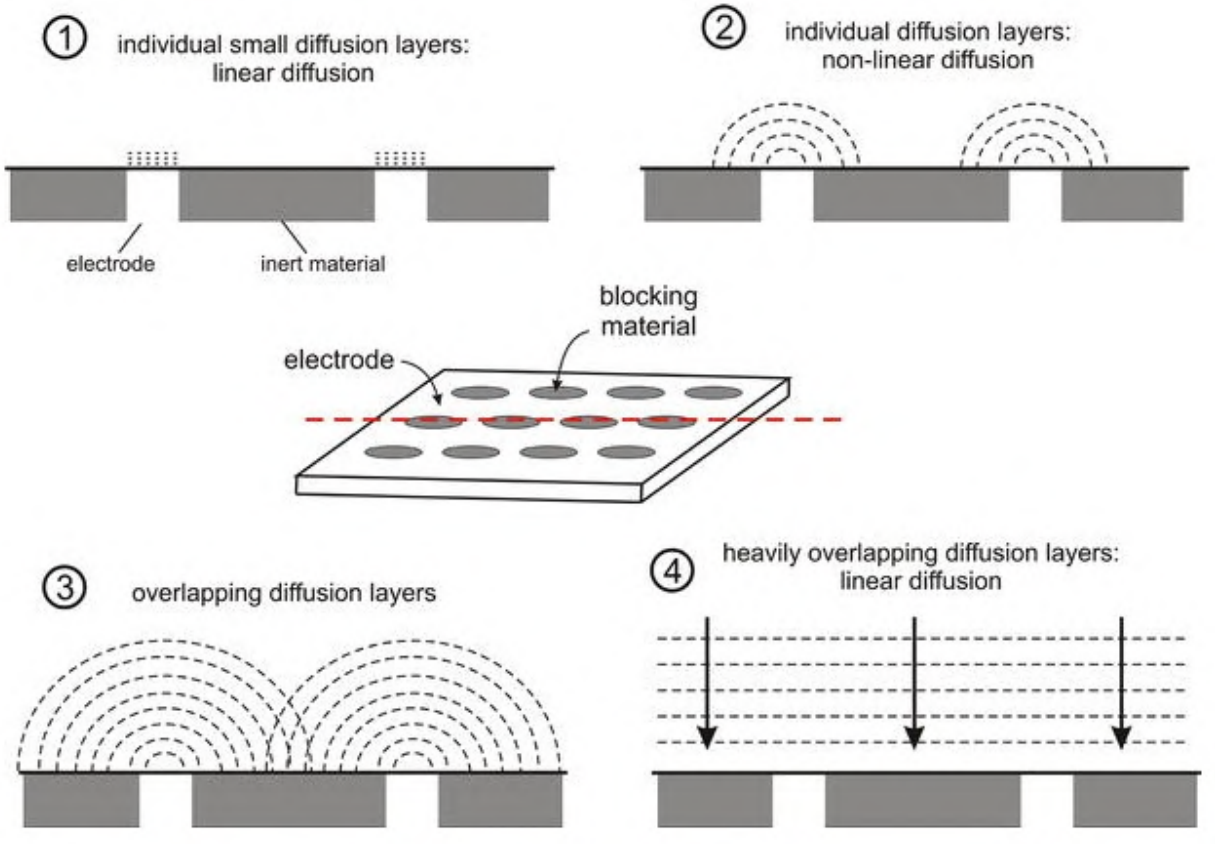


Figure 2.7: The four cases of varying diffusion layers of nanoparticles on a planar electrode (shown in center with nanoparticles labelled as blocking material). (1) Planar diffusion in nanoparticles on the electrode at fast scan rates where the diffusion layers of individual nanoparticles are compressed; (2) Non-planar diffusion at nanoparticles on the electrode at slow scan rates where the diffusion layers are large; (3) Diffusion layer overlap between closely adjacent nanoparticles resulting in convergent diffusion; (4) Diffusion layer of multiple nanoparticles overlap so heavily that the diffusion layers merge into linear diffusion zone over the entirety of the electrode area. Reproduced from Davies *et al*[12]

The four cases shown above in Fig. 2.7 result in changes in diffusional behaviour, and thus varying voltammetric response. The first (1) and second case (2) describe isolated nanoparticle behaviour at high and low scan rates as previously discussed. The third case (3) shows diffusion layer overlap between two nanoparticles establishing a non-linear and convergent diffusion regime with an overlap region. The non-linear diffusion and overlapping diffusion layers results in a voltammetry response that is difficult to model, but presents as a combination of the peak response for Case 1 and 2. The fourth case (4) shows the diffusion layers between nanoparticles overlapping so heavily that the entire electrode experiences linear diffusion, so that the peak response behaves similarly to

that of an electrode with no nanoparticles on the surface *i.e.* linear diffusion as modelled by Fick's laws. Example voltammetry responses for the four cases are shown below in Fig. 2.8

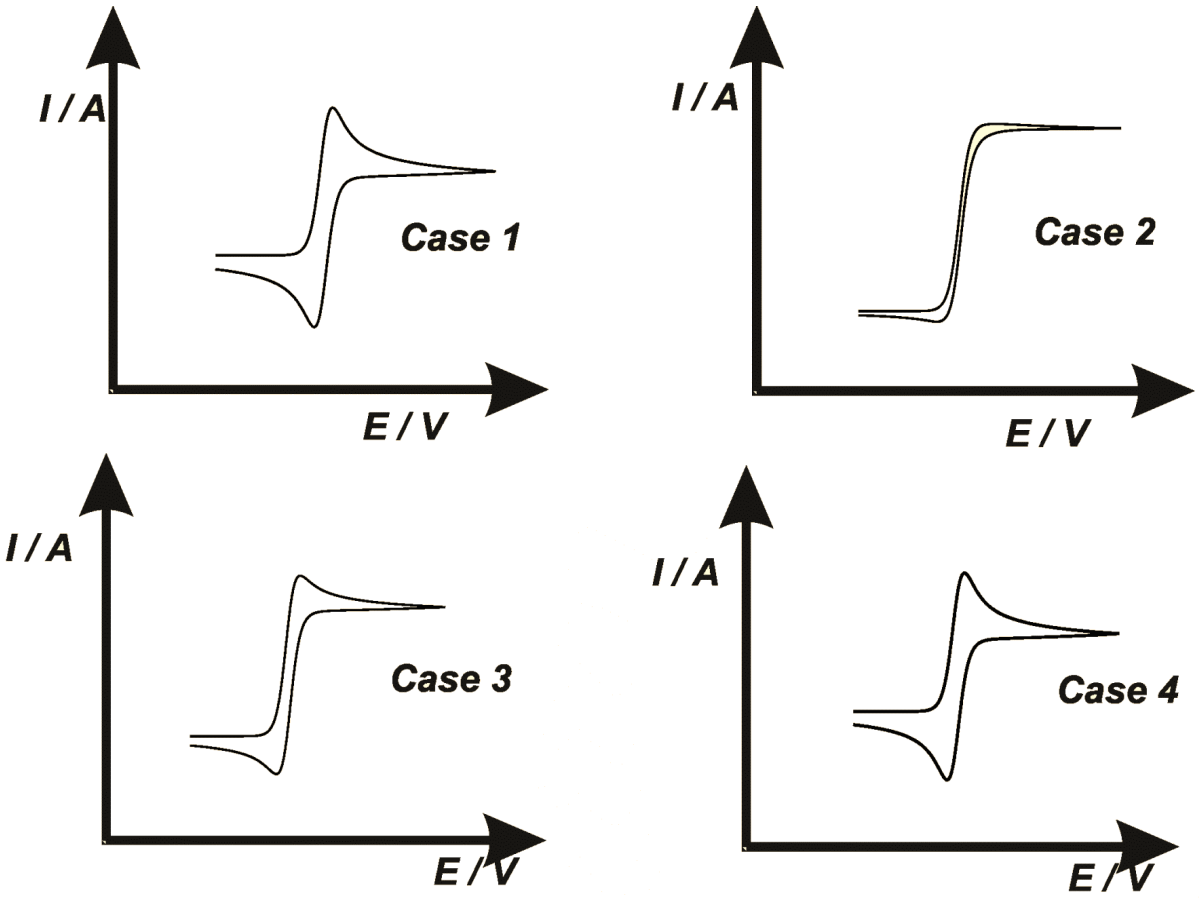


Figure 2.8: Example CV responses for cases 1-4 for nanoparticle diffusion, corresponding to (1)-(4) in Fig. 2.7 Reproduced from Fallyn W. Campbell.[13]

The work contained in Chapter 5 features random nanoparticle distribution on MWNTs, meaning that the voltammetry response for electroactive species diffusion to the electrode will be dependant on the diffusion behaviour outlined in this section. In this work, the main species that will diffuse to the nanoparticle sites will be CO_2, which the diffusion of is associated with an electrocatalytic current and cannot be discussed in relation to the theory found in this section. However, this can be applied to reactions of the nanoparticles with solution phase species that are not catalytic in nature.

2.2.4 Electrical Double Layer and Non-Faradaic Current

Placing a charged surface, such as the electrode, into a solution of ions will result in attraction of ions of opposite charge and repulsion of like charges. This ion distribution in the immediate vicinity of the electrode surface is known as the electrical double layer.[1,2]

The structure of the electrical double layer can modelled by the Stern model,[1,2] which describes the structure of the electrical double layer as composed of multiple layers which describe the ion distribution as the distance from the electrode increases.[1,2]

The Stern model of the elecrical double layer for a positively charged metal surface in an ionic solution is shown below in Fig. 2.9.

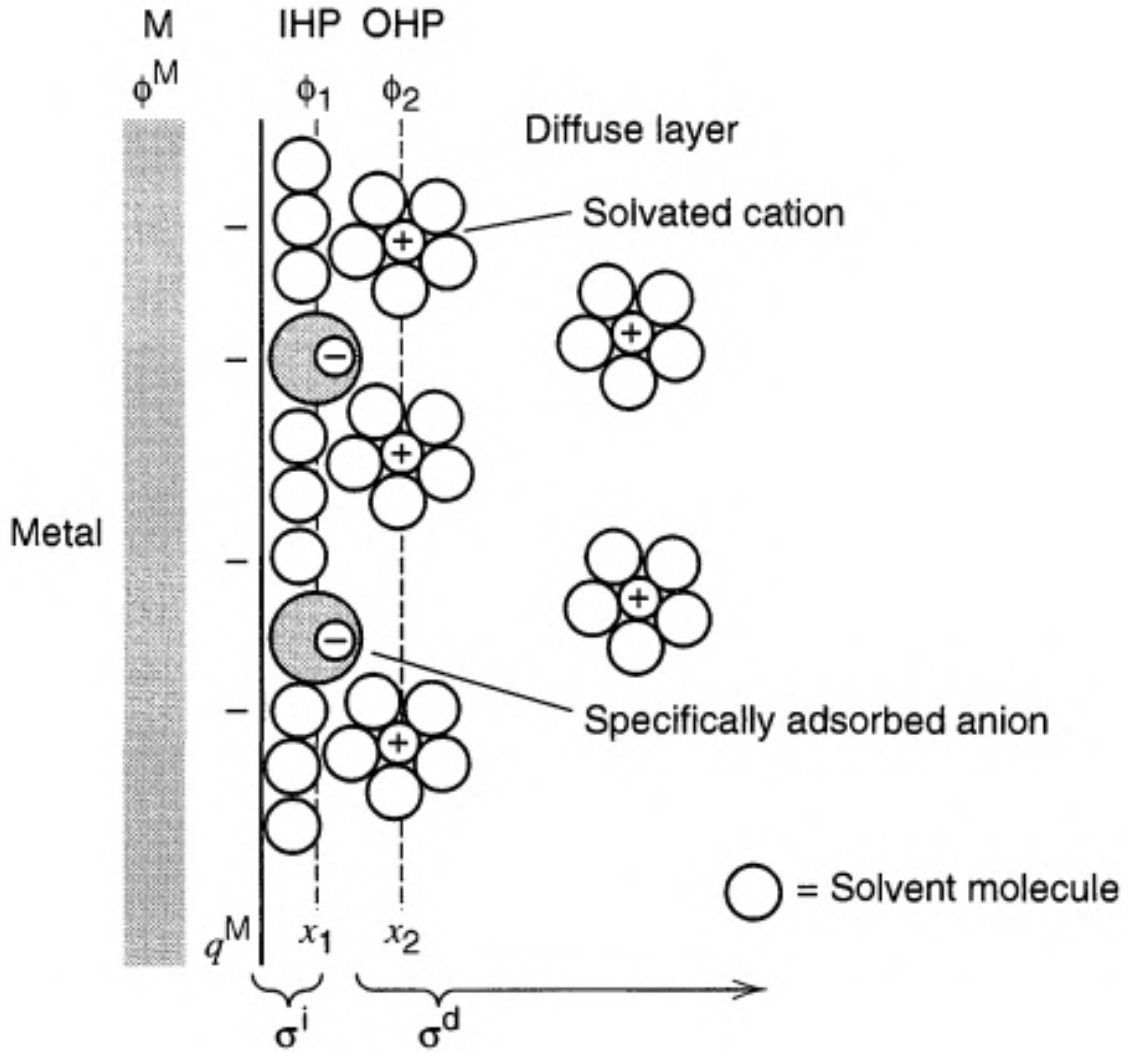


Figure 2.9: Stern model of the electrical double-layer under conditions in which anions are specifically adsorbed to a positively charged metal surface. Adapted from Bard and Faulkner.[2]

The model describes three layers that compose the electrical double layer region: the inner Helmholtz plane (IHP), the outer Helmholtz plane (OHP), and the diffuse layer. The IHP, also known as the stern layer, is the layer closest to the electrode, being composed of ions and solvent molecules on the electrode that are specifically adsorbed[2] The IHP is defined as the axis through the centre of the specifically adsorbed ions on the electrode

surface x_1. The OHP is composed of solvated ions that can approach the electrode surface only to a distance x_2, and is defined by the locus of the of centers of the nearest solvated ions at x_2.[2] Due to the specifically adsorbed ions in the IHP, the interaction of solvated ions with the charged metal surface involve exclusively long range electrostatic forces, so that their interaction is essentially independant of the chemical properties of the ions. These ions that are electrostatically interacting with the metal surface are said to be nonspecifically adsorbed. Beyond the OHP, thermal agitation in the solution results in the nonspecifically adsorbed ions being distributed in a three dimensional region known as the diffuse layer.

The structure of the electrical double layer, where the oppositely charged planes of the IHP and the OHP seperated by a dielectric solvent result in a capacitance known as the double layer capacitance C_{dl}. The C_{dl} is decribed by Eq. (2.29) below:

$$\frac{Q}{E} = C_{dl} \tag{2.29}$$

where Q is the charge in coloumbs stored in the capacitor, E is the potential across the capacitor in V, and C_{dl} is the double layer capacitance in Farads (F). Due to the double layer capacitance, a charging current will be passed so that Eq. (2.29) is satisfied. This current has no chemical meaning and is purely physical, thus it is distinct from the Faradaic current associated with redox reactions and is also referred to as non-Faradaic current.[1,2] Non-Faradaic decays exponentially over time at a rate much faster than the Faradaic current ($t^{\frac{-1}{2}}$ for diffusion controlled processes, t^{-1} for surface confined processes), so for constant potential measurements it can be assumed that a majority of the current contribution after the initial timestep of the measurement are due to Faradaic current.[1,2]

However, in experiments in which the potential is changed continuously (*e.g.* CV) the non-Faradaic current wil be present throughout the measurement, and will be greater the greater the capacity of C_{dl} is. Therefore to minimise the contribution of non-Faradaic currents in potential sweep experiments, the capacity of the C_{dl} should be minimised. The capacity for a plate capacitor C is given by Eq. (2.30) below:

$$C = \epsilon_0 \epsilon_r \frac{A}{D} \tag{2.30}$$

Where ϵ_0 is the electric field constant, ϵ_r is the relative permittivity of the medium between the plates, d is the distance between the two plates, and A is the surface area of the two plates. The only factor influencing capacity that can be changed experimentally is the area A, so by reducing the area of the working electrode used for measurement,

non-Faradaic current can be decreased.[1,2] In regards to this work, this is why potential sweep experiments were conducted using a smaller area Glassy carbon electrode (GCE), whilst the constant potential experiments for CO_2RR were performed with the larger area carbon paper electrodes. Additionally, non-Faradaic current contributions are further minimised due to the fact digitial potentiostats do not provide true linear potential sweep, but instead apply discrete steps of potential to approximate a linear sweep.This means recording the current after the actual step during the linear steady potential will exclude a large contribution of non-Faradaic current as it will have decayed by that point.[1,2]

2.2.5 Chrono- techniques

Chronopotentiometry and Chronoamperometry are electrochemical techniques in which either a constant current or potential respectively is applied to the electrode and the resulting potential or current respectively is measured as a function of time.[2] Compared to voltammetric techniques, chrono- techniques were much simpler in applications to this work, with chronoamperometry being used to apply the constant potential required for electrocatalytic reactions, and chronopotentiometry used to gauge the stability of a reaction by seeing whether the potential decreases over time at the current achieved at electrocatalytic potentials.

In chronoamperometry experiments utilising electrocatalysts, the applied overpotential required for CO_2RR is typically much larger than equilibrium potentials associated with the reduction of the electrocatalysts on the surface, therefore it can be assumed that all of the electrocatalyst on the surface is reduced instantaneously alongside any other electroactive species that have built up at the surface of electrode. This results in a very large current density at $t = 0$ associated with reduction of the electrocatalyst and any other electroactive species that has accumulated at the electrode surface. This current then rapidly decreases to the current density associated with just CO2RR and other unwanted catalytic processes by the time $t = 1$ is reached, hence the large spike at the beginning of chronoamperometry experiments found in this work. To be able to deconvolute the current associated with CO_2RR and the current associated with non-faradaic processes and unwanted side reactions, it is necessary to quantify the amounts of each reaction product.

Firstly, the current trace from $t = 1$ can be integrated to give a total amount of charge passed throughout the electrocatalysis via Faraday's law (Eq. (2.7)).

$$Q = \int_0^t idt = nzF \tag{2.7}$$

Following this, the quantification of the products of the electrocatalysis experiment allows for the calculation of a theoretical amount of charge that would be associated with

the formation of each product via the stoichiometric relationship between charge and the number of electrons for a given reduction, with this being also given by Faraday's law (Eq. (2.7)). Obtaining both of these quantities permits calculation of a measure of catalytic selectivity known as FE Eq. (2.31).[14]

$$FE = \frac{znF}{Q} \times 100 \tag{2.31}$$

Since FE also represents a ratio of the amount of charge passed for a given product, the partial current density associated with the formation of said product at a given time can be deconvoluted from the total current density j_{total} by multiplying it with the FE.[14] These two parameters: $j_{product}$ and FE, act as useful measures of the activity and selectivity for a given electrocatalyst respectively, and are utilised frequently throughout this work and other works in literature for the benchmarking and comparison of an electrocatalyst.

Chronopotentiometry, in contrast to chronoamperometry, was used in this work for largely qualitative purposes only due to the quantitative inaccuracies inherent to the technique resulting from double layer charging.[2] As previously discussed in Section 2.1, current is analogous to electrochemical rate, so chronopotentiometry allows for the application of a rate associated with the CO_2RR process and to see if an electrocatalyst can maintain said rate without change in the reaction itself, *i.e.* the voltage experienced at the electrode.

Simply put, if the voltage is stable over time and also equal to the voltage that was seen in voltammetry at the voltage where applied current was measured, then the electrocatalyst can be assumed to be steadily facilitating electrocatalytic conversion as predicted. If the voltage were to increase, then to keep the applied electrochemical rate the catalyst is requiring more energy, ergo the catalyst has degraded in performance. Conversely if the potential were to decrease the catalyst could be said to have improved in performance but this did not occur in this work.

2.3 CO_2 Electrocatalysis

2.3.1 Basics

As the most oxidised form of carbon, CO_2 is intrinsically difficult to reduce, and this is reflected by a large potential requirement of -1.90 V vs SHE for CO_2 activation into $CO_2{}^{*-}$.[15–17] Past this initial activation step into the anion radical, further reduction is comparatively facile (Fig. 2.10), however issues arise due to the Hydrogen Evolution Reaction (HER) occurring at the required potentials for CO_2 activation, as the HER is parasitic and competes with active sites for the CO_2RR in heterogeneous electrocatalysis.[18]

	$E^{0'}$
$CO_2 + e^- \longrightarrow CO_2^{-\bullet}$	—1.90 V
$CO_2 + 2H^+ + 2e^- \longrightarrow HCOOH$	—0.61 V
$CO_2 + 2H^+ + 2e^- \longrightarrow CO + H_2O$	—0.52V
$CO_2 + 4H^+ + 4e^- \longrightarrow HCHO + H_2O$	—0.48 V
$CO_2 + 6H^+ + 6e^- \longrightarrow CH_3OH + H_2O$	—0.38 V
$CO_2 + 8H^+ + 8e^- \longrightarrow CH_4 + 2H_2O$	—0.24 V
$2H^+ + 2e^- \longrightarrow H_2$	—0.41 V

Figure 2.10: Equillibrium potentials (V vs SHE) for the CO_2RR and HER. Adapted from Ishida[17]

Owing to these factors, a CO_2RR electrocatalyst must be selective for CO_2 activation, whilst also suppressing the HER to maximise catalytic performance. The CO_2 activation step, specifically the binding of the CO_2 to the support, determines the further reduction mechanism and what products the reduction will be selective for.[19] There are 3 distinct binding modes of CO_2 to the support which determine the mechanism, these bindings being[19]:

- Direct to C, forming *COO
- Direct to the both Os, forming *OCO
- CO_2 insertion into a M−H bond, forming *OCHO

and these are outlined in Fig. 2.11.

These binding modes are followed single step Proton Coupled Electron Transfer (PCET), or two subsequent single step additions of e^- followed by H^+. In the case of the *OCHO, the only formable product is $HCOO^-$, whilst the *OCO the *COO are necessary for any other CO_2 reduction product.

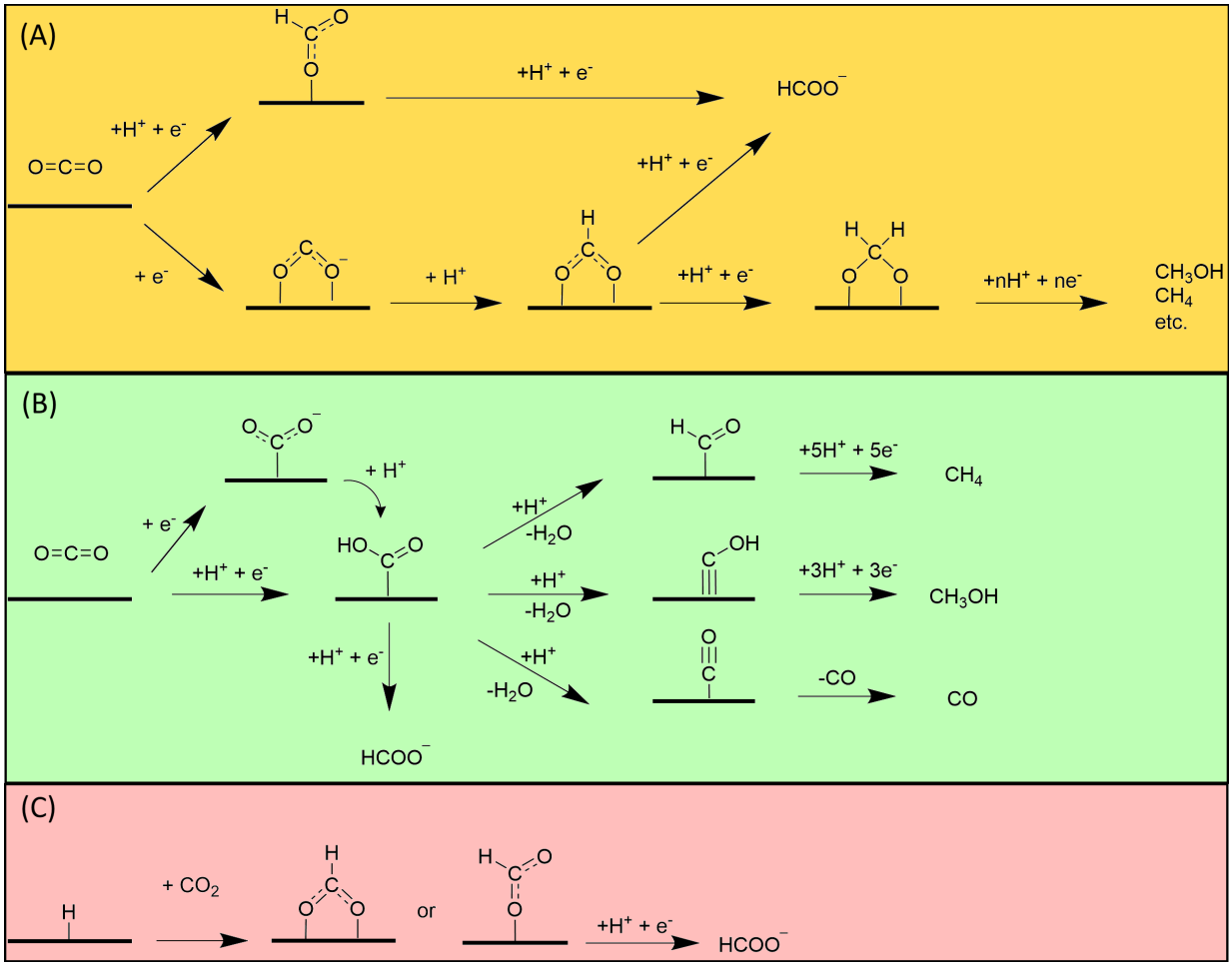


Figure 2.11: Scheme outlining the various mechanisms resulting from the way the CO_2 binds to a support. (A) Direct to both O atoms, forming *OCO; (B) Direct to C, forming *COO; (C) CO_2 insertion into a M−H bond, forming *OCHO[19,20]

Selectivity with such a wide variety of possible products is fully dependant on a catalyst's ability to stabilise or destabilise certain reaction intermediates, for example in most metals, the biformate H_2COO* intermediate is not stabilised and high in free energy,[20] resulting in most catalytic pathways via the OCO* yielding formate as a major product.[19–22] Therefore, for selective CO_2RR catalysts should stabilise specific intermediates whilst also having weak H binding to suppress the HER.

2.3.2 Role of the Electrolyte

For the CO_2RR to proceed in practice, CO_2 must be capable of reaching the electrode via mass transport in solution. Due to the poor solubility of CO_2 in water,[23] the carbonate equillibrium in water can be utilised to increase the CO_2 concentration in aqueous solution as shown in Eqs. (2.32) to (2.36).

$$CO_{2(g)} \rightleftharpoons CO_{2(aq)} \tag{2.32}$$

$$CO_{2(aq)} + H_2O_{(l)} \rightleftharpoons H_2CO_{3(aq)} \tag{2.33}$$

$$H_2CO_{3(aq)} \rightleftharpoons H^+{}_{(aq)} + HCO_3^-{}_{(aq)} \tag{2.34}$$

$$HCO_3^-{}_{(aq)} \rightleftharpoons H_{(aq)}{}^+ + CO_3^{2-}{}_{(aq)} \tag{2.35}$$

Overall:

$$CO_{2(aq)} + H_2O_{(l)} \rightleftharpoons H^+{}_{(aq)} + HCO_3^-{}_{(aq)} \rightleftharpoons 2H^+{}_{(aq)} + CO_3^{2-}{}_{(aq)} \tag{2.36}$$

In reality, the concentration of H_2CO_3 is neglible ($< 0.3\%$) when compared to that of dissolved CO_2[24] due to the disfavoured forward reaction, thus the concentration of H_2CO_3 is chemically inseparable to $CO_{2(aq)}$ and effectively equates the concentration of H_2CO_3 to $CO_{2(aq)}$.[25]

This makes metal bicarbonates the most frequently utilised electrolytes for the electrocatalytic CO_2RR, as consumed CO_2 is naturally replenished by the Eq. (2.36) equilibrium. Additionally, CO_2RR electrocatalysis necessitates sparging the solution with CO_2 to both increase CO_2 concentration, and also prevent electrolyte depletion due to CO_2 removal. Sparging CO_2 during electrocatalysis has the added effect of decreasing the electrolyte pH as Eq. (2.36) is pushed to the right, adding H^+.[25] Whilst decrease of pH initially seems unwanted due to the possibility of increasing the prevalence of the HER, when considering that the cell will be at reductive conditions during catalysis, the presence of generated OH^- at the electrode surface will decrease interfacial CO_2 concentration via conversion into $HCO_3{}^-$, meaning the generated H^+ aids in suppressing this surface alkalinity and increasing interfacial CO_2 concentration.[26] Additionally, we can infer that increasing $HCO_3{}^-$ capacity of solution will also increase interfacial CO_2 concentration via the same mechanism (Eq. (2.34)), and this has been experimentally proven by Singh *et al*.[27] Lastly, the reason $MHCO_3$ electrolytes are preferred over M_2CO_2 or MOH electrolytes is due to the fact that upon addition of CO_2 to the system, these electrolytes are converted into $MHCO_3$ via Eq. (2.36),[25] and due to this it is moot to use either of these electrolytes, especially in the case of M_2CO_3, as the sluggish kinetics associated with Eq. (2.33) requires impractically long gaseous CO_2 saturation times to reach its optimal CO_2 concentration.[25]

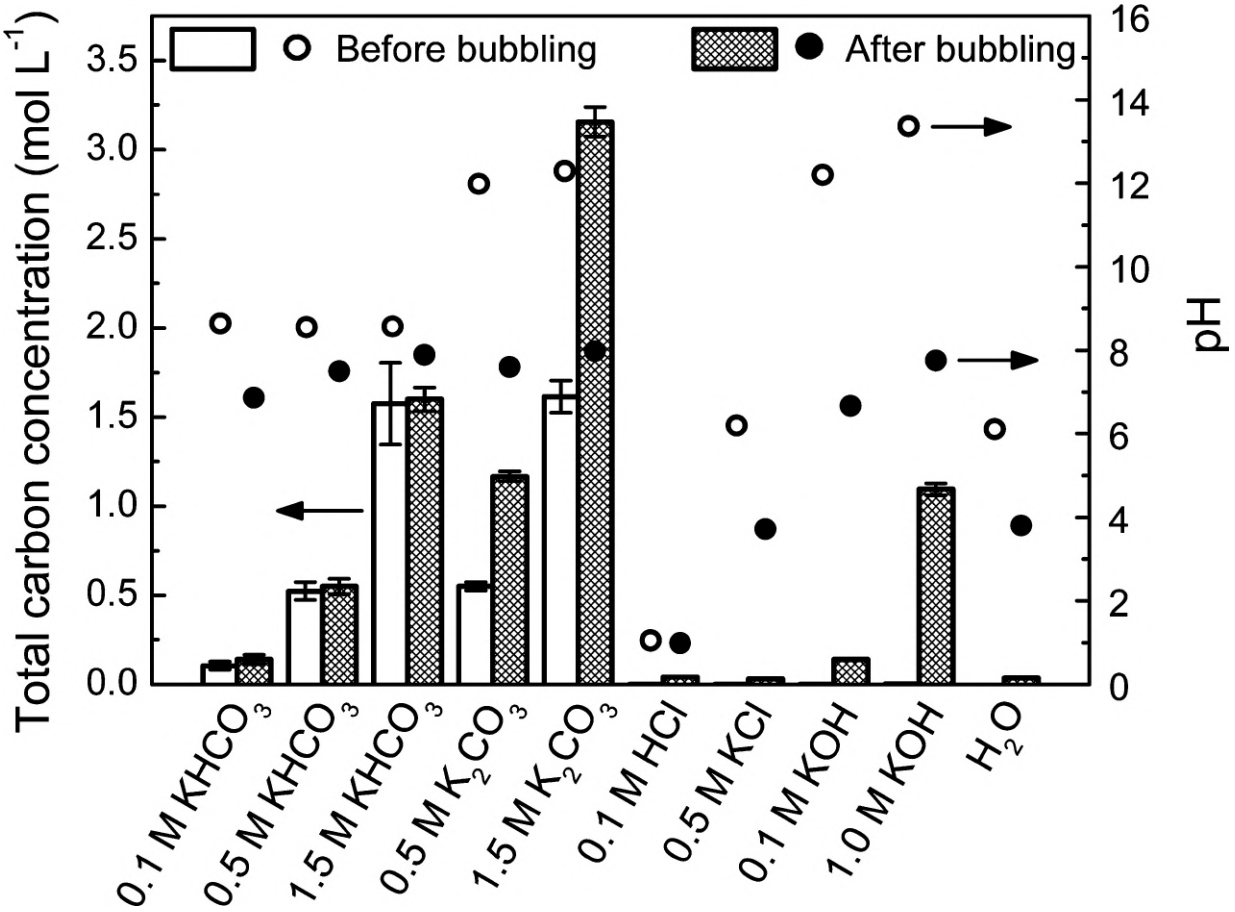


Figure 2.12: Total dissolved carbon concentration in different electrolytes before and after saturation with CO_2. Bars represent carbon concentration, circles represent pH. Adapted from Zhong *et al*[25]

With $MHCO_3$ established as the optimal electrolyte, next it is pertinent to discuss cation effects on the CO_2RR, as the electrolyte cation is required for CO_2RR by stabilising the activated CO_2^- intermediate via complex formation, and is essentially required as no CO_2RR can be observed in pure H_2SO_4 electrolyte on Au, Ag, or Cu.[26] The formation of a $M-CO_2^-$ complex stabilise CO_2 adsorption via electrostatic interaction, lowering the energy barrier of CO_2 adsorption by ~ 0.5 eV and also decrease the CO_2 activation angle from the linear 180° to 140°.[26] Whilst the cation affects the energetics, and therefore activity of the CO_2RR, it is unclear the impact of cations on CO_2RR selectivity. Cations play a large role in the HER, with alkali metal cations of larger hydrated size (K^+, Cs^+, etc) increasing HER activity.[28] However, it has also been evidenced that larger cation size has a positive impact on selectivity via reducing the interfacial pH, which increases interfacial CO_2 concentration. This opposite effect is due to the larger cations strong electrostatic field induced at the reaction interface promoting hydrolysis and acting as a pH buffer,[27] a fact which was experimentally confirmed by Ayemoba and Zhang *et al*.[29,30]

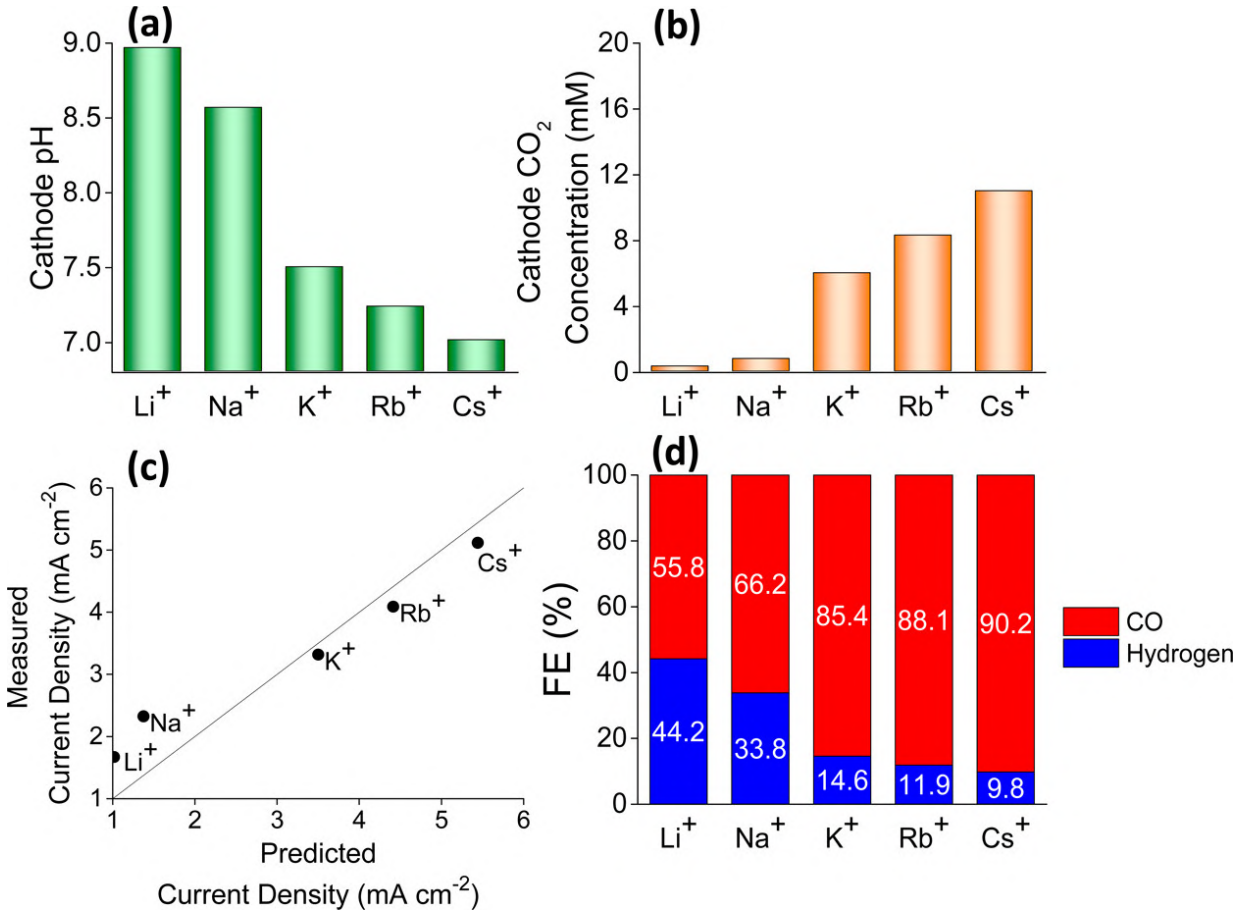


Figure 2.13: Calculated values of a) Cathode pH; b) Cathode CO_2 concentration ; c) j_{total}; d) FE_{CO} and FE_{H_2} produced on Ag at -1 V vs RHE in 0.1 M $MHCO_3$ (M = Li, Na, K, Rb, Cs) Adapted from Singh *et al*[27]

Considering these findings, $KHCO_3$ has seen commonplace use in CO_2RR literature due to the larger size cation promoting CO_2RR and the economic and scale-up issues associated with using $RbHCO_3$ and $CsHCO_3$,[21,31,32] and therefore $KHCO_3$ is used throughout the work presented in this thesis.

2.3.3 Inapplicability of Tafel Analysis for this work

Tafel Analysis is an extension of the Butler-Volmer equation (Eq. (2.17)), in which by selecting conditions in which the Butler-Volmer equation is reduced to a limiting form so that the electrochemical parameters α and and $j_\circ$ can be determined. The limiting forms of the Butler-Volmer equation (Eq. (2.17))

$$j = j^\circ \left[\exp\left(\frac{\alpha_A n F}{RT} \eta \right) \right] - \left[\exp\left(\frac{\alpha_C n F}{RT} \eta \right) \right] \tag{2.17}$$

are listed as follows:

- High positive overpotentials where $|j_{ox}| \gg |j_{red}|$, so that:

$$\log j = \log j_\circ + \frac{\alpha_A nF}{2.3RT}\eta \tag{2.37}$$

- High negative overpotentials where $|j_{ox}| \ll |j_{red}|$, so that:

$$\log -j = \log j_\circ - \frac{\alpha_C nF}{2.3RT}\eta \tag{2.38}$$

- Very low values of η where $\eta \ll \frac{RT}{\alpha_C nF}$ meaning the exponential terms of Eq. (2.17) can be expanded as a series, and then ignoring higher order terms leads to:

$$j = j_\circ \frac{nF}{RT}\eta \tag{2.39}$$

Specifically, Eqs. (2.37) and (2.38) are known as the Tafel equations, with Eq. (2.39) being a linear approximation of the Butler-Volmer equation Eq. (2.17). By plotting $\log j$ vs η, it is possible to obtain both α from the gradient in the form of $\pm\frac{\alpha_{A/C}nF}{2.3RT}$ (Tafel slope), and $j_\circ$ in the form of $\log j_\circ$ from the intercept. With these two aforementioned parameters, it is possible to obtain the kinetic information of an electrode reaction empirically, such as the mechanism and rate-determining step.[2] Put simply, it is possible to calculate both α and $j_\circ$ theoretically for a given reaction mechanism, and then compare to experimentally obtained values to determine said mechanism. Additionally, the $j_\circ$ and more relevantly, the Tafel slope, will vary with the electrode material indicating a change in reaction mechanism as the electrode changes during electrocatalysis.

For the above reasons, Tafel analysis finds itself widely employed in HER electrocatalysis,[33] due to the fact that product selectivity is essentially a non-issue and there is limited amount of possible HER reaction pathways, resulting in a limited amount of values that need to be calculated depending on the adsorption isotherm.[33–35] For example, for the metal catalysed two step reduction of hydrogen:

Step I:	$\mathrm{H^+ + e^- + M \longrightarrow M{-}H}$
Step II:	$\mathrm{2\,M{-}H \longrightarrow 2\,M + H_2}$

it has been determined theoretically that for a Langmuir adsorption isotherm, if the rate determining step is Step I, the Tafel slope value is 120 mV dec^{-1}, and for Step II it is 30 mV dec^{-1}. In comparison, it is easy to see why the use of Tafel analysis for obtaining mechanistic information related to the electrochemical CO_2RR is vastly more complex, as not only are there many more multi-stepped pathways for a given product, there are multiple potential products that can be formed from a given electrocatalytic reaction which all may proceed by completely different mechanisms. Complicating matters further still is the fact that the CO_2RR is often accompanied by the HER as a side reaction, resulting in the obtainable $j_\circ$ and α from Tafel analyses containing contribution from each electrode reaction that can occur at a given potential.

Whilst extremely difficult, it is not impossible to gain meaningful mechanistic data in relation to the CO_2RR from Tafel analysis, due to the aforementioned complications there are multiple conditions that an electrochemical system must satisfy before the results from Tafel analysis can provide meaningful data.[34,36] These conditions to obtain kinetic information are as follows[34,36]:

- No significant backward reaction
- No contribution of (pseudo-) capacitive current
- No mass transport limitations
- i vs E curves with two orders of current magnitude range
- 100% correction of Ohmic resistance
- No change in Ohmic resistance during the measurement
- Fixed temperature
- Potential independence number of active sites
- No potential-dependant changes to the catalyst
- No other processes contributing to the current

In addition to the conditions listed above, it is assumed that the experimental set up can prevent or meaningfully account for practical issues, such as bubble formation from gaseous products and the large pH gradients that tend to form at the electrode interface,[37] as these will further complicate Tafel analysis.[34] As a result for CO_2RR research in general, it is extremely difficult, but not impossible, to ensure that these conditions are satisfied, with one notable work by Van der Heijden *et al*[34] having been able to achieve a meaningful kinetic information relating to the CO_2RR on an Au electrode. The work by Van der Heijden *et al*[34] made use of an Au tipped Rotating Ring Disk Electrode (RRDE) to deconvolute the CO_2RR from the HER for the production of CO, and Van der Heijden *et al*'s[34] work in particular makes note to highlight the immense difficulty of satisfying the conditions for Tafel analysis to be kinetically meaningful.[34] The current consensus among

researchers interested in the electrokinetics of CO_2RR largely forego Tafel analysis, and suggest alternate means of monitoring reaction kinetics such as in-situ Raman and X-ray Photoelectron Spectroscopy (XPS) (spectroelectrochemistry).[36,38]

The reason to why Tafel analysis of CO_2RR catalysts struggle with validity is the "potential-independent number of active sites" condition, as competing reaction pathways will invalidate this condition.[36] One example of a commonly reported competing reaction pathway is the HER, which would then require the current contribution of HER to be deconvoluted from CO_2RR and accounted for.[36] Additionally, this can still be invalidated in some cases without HER, as potential dependant CO adsorption has been evidenced by Dunwell *et al*,[38] with CO adsorption on Ag decreasing from 0.2 V vs SHE to being absent at -0.4 V vs SHE.[38]

Another condition that CO_2RR catalysts struggle to meet is "No potential-dependant changes to the catalyst", as it has been frequently shown in mechanistic studies[20,39,40] that the applied potential to the catalyst can directly impact the product selectivity, and therefore making the pathway potential dependant.

These two conditions in particular assured that Tafel analysis is largely unsuitable for the two research topics explored in this thesis. Firstly, the work on polyphthalocyanines Chapter 4 was largely based off of the works evidencing a potential dependency of CH_3OH production on phthalocyanines,[37,40,41] so inherently Tafel analysis of the polyphthalocyanine research would not provide meaningful kinetic information. Secondly, in the work on p-block metals Chapter 5, competition with the HER and likely multiple competing pathways, were the reasons that Tafel analysis was not explored.

Unfortunately, it is rare for research works on CO_2RR to be aware of the limitations associated with Tafel analysis, and with the relative ease of constructing a Tafel plot from existing characterisation data (*e.g.* LSV and CV), slope values often are used to justify proposed mechanisms of an electrocatalyst by comparing the slope value to theoretically calculated slope values,[38,42] even though the catalyst is shown to produce multiple products at the potentials used for the calculation of the slope.[43–47] Lastly, it is necessary to mention that plots of $\log j$ vs η are not meaningless when the Tafel conditions are not met, as they represent the amount of potential necessary to apply to a given catalyst to raise the current density by a factor of 10, however this information is often of inconsequential when it comes the comparison of electrocatalysts. Therefore, the reported Tafel slopes contained in works referenced throughout this thesis are also largely disregarded as they do not contribute to the discussions throughout this work.

2.3.4 Practical Considerations for Electrocatalysis

2.3.4.1 Reference Electrodes

Reference electrodes are electrodes of an invariate potential to which the applied potential can be measured against so that the recorded current represents just that of the working electrode. Throughout this work, potentials are reported as vs Reversible Hydrogen Electrode (RHE) due to the convenience for comparison to other electrocatalysis works. The RHE, and by extension the Standard Hydrogen Electrode (SHE) are hydrogen electrodes, in which hydrogen is bubbled over platinum so that the potential of the $2\,H^+ + e^- \longleftrightarrow H_2$ couple can be used as a reference potential, with the SHE specifically being defined as 0 V at all temperatures. In particular, the SHE is the potential of the $2\,H^+ + e^- \longleftrightarrow H_2$ couple with standard conditions, *i.e.* 1 bar of pure hydrogen gas is used, this results in solution of a $[H^+]$ of 1 M. Furthermore this solution is assumed to be theoretically ideal, meaning there is no interactions between H^+ ions. By putting these parameters into the Nernst equation where the equillibrium constant is comprised of the ratio of activities of H_2 (pH_2/p°) and H^+ (pH) as shown by Eq. (2.40). Solving this with the numerical values results with Eq. (2.41):

$$E = 0 - \frac{RT}{2F}\ln\frac{pH_2/p^\circ}{\mathrm{pH}} \tag{2.40}$$

$$E = -0.059\,pH \tag{2.41}$$

simply meaning the potential deviates by 0.059 V per unit of pH (The pH for a SHE is 0). This then leads to a more practical reference electrode, the RHE, which is the SHE with a potential that varies with pH.

When using another reference electrode, *.g.* Ag/AgCl which has a potential of 0.210 V (3 M KCl), the scale is set so that 0 vs Ag/AgCl is 0.210 V vs SHE , *i.e.* adding 0.210 to the potential vs Ag/AgCl gives a potential in SHE, since it is defined by convention as $E_{cell} = 0$. Lastly, the potential in SHE can be converted to RHE via addition of the pH dependant term, so that our final expression for conversion of potential vs RHE is:

$$E_{RHE} = E + E_{Ref} + (-0.059\,pH) \tag{2.42}$$

Where E is the potential recorded with the reference electrode and E_{Ref} is the potential of the reference electrode. Conversion to the RHE scale is highly convenient for electrochemical research as it allows for facile cross comparisons between works whilst also

encompasses the pH effects on the potential. Additionally, some works choose to report potentials vs SHE, and in this case Eq. (2.42) can be used with the pH term set to 0.

2.3.4.2 Rotating Disk Electrodes

Rotating disk electrodes are working electrodes which are capable of rotation during electrochemical analysis to introduce convective mass-transport to the electrode, resulting in the reactant being convected to the electrode whilst the produce is driven away from the electrode surface.[48]

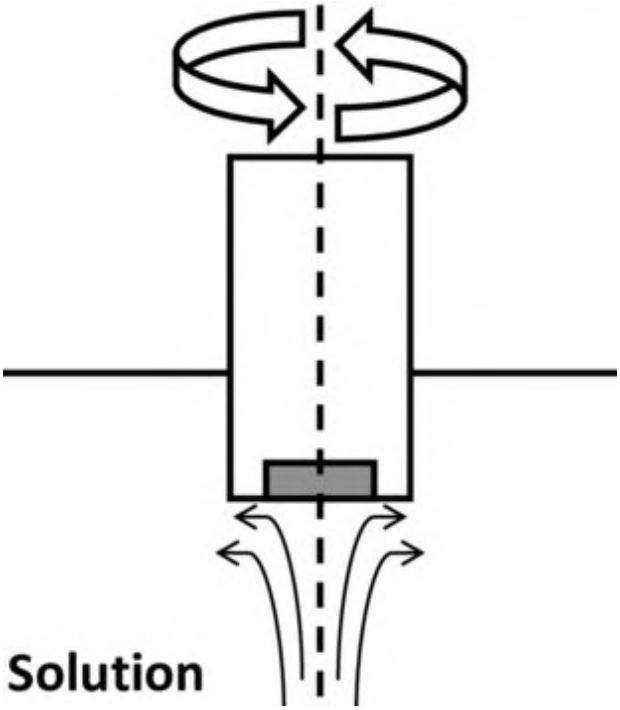


Figure 2.14: Schematic of a RDE in operation. Arrows in solution represent the flow of electrolyte across the electrode. Adapted from Bruno Alarcon Fernandes Previdello.[49]

As previously discussed in Section 2.2.2, a diffusion layer is established once the supply of electroactive material is depleted at the electrode surface, resulting in a current limited by the rate of diffusion of the species to the electrode. In a RDE setup, this diffusion limitation is circumvented by introducing convective mass transport induced by rotation, thus rather than a typical peak shape in solution phase voltammetry, the current will reach a steady state plateau dictated by the rate of convection of the solution phase species, *i.e.* the rotation rate.[1,2] An example of the effect of rotation rate on diffusion controlled voltammetry is given in Fig. 2.15 below.

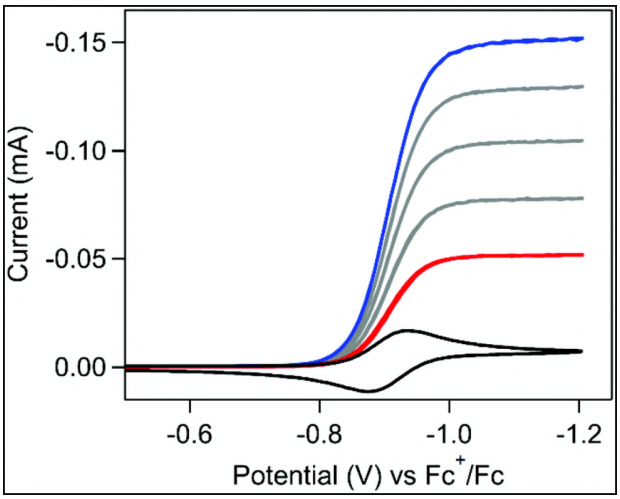


Figure 2.15: Comparison of stationary CV (black) and RDE voltammograms of 0.5 mM $Co(dmgBF_2)_2(CH_3CN)_2$ in 0.25 $[NBu_4][PF_6]$ acetonitrile solution. Rotation rates for RDE voltammograms range from $42 rad^{-1}$ (red) to $377 rad^{-1}$ (blue). Figure reproduced from Lee *et al*[50]

.

The control of limiting current via convection allows for the determination of the diffusion constant D in the Butler-Volmer Equation via the use of the Koutecky Levich equation Eqs. (2.43) and (2.44):

$$\frac{1}{i_m} = \frac{1}{i_K} + \frac{1}{B\omega^{0.5}} \tag{2.43}$$

$$B = (0.620)nFAD^{\frac{2}{3}}v^{\frac{-1}{6}}C \tag{2.44}$$

Where i_m is the measured current, i_K is the kinetic current and $B\omega^{0.5}$ is the mass transport current i_{MT} represented by the Levich constant B and the angular rotation rate ω. In this work, the electrochemical processes that take place on the electrode are surface confined and not influenced by mass transport of species from solution, or CO_2RR which is influenced by mass transport but steady state currents are not practical to achieve. Therefore the Koutecky-Levich equation cannot be utilised to obtain information for this work, but is presented for completeness.

In the electrochemical CO_2RR, the cathodic reaction is influenced by the rate of CO_2 supply to the electrode at high current densities.[51] For aqueous CO_2 as is utilised in this work (Section 2.3.2), the CO_2RR occurs at the liquid-liquid electrolyte-electrode interface, and at high current densities a depletion layer can form on the electrode due to faster rates of reduction compared to mass-transport of CO_2 from diffusion. This depletion

layer results in a limitation of current at the electrode and vacant active sites which can potentially be occupied by H, resulting in a drop in selectivity due to an increase in HER activity.[51] At lower current densities (< 1 mA), the CO_2 depletion layer is not formed during reudction and thus current limitation is not encountered.[18] The current densities encountered in the voltammetry in this work however were frequently > 3 mA, so it was necessary to increase the mass transport of CO_2 to the electrode to prevent any potential current limitation resulting from the CO_2 depletion layer.[14,18]

For batch electrocatalysis experiments, this depletion layer was alleviated via stirring of the solution and the sparging of CO_2 resulting in convective mass transport, however for voltammetry, the non-laminar flow of electrolyte introduced from stirring results in distortion of the voltammetry trace, whilst additionally not being sufficient to remove small bubbles on the electrode surface that could form in the CO_2RR region. Therefore, it was practical to use a RDE for voltammetry due to the high rotation rate experienced by the electrode and the laminar flow of electrolyte experienced by the RDE.

Additionally, due to the catalyst systems being surface confined, the presence of redox peaks in the voltammetry of the catalyst material are maintained when introducing convective mass-transport, whilst the rotation induced convection removes unwanted peaks from product reooxidation or unwanted side reactions from increased alkalinity (e.g Cannizzaro Reaction), reduces contribution of non-faradaic charging currents, and decreases the overpotential of redox events. An example of stationary voltammetry compared to voltammetry utilising a rotating RDE for the In on multi-walled nanotubes electrocatalyst is given in Fig. 2.16, where it can be seen that the RDE trace has more cathodically shifted redox peaks, less voltammogram area which corresponds to lower capacitive charging of the double layer, and a higher achieved current density at -1.05 V vs RHE (albeit minimally).

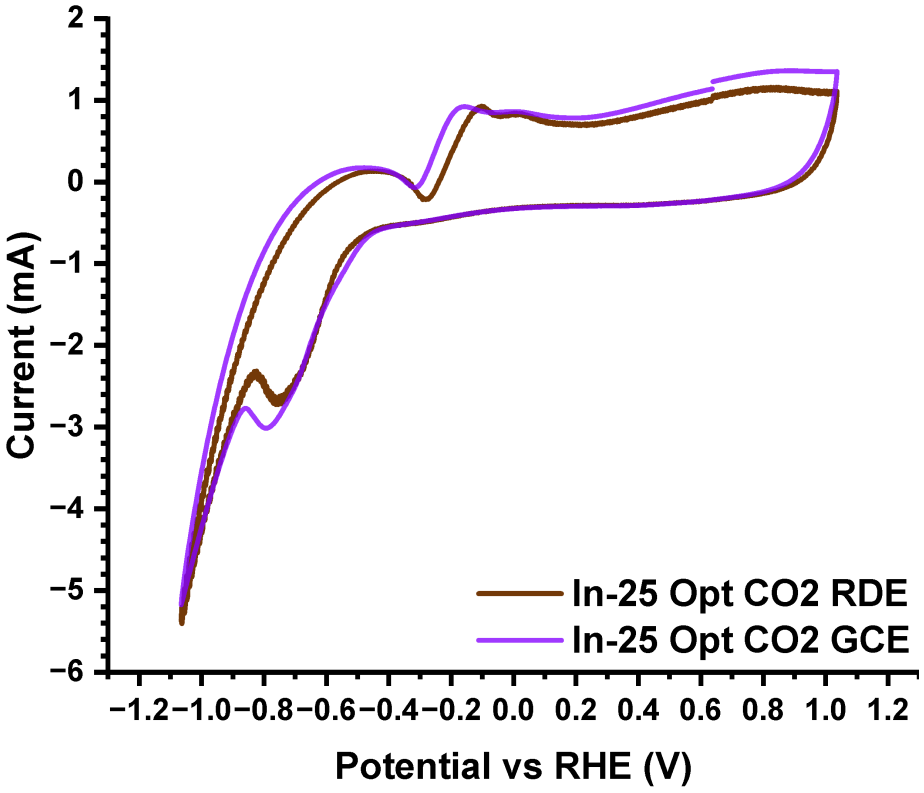


Figure 2.16: Overlaid CVs of In-25 Opt using a GCE and a RDE with identical diameters utilising CO_2 saturated 0.5 M $KHCO_3$ as an electrolyte at a scan rate of 0.005 Vs^{-1}. The RDE at a rotation rate of 1600 rpm

Whilst the RDE provides advantages within the voltammetry of CO_2RR electrocatalysts, particularly with confirmation of surface confined processes, there are disadvantages that can be associated with the use of a RDE for CO_2RR studies. Firstly, as previously mentioned above, the reduction of interfacial alkalinity at the electrode can negatively impact co_2rr due to the suppression of water reduction related HER, reducing the availability of protons required for the CO_2RR and therefore the observed electrocatalytic current.[52] This effect is prevalent at low current densities (< 3.5 mA) in voltammetry, above this point the increased flux of CO_2 to the electrode from convection results in an increase of current density compared to stationary voltammetry.[52] Additionally the rotation of the electrode introduces a shear force on the electrode materials, increasing the susceptibility of the electrocatalyst layer to delamination in the electrolyte. Additionally, even partial delamination can result in the electrolyte being forced underneath the electrocatalyst layer and giving rise to a large contact resistance to the electrocatalyst layer, increasing the overpotential of electrochemical processes and necessitating ink formulations with good adhesion to the electrode surface. Lastly, the rotation of the electrode can accelerate leaching of species from the electrode, resulting in potentially greater loss of adsorbed metal species to solvation than a stationary electrode.

Despite these disadvantages, it was deemed more beneficial to utilise a RDE for voltammetry than a stationary electrode. The reduction in bubble shielding on the surface

of the electrode, reduction in side reactions such as the Cannizzaro reaction, ability to determine whether a peak arises from a surface confined or diffusion controlled process, and increase of co_2 flux to the electrode more than account for the previously discussed downsides, as the experimental work contained within this thesis is particularly concerned with characterisation via electrochemical behaviour, alongside increasing the selectivity and activity during co_2rr conditions, in which bubbles are prevalent and the current frequently achievesvalues $>$ 3.5 mA.

2.3.4.3 Electrochemical cell

For chronoamperometry experiments with the aim of testing electrocatalytic performance, a H-type cell was employed to separate the counter electrode reactions from the electrocatalytic reduction occuring at the working electrode. H-Cells are two compartment electrochemical cells separated by a proton or anion exchange membrane which allows the counter electrode to balance the overall cell reaction whilst preventing the counter electrode oxidation of the products produces as a result of CO_2RR.[53] This work made use of a Nafion ©-117 proton exchange membrane, which selectively allows transport of generated H^+ in the counter electrode compartment to the working electrode compartment. Crucially, the use of a proton exchange membrane instead of an anion exchange membrane prevents transport of the produced $HCOO^-$ anions into the counter electrode compartment.[54]

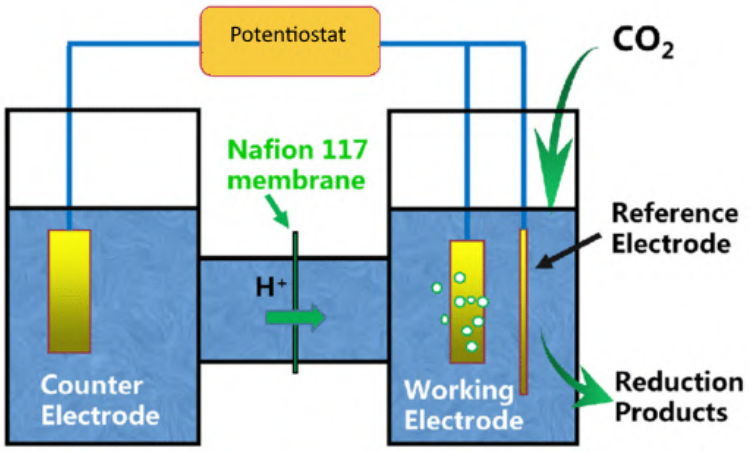


Figure 2.17: Schematic of a H-cell which this work utilises for chronoamperometry measurements. Image adapted from Tan et al[53]

2.4 Experimental Techniques

2.4.1 Thermo-Gravimetric Analysis

Thermo-Gravimetric Analysis (TGA) is a technique in which the mass of a given sample is measured as a function of temperature whilst the sample is subjected to a controlled

temperature program (typically up to 1000 °C) in a controlled atmosphere.[55] The controlled atmosphere of the TGA is provided by a purge gas which is flowed over the sample during heating, and can be either inert using gases such as N_2 or Ar, reducing with gases such as H_2, or relevant to this work, oxidising with gases such as O_2 or air.[55] A TGA experiment results in a temperature-weight profile, which will provide information regarding changes to the sample due to heating, with the TGA plots in this work following a similar pattern: Firstly, the TGA plot is relatively stable, with the weight% remaining near 100%, albeit typically with a minor decrease due to evaporation of residual solvents in the sample such as water contained in the atmosphere. Following this, a thermal decomposition event in the sample occurs, with one or two large decreases in the weight% of the sample at a given temperature due to the thermal decomposition of a sample. This thermal decomposition event can be quantified by using the derivative weight%, which can give the temperature in which the rate of mass loss is the steepest. Lastly, following the thermal decomposition the remainder of the plot gives the residual weight of the sample, and provides information on components of the sample such as metals that are not decomposed into gases during the thermal decomposition event.

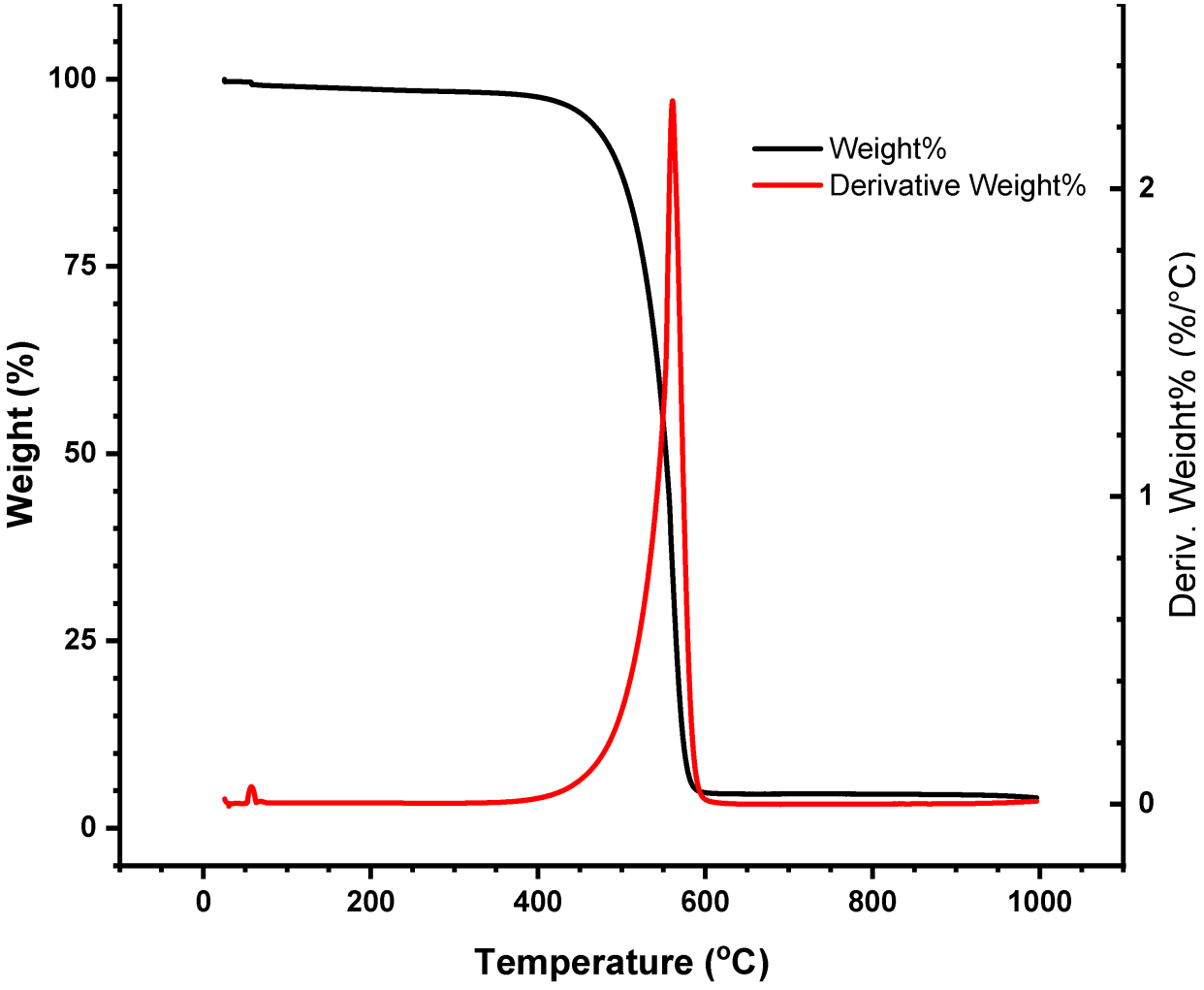


Figure 2.18: TGA plot of MWNT with derivative weight% plot overlaid.

The use of TGA allows for the determination of the residual metal loading of the catalysts used in this work, as components of the catalyst system such as the MWNTs and the polymer Polyphthalocyanine (PPc) are combustible and will be converted to CO_2 and N_2 in an oxidising atmosphere, whilst the metals will remain as solids throughout the heating program, and will be converted into their corresponding metal oxides. Shifts in the decomposition temperature in a TGA are valuable in confirming a change to the composition of the catalyst, particularly in reference to adsorbed nanoparticles, as these will catalyse the thermal decomposition of the MWNT. In this regard TGA can be a useful indicator of whether a synthesis has been successful in modifying the MWNT surface. The structure of the decomposition event can also provide valuable information, as if the decomposition is not one singular large change in gradient, but instead multiple, this can suggest a multiply staged decomposition in which a reaction takes during the decomposition event.

2.4.2 Transmission electron microscopy

Transmission electron microscopy (TEM) is a technique that allows for imaging and analysis of nanoscale materials below the diffraction limit of optical microscopes, such as CNTs and adhered nanostructures. A typical transmission electron microscope functions via the acceleration of electrons from an electron source through focussing electromagnetic lenses, and then are transmitted through the sample into a detector, such as a screen or camera, producing an image.[56]

As the accelerated electron beam travels through the microscope column various electromagnetic lenses are used to focus and align the electron beam, with a major limiting factor regarding the resolution of an electron microscope is the quality of the lenses used, which often possess various aberrations. To account for this, it is possible to use Aberration corrected-transmission electron microscopy (AC-TEM), which provide the potential for far greater resolution, but are more expensive and elaborate to operate.

When an electron beam comes in contact with a sample, the electrons are able to interact with it in multiple ways. In a thin sample, a majority of electrons can transmit through the sample without scattering, but some will scatter through either elastic scattering (neglible change of kinetic energy) or inelastic scattering (significant change of kinetic energy).[56] Variations in degree of elastic scattering of electrons contribute to distinct areas in the detector/camera with higher and lower intensity, which gives rise to areas of contrast in the detector, allowing for a TEM image to be formed. Additionally, a higher degree of electron scattering will occur with increasing the atomic weight of the atom in the sample s (rutherford scattering) or increasing sample thickness, resulting in differences in contrast known amplitude contrast.[56] Additionally, another contributor to contrast is known as phase contrast. Phase contrast results from interactions with the sample causing diffraction of incident electrons at specific angles, leading to constructive interference of the exit wave of electrons, giving rise to contrast in the image.[56]

By utilising alternate detector configurations, the contributions from phase contrast and amplitude contrast can be accentuated to obtain more information about a given sample, as they arise from seperate characteristics in the sample. Due to the elastic and inelastic scattering of electrons resulting in diffraction at specific angles after transmission through the sample, by altering the position of the electron detector beneath the sample, it is possible to remove phase contrast and obtain images in which contrast arises from amplitude contrast only. Changing the detector angle allows for Bright-field (BF) imaging and Dark-field (DF) imaging (see Fig. 2.19).

It is important to note that DF imaging can only be achieved using Scanning transmission electron microscopy (STEM). STEM is fundametally the same technique as TEM, however the beam optics are altered so that the electron beam converges on a small point and then is rastered over the sample.[56] STEM allows for the use of both the BF and DF detectors, whilst TEM can only be used for BF imaging.[56]

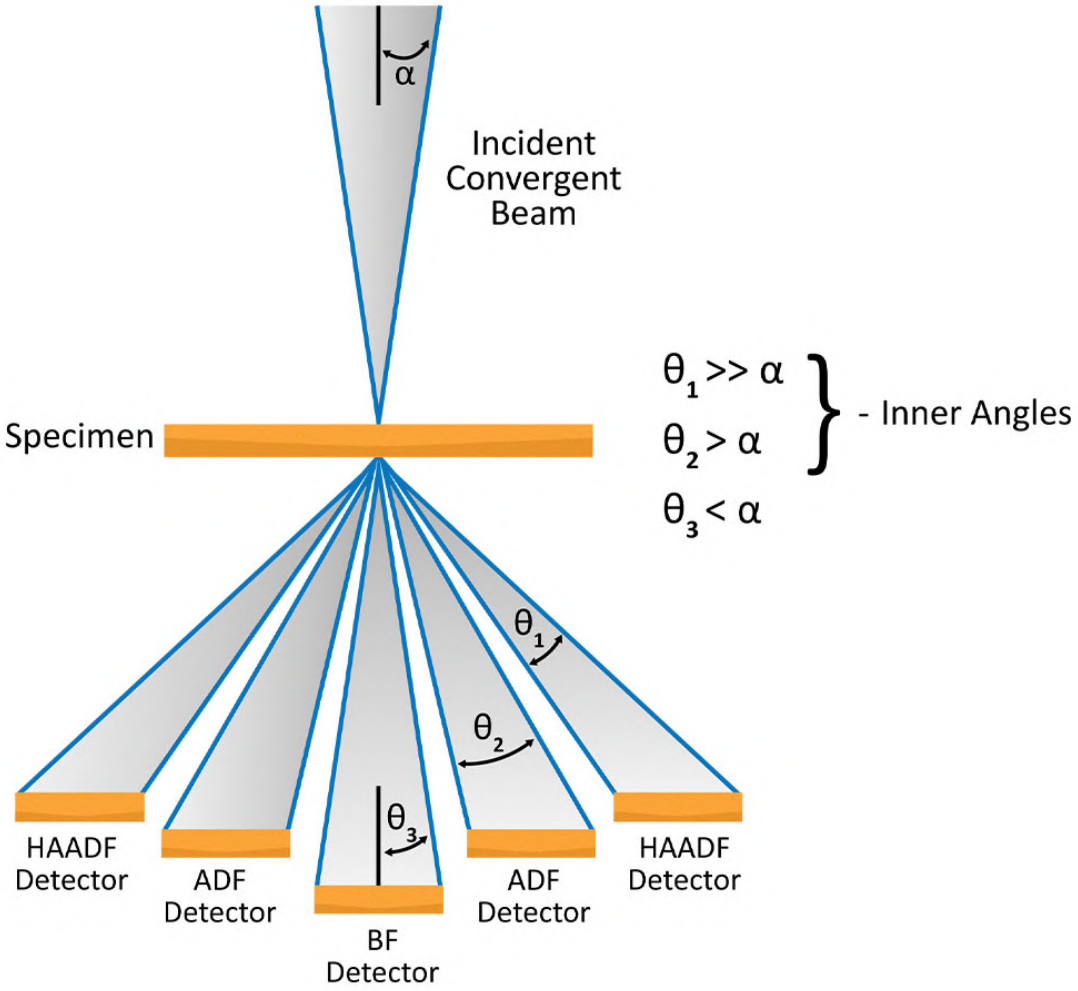


Figure 2.19: Diagram demonstrating the difference in detector positioning for BF, annular DF, and High-Angle Annular Dark Field (HAADF). Reproduced from Transmission Electron Microscopy: a Textbook for Materials by D. B. Williams and C. B. Carter.[56]

In BF imaging, the detector is positioned directly below the sample (see Fig. 2.19), meaning the detected electrons those which undergo transmission and elastic and inelastic scattering, meaning the resulting image contrast results from amplitude and phase contrast, with the contributions from phase contrast allowing greater resolution of crystalline features in the sample.[56] In regards to this work, this results in BF imaging being more suitable for the imaging of samples composed of lighter elements with crystallinity, such as MWNTs, and also being used to resolve crystalline planes for d-spacing determination.[56] Additionally, despite contrast in BF images resulting primarily from phase contrast from sample crystallinity, it is still possible to resolve amorphous, non-crystalline samples due to the aforementioned amplitude contrast.[56]

In DF imaging, the detector is annular and positioned at angle from the BF detector (see Fig. 2.19), which results in the only detected electrons being those that undergo elastic scattering and inelastic scattering, completely eliminating phase contrast and.[56], meaning that higher Z number atoms will result in a higher degree of electron scattering, and will increase intensity, and therefore contrast, in the resulting image.[56] Increasing the angle of the detector further allows for HAADF imaging, which consists only of the inelastically scattered electrons from rutherford scattering, making the image contrast entirely depending on the z number of the atoms in the sample. Practically for this work, this makes DF imaging more suitable for the detection of heavier elements, with regions of contrast in the image primarily associated with heavier nuclei, and therefore making it highly suitable for resolving single metal atoms on the surface of MWNTs not visible in BF images.

A comparitive example of how BF imaging and DF imaging are relevant for this work is illustrated in Fig. 2.20, in which the single Cu atoms are only resolvable in the DF image, whilst the d-spacing from MWNT walls are more defined in the BF image.

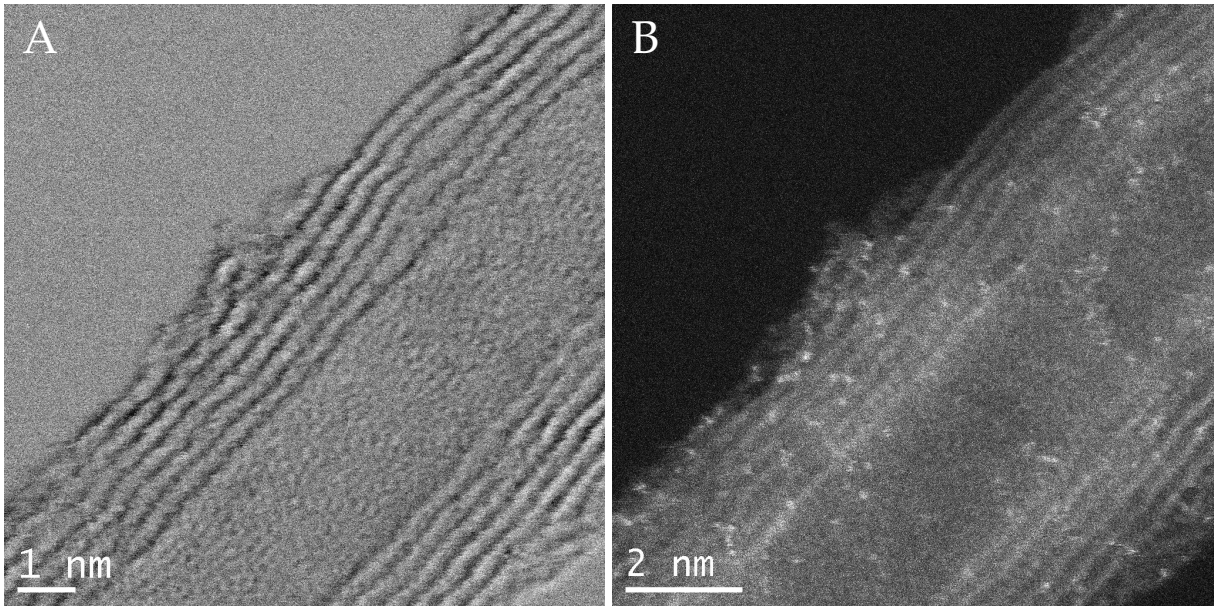


Figure 2.20: Aberration corrected-scanning transmission electron microscopy (AC-STEM) images of Cu/CoPPc/MWNT illustrating the differences in information that can be obtained from bright-field and dark-field imaging. (A) shows a BF AC-STEM image of Cu/CoPPc/MWNT, in which the graphitic d-spacing from the MWNT is resolved at a high contrast and the single Cu atoms on the surface are not discernable due to the lack of crystallinity, and hence, phase contrast. (B) shows a DF AC-STEM image of the same region as Fig. 2.20A, in which the single Cu atoms on the surface are easily resolved, whilst the contrast from the MWNT walls are much less pronounced due to the differences in Z number between carbon and copper resulting in a greater degree of rutherford scattering from the Cu single atoms.

Chapter 2 Bibliography

(1) D. Pletcher, R. Greff, R. Peat, L. M. Peter and J. Robinson, *Instrumental methods in electrochemistry*, Woodhead Publishing Limited, 80 High Street, Sawston, Cambridge, CB22 3HJ, reprint, 2001.

(2) A. J. Bard, L. R. Faulkner and H. S. White, *Electrochemical Methods: Fundamentals and Applications*, John Wiley & Sons, Ltd, 3, illustr, 2022.

(3) Georgia Institute of Technology, *Galvanic Cell Diagram*, 2011.

(4) N. Elgrishi, K. J. Rountree, B. D. McCarthy, E. S. Rountree, T. T. Eisenhart and J. L. Dempsey, "A Practical Beginner's Guide to Cyclic Voltammetry", *Journal of Chemical Education*, 2018, **95**, 197–206.

(5) R. Guidelli, R. G. Compton, J. M. Feliu, E. Gileadi, J. Lipkowski, W. Schmickler and S. Trasatti, "Defining the transfer coefficient in electrochemistry: An assessment (IUPAC Technical Report)", *Pure and Applied Chemistry*, 2014, **86**, 245–258.

(6) W. V. Mayneord, "John Alfred Valentine Butler, 14 February 1899 - 16 July 1977.", *Biographical memoirs of fellows of the Royal Society. Royal Society (Great Britain)*, 1979, **25**, 145–178.

(7) H. Yamada, K. Yoshii, M. Asahi, M. Chiku and Y. Kitazumi, "Cyclic Voltammetry Part 1: Fundamentals†", *Electrochemistry*, 2022, **90**, 102005.

(8) E. Laviron, "Adsorption, autoinhibition and autocatalysis in polarography and in linear potential sweep voltammetry", *Journal of Electroanalytical Chemistry*, 1974, **52**, 355–393.

(9) M. López-Tenés, J. González, E. Laborda and A. Molina, "Insights into the cyclic voltammetry of surface-confined molecules undergoing two-electron transfers of any reversibility and any ordering of the formal potentials: Unravelling the apparent governing factors", *Electrochimica Acta*, 2023, **462**, 142694.

(10) I. Streeter and R. G. Compton, "Diffusion-limited currents to nanoparticles of various shapes supported on an electrode; spheres, hemispheres, and distorted spheres and hemispheres", *Journal of Physical Chemistry C*, 2007, **111**, 18049–18054.

(11) B. A. Brookes, T. J. Davies, A. C. Fisher, R. G. Evans, S. J. Wilkins, K. Yunus, J. D. Wadhawan and R. G. Compton, "Computational and experimental study of the cyclic voltammetry response of partially blocked electrodes. Part 1. Nonoverlapping, uniformly distributed blocking systems", *Journal of Physical Chemistry B*, 2003, **107**, 1616–1627.

(12) T. J. Davies, C. E. Banks and R. G. Compton, "Voltammetry at spatially heterogeneous electrodes", *Journal of Solid State Electrochemistry*, 2005, **9**, 797–808.
(13) F. W. Campbell, Ph.D. Thesis, University of Oxford, 2010.
(14) E. L. Clark, J. Resasco, A. Landers, J. Lin, L. T. Chung, A. Walton, C. Hahn, T. F. Jaramillo and A. T. Bell, "Standards and Protocols for Data Acquisition and Reporting for Studies of the Electrochemical Reduction of Carbon Dioxide", *ACS Catalysis*, 2018, **8**, 6560–6570.
(15) H. A. Schwarz and R. W. Dodson, "Reduction potentials of CO2- and the alcohol radicals", *Journal of Physical Chemistry*, 1989, **93**, 409–414.
(16) Y. Yamazaki, H. Takeda and O. Ishitani, "Photocatalytic reduction of CO2 using metal complexes", *Journal of Photochemistry and Photobiology C: Photochemistry Reviews*, 2015, **25**, 106–137.
(17) H. Ishida, in *Carbon Dioxide Chemistry, Capture and Oil Recovery*, ed. I. Karamé, J. Shaya and H. Srour, InTech, 2018, ch. 2.
(18) A. Goyal, G. Marcandalli, V. A. Mints and M. T. Koper, "Competition between CO2Reduction and Hydrogen Evolution on a Gold Electrode under Well-Defined Mass Transport Conditions", *Journal of the American Chemical Society*, 2020, **142**, 4154–4161.
(19) R. Kortlever, J. Shen, K. J. P. Schouten, F. Calle-Vallejo and M. T. Koper, "Catalysts and Reaction Pathways for the Electrochemical Reduction of Carbon Dioxide", *Journal of Physical Chemistry Letters*, 2015, **6**, 4073–4082.
(20) J. S. Yoo, R. Christensen, T. Vegge, J. K. Nørskov and F. Studt, "Theoretical Insight into the Trends that Guide the Electrochemical Reduction of Carbon Dioxide to Formic Acid", *ChemSusChem*, 2016, **9**, 358–363.
(21) Z. Yang, F. E. Oropeza and K. H. Zhang, "P-block metal-based (Sn, In, Bi, Pb) electrocatalysts for selective reduction of CO2to formate", *APL Materials*, 2020, **8**, 60901.
(22) S. Li, Y. Liu, D. Xu and H.-g. Wang, "Conjugated polycopper phthalocyanine as the anode-active material with high specific capacity for lithium-organic batteries", *Materials Letters*, 2023, **333**, 133682.
(23) L. W. Diamond and N. N. Akinfiev, "Solubility of CO2 in water from -1.5 to 100°C and from 0.1 to 100 MPa: Evaluation of literature data and thermodynamic modelling", *Fluid Phase Equilibria*, 2003, **208**, 265–290.
(24) K. Al-Anezi and N. Hilal, "Effect of carbon dioxide in seawater on desalination: A comprehensive review", *Separation and Purification Reviews*, 2006, **35**, 223–247.
(25) H. Zhong, K. Fujii, Y. Nakano and F. Jin, "Effect of CO2 bubbling into aqueous solutions used for electrochemical reduction of CO2 for energy conversion and storage", *Journal of Physical Chemistry C*, 2015, **119**, 55–61.
(26) G. Marcandalli, M. C. Monteiro, A. Goyal and M. T. Koper, "Electrolyte Effects on CO2 Electrochemical Reduction to CO", *Accounts of Chemical Research*, 2022, **55**, 1900–1911.

(27) M. R. Singh, Y. Kwon, Y. Lum, J. W. I. I. I. Ager and A. T. Bell, "Hydrolysis of Electrolyte Cations Enhances the Electrochemical Reduction of CO2 over Ag and Cu", *Journal of the American Chemical Society*, 2016, **138**, 13006–13012.

(28) S. Xue, B. Garlyyev, S. Watzele, Y. Liang, J. Fichtner, M. D. Pohl and A. S. Bandarenka, "Influence of Alkali Metal Cations on the Hydrogen Evolution Reaction Activity of Pt, Ir, Au, and Ag Electrodes in Alkaline Electrolytes", *ChemElectroChem*, 2018, **5**, 2326–2329.

(29) O. Ayemoba and A. Cuesta, "Spectroscopic Evidence of Size-Dependent Buffering of Interfacial pH by Cation Hydrolysis during CO2 Electroreduction", *ACS Applied Materials and Interfaces*, 2017, **9**, 27377–27382.

(30) F. Zhang and A. C. Co, "Direct Evidence of Local pH Change and the Role of Alkali Cation during CO2 Electroreduction in Aqueous Media", *Angewandte Chemie - International Edition*, 2020, **59**, 1674–1681.

(31) Federal Institute for Geosciences and Natural Resources, *Preismonitor (Report)*, tech. rep., Federal Institute for Geosciences and Natural Resources, 2020, p. 3.

(32) S. Rajendrachari, K. K. Somashekharappa, R. S. Mahale, S. Vasanth and S. P. Chikkegouda, in *Frontiers in Voltammetry*, ed. S. Rajendrachari, K. K. Somashekharappa, S. P. Chikkegouda and S. Vasanth, IntechOpen, Rijeka, 2022, Ch. 4.

(33) A. P. Murthy, J. Theerthagiri and J. Madhavan, "Insights on Tafel Constant in the Analysis of Hydrogen Evolution Reaction", *Journal of Physical Chemistry C*, 2018, **122**, 23943–23949.

(34) O. van der Heijden, S. Park, R. E. Vos, J. J. Eggebeen and M. T. Koper, "Tafel Slope Plot as a Tool to Analyze Electrocatalytic Reactions", *ACS Energy Letters*, 2024, **9**, 1871–1879.

(35) F. Bao, E. Kemppainen, I. Dorbandt, R. Bors, F. Xi, R. Schlatmann, R. van de Krol and S. Calnan, "Understanding the Hydrogen Evolution Reaction Kinetics of Electrodeposited Nickel-Molybdenum in Acidic, Near-Neutral, and Alkaline Conditions", *ChemElectroChem*, 2021, **8**, 195–208.

(36) Y. Zhang, S. X. Guo, X. Zhang, A. M. Bond and J. Zhang, "Mechanistic understanding of the electrocatalytic CO2 reduction reaction – New developments based on advanced instrumental techniques", *Nano Today*, 2020, **31**, 100835.

(37) E. Boutin, M. Wang, J. C. Lin, M. Mesnage, D. Mendoza, B. Lassalle-Kaiser, C. Hahn, T. F. Jaramillo and M. Robert, "Aqueous Electrochemical Reduction of Carbon Dioxide and Carbon Monoxide into Methanol with Cobalt Phthalocyanine", *Angewandte Chemie - International Edition*, 2019, **58**, 16172–16176.

(38) M. Dunwell, W. Luc, Y. Yan, F. Jiao and B. Xu, "Understanding Surface-Mediated Electrochemical Reactions: CO2 Reduction and beyond", *ACS Catalysis*, 2018, **8**, 8121–8129.

(39) N. J. Firet and W. A. Smith, "Probing the Reaction Mechanism of CO2 Electroreduction over Ag Films via Operando Infrared Spectroscopy", *ACS Catalysis*, 2017, **7**, 606–612.

(40) X. Chen, D. Wei and M. S. Ahlquist, "Aggregation and Significant Difference in Reactivity Therein: Blocking the CO2-to-CH3OH Reaction", *Organometallics*, 2021, **40**, 3087–3093.
(41) Y. Wu, Z. Jiang, X. Lu, Y. Liang and H. Wang, "Domino electroreduction of CO2 to methanol on a molecular catalyst", *Nature*, 2019, **575**, 639–642.
(42) S. Fletcher, "Tafel slopes from first principles", *Journal of Solid State Electrochemistry*, 2009, **13**, 537–549.
(43) S. Kapusta and N. Hackerman, "Carbon Dioxide Reduction at a Metal Phthalocyanine Catalyzed Carbon Electrode", *Journal of The Electrochemical Society*, 1984, **131**, 1511–1514.
(44) Y. Chen, C. W. Li and M. W. Kanan, "Aqueous CO 2 Reduction at Very Low Overpotential on Oxide-Derived Au Nanoparticles", *Journal of the American Chemical Society*, 2012, **134**, 19969–19972.
(45) Q. Lu, J. Rosen, Y. Zhou, G. S. Hutchings, Y. C. Kimmel, J. G. Chen and F. Jiao, "A selective and efficient electrocatalyst for carbon dioxide reduction", *Nature Communications*, 2014, **5**, 3242.
(46) J. Shen, R. Kortlever, R. Kas, Y. Y. Birdja, O. Diaz-Morales, Y. Kwon, I. Ledezma-Yanez, K. J. P. Schouten, G. Mul and M. T. Koper, "Electrocatalytic reduction of carbon dioxide to carbon monoxide and methane at an immobilized cobalt protoporphyrin", *Nature Communications*, 2015, **6**, DOI: 10.1038/ncomms9177.
(47) N. Han, Y. Wang, L. Ma, J. Wen, J. Li, H. Zheng, K. Nie, X. Wang, F. Zhao, Y. Li, J. Fan, J. Zhong, T. Wu, D. J. Miller, J. Lu, S. T. Lee and Y. Li, "Supported Cobalt Polyphthalocyanine for High-Performance Electrocatalytic CO2 Reduction", *Chem*, 2017, **3**, 652–664.
(48) J. J. Jarju, M. C. Figueiredo and Y. V. Kolen'ko, in *Frontiers of Nanoscience*, ed. A. J. Wain and E. J. F. B. T. .-. F. o. N. Dickinson, Elsevier, 2021, vol. 18, pp. 343–420.
(49) B. Alarcon Fernandes Previdello, Theses, Université de Grenoble, 2013.
(50) K. J. Lee, C. T. Gruninger, K. M. Lodaya, S. Qadeer, B. E. Griffith and J. L. Dempsey, "Analysis of multi-electron, multi-step homogeneous catalysis by rotating disc electrode voltammetry: Theory, application, and obstacles", *Analyst*, 2020, **145**, 1258–1278.
(51) Y. Zhou, K. Wang, S. Zheng, X. Cheng, Y. He, W. Qin, X. Zhang, H. Chang, N. Zhong and X. He, "Advancements in electrochemical CO2 reduction reaction: A review on CO2 mass transport enhancement strategies", *Chemical Engineering Journal*, 2024, **486**, 150169.
(52) A. H. da Silva, R. E. Vos, R. J. Schrama and M. T. Koper, "Design of a Rotating Disk Electrode setup operating under high pressure and temperature: Application to CO2 reduction on gold", *Electrochimica Acta*, 2024, **498**, 144612.
(53) W. Tan, B. Cao, W. Xiao, M. Zhang, S. Wang, S. Xie, D. Xie, F. Cheng, Q. Guo and P. Liu, "Electrochemical Reduction of CO 2 on Hollow Cubic Cu 2 O@Au Nanocomposites", *Nanoscale Research Letters*, 2019, **14**, 63.

(54) F. Habibzadeh, P. Mardle, N. Zhao, H. D. Riley, D. A. Salvatore, C. P. Berlinguette, S. Holdcroft and Z. Shi, "Ion Exchange Membranes in Electrochemical CO2 Reduction Processes", *Electrochemical Energy Reviews*, 2023, **6**, 26.
(55) R. B. Prime, H. E. Bair, S. Vyazovkin, P. K. Gallagher and A. Riga, in *Thermal Analysis of Polymers: Fundamentals and Applications*, 2008, pp. 241–317.
(56) D. B. Williams and C. B. Carter, *Transmission electron microscopy: A textbook for materials science*, Springer New York, 2009, pp. 1–760.

Chapter 3

Multi-Walled Carbon Nanotubes as supports for the electrochemical CO_2 reduction reaction

3.1 Structure and Properties of Single-Walled Carbon Nanotubes

3.1.1 Carbon Nanotube Structure

CNTs are composed of sp^2 hybridised carbons covalently bonded together in a tubular structure. A singular CNT, known more commonly as a SWNT can be more simply thought of as a 2D graphene sheet that has been rolled into a tube along some axis on the lattice.

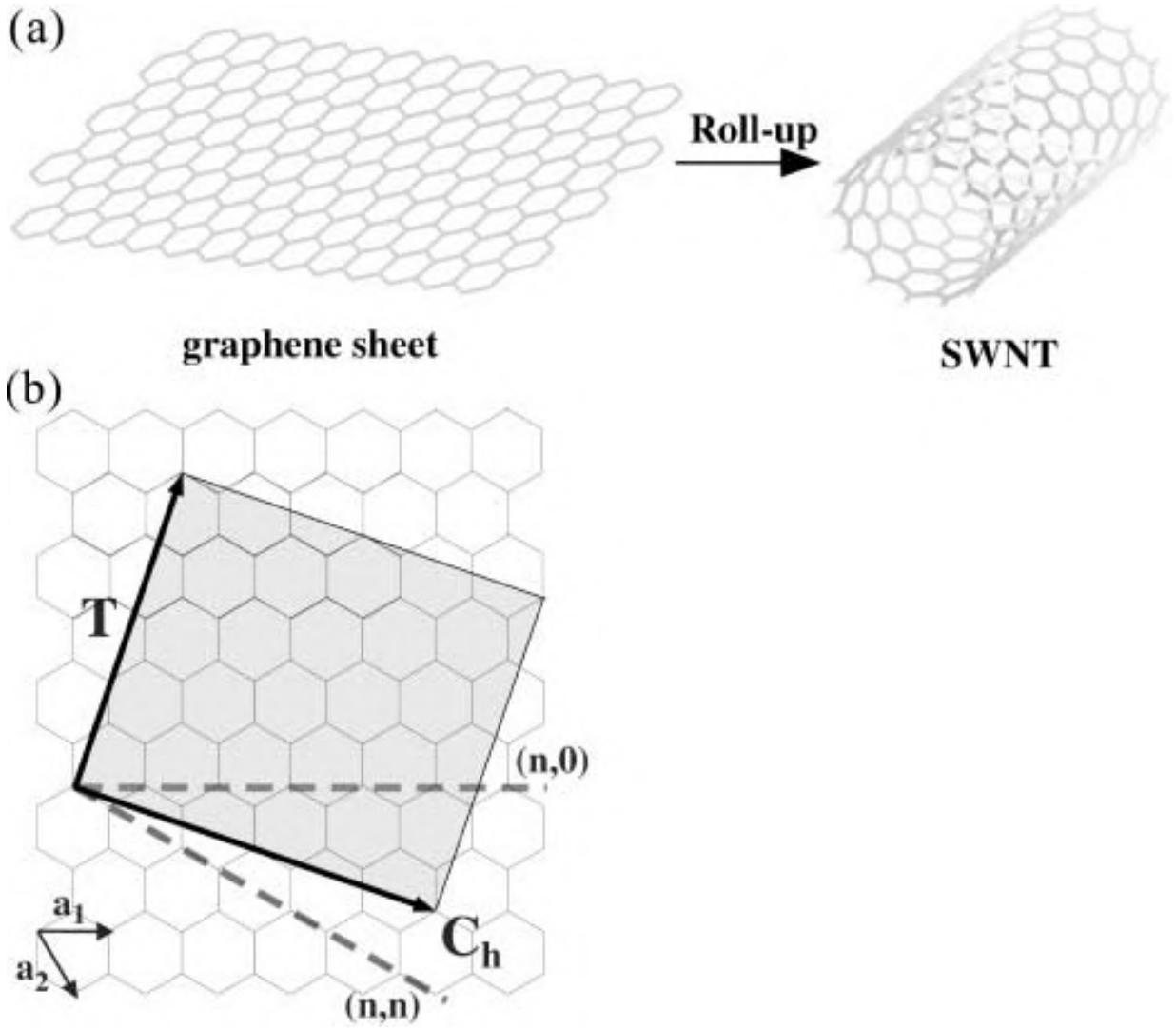


Figure 3.1: CNT from rolling a graphene sheet.[1,2]

Utilising the idea of a graphene sheet rolled up to form a tube allows the mathematical description of the different chiralities of carbon nanotubes by using a variable vector to roll the graphene lattice along into a tube, the nanotube structure varies depending on the vector chosen. This vector, referred to as the R, connects two carbon atoms on the 2D graphene lattice from which the lattice is rolled along.

The roll-up vector is described in units of the lattice vectors of the graphene primitive unit cell: a_1 and a_2 via the formula Eq. (3.1), where m and n are described as the chiral indices of the nanotube. Chiral indices in the form $[n, m]$ are used to describe different structures of a carbon nanotube.

$$R = ma_1 + na_2 \tag{3.1}$$

These chiral indices define not only the structure of a nanotube, but the various structures also display different electronic properties and some chemical properties.[3]

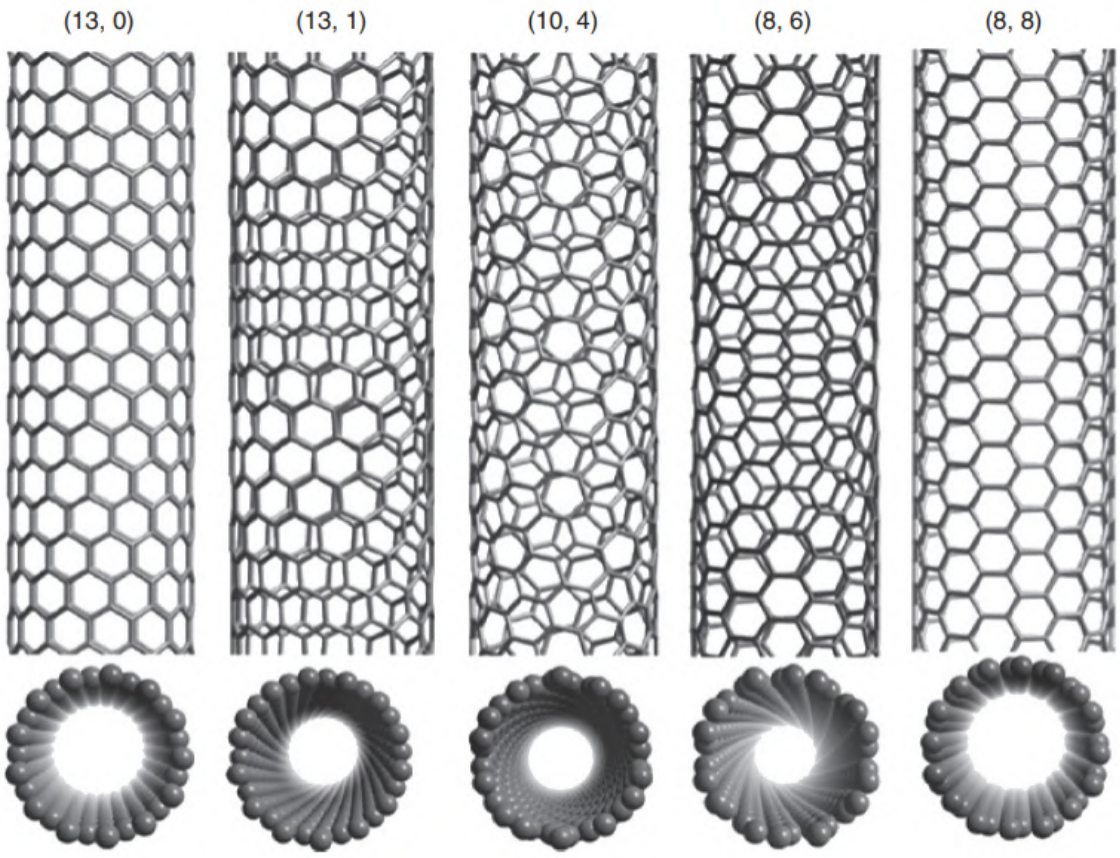


Figure 3.2: Examples of SWNT with varying chiral indices. Notably on the far left and far right are a zigzag CNT and an armchair CNT respectively.[4]

The roll-up vector R by definition describes the circumference of the nanotube. This allows a determination of the diameter D_{NT} of a CNT by treating it as the diameter of a circle.

$$D_{NT} = \frac{R}{\pi} \tag{3.2}$$

Carbon nanotubes, whilst explained from a theoretical standpoint as rolled-up graphene, exhibit vastly different properties to graphene due to the tube-like structure they adopt. Nanotube sidewalls exhibit higher reactivity than a graphene sheet due to the strain imposed by the curvature of the sidewall. This strain is due to π-orbital misalignment (ϕ) and the pyrimidalisation angle (θ_P) which are intrinsically linked to the nanotube diameter.

Pyramidalisation angle is effectively a way to measure the sp^3 character of the nanotube bond, as the angle approaches tetrahedral at $\theta_P = 19.5°$, more steric strain is induced in the trigonal sp^2 structure of the nanotube.[3,5]

The π-orbital misalignment is determined by the structure of the nanotube, more specifically where the CNT bonds lie in relation to the lattice axes:

- Whilst parallel to to the circumference (perpendicular to the nanotube axis): $\phi = 0$
- When not parallel to the circumference: $\phi \neq 0$

In reality, CNTs do not have a point of $\phi = 0$, and exist strained around the wall of the tube. This strain induced by θ_P and ϕ is inversely proportional to D_{NT}, which counter-intuitively means larger diameter nanotubes are less reactive and more stable than smaller diameter nanotube.

[n,m]	diameter (nm)	θ_P (deg)	ϕ (deg)	[n,m]	diameter (nm)	θ_P (deg)	ϕ (deg)
10,0	7.81	5.15	0, 18.5	5,5	6.76	5.97	0, 21.3
12,0	9.37	4.30	0, 15.3	6,6	8.11	4.99	0, 17.6
14,0	10.93	3.69	0, 13.1	7,7	9.47	4.27	0, 15.0
16,0	12.49	3.24	0, 11.4	8,8	10.82	3.74	0, 13.1
18,0	14.05	2.88	0, 10.1	9,9	12.17	3.33	0, 11.6
20,0	15.6	2.59	0, 9.1	10,10	13.52	3.00	0, 10.4

Table 3.1: Table illustrating relationship between structure, diameter, and strain in SWNTs[5]

3.1.2 Electronic Properties of Carbon Nanotubes

Structural determination of CNTs is of key importance for electrochemical investigation, as structure is intrinsically linked to the electrical properties of a nanotube.[6]

CNTs are treated as rolled-up graphene for structural determination, so by looking at the electronic structure of graphene we can work to derive the electronic structure of CNTs. Graphene has an infinitely large number of electronic levels that form the valence band and conduction band based on the Linear Combination of Atomic Orbitals (LCAO), meaning graphene is electronically continuous with a band gap of effectively 0.[7]

This indicates graphene is electronically metallic due to the absence of a band gap in its electronic structure, resulting in high electrical conductivity.[7] An absence of band gap denotes the Fermi level (E_F) is situated at the energy of the conduction band meaning there no forbidden states exist for electrons in between both the filled valence and empty conduction bands. This results in high conductivity due to the little energy required for electron excitation from the electron filled valence band to the empty conduction band.

As the conduction bands are formed from a set of filled and non-filled Molecular Orbitals

(MOs) in graphene, when applied to a SWNT rolled from a 2D graphene sheet, the roll up vector (and therefore the chiral indices) will determine whether a CNT's Highest Occupied Molecular Orbital (HOMO)-Lowest Unoccupied Molecular Orbital (LUMO) symmetry is preserved. This HOMO-LUMO symmetry determines whether the Fermi level will fall within the conduction band (metallic behaviour), or if it falls at the top of the valence band, which will separate the conduction and valence bands by a set of forbidden energy states, known as a band gap (semi-conducting behaviour)..[4]

In a graphene system, the band gap is incredibly small or nil, meaning CNTs always will at minimum behave as semi-conductors and may never behave as an electrical insulator.[4]

The electronic structure of a given CNTs sturcture can be determined from the chiral indices, as they represent the roll-up vector of the graphene, and consequently the HOMO-LUMO symmetry. The determination of electronic behaviour from chiral indices is as follows[4]:

- Armchair nanotubes $(n = m)$ are practically all metallic.
- Zigzag $(n|m = 0)$ and chiral $(n \neq m \neq 0)$ nanotubes are zero band-gap semiconductors (effectively also metallic) only if $(n - m = 3k)$ where $k \in \mathbb{Z}$, $0 \in \mathbb{Z}$
- For any other combination of indices $(n - m \neq 3k)$, CNTs are large band gap semi-conductors (relative to graphene).

Despite this, semi-conducting CNTs $(n - m \neq 3k)$ exhibit a band gap which is inversely proportional to D_{NT}.[4] therefore CNTs begin to exhibit more metallic character as diameter size increases and curvature of the wall is not too great (0.7 nm or greater).[4,8] This results in $3/4$ of all CNTs being semi-conducting, and therefore a majority of CNTs in any given electrochemical experiment will be semi-conducting, with a still significant $1/4$ metallic.[8]

However, singular CNTs are difficult to chirally isolate without the use of specialised methods,[9] with a large majority of electrochemical research utilising CNTs as purchased or purified with acid or heat treatment,[10] so unless otherwise stated by the investigation author, in this work, CNTs are assumed racemic with their electronic structures being $3/4$ semi-conducting, $1/4$ metallic.

3.1.3 Multi-Walled Carbon Nanotubes

MWNTs, similar to SWNTs are comprised of sp^2 hybridised carbon covalently bonded in a tubular structure, with the key difference being that MWNTs are comprised of multiple concentric CNTs layers forming one tubular nanostructure[11] (Fig. 3.3).

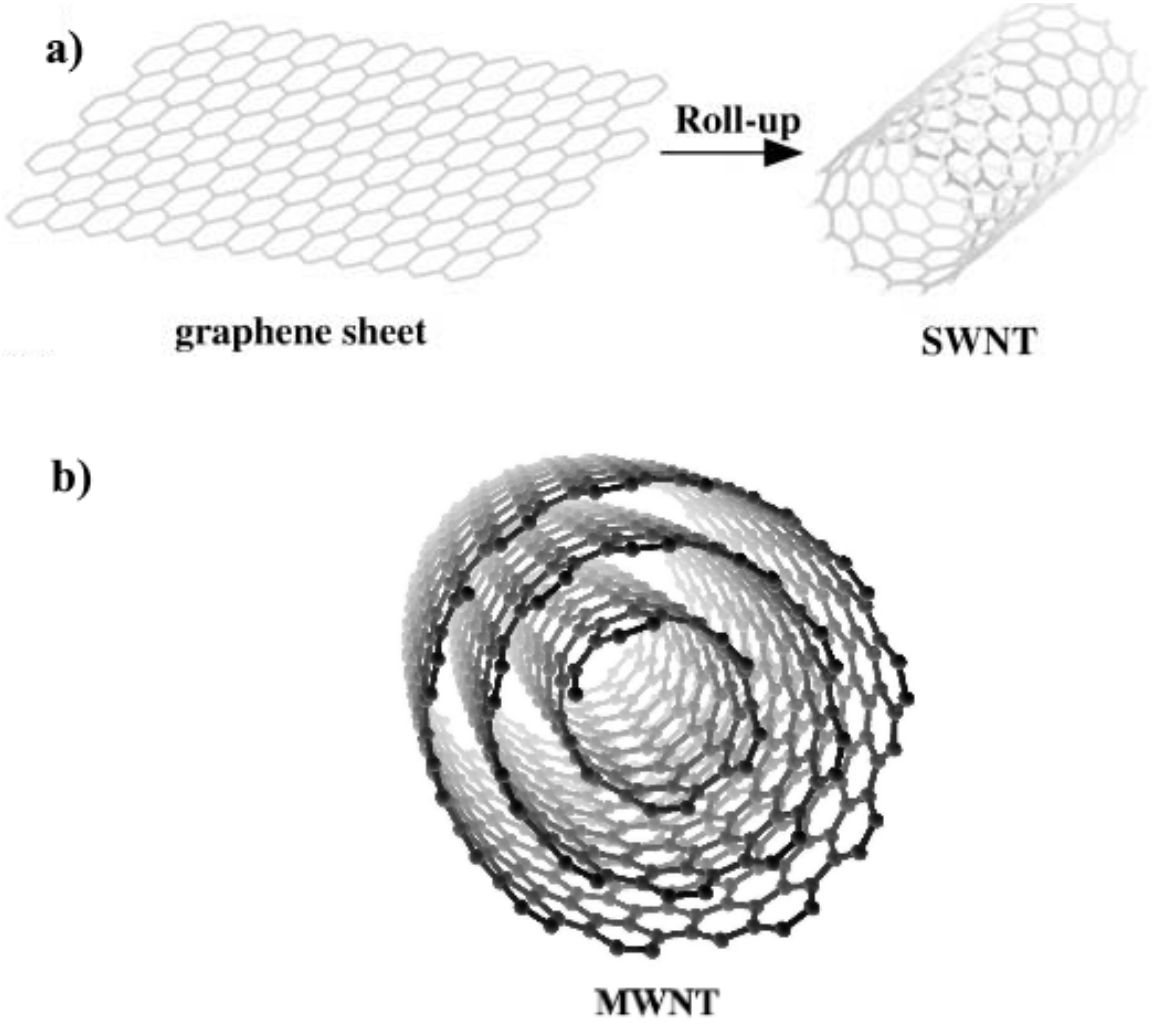


Figure 3.3: Diagram illustrating a) the relationship between graphene and single-walled nanotubes and b) structure of multi-walled nanotubes. Images adapted from a) Odom *et al*[1]; b) Goze-Bac[12]

As a result of their concentric structure, MWNTs have typically much larger D_{NT}'s than their single-walled counterparts[11] whilst also retaining the exceptional electrical conductivity found in SWNTs, supporting current densities of up to 10^6 A cm^{-2}[13] with conductivities of 10^4 S m^{-1}. Similarly to SWNTs, the electrical properties of MWNTs are influenced by chirality, however it is largely determined by the outermost walls of the MWNT.[14] Notably, the inner walls do not necessarily feature the same chirality as the outside wall, with the inner wall-to-wall interactions having a non-negligible effect on the electrical properties.[15] The inner wall-to-wall interactions have been shown to actually improve conductivity as MWNTs D_{NT} increases due to the inner walls facilitating electron transport, and at sufficient length (*ca.* 7 μm) and diameter, can outperform copper and even SWNTs.[16,17]

3.1.4 Multi-Walled Carbon Nanotubes as electrocatalyst supports

MWNTs find use in electrocatalysis over SWNTs due to higher average diameters and lower cost of production,[11] alongside the aforementioned outstanding electrical properties. The larger diameters in particular better allow catalytic systems of interest to attach to the surface of the MWNT favourably, which is particularly pertinent in studies making use of organic molecules such as phthalocyanines,[18] as the low diameters of SWNTs[4] would induce significant structural distortion of less favourable Van Der Waals interactions to the SWNT support. In addition, it has been extensively evidenced that the facile electron transport provided by MWNTs provides a reduction in η, increased current density, and improved selectivity for the electrochemical CO_2RR[19–25]

One point of note is the electrochemical activity of MWNTs, as it remains a point of contention within research, with many researchers assuming the outer wall of MWNTs is analogous to that of Highly-Ordered Pyrolytic Graphite (HOPG) with only electron transfer from the MWNT ends contributing redox behaviour.[26] However, it has also been evidenced that the redox behaviour actually stems from thin layer diffusion within the porous layer of a multiply layered MWNT electrode.[27,28] Thankfully, these concerns are largely relevant to the field of electrochemical sensing,[19] and it has been evidenced that MWNT do not play a role in either the HER[29] and there is no evidence for electrochemical CO_2RR occurring on MWNTs alone.

3.1.5 Electrochemistry

3.1.5.1 Voltammetry

To evaluate the impact MWNT has as an electrocatalytic support for the CO_2RR, CV and LSV of MWNTs was conducted and is shown in Fig. 3.4.

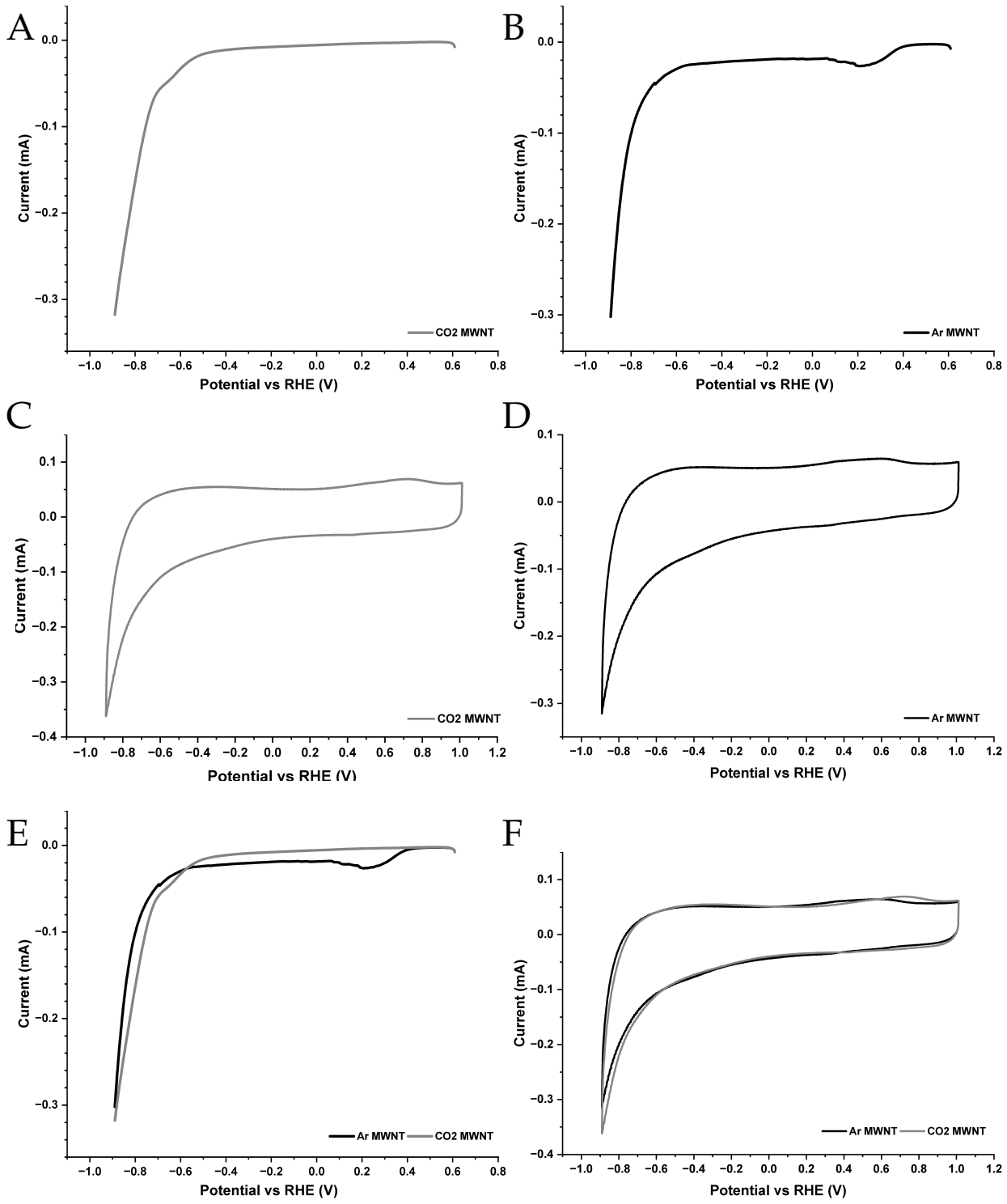


Figure 3.4: (A) LSV plot of MWNTs using a RDE at a scan rate of 0.05 v in CO_2 saturated 0.5 M $KHCO_3$ electrolyte at 1600 rpm; (B) LSV plot of MWNTs using a RDE at a scan rate of 0.05 V s^{-1} in Ar saturated 0.5 M $KHCO_3$ electrolyte at 1600 rpm; (C) CV plot of MWNTs using a RDE at a scan rate of 0.05 V s^{-1} in CO_2 saturated 0.5 M $KHCO_3$ electrolyte at 1600 rpm; (D) LSV plot of MWNTs using a RDE at a scan rate of 0.05 V s^{-1} in Ar saturated 0.5 M $KHCO_3$ electrolyte at 1600 rpm; (E) Overlaid LSV plots of MWNTs using a RDE at a scan rate of 0.05 V s^{-1} in CO_2 (gray) and Ar (black) saturated 0.5 M $KHCO_3$ electrolyte at 1600 rpm; (F) Overlaid CV plots of MWNTs using a RDE at a scan rate of 0.05 V s^{-1} in CO_2 (gray) and Ar (black) saturated 0.5 M $KHCO_3$ electrolyte at 1600 rpm

As can be seen in Fig. 3.4, the MWNTs appear to have minimal CO_2RR activity alone, as the current passed is on the scale of μA, however there is still some catalytic activity towards HER beginning at ~ -0.55 V vs RHE (Figs. 3.4A and 3.4B). Notably, the catalytic current reached at -0.9 V vs RHE is slightly higher in CO_2 compared to Ar, which could be attributed to: the increased pH resulting from CO_2 saturation as a result of the bicarbonate buffer outlined in Section 2.3.2, metal MWNT internal catalyst activity towards HER,[11] or minor CO_2RR activity (although is unlikely due to the difficulty of CO_2 activation[30]). It is also possible that this minor increase in activity may result from trace exposed MWNT metal internal catalyst having CO_2RR activity, but due to the carbon enclosed nature of these metal catalyst sites, it is unlikely to be the case.[11] Lastly, in Fig. 3.4B and more subtly in Fig. 3.4F, what appears to be a redox feature can be observed at $\sim$ 0.2 V vs RHE , which likely arises from either thin layer diffusion in the porous layer of the electrode, or surface defects on the MWNT giving rise to redox active quinone-like sites on the surface..[27,28]

Chapter 3 Bibliography

(1) T. W. Odom, J. H. Hafner and C. M. Lieber, in *Carbon Nanotubes*, Springer Berlin Heidelberg, Berlin, Heidelberg, 2007, vol. 80, pp. 173–211.

(2) S. Yamamoto, S. V. Dudkin, M. Kimura and N. Kobayashi, in *Handbook of Porphyrin Science: With Applications to Chemistry, Physics, Materials Science, Engineering, Biology and Medicine - Volume 45: Phthalocyanine Synthesis and Computational Design of Functional Tetrapyrroles*, WORLD SCIENTIFIC, 2019, vol. Volume 45, pp. 1–168.

(3) D. Tasis, N. Tagmatarchis, A. Bianco and M. Prato, *Chemistry of carbon nanotubes*, ed. V. A. Basiuk and E. V. Basiuk, American Scientific Publishers, Stevenson Ranch, Calif., 2006, vol. 106, pp. 87–117.

(4) M. Monthioux, P. Serp, E. Flahaut, M. Razafinimanana, C. Laurent, A. Peigney, W. Bacsa and J.-M. Broto, in *Springer Handbook of Nanotechnology*, Springer Berlin Heidelberg, Berlin, Heidelberg, 2007, pp. 43–112.

(5) S. Niyogi, M. A. Hamon, H. Hu, B. Zhao, P. Bhowmik, R. Sen, M. E. Itkis and R. C. Haddon, "Chemistry of Single-Walled Carbon Nanotubes", *Accounts of Chemical Research*, 2002, **35**, 1105–1113.

(6) J. W. Mintmire, B. I. Dunlap and C. T. White, "Are fullerene tubules metallic?", *Phys. Rev. Lett.*, 1992, **68**, 631–634.

(7) D. W. Boukhvalov, M. I. Katsnelson and A. I. Lichtenstein, "Hydrogen on graphene: Electronic structure, total energy, structural distortions and magnetism from first-principles calculations", *Physical Review B - Condensed Matter and Materials Physics*, 2008, **77**, 35427.

(8) E. A. Laird, F. Kuemmeth, G. A. Steele, K. Grove-Rasmussen, J. Nygård, K. Flensberg and L. P. Kouwenhoven, "Quantum transport in carbon nanotubes", *Reviews of Modern Physics*, 2015, **87**, 703–764.

(9) M. Karandish, S. Fardindoost and G. Pazuki, "A Novel Approach in Sorting Chirality Species of Single-Wall Carbon Nanotubes Based on an Aqueous Two-Phase System of Polymer-Salt", *Scientific Reports*, 2020, **10**, 2025.

(10) N. Sezer and M. Koç, "Oxidative acid treatment of carbon nanotubes", *Surfaces and Interfaces*, 2019, **14**, 1–8.

(11) Á. Kukovecz, G. Kozma and Z. Kónya, in *Springer Handbook of Nanomaterials*, ed. R. Vajtai, Springer Berlin Heidelberg, Berlin, Heidelberg, 2013, pp. 147–188.

(12) C. Goze-Bac, Accreditation to supervise research, université montpellier 2, 2008.

(13) K. Kaneto, M. Tsuruta, G. Sakai, W. Y. Cho and Y. Ando, "Electrical conductivities of multi-wall carbon nano tubes", *Synthetic Metals*, 1999, **103**, 2543–2546.
(14) S. Frank, P. Poncharal, Z. L. Wang and W. A. De Heer, "Carbon nanotube quantum resistors", *Science*, 1998, **280**, 1744–1746.
(15) P. G. Collins, M. S. Arnold and P. Avouris, "Engineering carbon nanotubes and nanotube circuits using electrical breakdown", *Science*, 2001, **292**, 706–709.
(16) H. J. Li, W. G. Lu, J. J. Li, X. D. Bai and C. Z. Gu, "Multichannel ballistic transport in multiwall carbon nanotubes", *Physical Review Letters*, 2005, **95**, 86601.
(17) A. Naeemi and J. D. Meindl, "Compact physical models for multiwall carbon-nanotube interconnects", *IEEE Electron Device Letters*, 2006, **27**, 338–340.
(18) H. Yang, N. Guo, S. Xi, Y. Wu, B. Yao, Q. He, C. Zhang and L. Wang, "Potential-driven structural distortion in cobalt phthalocyanine for electrocatalytic CO2/CO reduction towards methanol", *Nature Communications*, 2024, **15**, 7703.
(19) I. Dumitrescu, P. R. Unwin and J. V. MacPherson, "Electrochemistry at carbon nanotubes: Perspective and issues", *Chemical Communications*, 2009, 6886–6901.
(20) Y. Xing, M. Cui, P. Fan, J. Ren, C. Zhang, N. Li, X. Wen and X. Ji, "Efficient and selective electrochemical reduction of CO2 to formate on 3D porous structured multi-walled carbon nanotubes supported Pb nanoparticles", *Materials Chemistry and Physics*, 2019, **237**, 121826.
(21) Z. Yang, F. E. Oropeza and K. H. Zhang, "P-block metal-based (Sn, In, Bi, Pb) electrocatalysts for selective reduction of CO2to formate", *APL Materials*, 2020, **8**, 60901.
(22) N. Li, P. Yan, Y. Tang, J. Wang, X. Y. Yu and H. B. Wu, "In-situ formation of ligand-stabilized bismuth nanosheets for efficient CO2 conversion", *Applied Catalysis B: Environmental*, 2021, **297**, 120481.
(23) S. Li, Y. Liu, D. Xu and H.-g. Wang, "Conjugated polycopper phthalocyanine as the anode-active material with high specific capacity for lithium-organic batteries", *Materials Letters*, 2023, **333**, 133682.
(24) C. Genovese, C. Ampelli, S. Perathoner and G. Centi, "Electrocatalytic conversion of CO2 to liquid fuels using nanocarbon-based electrodes", *Journal of Energy Chemistry*, 2013, **22**, 202–213.
(25) K. Zhao and X. Quan, "Carbon-based materials for electrochemical reduction of CO2to C2+oxygenates: Recent progress and remaining challenges", *ACS Catalysis*, 2021, **11**, 2076–2097.
(26) C. E. Banks, M. R. Moore, T. J. Davies and R. G. Compton, "Investigation of modified basal plane pyrolytic graphite electrodes: Definitive evidence for the electrocatalytic properties of the ends of carbon nanotubes", *Chemical Communications*, 2004, 1804–1805.
(27) I. Streeter, G. G. Wildgoose, L. Shao and R. G. Compton, "Cyclic voltammetry on electrode surfaces covered with porous layers: An analysis of electron transfer kinetics at single-walled carbon nanotube modified electrodes", *Sensors and Actuators, B: Chemical*, 2008, **133**, 462–466.

(28) A. Kaliyaraj Selva Kumar and R. G. Compton, "Understanding Carbon Nanotube Voltammetry: Distinguishing Adsorptive and Thin Layer Effects via "single-Entity" Electrochemistry", *Journal of Physical Chemistry Letters*, 2022, **13**, 5557–5562.

(29) M. Ahmed, G. Kour, Z. Sun, A. Du and X. Mao, "Activating Hydrogen Evolution Reaction on Carbon Nanotube via Aryl Functionalisation: The Role of Hybrid sp2–sp3 Interface and Curvature", *Nanomaterials*, 2023, **13**, DOI: 10.3390/nano13142122.

(30) H. A. Schwarz and R. W. Dodson, "Reduction potentials of CO2- and the alcohol radicals", *Journal of Physical Chemistry*, 1989, **93**, 409–414.

Chapter 4

Cobalt Phthalocyanines on Multi-Walled Carbon Nanotubes for the electrochemical Carbon Dioxide Reduction Reaction

4.1 Background

Cobalt Phthalocyanine (CoPc) is a metallomacrocylic molecule which is well-known catalyst for the CO_2RR (Fig. 4.1).

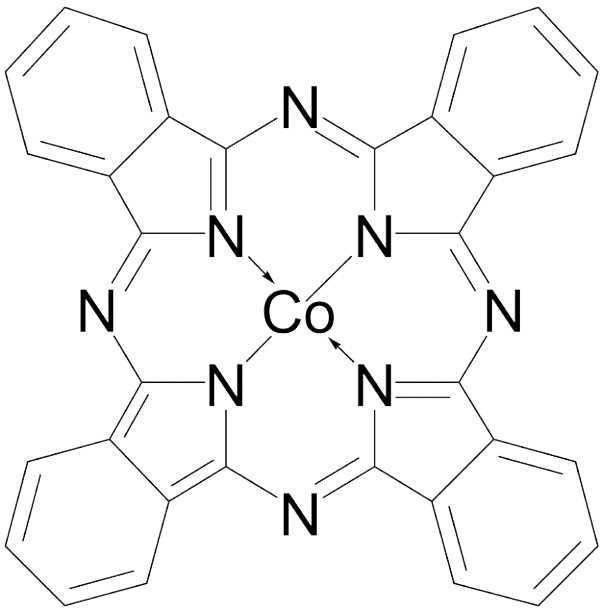


Figure 4.1: CoPc structure

Its catalytic activity was first reported in 1984 by Lieber and Lewis,[1] in which CoPc was deposited onto carbon electrodes via a dropcasting method using a THF/CoPc solution and found to convert CO_2(g) to CO(g) at a Faradaic efficiency of around 55-60% with a moderate overpotential ($\eta =\sim 400$ mV).[1] Notably, the work by Lieber and Lewis highlight an issue with stability of the catalyst, an issue that would remain a constant problem for future CoPc electrocatalysis research.[2,3]

Later that year in September of 1984, Kapusta and Hackerman[4] published their investigation into both CoPc and Nickel Phthalocyanine (NiPc) on carbon electrodes for solubised CO_2 using CO_2 saturated 0.1 M $NaHCO_3$ solution, and reported the production of both formate and methanol via CoPc to be 60 FE% for formate, 5 FE% methanol, and assumedly the rest towards CO. The formation of formate and methanol via use of CoPc-based electrocatalysts by Kapusta and Hackerman[4] stands out given the time of publication, as methanol production using CoPc would not be reported again in literature until 2019,[2,5] and $HCOO^-$ production not being reported outside of non-faradaic processes to date[3] (See Section I for further discussion).

Research work making use of CoPc as a CO_2RR catalyst would continue from 1984 to 2019 with work optimising the CO_2 to CO conversion by increasing the availability of active sites and adapting the system for use in heterogeneous catalysis by supporting CoPc on carbon fibres,[6] use of polymeric Cobalt Polyphthalocyanine (CoPPc),[7] or production of a CoPc Covalent Organic Framework (COF).[8] Optimisations towards CO production over the years resulted in multiple reported works with FE_{CO} of $> 99\%$[9,10] at overpotentials as low as $\eta =\sim -0.55$ V vs RHE. Additionally, almost all work conducted on CoPc based catalysts make use of CNTs[5,7,9–11] as supports due to their highly conductive nature and high surface area for dispersion of the CoPc molecular catalyst.

Research into CoPc was largely focussed on the reduction of the CO_2 to CO overpotential up to 2019, in which the work by Boutin *et al*[5] established that production of CH_3OH is possible via additional further reduction of CO at a FE_{CH_3OH} of 18% in 1 M KOH.[5] Boutin *et al*'s[5] work was closely followed with a work later that year by Wu *et al*,[2] in which by utilising molecularly dispersed CoPc on MWNTs were capable of achieving FE_{CH_3OH} of 44% over the course of 1 hour in 0.1 M $KHCO_3$. The key to the CH_3OH production capability of CoPc as stated by Wu *et al*[2] is polarization of the CoPc electrode more negative than -0.77 V vs RHE. Lastly, inspired by the work of Boutin and Wu et al,[2,5] Chen *et al*[12] conducted an investigation into why the CoPc/MWNT system was capable of producing CH_3OH when previously it was not seen as a product. Using computational methods, Chen *et al*[12] rationalised this difference in selectivity as being dependant on the degree of aggregation of the CoPc due to differences in the CO dissociation step with monomeric CoPc (Fig. 4.2A). Monomeric CoPc is stated to have a low enough energy barrier for the further reduction of CO to CH_3OH via addition of another electron to the the CoPc$-$CO intermediate, whilst in the dimeric CoPc this route is disfavoured and results in CO dissociation (Fig. 4.2B).

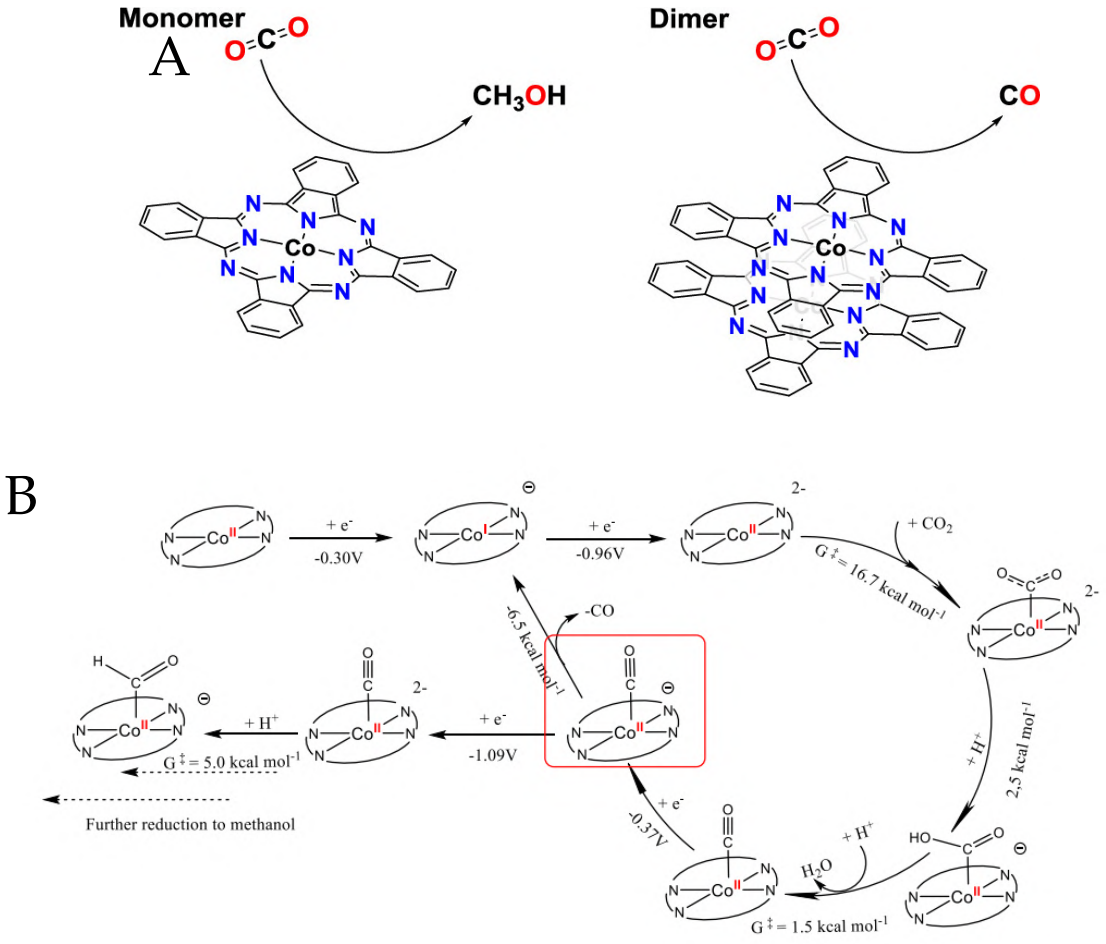


Figure 4.2: (A) Top: Schematic outlining the difference in product selectivity between monomeric CoPc and dimeric CoPc. Adapted from Chen *et al*[12]; (B) Bottom: Catalytic mechanism for the production of either CH_3OH or CO from CoPc. The critical step in product selectivity is highlighted with a red box. Adapted from Chen *et al*[12]

4.1.1 Cobalt Phthalocyanine for CH_3OH production

To further elaborate on the initial works revealing CH_3OH activity from CoPc: Boutin *et al*,[5] Wu *et al*,[2] and Kapusta and Hackerman,[4] further exploration into the conditions and findings must be considered. Firstly, both Boutin and Wu *et al*'s[2,5] work prepare the CoPc/MWNT catalyst by physical mixing of CoPcs and MWNTs via sonication, then preparation of the electrode via an ink composed of the dispersed catalyst in organic solvent followed by addition of a Nafion^{TM} binder solution. In contrast, Kapusta and Hackerman[4] describe deposition of CoPc directly onto a GCE using sulfuric acid dilution with water. Herein, the following works are discussed in an order which allows discussion of the relevant catalytic properties and chemistry of CoPc for the CO_2RR

4.1.1.1 Boutin *et al*[5]

In the work by Boutin *et al*'s[5] work CH_3OH was first detected -0.88 V vs RHE at an FE_{CH_3OH} of 0.3% in CO_2 saturated 0.5 M $KHCO_3$ at a pH of 7.2 after 3 hr electrolysis. At pH 7 using CO and HCOO as feedstocks at potentials of 0.89 V vs RHE for 2 hours in 0.1 M KH_2PO_4/K_2HPO_4 resulted in a FE_{CH_3OH} of 1.1% and 0% respectively. Increasing the potential to 0.99 V vs RHE under CO feed gas increased the FE_{CH_3OH} to 2.3% with a j_{CH_3OH} of 0.06 mA cm^{-2}. When the pH is increased to 13 via use of a 0.1M KOH electrolyte with CO gas feedstock, CH_3OH is detectable at potentials as low as -0.54 V vs RHE, with the optimal potential for CO at pH 13 being -0.64 V vs RHE with a FE_{CH_3OH} of 14.3%. Most interestingly, utilisation of HCHO feedstock at pH 13 results in an increase of FE_{CH_3OH} to 18.2% at -0.54 V vs RHE and 11.6% at -0.64 V vs RHE. Production of CH_3OH from CO_2 and CO feedstocks was confirmed via ^{13}C isotopic labelling of the feed gas to be a result of the CO_2RR. For all experiments, the rest of the FE_{total} was comprised of H_2, however $HCOO^-$ was observed as a product resulting from non-faradaic processes.

These results allude to the mechanism later to be outlined by Chen *et al*,[12] in which CoPc−CO and CoPc−CHO are stated to be intermediates in the CoPc catalysis mechanism towards methanol, with the latter CoPc−CHO intermediate predicted to be beyond the critical CO dissociation step (Fig. 4.2B) and therefore explaining the comparatively large jump in selectivity observed. Additionally, the $HCOO^-$ feedstock producing no CH_3OH is explained by this mechanism[12] due to absence of a formate intermediate or any interconversion routes between HCHO and $HCOO^-$ (Fig. 4.2B). The work by Boutin *et al*[5] makes particular note of the Cannizzaro reaction[13] that can spontaneously take place in alkaline media, or in neutral media at the cathode where localised high pH build-up can occur.[14] The Cannizzaro reaction results in the conversion of formaldehyde to a primary alcohol and carboxylic acid, so relevant for this work it is possible for two formaldehyde molecules to produce methanol and formate[13] at the electrode non-Faradaically,[14] and explains formate production in CoPc electrocatalysis despite no feasible mechanism.[12]

Regarding the catalytic stability of CoPc, at potentials exceeding -0.94 V vs RHE the CH_3OH production efficiency begins to trend downwards and is concurrent with large increase in H_2 production. Additionally, after a few hours at the optimum potential of -0.54 V vs RHE , methanol activity begins to decrease. This catalytic instability over long periods is not associated with the high pH utilised due to previously demonstrated high pH stability over 10 hrs by Wang *et al*,[11] and is instead attributed to reductive hydrogenation of the C=N bonds in CoPc which has been demonstrated previously in works dating back to 1953.[15] This implies a intrinsic issue of overpotential η with regards to CoPc, as more negative potentials are required for CH_3OH formation, however these more negative potentials result in expedited reductive deactivation of the CoPc catalyst.

4.1.1.2 Wu *et al*[2]

In the work by Wu *et al*,[2] CH_3OH production using CoPc/MWNT is first observed at the potential of -0.82 V vs RHE in 0.1 M $KHCO_3$ electrolyte saturated with CO_2 at pH 6.8 over 1 hour at a FE_{CH_3OH} of $\sim 5-7\%$, and the optimal potential for CH_3OH production was found to be -0.94 V vs RHE with a FE_{CH_3OH} of 44% under the same conditions. The FE_{CH_3OH} reported are considerably higher than those reported by Boutin *et al*, and analysis via electron microscopy supports this due to the molecular dispersion of the CoPc on the MWNT support, with CoPc units separate on the MWNT support with little to no aggregation. This single unit dispersion of the CoPc/MWNT is predicted by Chen *et al*[12] to have a significant effect on CH_3OH selectivity. Interesting to note is the synthesis method of CoPc/MWNT does not significantly differ between Boutin and Wu *et al*,[2,5] the only difference between the methods being that Wu *et al*[2] conducted pretreatment of the MWNT support via sonication in 5% HCl and post synthesis lyophilisation. This would suggest that pretreatment of MWNT increases dispersion of monomeric CoPc units.

Similarly to Boutin *et al*,[5] Wu *et al*[2] conducted further testing using CO as a feedstock during the electrocatalysis, and similarly found that with CO the overpotential decreased for CH_3OH production, with observed CH_3OH production at -0.77 V vs RHE and at -0.83 V vs RHE achieved a FE_{CH_3OH} of 28%. These findings further validate the predicted mechanism by Chen *et al*,[12] as CO dissociation is the critical step in product selectivity Fig. 4.2B.

Regarding catalytic stability, FE_{CH_3OH} begins to dramatically decrease at potentials more negative than -0.94 V vs RHE for CO_2 and -0.83 V vs RHE for CO, dropping to $< 10\%$ at -1.05 V vs RHE for CO_2 and -0.97 V vs RHE for CO. Additionally, beyond 1 hour, the FE_{CH_3OH} appears to exponentially decay, reaching an FE_{CH_3OH} of 0.6% after only 5 hours. This is attributed to reductive deactivation of CoPc via hydrogenation, as post-mortem microscopy excluded the possibility of reductive demetalation.[2] Furthermore, UV-Vis spectroscopy strongly suggested reductive hydrogenation of CoPc, corroborating Boutin *et al*,[5] as chemically reduced CoPc with $NaBH_4$ had the same absorbance peaks as the post-mortem catalyst, whilst the free base H_2Pc spectra did not.

To combat this reductive deactivation of CoPc, Wu *et al*[2] further investigated a modified CoPc$-NH_2$ catalyst and noted a dramatically increased stability over time, with 12 hr electrocatalytic testing resulting in a FE_{CH_3OH} of 28%. This increase in stability was attributed to the likely lower pK_a and larger conjugation system decreasing to reductive deactivation via hydrogenation.[2] Unfortunately the CoPc$-NH_2$ catalyst also had an increased selectivity towards CO, achieving a maximum of FE_{CH_3OH} of 41%.

The work by Wu *et al* demonstrates a higher achievable FE_{CH_3OH} for CoPc catalyst systems than was predicted by Boutin *et al*,[5] however both works highlight the key limitation of CoPc, this limitation being the low long term stability due to overlap between the overpotential for FE_{CH_3OH} and the reductive deactivation potential of the

catalyst. This limitation was the primary inspiration behind the research conducted on PPc/MWNTs in this thesis.

4.1.2 Polyphthalocyanines on Multi-Walled Carbon Nanotubes

PPc/MWNT are known electrocatalysts for the CO_2RR and have been shown in literature to produce CO at moderate overpotentials (η = 0.5) V vs RHE with high FEs ($>$ 90%) and current densities (50 mA cm^{-2} for geometric surface areas), and long term stability.[3,7,16] As of the time of writing, CH_3OH has not been observed as a CO_2RR product in current literature, however PPcs present a potential solution to the stability issues faced by CoPc/MWNT (Section 4.1.1) as it has an inherent stability to reductive hydrogenation due being a comparatively much larger conjugated system than single unit CoPc.[2,16] Additionally it presents potential to provide an increase of single Co atom active sites orders of magnitude larger than CoPc/MWNT due to the fact that active sites are forced in immediate vicinity to eachother due to the polymeric structure, potentially resulting in a support with high coverage of CoPc active sites as each site is theoretically a half width of the CoPc monomers distance away from each other (Fig. 4.3).

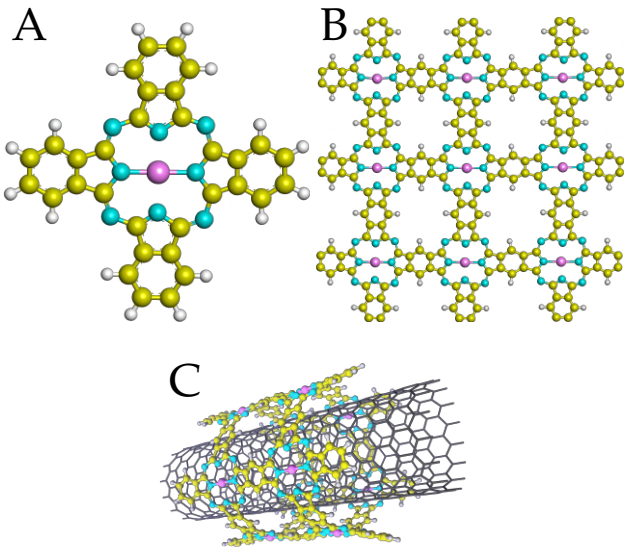


Figure 4.3: (A) Molecular model of CoPc with carbon atoms coloured yellow, nitrogen atoms coloured blue, cobalt atoms coloured pink, and hydrogen atoms coloured white; (B) Molecular model of CoPPc with the same colour scheme as Fig. 4.3A. Hydrogen atoms along the edge are omitted to show a repeating polymer structure; (C) Molecular model of CoPPc/MWNT with the nanotube carbon atoms coloured black and the the same colour scheme as Fig. 4.3A. The MWNT is presented as a SWNT for sake of simplicity.

A single layer polyphthalocyanine on a MWNT support as seen in Fig. 4.3C would be the hypothetically ideal electrocatalyst for CH_3OH production due to the aforementioned high active site density and stability, but importantly due to being composed of a single layer of CoPc with no stacking which is predicted to be a critical feature for CH_3OH

production.[12] However, a critical flaw of supported phthalocyanines is the lack of control aggregation of the polymer, with prior works investigating CoPPc/MWNT having average polymer layer thicknesses of $4 - 5$ nm.[7,16,17]

This aggregation is potentially controlled via production of CoPc based COFs,[8,18] allowing the production of single layer polyphthalocaynines.[18] Notably however, single layer CoPc COFs have not been shown to produce CH_3OH at the potential ranges outlined by Boutin and Wu *et al*,[2,5] as was the case in the work by Lu *et al*[18] who examined ultrathin single layer CoPc COF on MWNTs and observed no liquid products.[18] The reason for this difference in selectivity between CoPc[2,5] and CoPc COFs investigated by Lu *et al*[18] is unclear, but is likely a result of the covalent linkers required for COF formation impacting the favourability of the CO dissociation/reduction step due to the electron withdrawing effect of the methoxy- substituents in the linker tuning the Co active sites electronic configuration.[18,19] Additionally, the hydrophobicity of the CoPc COF investigated by Lu *et al*[18] may have also played a role in the lack of CH_3OH production, as whilst hydrophobicity would increase affinity to CO_2 due to likewise hydrophobicity,[18–20] it would also both decrease affinity to CO due to it's polarity, and also inhibit diffusion of H^+ sources and electrolyte access to active sites, lowering the energy barrier for CO desorption instead of further protonation.[7,19,20] Due to the COF linkers having an inherent effect on the electronic structure of the the Co centre,[21] with these electronic effects not easily predicted due to non-conformity to the expected trend with regard to the inductive effect of the linkers,[19,21] it was determined that work into CoPc COFs in the pursuit of CH_3OH was unwise at the onset the research project due to the lack of available information at the project onset to inform catalyst design.[21]

Optimisation of CoPPc/MWNT structure to reduce aggregation alongside targeted electrocatalytic testing in the -0.88 — -1.04 V vs RHE potential range was selected to be the primary aim of this research work, as application of the insights from Chen *et al*[12] regarding aggregation, and the suggestion in this work that via CoPc polymerisation CH_3OH formation was possible, alongside the insights gained from the work by Boutin and Wu *et al*[2,5] on the catalytic system used and potential ranges proven successful for CH_3OH formation suggested the potential for a CoPPc/MWNT to produce CH_3OH. Two prominent research works investigating CoPPc/MWNT synthesis and electrocatalysis by Han *et al*[16] and Chen *et al*[7] previously synthesised CoPPc/MWNT electrocatalysts for high FE_{CO} production presented potential for optimisation and potential CH_3OH production capability when considerations for aggregation and potential were applied. Both works use a one-pot synthesis to produce a polymer encapsulated MWNT CoPPc/MWNT catalyst, with the difference between the two works being the choice of solvent for this synthesis and precursor amounts (See Section 4.2.1 for further viability and comparison of the synthesis methods). Notably these works produced CoPPc/MWNT catalysts with average polymer thicknesses of 4 nm[7] and 5 nm,[16] much larger than the thickness of a single layer of CoPPc/MWNT is to be expected at 0.9 nm.[18] The work by Chen *et al*[7] synthesises three CoPPc/MWNT catalysts using different MWNT outer diameters

of $10-20$ nm, $20-30$ nm and $30-50$ nm finds that the $20-30$ nm MWNT gave the lowest degree of aggregation with the smallest thickness observed being 3.2 nm, with the $10-20$ nm producing a polymer layer with severe aggregations and $30-50$ nm producing a polymer layer thickness of 10 nm.[7] As such, for this work a MWNT diameter of 30 ± 15 nm was selected (Section 4.2.1) to reduce aggregation. Additionally, both Han and Chen *et al*[7,16] do not feature any pretreatment of their MWNTs, and therefore likely encounter additional aggregation due to irregularities on the MWNT surface due to the amorphous carbon found in untreated CNTs, so this optimisation was also incorporated into this work.

4.1.3 Copper as a co-catalyst for the electrochemical Carbon Dioxide Reduction Reaction

Copper is a well known CO_2RR electrocatalyst, being one of the most commonly used metals for the CO_2RR due to it's unique ability among heterogeneous catalysts to produce C_{2+} products such as ethylene and ethanol from the CO_2RR.[22–24] With this ability comes issues with selectivity, as Cu catalysts can catalyse the production any CO_2 reduction product, from CO and HCOOH up to EtOH and Pr^{n}OH,[22,24,25] meaning it is necessary to produce catalytic systems that tune this selectivity towards a single product via: bimetallic co-catalysts,[26,27] support effects,[25] macrocycle incorporation,[28] or size control.[25,29] Out of these methods, co-catalytic systems and macrocycle incorporation were of particular interest due to the applicability to the research focussed around CoPPc/MWNTs as depositing Cu atoms onto CoPPc/MWNT and synthesis of Copper Polyphthalocyanine on Multi-Walled Carbon Nanotubes (CuPPc/MWNT)[17] were in scope of the project. Regarding co-catalytic systems, the N atoms on the inner ring of CoPc pose ideal binding sites for Cu atoms due the nitrogen lone pair in the phthalocyanine ring.[30,31] This potential binding site would place both Co and Cu in very close proximity to each other, and could allow for potential tuning of Cu selectivity via a tandem mechanism in which Cu utilises CO or CH_3OH produced at the CoPc catalytic site for production of further reduced products.[26,27]

Regarding CuPPc/MWNT, work by Karapinar *et al*[17] investigated CuPPc/MWNT and found CO and H_2 as the only products with a FE_{CO} of 80% at a potential of -0.7 V vs RHE.[17] The CuPPc/MWNT investigated in Karapinar *et al*'s work had already been tested within the potential range of CH_3OH formation in CoPc,[2,5] with it only achieving a decrease in FE_{CO} with increasing negative potential.[17] Noteworthy however was the incredibly low coverage of CuPPc/MWNT investigated by Karapinar *et al*,[17] as compared to previously demonstrated CoPPc/MWNT syntheses,[7,16] only partial areas of the MWNT are covered with Copper Polyphthalocyanine (CuPPc) with *ca.* $9-12$ Cu atoms visible in the AC-STEM imaging.[17] This is in contrast to the near complete coverage obtained by Han and Chen *et al* with CoPPc.[7,16] The incomplete coverage opened some scope for research into CuPPc/MWNT as part of this research project to

potentially improve or observe changes in selectivity due to more complete coverage CuPPc/MWNT owing to alternative synthetic methods being utilised (See Section 4.3.1).

Addendum: In October 2024, after the experimental portion of this work was concluded and during the writing of this thesis, work by Chala *et al*[27] would go on to confirm the feasibility of a Co-Cu tandem mechanism for the production of EtOH at a FE_{EtOH} of 70%. This tandem mechanism makes use of Co and Cu in close proximity on a nitrogen doped support, which allowed for a spillover mechanism of CO produced on the Co onto Cu in which C−C coupling would occur.[27] The catalytic systems explored in this work and in the work by Chala *et al*[27] share a common motivation in that nitrogen-bound Co producing CO would allow Cu higher selectivity via the use of an already reduced CO_2 intermediate. For reasons further explored in Sections 4.2.2 and 4.2.3, activity due to the mechanism outlined by Chala *et al*[27] in the Cu/CoPPc/MWNT catalyst investigated in this work would not be possible, due to an electrochemical metal displacement producing a mixed CoPPc/CuPPc MWNT system where distance between the two metal atoms would be too great for it to occur (Section 4.2.3.1).

4.2 Cobalt Polyphthalocyanine on Multi-Walled Carbon Nanotubes

4.2.1 Synthesis

4.2.1.1 Synthesis Mechanism

The polyphthalocyanine synthesis in this work follow a cyclo-tetramerization mechanism in which a tetra-substituted phthalonitrile, specifically 1,2,4,5−tetracyanobenzene (TCB), undergoes nucleophillic attack from the alkoxide OR^- anion generated by deprotonation of alcohol by 1,8−diazobicyclo(5.4.0) undec−7-ene (DBU) (Fig. 4.4).[32,33] The nucleophillic attack of the alkoxide anion leads to the formation of a 1-alkoxy−3-iminoisoindolenine intermediate, which then reacts via nucleophillic attack with TCB unit forming a dimer.[33] The formation of the phthalonitrile dimer is where the mechanism diverges depending on the presence of a metal cation:

- With a metal cation present, two dimers template around the metal center and cylise to form a phthalocyanine unit.
- Without a metal cation present, the dimer reacts with another phthalonitrile to form a trimer, which then proceeds to react with a fourth phthalonitrile, forming a phthalocyanine unit

Once the phthalocyanine unit has formed, the use of a tetra-substituted phthalonitrile allows the unit cyano- groups on the ends, which can further react with more phthalonitrile units in a repeated nucleophillic attack mechanism, allowing the formation of a polyphthalocyanine.

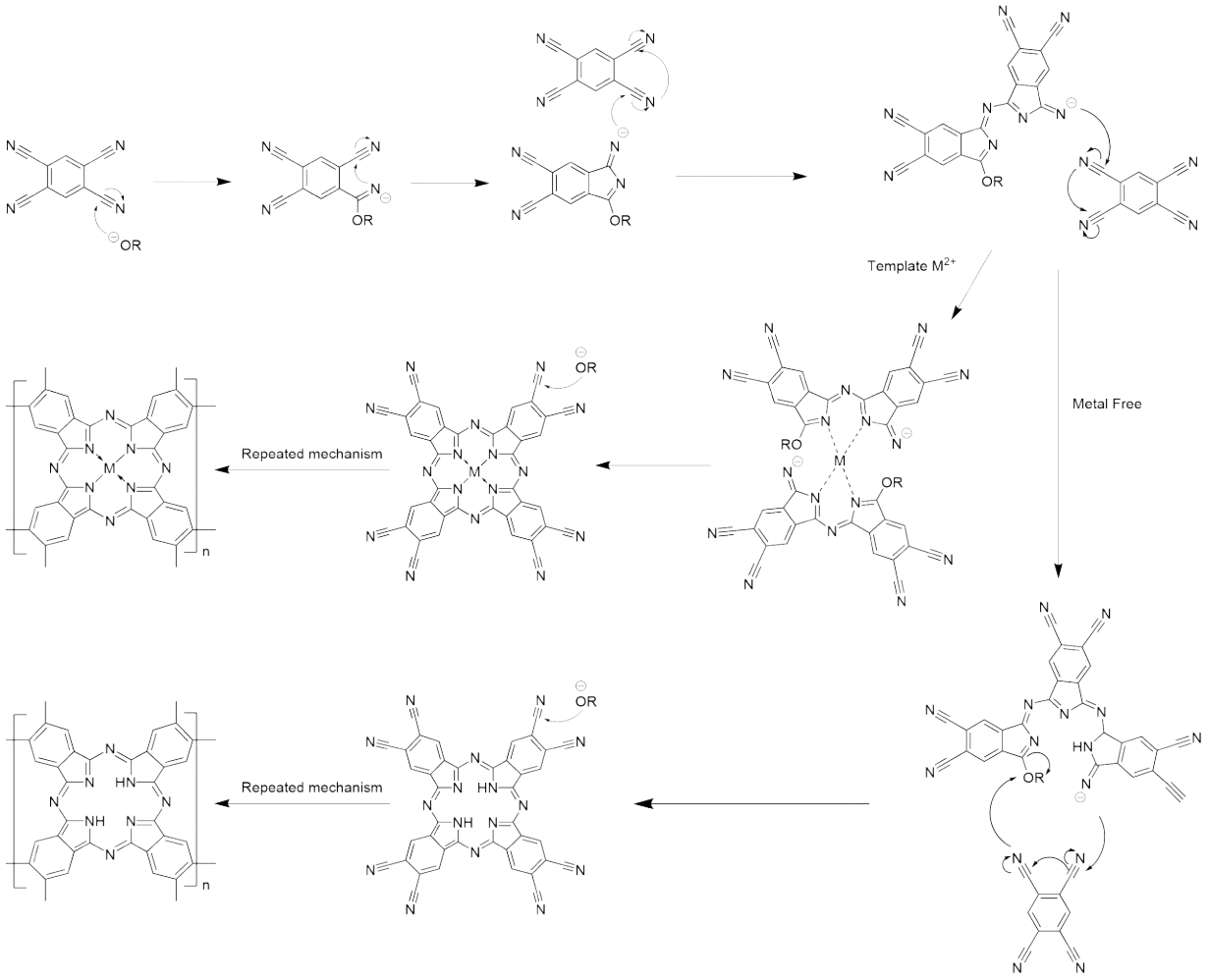


Figure 4.4: Reaction mechanism of 1,2,4,5-tetracyanobenzene to form either a metallopolyphthalocyanine, or a polyphthalocyanine. Adapted from Yamamoto *et al*[33]

Due to the templation via the metal cation, metallophthalocyanines, and by extension, metallopolyphthalocyanines, have a generally higher yield than metal free synthesis.[33] To synthesise CoPPc/MWNT, the synthesis method outlined in Fig. 4.4 is conducted in the presence of MWNTs, which results in polymer formation on the surface of the nanotubes due to the favourable Van der Waals interactions between the MWNTs and the TCB, resulting in a majority of the polymerisation taking place on the surface of the nanotube.[7,16,34,35]

4.2.1.2 Water Synthesis

Initially, CoPPc/MWNT was first synthesised following the one-pot solvothermal method outlined by Chen *et al*,[7] in which MWNTs were first pretreated by refluxing in HNO_3 (3 M) for 3 hours, and washed with copious water and then aqueous NaOH (20 mL, 1 M), followed by copious water, and copious acetone and dried *in vacuo* to produce pretreated MWNTs. The pretreated MWNTs (100 mg) were dispersed in water

(80 mL) via sonication. To this dispersion TCB (100 mg), anhydrous $CoCl_2$ (36 mg), and DBU (86 mg) were added and re-dispersed via sonication, equating to a molar ratio of TCB:$CoCl_2$:DBU of 2:1:2. This mixture was then transferred to a sealed solvothermal vessel and hydrothermally heated at 180 °C for 8 hours.[7] The final product was collected via vacuum filtration with a Polytetrafluoroethylene (PTFE) filter, and washed with ethanol and water, and then dried in a vacuum desiccator. The collection, washing and drying steps were not the same as the literature method outlined,[7] utilising vacuum filtration rather than centrifugation and lyophilization, however other tested synthesis techniques utilise vacuum filtration and vacuum desiccation with additional, more thorough washing with chloroform and 5% hydrochloric acid and successfully obtained CoPPc/MWNT (see Section 4.2.1.3). As the vacuum washing and drying steps have been shown to produce CoPPc/MWNT, the product collection will not be considered in regards to synthesis viability.

Additionally, the synthesis outlined by Chen *et al*[7] was attempted with microwave heating in a sealed microwave vessel to the same temperature of 180 °C at 500 W and also at 1000 W for 2.5 hours with the same washing procedure as outlined above. The microwave heating was conducted for comparison to the synthesis outlined by Han *et al*[16] which makes use of 1-pentanol as a solvent.

The synthesis method outlined by Chen *et al*[7] when performed both solvothermally and with microwave assistance resulted in multiple unsuccessful syntheses, with the CoPPc/MWNTs produced appearing to be identical to bare MWNTs under TEM. Additionally, there was no evidence of any solid polymer formation in the reaction mixture post solvothermal heating

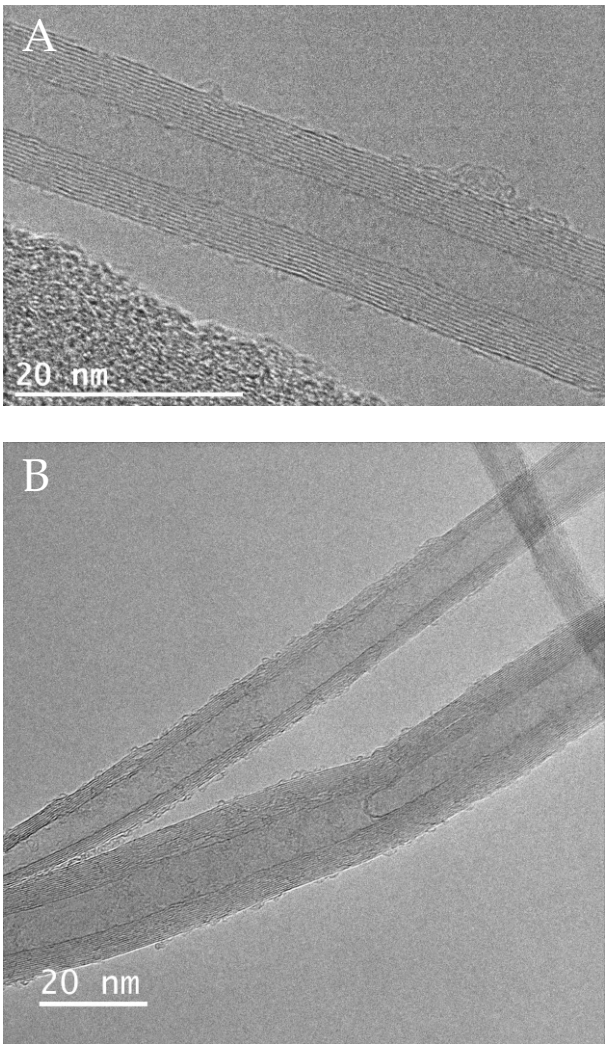


Figure 4.5: (A) TEM image of solvothermally synthesised CoPPc/MWNTs using water as a solvent; (B) TEM image of bare MWNTs

To understand the reason for the solvothermal synthesis' failure, it is important to further explore the reaction conditions used and what impact using water as a solvent would have instead of the conventionally used alcohol solvents. Firstly, the hydroxide ion OH^- both has been predicted to be more suitable for phthalocyanine synthesis,[32] and has been experimentally shown by Zanotti *et al*[36] to synthesise CoPc when using KOH in anisole, a solvent unable to form an OR^- anion under the basic reaction conditions required.[36] It is important to note that the anisole-KOH synthesis was conducted without water present in the reaction mixture, and concerns are raised in the work about the side reactions with the phthalonitrile due to the nucleophilicity of the OH^- anion,[37,38] which is the likely cause of the low CoPc yield achieved by Zanotti *et al* utilising KOH of 26%,[36] much lower than syntheses that make use of OR^- instead.[16,32,33]

The phthalonitrile side reactions induced by OH^- does not conclusively discredit a

CoPPc synthesis using H_2O, as successful CoPc syntheses have been achieved using OH^-[36,39,40] previously. Rather, there is more conclusive reason the synthesis was not reproducible, and is believed to be specifically caused by Chen *et al*'s[7] use of DBU added to water to generate OH^- from H_2O. With regards to the chemistry of DBU, It has been widely known that DBU can undergo complete hydrolysis in just H_2O to form a lactam product at temperatures at or above 85 °C, consuming any generated OH^-.[41] Additionally, an investigation by Hyde *et al*[42] further explores the hydrolytic instability of DBU, and finds that amounts of water on the ppm scale result in appreciable hydrolysis, and that hydrolysis occurs under ambient temperatures on shorter time scales (4 hours).

With the insights from Hyde *et al*'s work,[42] it becomes clear why the synthesis method outlined by Chen *et al*[7] was not able to be reproduced, as the method calls for DBU to exist in an excess of water at both ambient temperatures during the sonication step, and also at and beyond the temperatures where complete hydrolysis is expected to occur in H_2O, which would almost certainly result in complete hydrolysis of the relatively low amounts of DBU catalyst far before reaching the much higher temperatures needed for polyphthalocyanine synthesis at 180 °C.[7,16,33,43–45] The most likely explanation for the CoPPc/MWNT material reported by Chen *et al*[7] is that the data reported was collected from their synthesis performed using C_2H_5OH as a solvent rather than H_2O. Ethanol would reliably produce CoPPc under these conditions and organic solvents effectively eliminate DBU hydrolysis over the timescales used in the synthesis. The prior evidence explored,[36,41,42] the failure of efforts conducted to reproduce the water solvent synthesis, and the fact that prior research which makes use of OH^- exclusively make use of a Brønsted bases like metal hydroxides,[33,36,39,40,43] suggest that water as a lone solvent is not viable for polyphthalocyanine synthesis, a sentiment directly supported by a comprehensive review on phthalocyanine synthesis in green solvents by Zanotti *et al*.[40]

4.2.1.3 1-Pentanol Synthesis

Due to the irreproducability of the hydrothermal synthesis, a 5 times scaled up microwave assisted synthesis utilising 1-pentanol as outlined by Han *et al*[16] was performed instead. MWNTs were pretreated by refluxing in ceHNO3 (3 M) for 3 hours, and washed with copious water and then aqueous NaOH (20 mL, 1 M), followed by copious water, and copious acetone and dried *in vacuo* to produce pretreated MWNTs. To a PTFE microwave vessel, pretreated MWNTs (100 mg) and 1-pentanol (25 mL) were added and dispersed via sonication. To this dispersion TCB (100 mg), anhydrous $CoCl_2$ (36 mg), and DBU (86 mg) were added and re-dispersed via sonication, equating to a molar ratio of TCB:$CoCl_2$:DBU of 2:1:2. The PTFE microwave vessel was then sealed and heated to 180 °C at 1000 W for 2.5 hours. The final product was collected by vacuum filtration utilising a PTFE filter, and was sequentially washed with ethanol (20 mL), chloroform (20 mL), 5% hydrochloric acid (20 mL), excess ethanol, and finally excess water until the washings contained no acids or organic solvents. The washed CoPPc/MWNTs were dried on the vacuum filter for 1-2 hours, and then transferred to a vacuum desiccator for

24 hours to further dry. The 1-pentanol synthesis[16] resulted in the successful synthesis of CoPPc/MWNT, which was confirmed by TEM imaging (Section 4.2.2.1), alongside electrochemical characterisation (Section 4.2.3). The success of the 1-pentanol synthesis, which utilises the same precursor ratio as the water synthesis[7] (which was also tested utilising microwave assisted heating at the same temperature and power), further evidences that water alone is not a suitable solvent for Metal Polyphthalocyanine on Multi-Walled Carbon Nanotubes (MPPc/MWNT) synthesis.

4.2.2 Characterisation

4.2.2.1 Electron Microscopy

The CoPPc/MWNT catalyst synthesised via the 1-pentanol synthesis (Section 4.2.1.3) were analysed via High Resolution-Transmission Electron Microscopy (HR-TEM) imaging to confirm whether the synthesis was successful and to gain structural information regarding the potential catalyst.

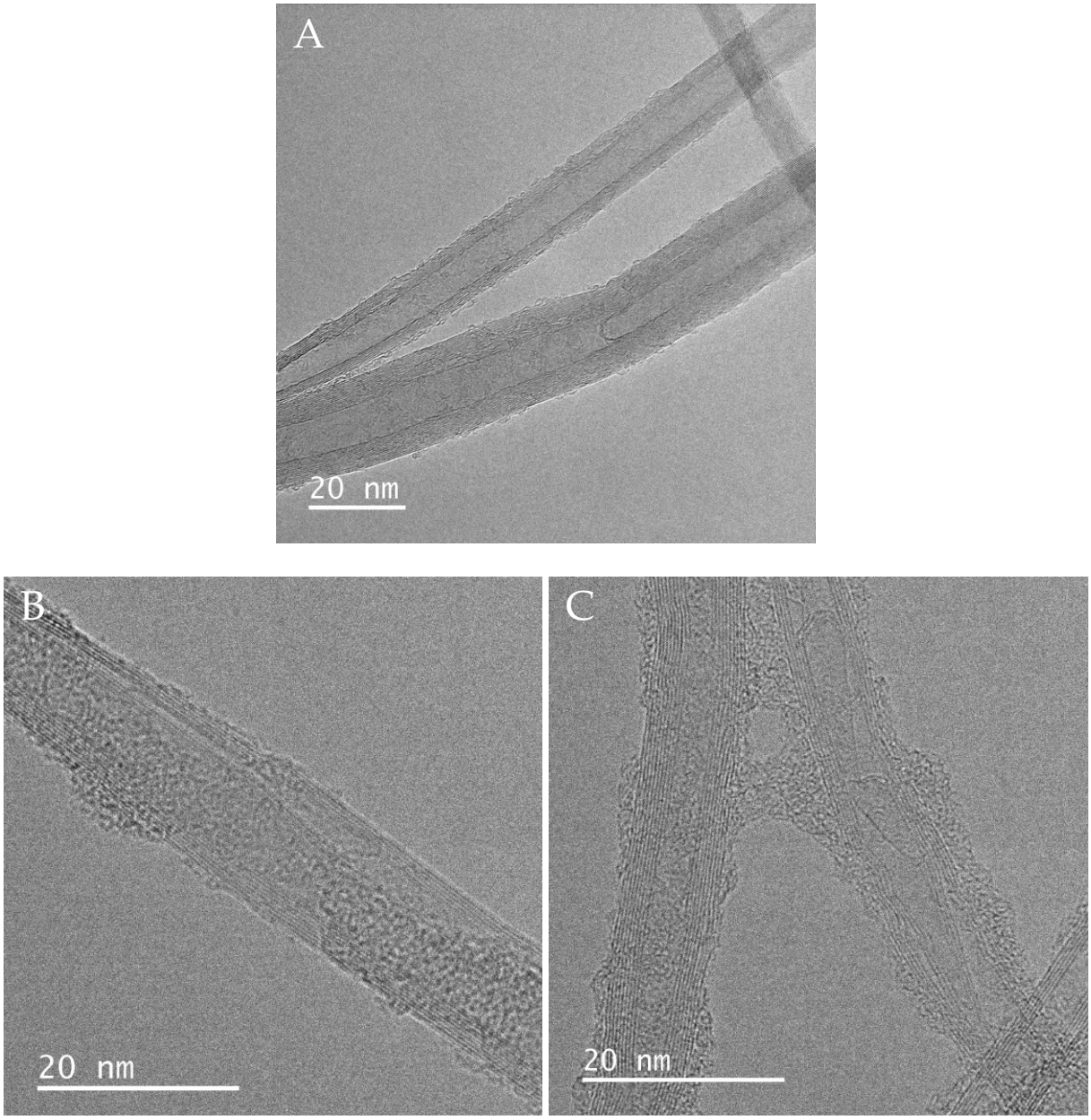


Figure 4.6: (A) TEM image of Treated PD30L1-5 MWNTs; (B) TEM image of a single CoPPc/MWNT; (C) TEM image of two CoPPc/MWNTs in proximity to each other, with the polymer connecting two CoPPc/MWNTs.

The TEM images in Fig. 4.6 show a clear amorphous layer on the surface of the MWNT (Figs. 4.6B and 4.6C) which is absent in the bare MWNTs (Fig. 4.6A). of an average thickness ranging from 2 nm to 5 nm when measured over multiple imaged sites. The average thickness of the polymer layer is lower than the average thickness of 5 nm achieved by Han *et al*.[16] However, the CoPPc/MWNTs synthesised in this work does not achieve complete coverage of the MWNTs, as some areas on the nanotube surface do not feature an visible amorphous polymer layer (Fig. 4.6B) Additionally, it was observed

that the CoPPc polymer on the surface of the MWNTs could form in the pores resulting from MWNT entanglement due to the higher surface area that arises from interstitial pore sites.[46] The polymer formation at the interstitial pores result in polymer formation that can conjoin MWNTs together (Fig. 4.6C), which have a detrimental impact on the electroactive surface area of the CoPPc/MWNT catalyst.

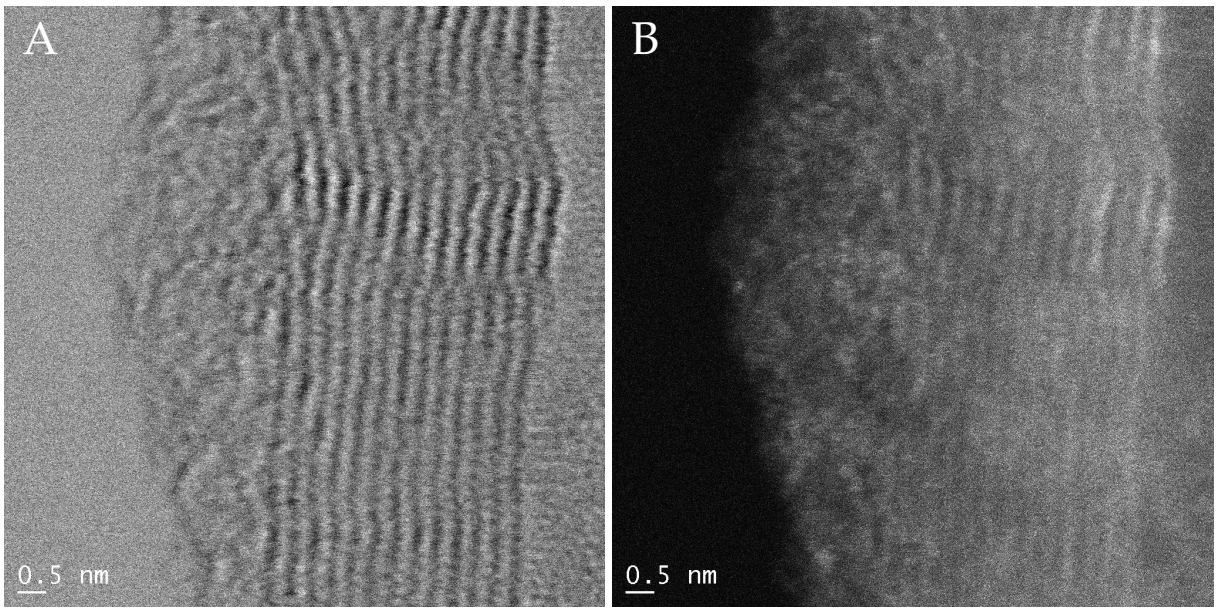


Figure 4.7: (A) BF AC-STEM image of CoPPc/MWNTs; (B) DF AC-STEM image of CoPPc/MWNTs. Both images were taken on the same region of CoPPc/MWNT.

In addition to HR-TEM imaging, the CoPPc/MWNTs samples were further imaged via AC-STEM higher magnification images capable of resolving single metal atoms on the surface of the catalyst material (Fig. 4.7). The AC-STEM images further illustrate the amorphous polymer layer on the surface, with a clear change in structure visible from the amorphous polymer layer and the graphitic MWNT walls. Additionally, observed in the DF AC-STEM images were small regions of higher contrast (white spots) in the polymer layer (Fig. 4.7B), resulting from the higher atomic size of the central Co atoms in the phthalocyanine ring compared to the C and N atoms also present in the material.[47]

4.2.2.2 Other techniques

Additional characterisation of CoPPc/MWNT was conducted via TGA to determine residual metal loading via comparison to bare MWNT (Fig. 4.8).

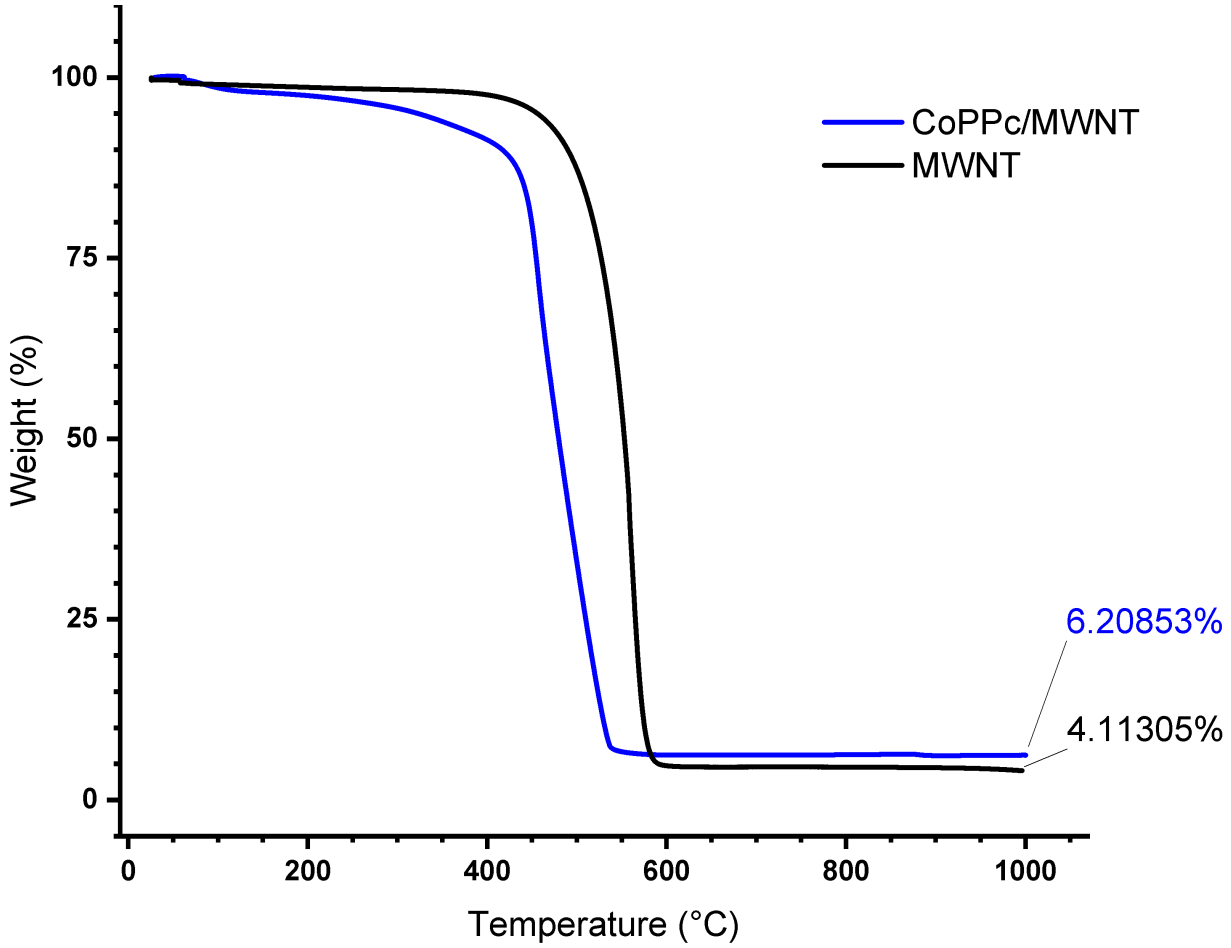


Figure 4.8: Weight% vs Temperature TGA plot of CoPPc/MWNT compared to MWNT

The residual loading difference in the TGA analysis accounts for the MWNT metal internal catalyst loading resulting from the MWNT synthesis,[48] resulting in the difference between the two residual loadings after thermal decomposition being attributed to the Co metal loading of the CoPPc/MWNT. The Co weight% loading of the CoPPc/MWNT calculated from Fig. 4.8 is 2.09548%. Additionally, with CoPPc on the surface of the MWNT, the decomposition temperature is shifted negatively, indicating the presence of a thermal decomposition catalyst in the Co centers.

4.2.3 Electrochemistry

4.2.3.1 Voltammetry

To assess the catalytic activity of CoPPc/MWNT, LSV was performed using a dropcasted RDE at 1600 rpm in a single compartment cell at very low scan rates to ensure redox processes had time to complete and gas products from CO_2RR or HER would not stay adhered onto the electrode, reducing available surface area. The LSV studies were performed in presaturated in 0.5 M $KHCO_3$ with either CO_2 or Argon to increase or decrease the current contribution of CO_2RR at reductive potentials respectively (Fig. 4.9).

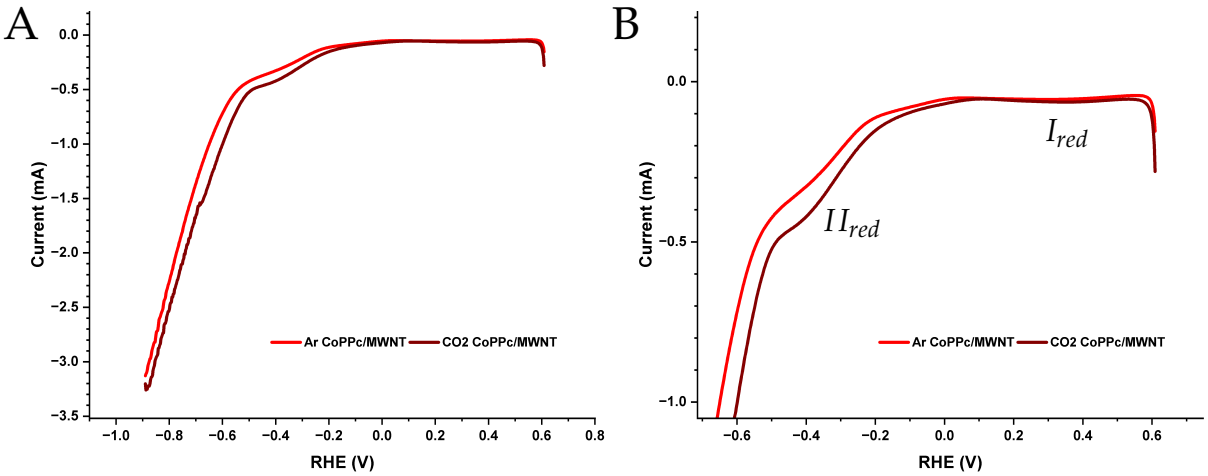


Figure 4.9: (A) LSV plot of CoPPc/MWNT using a RDE at a scan rate of 0.005 V s^{-1} in 0.5 M $KHCO_3$ electrolyte; (B) The same voltammogram without the CO_2RR region to better illustrate reduction peaks labelled I_{red} and II_{red}

As seen in Fig. 4.9A, in CO_2 saturated electrolyte, the CO_2RR electroreduction 'tail' feature occurs at around -0.49 V vs RHE, whilst in argon saturated electrolyte, this feature occurs at -0.54 V vs RHE, resulting in a difference between the two saturations of 0.04 V for CoPPc/MWNT. The reduction peaks in Fig. 4.9B labelled I_{red} and II_{red} correspond to the reductions associated with the Co^{2+}/Co^{+} and $Co^{+}Pc^{2-}/Co^{2+}Pc^{4-}$ redox couples respectively.[12,49,50] Notably, the I_{red} peak in Ar saturated electrolyte has a peak maximum slightly negatively shifted from the one in CO_2, with an $E_{\frac{1}{2}}$ value of 0.30 V vs RHE in Ar compared to 0.35 V vs RHE in CO_2, indicating the reduction is impacted by the pH of the electrolyte solution or $HCO3^{-}$ concentration.

To further characterise the synthesised CoPPc/MWNT and gain insight into its electrochemical properties, CV was performed following the LSV analysis using the same dropcasted RDE electrode with the same experimental conditions with the same rotation rate of 1600 rpm (Fig. 4.10).

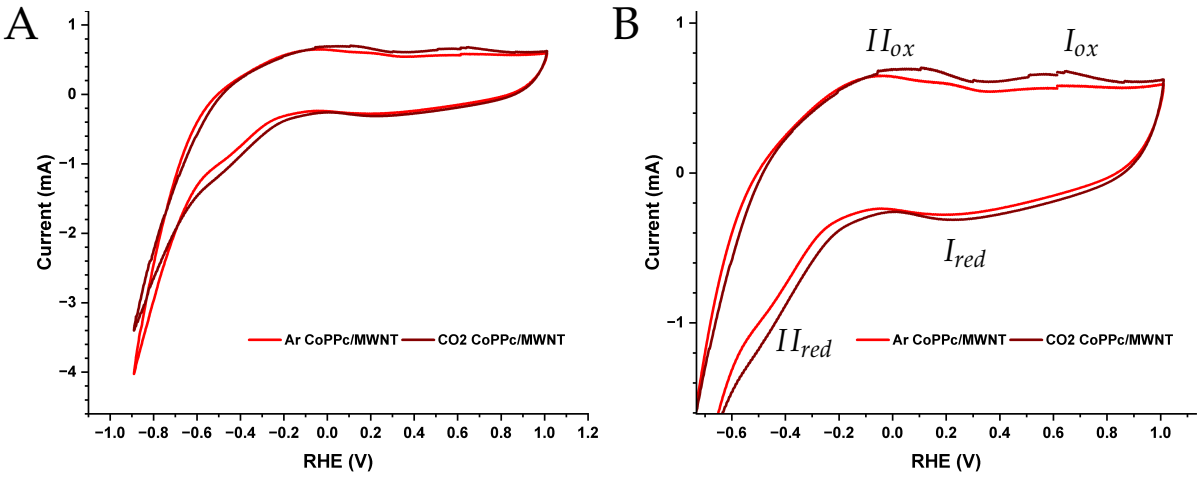


Figure 4.10: (A) CV plot of CoPPc/MWNT using a RDE at a scan rate of 0.05 V s^{-1} in 0.5 M $KHCO_3$ electrolyte at 1600 rpm; (B) The same voltammogram without the CO_2RR region to better illustrate reduction peaks labelled $I_{ox/red}$ and $II_{ox/red}$.

The CV analysis reveals two pairs of redox peaks, $I_{(ox/red)}$ and $II_{(ox/red)}$, revealing the corresponding oxidation peaks associated with the observed reduction peaks in the LSV analysis (Fig. 4.9B). Between the CO_2 and Ar saturated electrolyte the voltammograms appear mostly similar, with the CO_2 saturated CV featuring peaks with a higher charge transfer compared to the argon saturated CV.

4.2.4 Electrocatalysis

4.2.4.1 CO_2

To test the catalytic activity of CoPPc/MWNT, four potentials were tested for CO_2 reduction product formation for one hour: -0.85, -0.95, -1.05, and -1.15 V vs RHE. In these initial experiments, the synthesised CoPPc/MWNT was found to produce CH_3OH, which has not before been seen for polymeric cobalt phthalocyanine catalysts, only single unit catalysts.[2,5] Due to this first ever methanol production, and the initial lack of availability for gas product testing during the early stages of the project, the preliminary optimum potential experiments focus was on the optimum potential for CH_3OH production with only liquid products being analysed by quantitative Nuclear Magnetic Resonance (NMR). The optimum potential for methanol production was found to be -1.05 V vs RHE with a FE of 4.58%, j of 22 mA cm^{-2}, and a partial j_{CH_3OH} of 1.01 mA cm^{-2}. The potential of -1.05 V vs RHE was kept constant in future chronoamperometry as it was the optimum potential for liquid product formation, and was also directly comparable to the optimum potential reported in the work of Wu *et al.*[2]

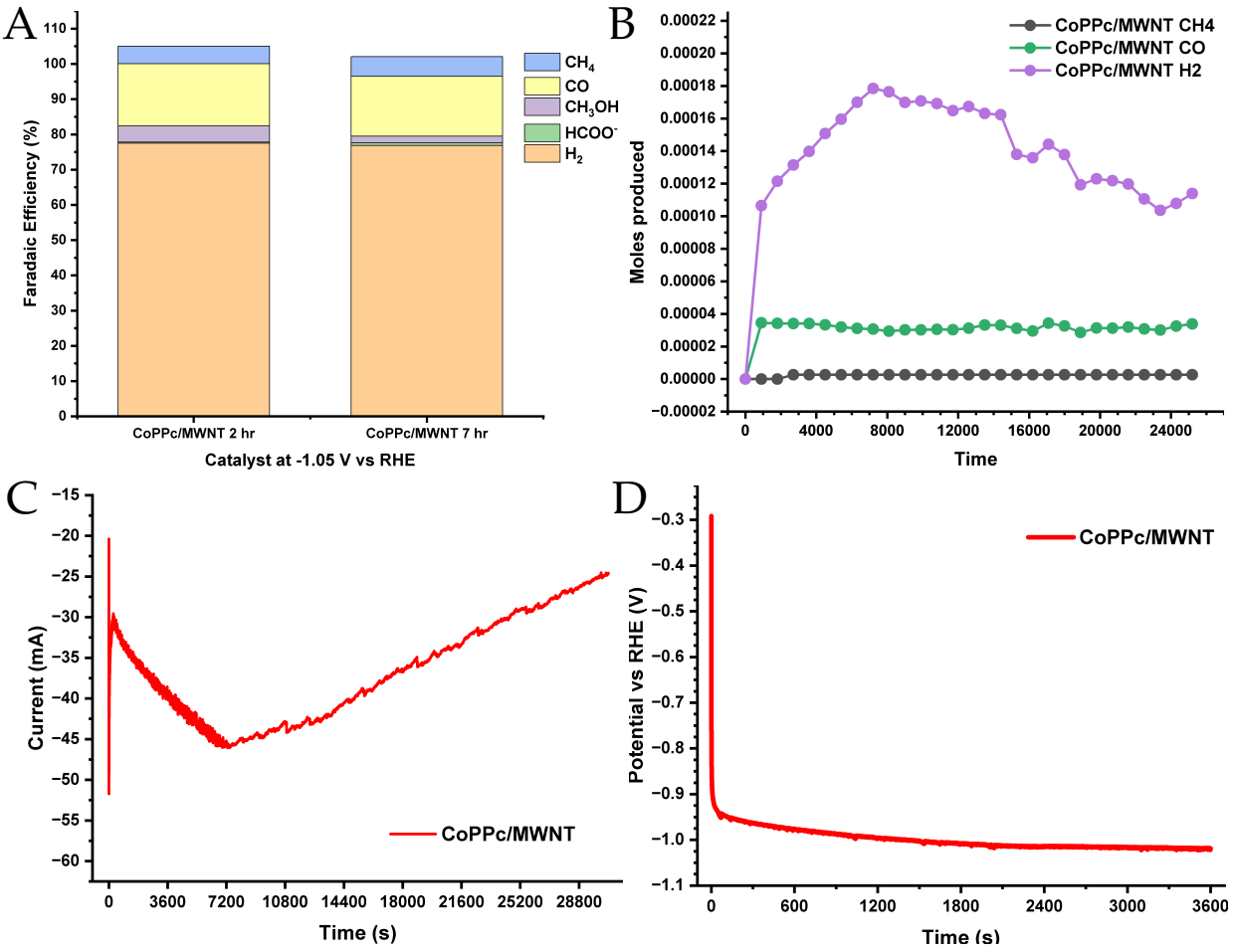


Figure 4.11: (A) Stacked bar chart showing individual product Faradaic efficiencies of CoPPc/MWNT over 2 hours and 7 hours of electrocatalysis at -1.05 V vs RHE; (B) Moles of gas produced every 900 seconds over 7 hours by CoPPc/MWNT during electrocatalysis at -1.05 V vs RHE; (C) Chronoamperometry trace of CoPPc/MWNT at -1.05 V vs RHE over the 7 hours that product formation was observed. (See Section II); (D) Chronopotentiometry using an RDE of CoPPc/MWNT at a constant current of 4 mA

Once available, full gas and liquid product analysis was conducted using Gas Chromatography (GC) and quantitative NMR (see Section II.1.4 for experimental details) respectively over the course of 18 hours for stability testing (Fig. 4.11). Over the 18 hour electrocatalysis the high current density resulted in the counter electrode depleted the electrolyte in the counter electrode compartment after around 2 hours, and the catalytic activity decreased over the next 5 hours until no new product formation was detected (Fig. 4.11C). To ensure that the counter electrolyte caused the loss of catalytic activity, and not the catalyst catalyst deactivation, a fresh 0.5 M $KHCO_3$ electrolyte was added to the counter electrode compartment after the collection of the final data point but before the potential application had ended. The addition of the fresh counter electrolyte caused the current density to immediately increase from near 0 back to $\sim 30 - 40$ mA cm^{-2} indicating the the cause of potential loss was indeed due to the counter electrolyte.

The electrocatalysis results reveal a difference in product selectivity to previously reported CoPPc/MWNT[7,16] as the product selectivity has switched from solely CO to the primary products being H_2 and CO, with new minor product formation of CH_4 and CH_3OH (Fig. 4.11A). The increase in H_2 formation is likely a result of the higher applied potential of the catalyst, combined with the incomplete coverage of the MWNT caused higher selectivity towards H_2. Whilst single product selectivity has dramatically decreased compared to previously synthesised CoPPc/MWNT, the emergence of CH_3OH and CH_4 as reduction products represent an important finding for Cobalt Phthalocyanine based catalysts, as the six electron reduction barrier to methanol has been surpassed now with the eight electron reduction towards methane being shown possible.

As the long term stability of the CoPPc/MWNT catalyst could not be feasibly assessed beyond 2 hours due to the high activity of the catalyst, chronopotentiometry was used Fig. 4.11D to further assess catalyst stability, particularly whether the catalyst has any changes in product selectivity as these changes would be reflected as a change in observed potential in chronopotentiometry.[51] Chronopotentiometry was performed at a constant current of 4 mA as this was current observed at -1.05 V vs RHE from a preliminary LSV scan of CoPPc/MWNT using an RDE at 2500 rpm (Section II), additionally this current was consistent with prior voltammetry experiments as currents close to 4 mA was observed at $\sim$ -1.05 V vs RHE (Figs. 4.9 and 4.10A). The chronopotentiometry revealed the slow increasing of potential, converging towards $\sim$ -1.05 V vs RHE, indicating a mostly stable product formation rate until a maximum rate is reached. This conclusion is further supported by the gas product production over the electrocatalysis (Fig. 4.11B), which show stable rates of CO and CH_4 production, with the H_2 production slowly increasing until a plateau is reached, before decreasing due to counter electrolyte depletion.

4.3 Copper Polyphthalocyanine on Multi-Walled Carbon Nanotubes

4.3.1 Synthesis

The synthesis of CuPPc/MWNT was performed using the same synthesis outlined in Section 4.2.1, with the metal source of $CoCl_2$ replaced with $CuCl_2$ and the amount adjusted to match the same molar amount of previously used $CoCl_2$. To synthesise CuPPc/MWNT, to a PTFE microwave vessel, MWNTs (100 mg) and 1-pentanol (25 ml) were added and dispersed via sonication. To this dispersion TCB (100 mg), anhydrous $CuCl_2$ (37.28 mg), and DBU (86 mg) were added and re-dispersed via sonication, equating to a molar ratio of TCB:$CuCl_2$:DBU of 2:1:2. The PTFE microwave vessel was then sealed and heated to 180 °C at 1000 W for 2.5 hours. The final product was collected by vacuum filtration utilising a PTFE filter, and was sequentially washed with ethanol (20 mL), chloroform (20 mL), 5% hydrochloric acid (20 mL), excess ethanol, and finally

excess water until the washings contained no acids or organic solvents. The washed CuPPc/MWNTs were dried on the vacuum filter for 1-2 hours, and then transferred to a vacuum desiccator for 24 hours to further dry.

4.3.2 Characterisation

4.3.2.1 Electron Microscopy

The HR-TEM of CuPPc/MWNT catalyst (Fig. 4.12) reveals polymer formation on the surface of the MWNT with an average thickness of $\sim 1-2$ nm (Fig. 4.12B), with no large aggregations long the surface. This polymer layer is much thinner on average than the CoPPc polymer seen in Figs. 4.6B and 4.6C, with complete coverage of the MWNT surface.

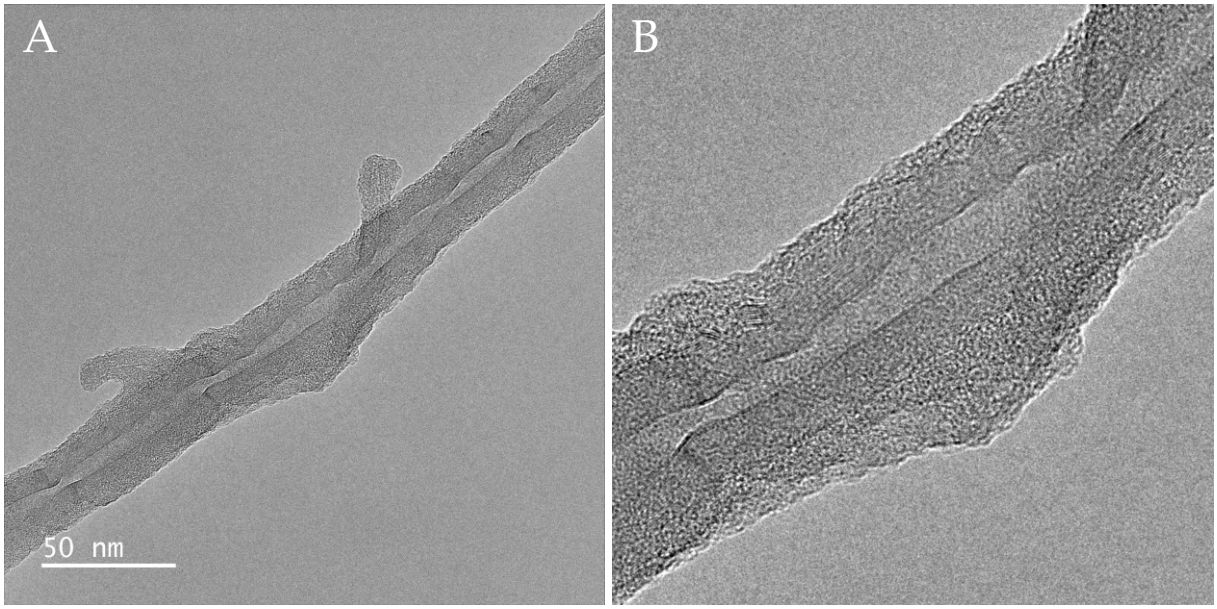


Figure 4.12: (A) HR-TEM image of CuPPc/MWNTs, the outcroppings seen in this image result from a smaller MWNT adhered to a larger MWNT by the polymer formation on the surface; (B) HR-TEM image in (A) zoomed in to better illustrate polymer formation on the surface of CuPPc/MWNTs.

The polymer formation has resulted in the binding of larger and smaller MWNTs together, as can be seen in Fig. 4.12A. The smaller sized MWNT adhered to the larger MWNT in Fig. 4.12A does not appear to have originated from the MWNT it is adhered to during MWNT prodcution, as both ends of the MWNT are present and no obvious sites the small tube could have spawned from being present in the large tube. Dark spots in the CuPPc/MWNT most likely correspond to Cu centers of the CuPPc (Fig. 4.12B), however due to Cu's visibility in HR-TEM, it can be inferred that despite the apparent low degree of aggregation that the polymeric layer contains many layers of CuPPc taking a compact form which gives rise to this TEM contrast.[47] This is apparent when in comparison

to CoPPc/MWNT as seen in Fig. 4.6C, where a clear amorphous polymeric layer is present with a lower density of the darker spots within the amorphous layer compared to CuPPc/MWNT (Fig. 4.12B).

4.3.2.2 Other techniques

For weight loading determination, TGA of CuPPc/MWNT was conducted, resulting in a Cu metal weight loading of 1.06087% when accounting for MWNT internal metal catalyst (Fig. 4.13).

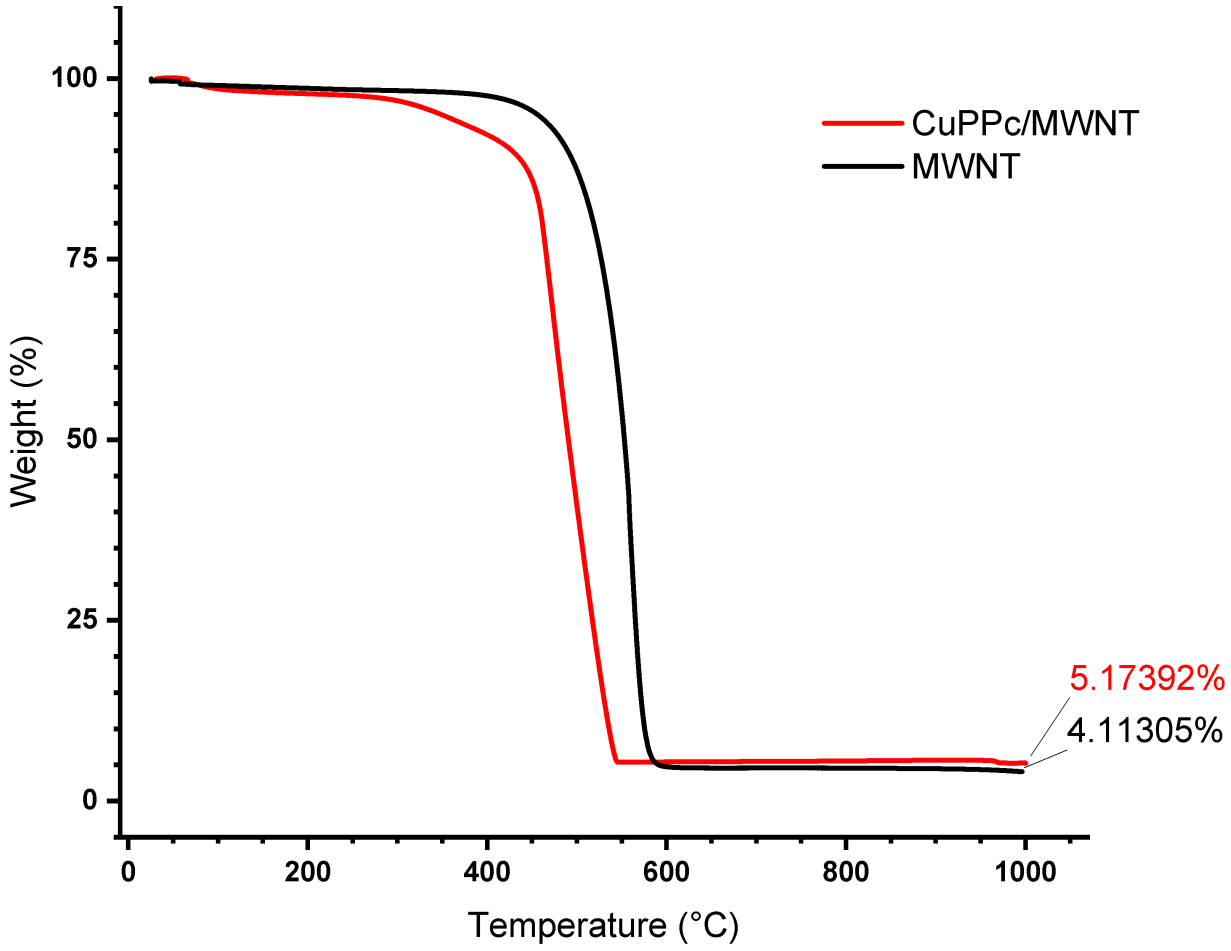


Figure 4.13: Weight% vs Temperature TGA plot of CuPPc/MWNT compared to MWNT

4.3.3 Electrochemistry

4.3.3.1 Voltammetry

To assess the redox activity of CuPPc/MWNT for comparitive analysis to Cu/CoPPc/MWNT, CV was performed using a dropcasted carbon paper electrode with an area of $1 \times 1\,cm^2$. LSV and the use argon saturated electrolyte were regrettably omitted due to time constraints. The CV of CuPPc/MWNT is shown in Fig. 4.14.

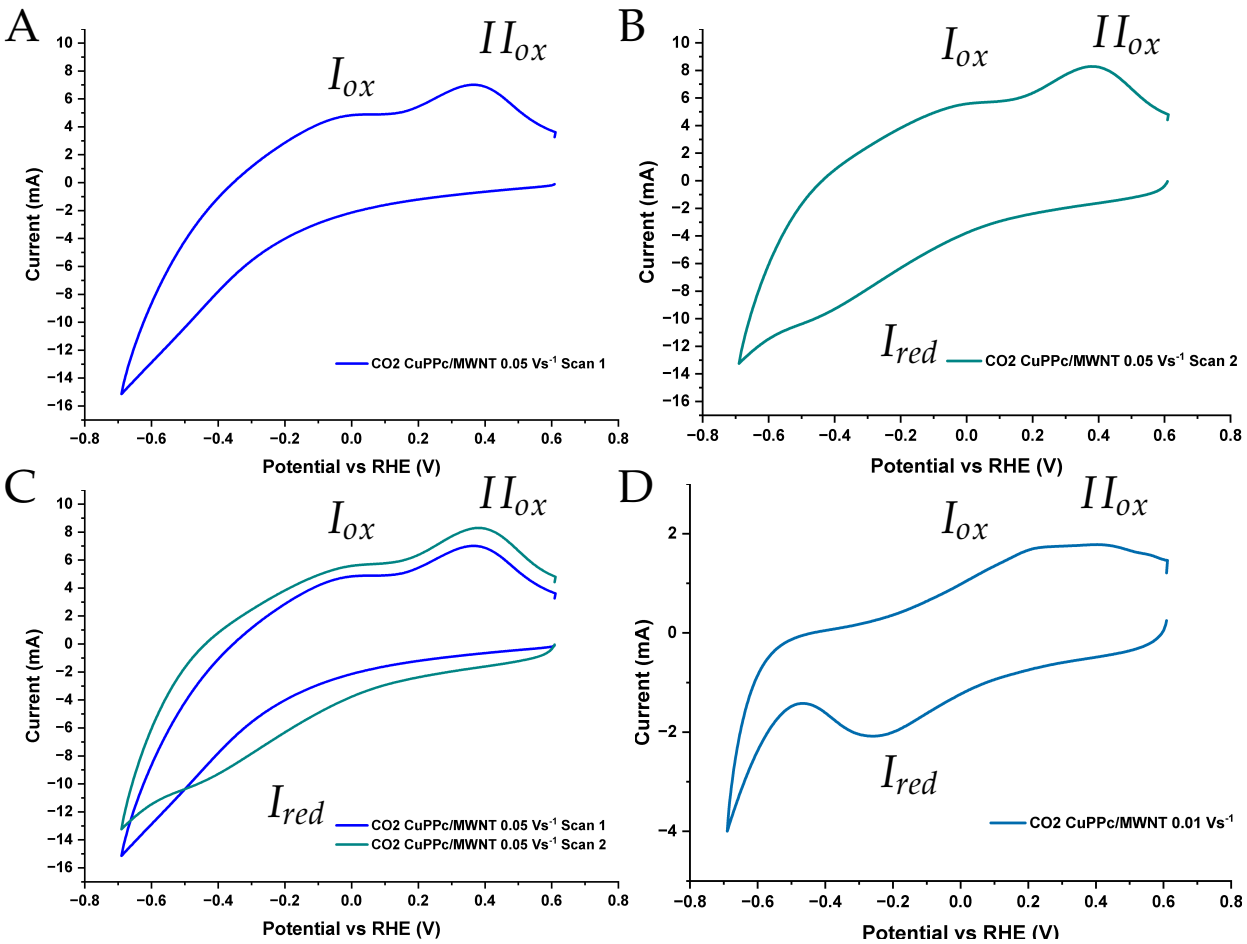


Figure 4.14: (A) Initial CV scan of CuPPc/MWNT in CO_2 saturated $KHCO_3$ at 0.05 V s^{-1} with redox peaks labelled; (B) Second CV scan of CuPPc/MWNT in CO_2 saturated $KHCO_3$ conducted immediately after Fig. 4.14A with redox peaks labelled; (C) Figs. 4.14A and 4.14B overlaid for ease of comparison; (D) CV scan of CuPPc/MWNT in CO_2 saturated $KHCO_3$ at at 0.01 V s^{-1} with redox peaks labelled. Experiment conducted after both Figs. 4.14A and 4.14B.

The CVs experiments of CuPPc/MWNT reveal a three peaks, one reduction labelled I_{red}, and two oxidation labelled I_{ox}/II_{ox} (Fig. 4.14), compared to CoPPc/MWNT's two paired redox couples. The reduction in CuPPc/MWNT in literature is attributed to the Pc^{2-}/Pc^{3-} redox couple,[52] however the II_{ox} peak appears to be a irreversible oxidation which deactivates the catalyst. When conducting further scans at both 0.05 V s^{-1} (Fig. 4.14B) and 0.01V s^{-1} (Fig. 4.14D), there is an observed decline in the catalytic activity of CuPPc/MWNT, with a decrease in the achieved current (Fig. 4.14B), and at the lower scan rate the I_{red} peak is much more prominent and the onset potential increases drastically, from $0.0 - -0.2$ V vs RHE in Fig. 4.14A, to -0.5 V vs RHE in Fig. 4.14D. The shift in potential of the $I_{ox/red}$ couple alongside the change in shape of the I_{red} peak in the 0.01V s^{-1} CV implies that the II_{ox} peak is an irreversible oxidative deactivation of the catalyst, due to the peak's consistent appearance in the voltammograms, and loss in intensity over the multiple scans implying that the multiple scans results in more and more inactive catalyst.

Notably, no Cu metal centre peaks can be seen in the CVs of CuPPc/MWNT due to the Cu metal centre's d-orbitals positioning between the HOMO and LUMO of the Pc^{2-} ligand. This means that redox activity can only be attributed to electron transfer regarding the Pc ligand and there will be no electron transfer to the cupc metal centre.[52]

4.3.4 Electrocatalysis

To test the catalytic activity of CuPPc/MWNT, four potentials were tested for CO_2 reduction product formation for one hour: -0.85, -0.95, -1.05, and -1.15 V vs RHE. These initial experiments were conducted under the same conditions to CoPPc/MWNT (Section 4.2.4.1), and the CuPPc/MWNT was found to produce $HCOO^-$ as it's primary liquid product at a maximum FE of 23% at a potential of -1.05 V vs RHE, no other liquid products were observed. The chronoamperometry experiments were performed with liquid analysis only in a cell not connected to a GC, which similarly to CoPPc/MWNT and Cu/CoPPc/MWNT in this open configuration, yielded a flat, consistent current density of $\sim 20\,\text{mA cm}^{-2}$.

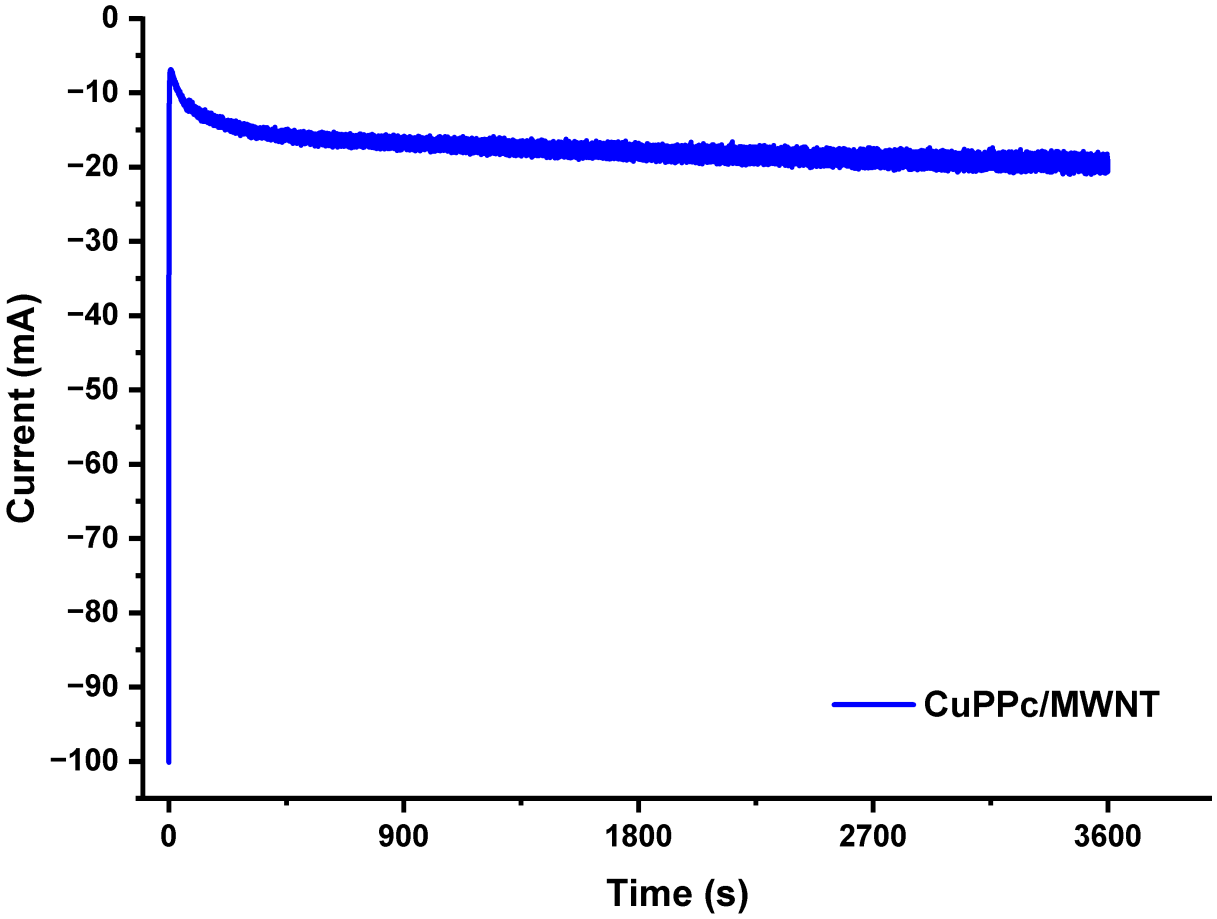


Figure 4.15: Chronoamperometry of CuPPc/MWNT dropcasted on carbon paper in a 1x1 cm^{-2} area at a constant potential of -1.05 V vs RHE in CO_2 saturated $KHCO_3$ with continuous CO_2 flow through the electrolyte

The primary purpose of testing CuPPc/MWNT as a catalyst for the CO_2RR is to assist in the characterisation of Cu/CoPPc/MWNT by means of comparison, therefore further discussion into the catalysis of CuPPc/MWNT will not be explored.

4.4 Copper on Cobalt Polyphthalocyanine on Multi-Walled Carbon Nanotubes

4.4.1 Synthesis

The synthesis of Cu/CoPPc/MWNT was achieved by powder deposition magnetron sputtering of the CoPPc/MWNT (Section 4.2) using a copper target.

4.4.2 Characterisation

4.4.2.1 Electron Microscopy

The initial TEM imaging of Cu/CoPPc/MWNT reveals very little difference to CoPPc/MWNT (Section 4.2.3), with similar polymer coverage at an average width of 2 nm with areas of greater aggregation and areas of incomplete coverage (Fig. 4.16). Due to the similar size of Cu to Co, it is to be expected that the addition of Cu results in similar HR-TEM images to CoPPc/MWNT with contrast changes. To better reveal differences due to the sputtering of Cu, AC-STEM was used for improved contrast to differentiate metal atoms (Fig. 4.17).

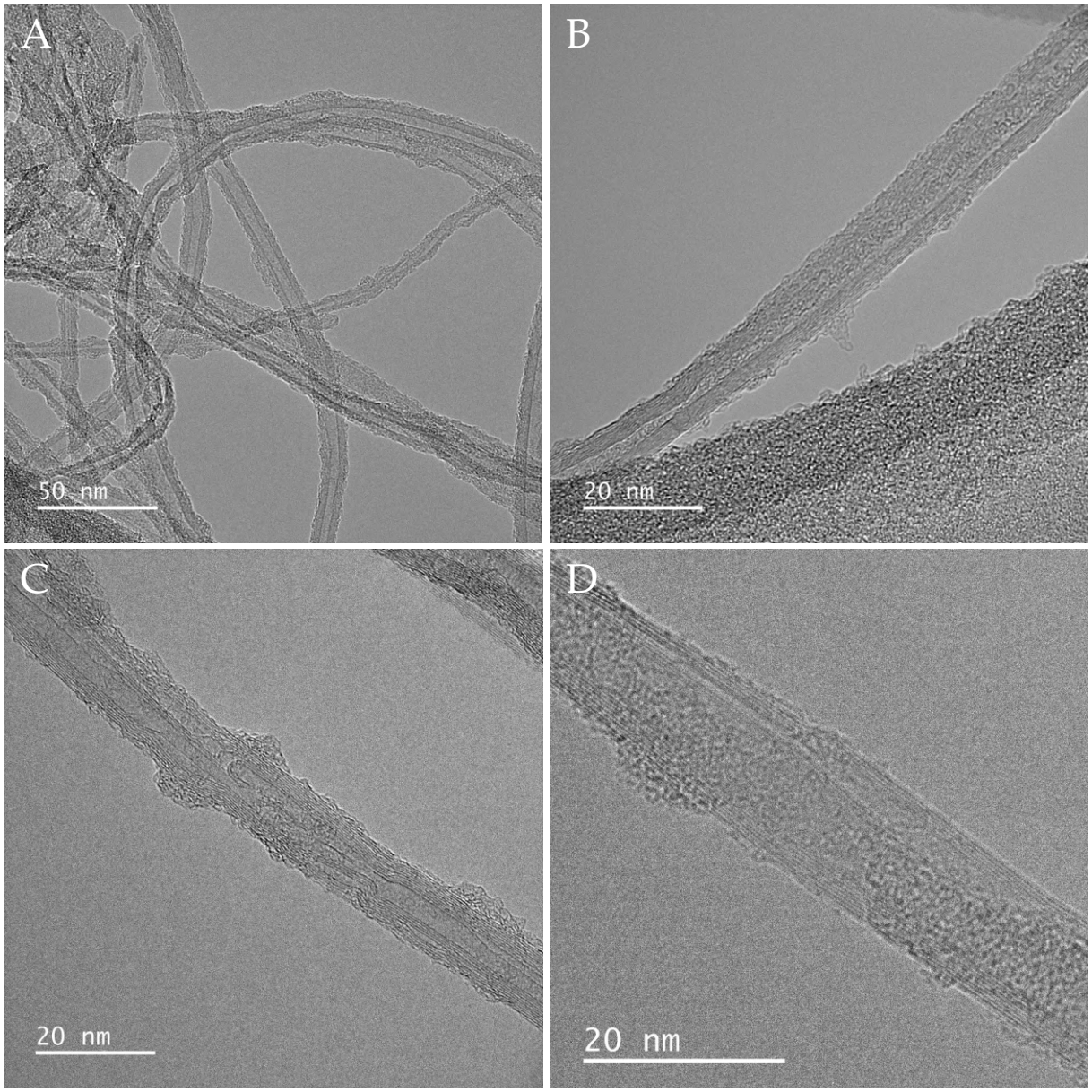


Figure 4.16: (A) TEM image showing an area overview of Cu/CoPPc/MWNT; (B) TEM image of a single Cu/CoPPc/MWNT illustrating polymer growth on the surface of the MWNT; (C) TEM image of Cu/CoPPc/MWNT illustrating areas of polymer aggregation on the surface; (D) TEM image of CoPPc/MWNT from Fig. 4.6B to illustrate the similarities between CoPPc/MWNT and Cu/CoPPc/MWNT.

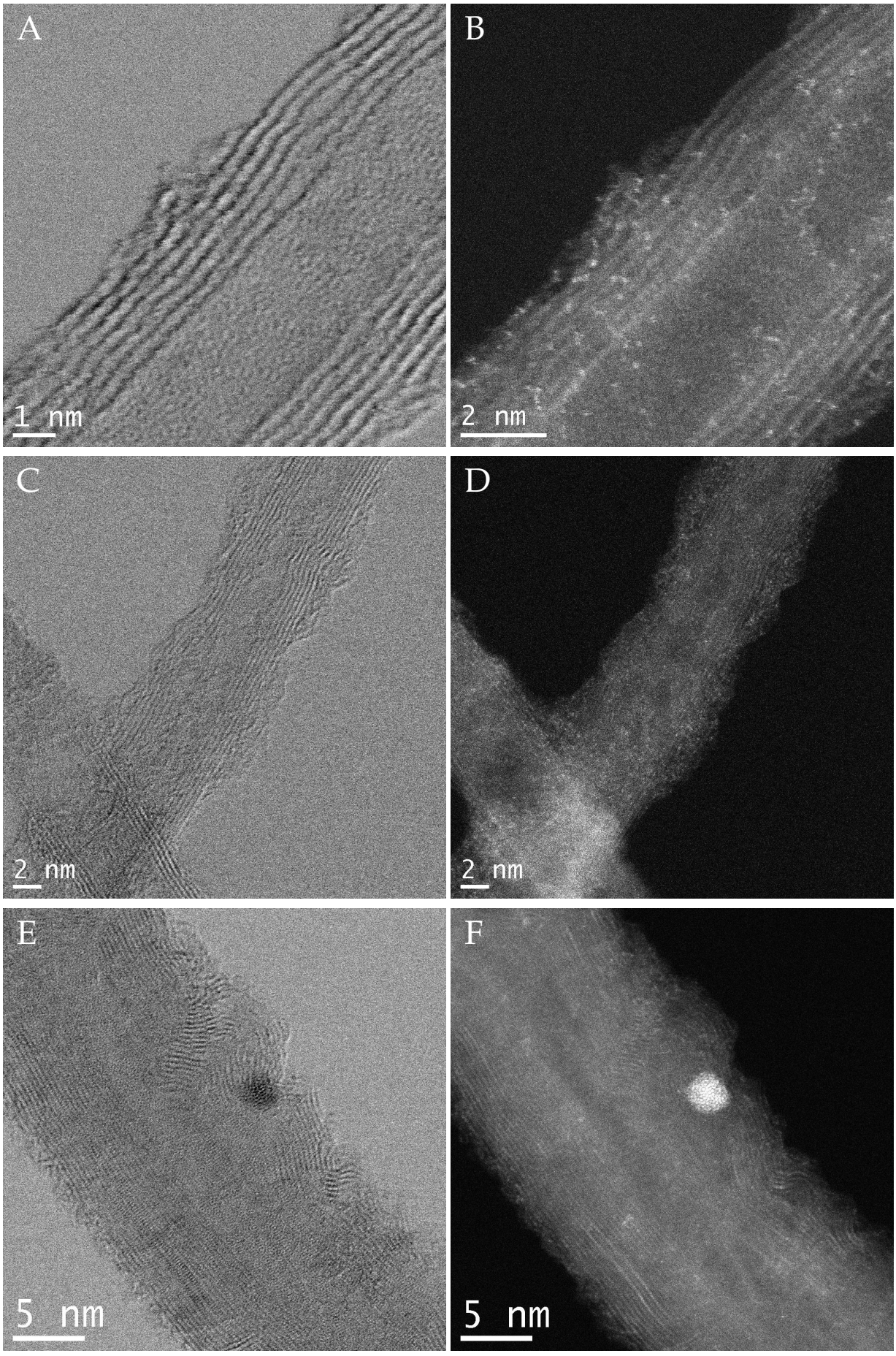


Figure 4.17: (A) BF and (B) DF images showing Cu single atoms as white specks on the surface of Cu/CoPPc/MWNT; (C) BF and (D) DF images showing a wider view of the Cu/CoPPc/MWNT catalyst; (E) BF and (F) DF images showing Cu nanocluster formation on the polymer surface.

The AC-STEM imaging more clearly reveals the sputtered Cu atoms on the surface of the polymer surface of Cu/CoPPc/MWNT, appearing as small spots of contrast/white specks in the DF AC-STEM imaging (Fig. 4.17B). Regions of the catalyst with polymer coverage appear to only contain Cu single atoms (Figs. 4.17B and 4.17D), whilst in areas with incomplete polymer coverage, metal nanocluster formation could be observed, with sparse single atoms in the regions that do have a polymer coating (Figs. 4.17E and 4.17F). The presence of Cu single atoms on polymeric regions of Cu/CoPPc/MWNT is most likely a result of the amorphous and "tangled" nature of the polymer, as the single atoms that fall on the polymer via magnetron sputtering are not able to migrate along the polymer surface to coalesce due to the high energy barrier induced by the polymer, whilst those that fall on bare regions of the MWNT have more favourable conditions to migrate and form Cu nanoclusters.

AC-STEM was also conducted on Cu/CoPPc/MWNT after the chemical process at -0.5 V vs RHE had occurred to gain insight on the effect of the process on the structure of Cu/CoPPc/MWNT (see Section 4.4.3.1 for further details and in-depth analysis). The Cu/CoPPc/MWNT was held at -0.5 V vs RHE for 5 minutes, and was subsequently removed from the carbon paper electrode via sonication in isopropyl alcohol to mitigate potential metal solvation.

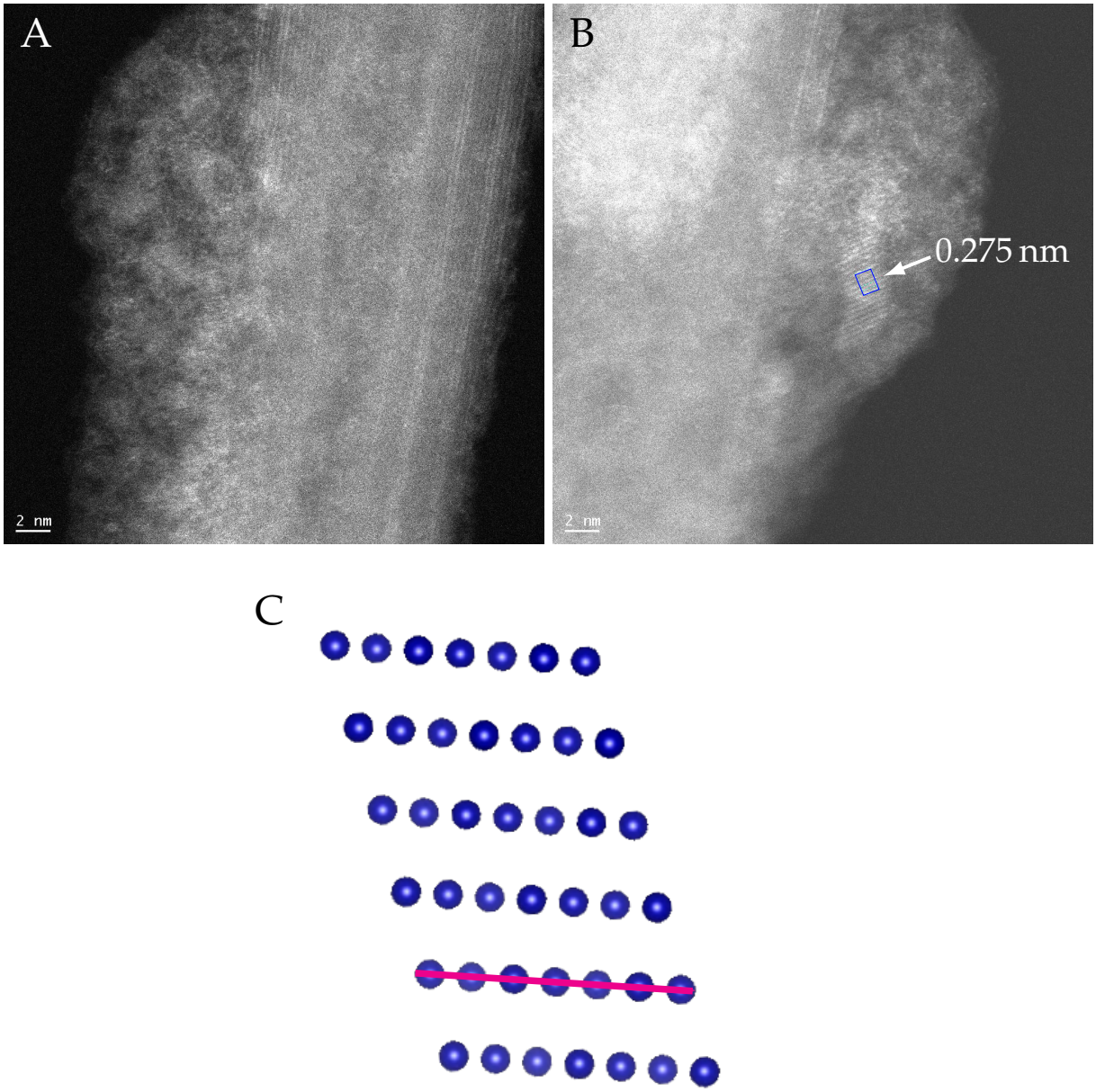


Figure 4.18: (A) DF AC-STEM image of Cu/CoPPc/MWNT after application of -0.5 V vs RHE for 5 *min* to allow the chemical process to occur in full; (B) Zoomed DF AC-STEM image of post potential application Cu/CoPPc/MWNT, crystalline region is outlined by blue square, with d-spacing value annotated; (C) Simulated crystal structure of $CoCO_3$[53] with C and O atoms omitted for clarity. Purple line indicates the $CoCO_3$ (1 -1 -4) plane corresponding to the d-spacing value measured in Fig. 4.18B.

The AC-STEM of the Cu/CoPPc/MWNT after polarisation more negative than > 0.5 V vs RHE (Fig. 4.18A) reveals that the Cu single atoms visible as white specks on the catalyst surface Figs. 4.17B and 4.17D have largely disappeared, implying the application of -0.5 V vs RHE and the associated chemical process involve a structural change involving the Cu single atoms. The loss of the Cu atoms is highly likely to be electrochemically

driven, as leaching of the Cu atoms into the solution is highly unlikely, as the preparation of the TEM grids for imaging pre-polarised Cu/CoPPc/MWNT involves sonication in isopropyl alcohol, which would remove the Cu atoms if leaching were to occur.

Notably, in the negatively polarised Cu/CoPPc/MWNT, it was observed that a new a crystalline structure was present in the polymer (Fig. 4.18B), featuring a d-spacing of 0.275 nm. Given the composition of the catalyst, electrolyte, and the d-spacing of the crystalline structure, potential crystal structures that involve Co, Cu, CO_3^{2-}, and HCO_3^- were simulated and potential crystal planes corresponding to the d-spacing of 0.275 nm were investigated, and it was concluded that the crystalline feature likely corresponds to the (1 -1 -4) plane of $CoCO_3$.[53]

To further investigate the environment of the Cu on the catalyst surface, Electron Energy Loss Spectroscopy Spectral Imaging (EELS-SI) was utilised to obtain single atom resolution information on the Cu/CoPPc/MWNT catalyst.

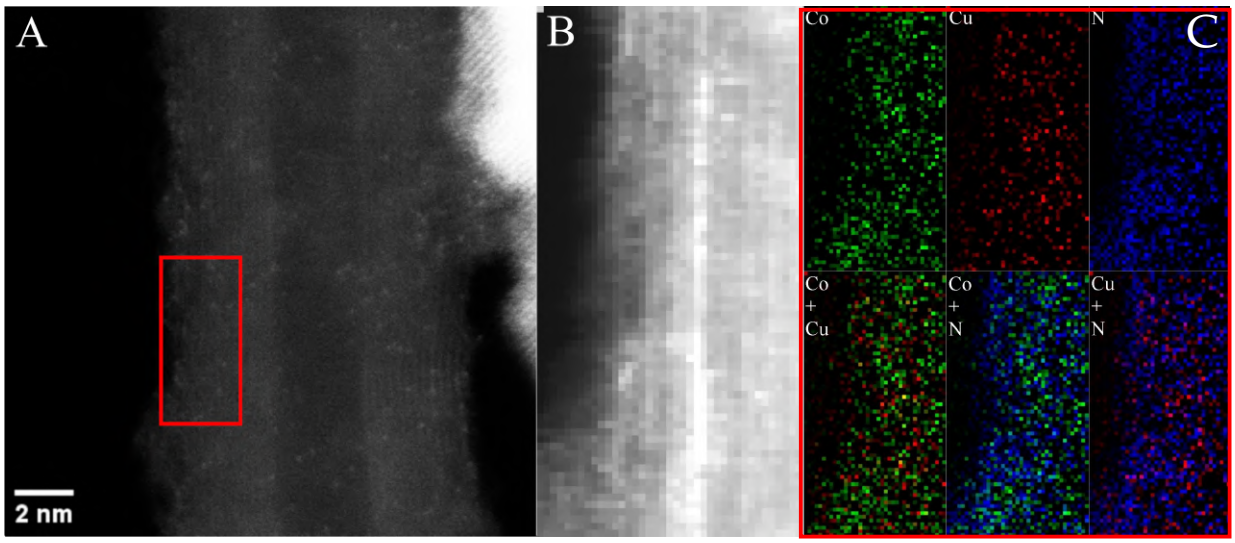


Figure 4.19: (A) Survey AC-STEM image of Cu/CoPPc/MWNT with a red box outlining the area used in Fig. 4.19B; (A) EELS-SI image of Cu/CoPPc/MWNT area denoted in Fig. 4.19A; (C) Single atom element maps of Co, Cu, and N both showing the individual elements, and maps with both Co and Cu together and each metal with N

The EELS-SI maps reveal both cobalt and copper exist in single atom form on the surface of the Cu/CoPPc/MWNT catalyst and are both co-located with nitrogen (Fig. 4.19A). The nitrogen signals result from the nitrogen atoms in the phthalocyanine ring (Fig. 4.1), so the cobalt atoms are to be expected to co-locate with nitrogen due to the nature of cobalts ligation to the phthalocyanine. The copper atom co-location indicates that the nitrogen atoms provide a preferential binding site on the polymer, and results in copper atoms in close proximity to the cobalt atoms, whilst also in the form of single atoms.

4.4.2.2 Other techniques

For weight loading determination, TGA of CuPPc/MWNT was conducted, resulting in a combined Cu and Co metal weight loading of 2.33368% when accounting for MWNT internal metal catalyst (Fig. 4.20, and a copper metal weight loading of 0.2382% when further subtracted from the TGA of CoPPc/MWNT (Fig. 4.8).

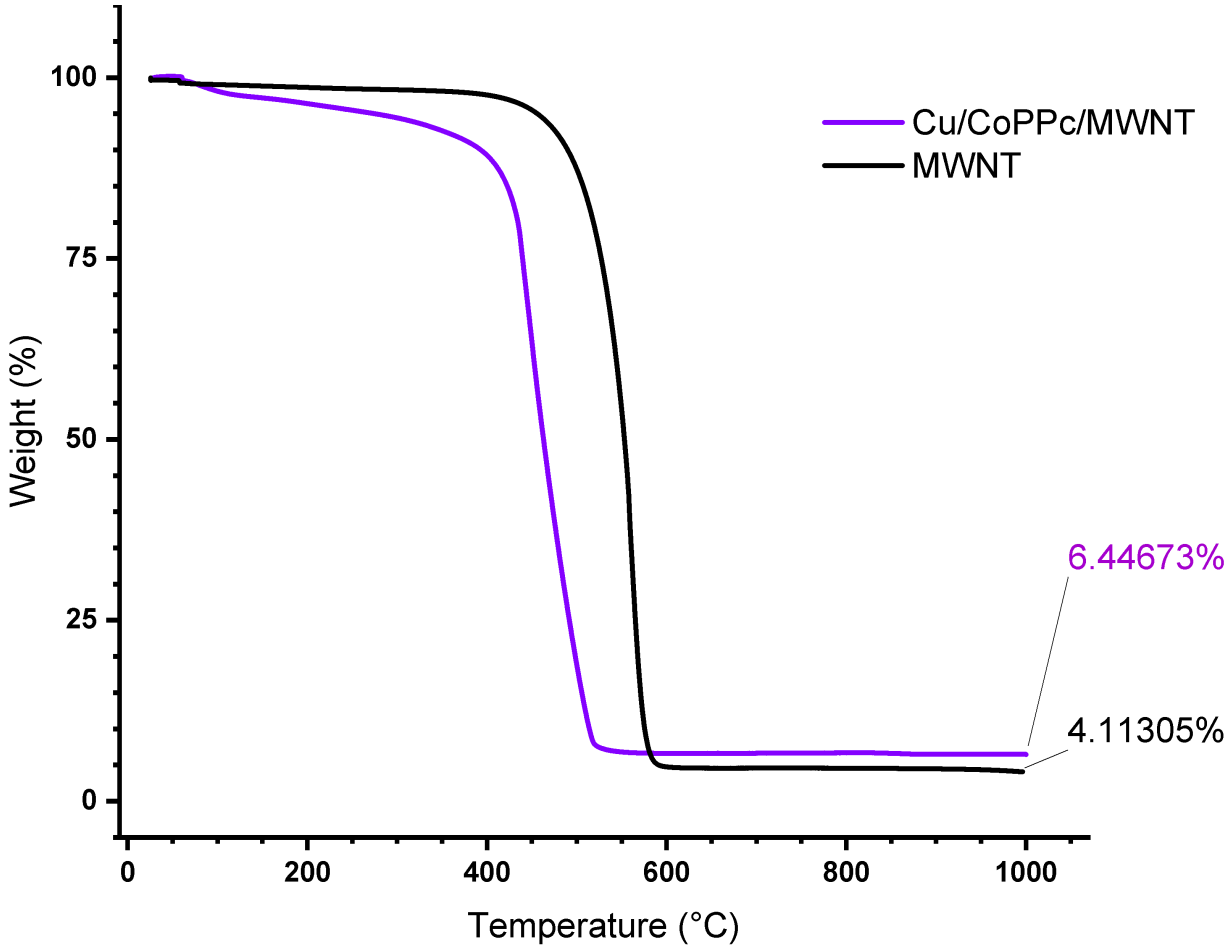


Figure 4.20: Weight% vs Temperature TGA plot of Cu/CoPPc/MWNT compared to MWNT

4.4.3 Electrochemistry

4.4.3.1 Voltammetry

To assess the catalytic activity of Cu/CoPPc/MWNT, LSV was performed using a drop-casted RDE at 1600 rpm in a single compartment cell at very low scan rates to ensure redox processes had time to complete and gas products from CO_2RR or HER would not stay adhered onto the electrode, reducing available surface area. The LSV studies were performed in presaturated in 0.5 M $KHCO_3$ with either CO_2 or Argon to increase or decrease the current contribution of CO_2RR at reductive potentials respectively (Fig. 4.21).

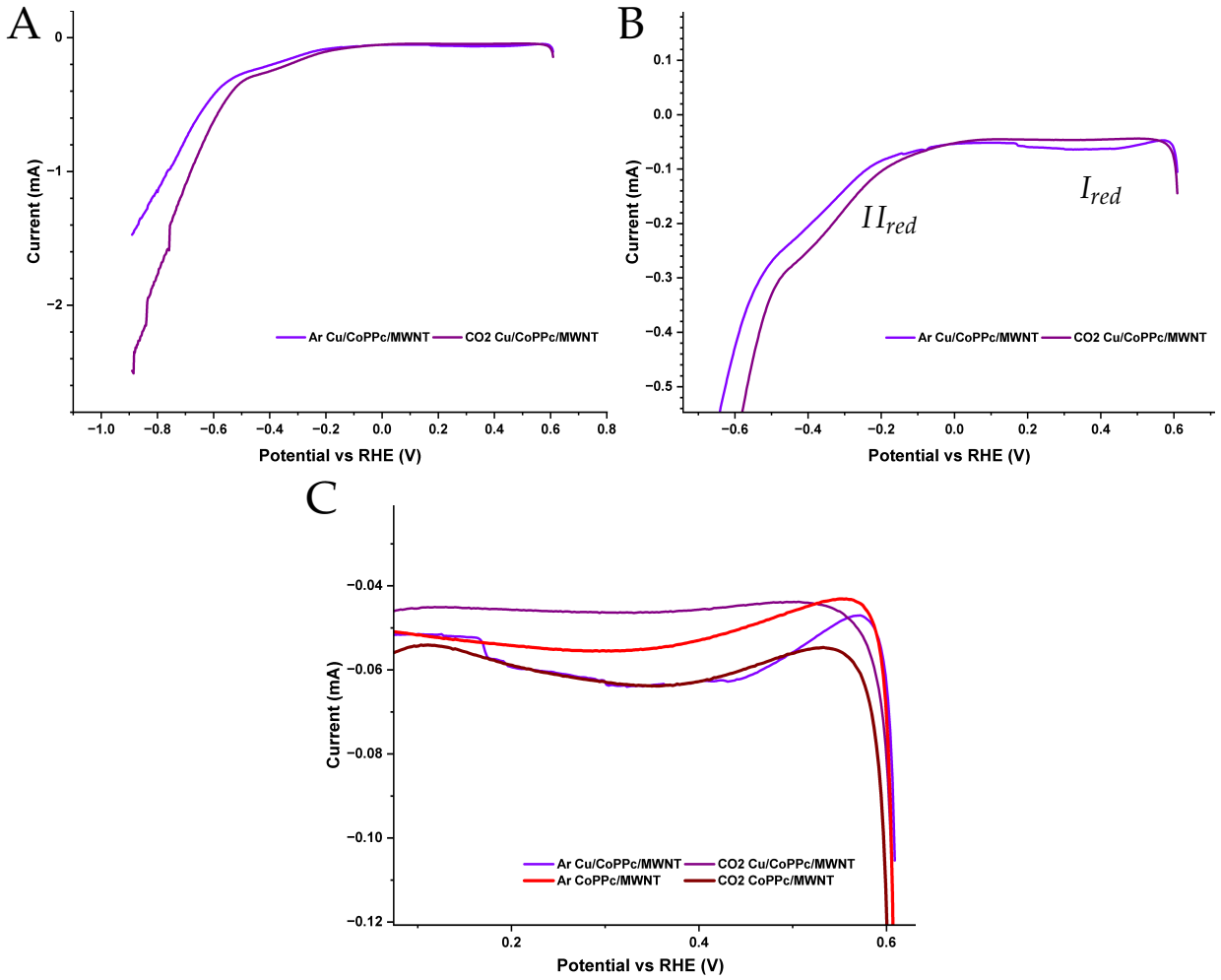


Figure 4.21: (A) LSV plot of Cu/CoPPc/MWNT using a RDE at a scan rate of 0.005 V s^{-1} in 0.5 M $KHCO_3$ electrolyte; (B) The same voltammogram in Fig. 4.9A without the CO_2RR region to better illustrate reduction peaks labelled I_{red} and II_{red}; (C) LSV plots from Fig. 4.9A and Fig. 4.21A of CoPPc/MWNT and Cu/CoPPc/MWNT zoomed to show the I_{red} region at 0.6 - 0.0 V vs RHE

As seen in Fig. 4.21A, in CO_2 saturated electrolyte, the CO_2RR electroreduction onset occurs at around -0.48 V vs RHE, whilst in argon saturated electrolyte, this feature occurs at -0.55 V vs RHE, resulting in an difference between the two of 0.07 V for Cu/CoPPc/MWNT. Compared to CoPPc/MWNT (Fig. 4.9), the CO_2RR onset potential occurs earlier at 0.01 mV, however Cu/CoPPc/MWNT achieved a lower current density at -1.7 V vs RHE of $-2.5\,mA\,cm^{-2}$ in CO_2 saturated electrolytes compared to $-3.2\,mA\,cm^{-2}$ achieved by CoPPc/MWNT.

The reduction peaks highlighted in Fig. 4.21B appear similar to those seen for CoPPc/MWNT (Fig. 4.9B), however the I_{red} peak in Cu/CoPPc/MWNT is prominent only in Ar saturated electrolyte, being still present in CO_2 saturated electrolyte, but practically negligible as it occurs on a μA order of magnitude. This is a difference in electrochemical behaviour compared to the CoPPc/MWNT I_{red} peak Figs. 4.9B and 4.21C,

which features in both CO_2 and Ar saturated electrolyte a slightly negatively shifted $E_{\frac{1}{2}}$ value in CO_2 (Fig. 4.9B).

During the initial LSV experiments for both CO_2 and Ar saturated electrolytes, at potentials below -0.5 V vs RHE , a purple colour was observed to be released from the electrode (Fig. 4.22), before becoming colourless after *ca.* 10 s. Notably, this only occurred the first time the Cu/CoPPc/MWNT electrode was polarised more negatively than -0.5 V vs RHE , as subsequent negative sweeps to and beyond this potential did not cause any purple colour to be observed.

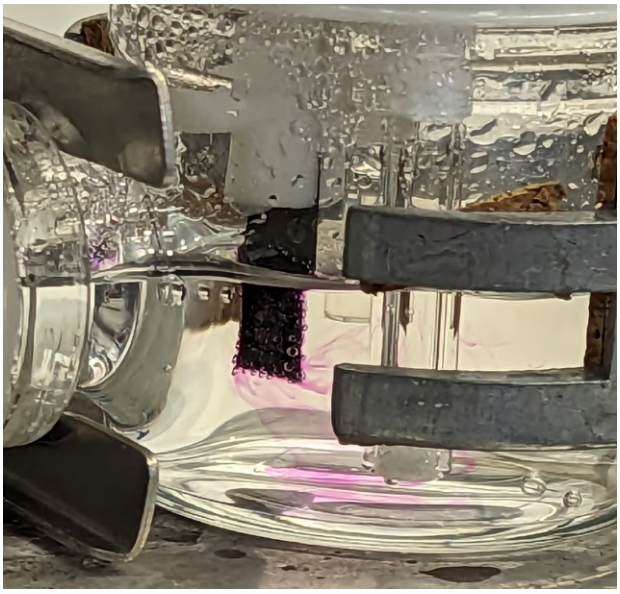


Figure 4.22: Photograph of the observed purple colour released from the Cu/CoPPc/MWNT electrode at -0.5 V vs RHE in a PTFE holder in a H-Cell with 0.5 M $KHCO_3$ electrolyte.

Subsequent LSV experiments on the catalyst after negative polarisation $>$ 0.5 V vs RHE (hereby referred to as Post-Cu/CoPPc/MWNT) reveal a change in electrochemical behaviour from the initial LSV as can be seen in Fig. 4.23.

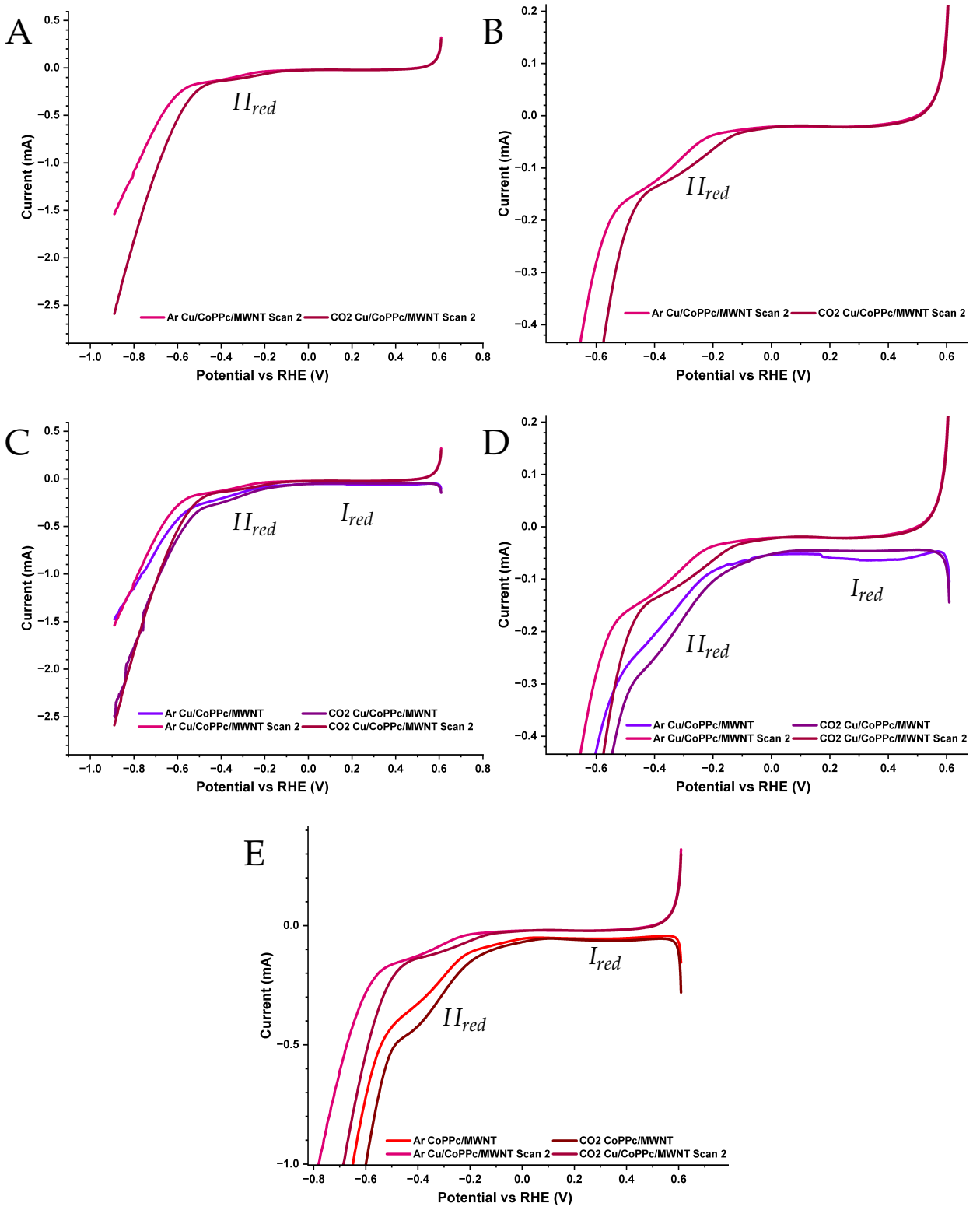


Figure 4.23: (A) Second scan LSVs of Cu/CoPPc/MWNT with the prominent reduction peak labelled and II_{red} (due to the absence of I_{red}); (B) The same voltammogram in Fig. 4.23A zoomed so that theCO_2RR region is omitted to better illustrate the II_{red} reduction peak; (C) Overlaid first and second scan LSVs of Cu/CoPPc/MWNT from Fig. 4.21A and Fig. 4.23A with reduction peak labelled II_{red}; (D) Overlaid LSVs from Fig. 4.23C zoomed in to omit the CO_2RR region to better illustrate reduction peaks I_{red} present in initial scan Cu/CoPPc/MWNT and II_{red} present in both first and second scans; (E) Overlaid LSVs of CoPPc/MWNT and the second scan Cu/CoPPc/MWNT from Fig. 4.21A and Fig. 4.23A respectively with the reduction peak in CoPPc/MWNT labelled I_{red} and the peak present in both CoPPc/MWNT and Cu/CoPPc/MWNT labelled II_{red}.

After the chemical process observed at -0.5 V vs RHE, the CO_2RR selectivity appears to improve. The LSV of post-Cu/CoPPc/MWNT Figs. 4.23A and 4.23C shows a similar CO_2RR onset potential of CO_2 electroreduction (when measured at beginning of the 'tail' feature without reduction peak overlap) of ~ -0.46 V vs RHE compared to Cu/CoPPc/MWNTs onset potential of ~ -0.48 V vs RHE, however it is evident that in CoPPc/MWNT the CO_2RR onset current is coincident with the II_{red} peak due to the steeper gradient of the peak. Furthermore, the LSV of Cu/CoPPc/MWNT shows an improved overpotential between CO_2 and Ar saturated electrolyte of $\eta = \sim 0.1$ V vs RHE compared to Cu/CoPPc/MWNTs ~ 0.07 V vs RHE. Additionally, the post-Cu/CoPPc/MWNT shows a significant difference in activity at -0.9 V vs RHE, with the CO_2 saturated electrolyte reaching a j of ~ -2.5mA cm^{-2}, with the Ar saturated electrolyte reaching only ~ -1.5 mA cm^{-2}, which is similarly seen in Cu/CoPPc/MWNT. This indicates the chemical process is associated with an increase in selectivity, but not activity of post-Cu/CoPPc/MWNT towards the CO_2RR.

Another difference in post-Cu/CoPPc/MWNT that can be observed is the complete loss of the I_{red} peak centred at 0.4 V vs RHE(Fig. 4.23D), corresponding to Co^{2+}/Co^{+},[12,49,50] is present only in CO_2 saturated electrolyte in LSVs of Cu/CoPPc/MWNT (Fig. 4.21B), implying the chemical process that occurs at -0.5 V vs RHE is linked to the first Co^{2+} reduction to Co^{+}, and results in the production of a purple coloured product is eliminated from the electrode. Given LSV evidence, this purple colour is most likely an aqueous cobalt species due to it's colour, implying an electrochemically driven displacement/elimination reaction. Before further conclusions can be drawn, CV of Cu/CoPPc/MWNT should be considered due to the limitations of LSV, being comprised only reduction events due to the monodirectionality of the scans.

The CV of Cu/CoPPc/MWNT was performed following the LSV analysis which featured the initial scans, using both a freshly dropcasted GCE and the same dropcasted RDE electrode with the same experimental conditions with the same rotation rate of 1600 rpm (Fig. 4.24).

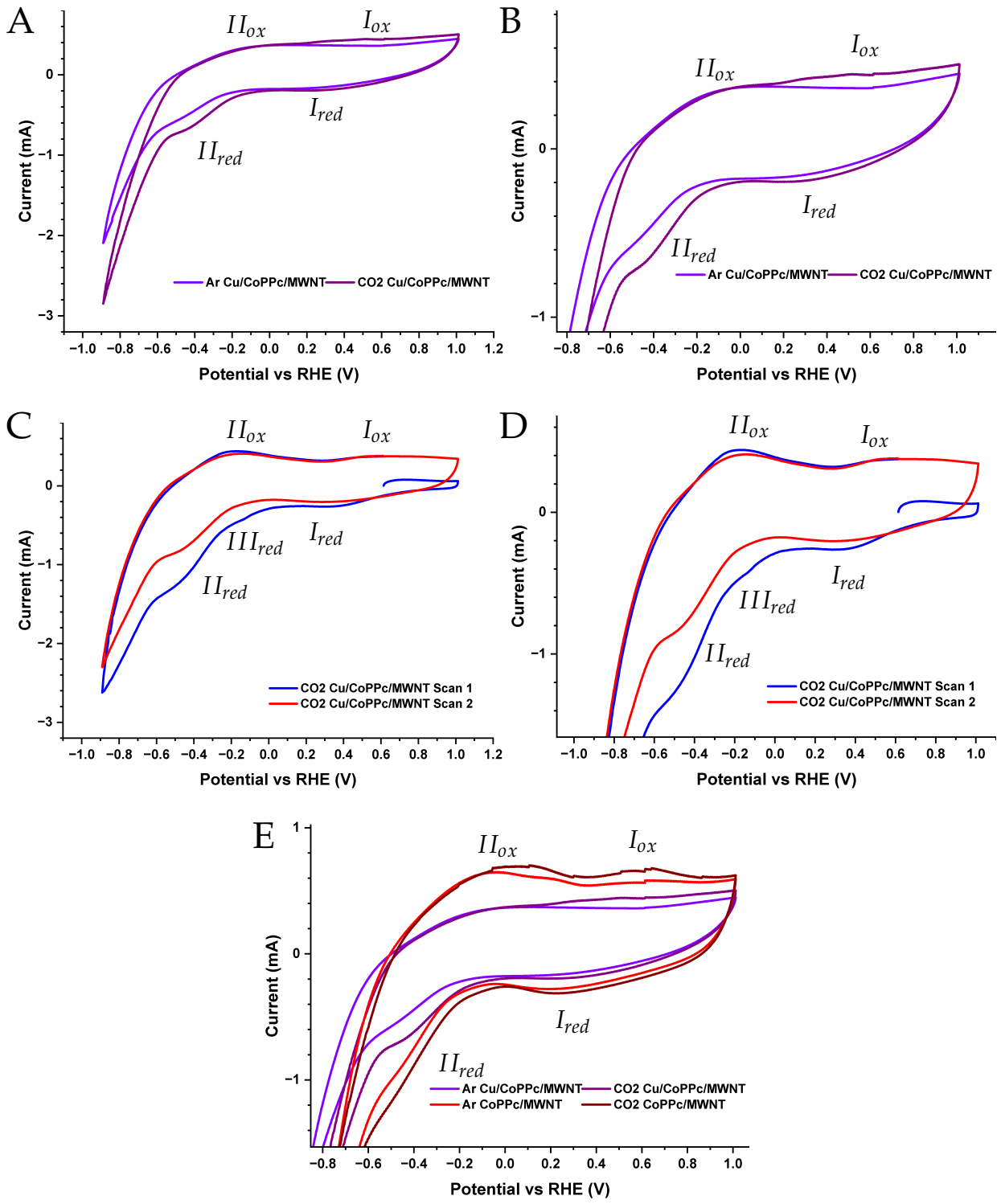


Figure 4.24: (A) CV plot of Cu/CoPPc/MWNT using a RDE at a scan rate of 0.05 V s^{-1} in 0.5 M $KHCO_3$ electrolyte at 1600 rpm with redox peaks labelled $I_{ox/red}$ and $II_{ox/red}$; (B) CV in Fig. 4.24A zoomed to omit the CO_2RR region to better illustrate redox peaks labelled $I_{ox/red}$ and $II_{ox/red}$; (C) Initial and subsequent CV scan of Cu/CoPPc/MWNT taken using a 3 mm GCE at a scan rate of 0.05 V s^{-1} in 0.5 M $KHCO_3$ electrolyte with redox peaks labelled $I_{ox/red}$, $II_{ox/red}$, and III_{red}; (D) CV in Fig. 4.24C zoomed to omit the CO_2RR region to better illustrate redox peaks labelled $I_{ox/red}$, $II_{ox/red}$, and III_{red}; (E) CV plots from Fig. 4.10A and Fig. 4.24A zoomed to omit the CO_2RR region to better illustrate redox peaks labelled $I_{ox/red}$ and $II_{ox/red}$

The CV plots of Cu/CoPPc/MWNT (Fig. 4.24) reveal that the I_{red} peak is still present in both Cu/CoPPc/MWNT and post-Cu/CoPPc/MWNT, with the higher scan rate resulting in an emphasis of the peaks due to the higher current. As seen in Figs. 4.24C and 4.24D, the initial scan has an increased current uptake in the reduction wave. This current increase begins with a new reduction peak, III_{red} centred at -0.2 V vs RHE, and is then followed by II_{red} at -0.4 V vs RHE, before the CO_2RR electroreduction feature begins at -0.5 V vs RHE. The III_{red} peak is only present in initial scans, and also in the higher scan rate 0.05 V s^{-1} voltammogram (Figs. 4.24C and 4.24D), as in the lower 0.001 V s^{-1} experiments (Fig. 4.21) it is encompassed by the II_{red} peak. Additionally, compared to CoPPc/MWNT, the $I_{ox/red}$ and $II_{ox/red}$ peaks in Cu/CoPPc/MWNT are less prominent and are associated with a lower charge passing over the redox events. Additionally, the $II_{ox/red}$ couple is noticeably charge unbalanced in Cu/CoPPc/MWNT, with the II_{ox} peak much smaller than the II_{red} peak, as opposed to CoPPc/MWNT, where the II_{ox} peak is much stronger.

To begin to elucidate the chemical process occurring at -0.5 V vs RHE in Cu/CoPPc/MWNT, evidence from the LSV experiments (Fig. 4.21), CV experiments (Fig. 4.24), AC-STEM Figs. 4.17 and 4.18, EELS-SI Fig. 4.19, and visual observations of the process Fig. 4.22 can be utilised to elucidate the nature of the process. A summary of key observations from these experiments are as follows:

I. The colour produced by the electrode at -0.5 V vs RHE is pink/purple and is released into the electrolyte.

   I.a. The pink/purple turns colourless after *ca.* 10 s.

II. On the catalyst surface exists single atom Cu in close proximity to the phthalocyanine Co centres.

   II.a. The Cu single atoms lie on/in close proximity to the N atoms in the phthalocyanine ring.

III. Crystalline structure observed in AC-STEM of post-Cu/CoPPc/MWNT corresponding to $CoCO_3$ found in the polymer layer.

IV. The chemical process occurs once at -0.5 V vs RHE and does not occur on subsequent scans.

V. Peak I_{red} becomingless prominent/absent after initial scans in LSV and CV

VI. $II_{ox/red}$ peaks still present post process.

   VI.a. $II_{ox/red}$ is charge imbalanced, with II_{ox} passing significantly less charge than II_{red}.

VII. Emergence of new III_{red} peak in initial scans with no associated oxidation peak that is absent in subsequent scans.

VIII. Increased current uptake starting at -0.2 V vs RHE in initial scans, whilst subsequent scans present a flat baseline until the CO_2RR onset.

Firstly, evidence point I. states that the chemical process produces a pink/purple colour that is released into the electrolyte from the electrode. From this it can inferred that this process involves the release of an aqueous Co^{2+} containing species, with the most likely candidates for this colour being $CoPc_{(aq)}$, $CoCl2_{(aq)}$, $CoCO3_{(aq)}$, $Co(HCO3)_{2(aq)}$, or $Co(OH)_{2(aq)}$.[32,54,55] From these candidates, CoPc can immediately be eliminated via sub evidence point I.a.. The phthalonitrile synthesis of the CoPPc/MWNT, and by extension, the Cu/CoPPc/MWNT, if producing single unit phthalocyanines, would produce tetracyano-CoPc (Section 4.2.1), which alongside unsubstituted CoPc, is insoluble in aqueous media.[56,57] The insolubility of any viable single unit phthalocyanines possibly present in the Cu/CoPPc/MWNT would have resulted in the formation of an coloured precipitate, and would not turn colourless as is observed in sub evidence point I.a.. This argument of solubility can be applied to also eliminate $CoCl_2$, as the extensive washing with H_2O and HCl during the synthesis would have likely removed any residual $CoCl_2$. Furthermore, $CoCl_2$ is highly unlikely to have a voltage dependant solvation from the electrode, and if it were present it would have most likely been dissolved without polarisation due to it's highly hygroscopic nature. This leaves $CoCO_3$, $Co(HCO_3)_2$, and $Co(OH)_2$ as the remaining candidates for the observed process, and evidence point III. strongly suggests the produced pink/purple species is $CoCO_3$.

To further narrow down the candidates for the produced species, cyclic voltammetry of Cu/CoPPc/MWNT was performed in Ar saturated 0.5 M Na_2SO_4 to determine if the purple colour was still produced in a non-carbonate electrolyte (Fig. 4.25).

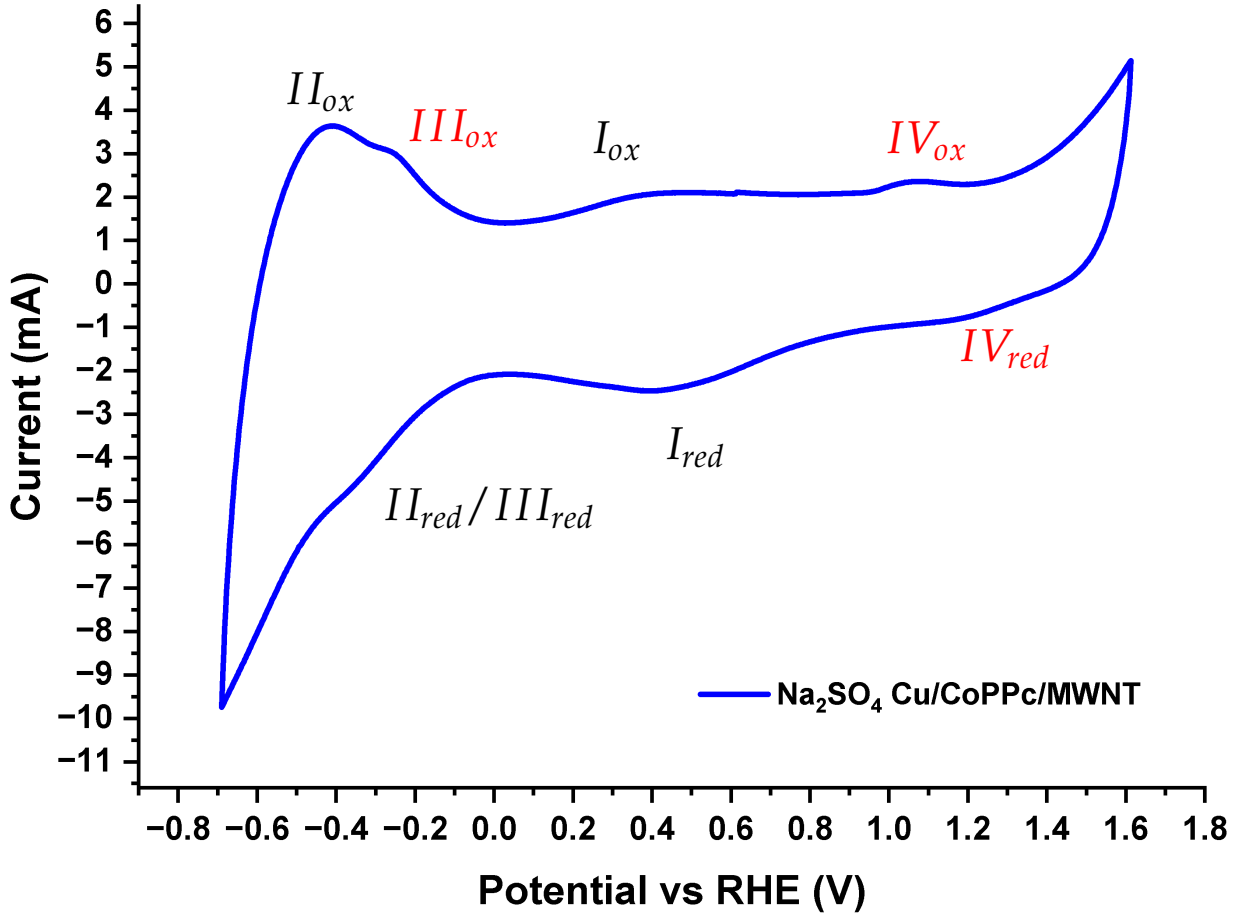


Figure 4.25: CV of Cu/CoPPc/MWNT in 0.5 M Na_2SO_4 at 0.05 Vs^{-1}. Peaks newly visible due to the change in electrolyte are annotated in red, whilst peaks that correspond to previously conducted voltammetry are annotated in black.

Firstly, during the CV of Cu/CoPPc/MWNT in Na_2SO4 the chemical process releasing a purple colour was observed, indicating the produced species is $Co(OH)_2$. From the CV of Cu/CoPPc/MWNT (Fig. 4.25), new peaks are present, due to being no longer obfuscated by the CO_2RR. The II_{ox} peak in the Na_2SO4 electrolyte splits into two distinct peaks: II_{ox} and III_{ox}, with III_{ox} previously not present likely due to CO_2 product oxidation/stripping at that potential in bicarbonate. Peaks II_{ox} and III_{ox} indicate a distinct oxidation of Pc is occuring separate to the Pc^{2-}/Pc^{4-} couple. Additionally, due to the increased potential window analysed, peaks IV_{ox} and IV_{red} are present at $\sim$ 1.2 V vs RHE and is associated with the $Co^{2+}Pc^{2-}/[Co^{3+}Pc^{2-}]^{+}$ redox couple, indicating that CoPPc is still present in the system.[58]

With the chemical species produced being identified as $Co(OH)_2$, it is evident that the source of the Co for the hydroxide formatiom must be the CoPPc, which further implies that the presence of Cu induces a demetalation of coppc/mwnt at -0.5 V vs RHE . Following this logic, this demetalation event is most likely to be an exchange of metal centres, where Cu is displacing Co, and forming copper centered phthalocyanines in the polyphthalocyanine. Insertion of Cu into the phthalocyanine ring is not implausible, as

evidence point II. states the Cu is exists in the form of single atoms, and sub evidence point II.a. states that these atoms also lie on the N atoms found in the phthalocyanine ring, meaning the Cu atoms are in close proximity to the Co metal centre, resulting in a feasible spatial position and structure for Cu to displace Co. Additionally, evidence point III. most likely indicates that $CoCO_3$ formation occurs after the release of $Co(OH)_2$ in the electrolyte, and the $CoCO_3$ species is formed in the in-situ in the electrolyte and was deposited on the electrode, resulting in the observed crystalline structure (Fig. 4.18).

To summarise the conclusions from evidence so far, evidence points I. to III. indicate, the process at -0.5 V vs RHE is an electrochemically driven metal displacement reaction, in which Cu displaces Co from the phthlaocyanine ring, which goes on to form $CoCO_3$ in the electrolyte, resulting in the purple colour released from the electrode and forming a co-polymeric CuPPc/CoPPc/MWNT in the process. Additionally, this hypothesis is supported by literature, as a similar electrochemically induced metal substitution at negative potentials was observed with metal oxide nanoparticles on FePc by Cheng *et al*.[59]

It is important to note that when considering the binding strength of the Co and Cu metal centres to Pc, Co is predicted to have a much greater affinity to the Pc ring when in the Co^{+} or Co^{2+} states[60] which would be present in this system, however, recent work by Yang *et al*[61] has shown that CoPc undergoes significant structural distortion under potentials applied for CH_3OH production, with this distortion shown in Fig. 4.26.

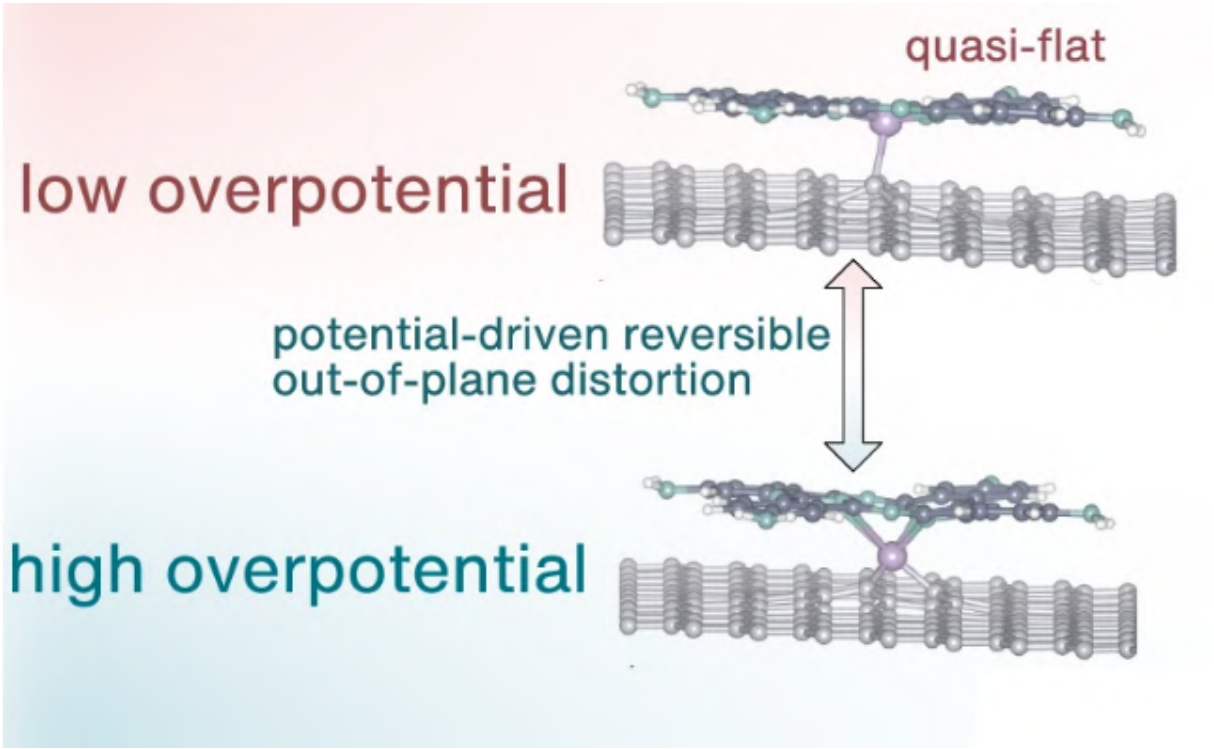


Figure 4.26: Structural distortion of CoPc at catalytic potentials. Adapted from Yang *et al*[61] and modified to show only the distorted geometry.

The potential-driven structural distortion may likely provide an adequate change in binding strength of the metal centres so that displacement of the Co with Co is favoured, and when considering both Cheng *et al*[59] and Yang *et al*'s[61] findings alongside the findings of this work, it seems plausible that a metal displacement could occur.

With a baseline concept and plausibility for the process established, further evidence points related to the electrochemistry of the material can be considered. Firstly, evidence point IV. suggests that the chemical process is an irreversible, one time change to the catalyst material, which supports the idea that the Cu incorporates into the polymer resulting in a co-polymeric CuPPc/CoPPc/MWNT.

When considering the change in peak behaviour as shown by evidence point V., it can be rationalised by considering the fact that CuPPc/MWNT will not have any associated phthalocyanine metal centre redox peaks (Section 4.3.3),[52] and thus would result in peaks characteristic to CuPPc/MWNT being indistinguishable to those of CoPPc/MWNT. This entails that the only changes that would be able to be seen in the electrochemical behaviour of Cu/CoPPc/MWNT would be the loss or decrease in peaks associated solely with Co and not the Pc ligand. With this fact in mind, evidence point V. strongly supports the possibility of co-polymer formation, as the I_{red} peak disappears after the chemical process at -0.5 V vs RHE in LSV at lower scan rates (Fig. 4.21), and in the higher scan rate CV experiments, Cu/CoPPc/MWNTs $I_{ox/red}$ couple is greatly diminished in comparison to CoPPc/MWNTs, strongly suggesting a loss of Co metal centres. This is additionally suported by evidence point VI., as the $II_{ox/red}$ couple is still present after the formation of Cu centred polyphthalocyanine units, as this peak couple is associated with $Co^{+}Pc^{2-}/Co^{2+}Pc^{4-}$ in CoPPc/MWNT, and Pc^{2-}/Pc^{3-} in CuPPc/MWNT.[58,62] This also goes on to explain sub evidence point VI.a., since the $II_{ox/red}$ couple in CuPPc/MWNT is charge imbalanced and chemically irreversible, as demonstrated both by literature[58] and this work (Fig. 4.14), the II_{ox} peak corresponding to Pc^{3-}/Pc^{2-} is greatly diminished, and is at a potential coincidental with the II_{ox} peak for CoPPc/MWNT at -0.2 V vs RHE. The coincidence of one electron and two electron oxidations from CuPPc/MWNT and CoPPc/MWNT respectively explains the peak splitting of II_{ox} into II_{ox} and III_{ox} observed in Fig. 4.25, as these peaks correspond to the separate Pc related reduction processes that would occur in a copolymerised system.

To decisively attribute the chemical process to co-polymer formation relies heavily on whether a feasible mechanism can be elucidated, especially due to the unintuitive nature of an oxidation of cobalt occurring at reductive potentials. In efforts to elucidate the mechanism, the redox behaviour of CoPPc/MWNT must be used in tandem with both evidence point VII. and evidence point VIII.. Firstly, evidence point VII. indicates a redox event occurs before the chemical change, and this redox event initially appears to be associated with the Cu^{2+}/Cu couple.[63] Firstly, outlining the reduction processes that occur in LSVs of Cu/CoPPc/MWNT (Fig. 4.21) is helpful in establishing the oxidation states of involved species. These reduction processes are described below by Eqs. (4.1)

to (4.3):

$$I_{red} : Co^{2+} + Pc^{2-} + e^- \longrightarrow Co^+ + Pc^{2-} \qquad V = \quad 0.4\,\text{vs RHE} \tag{4.1}$$

$$II_{red} : Co^+ + Pc^{2-} + e^- \longrightarrow Co^{2+} + Pc^{4-} \qquad V = -0.4\,\text{vs RHE} \tag{4.2}$$

$$III_{red} : Cu^{2+} + O^{2-} + 2\,H^+ + 2e^- \longrightarrow Cu + H_2O \qquad V = -0.2\,\text{vs RHE} \tag{4.3}$$

These reduction peaks occur on the initial scan, and occur in the sequence of $I_{red} \rightarrow III_{red} \rightarrow II_{red}$, with III_{red} being a PCET. It follows that preceding the chemical process at -0.5 V vs RHE, the oxidation states of the involved species are: Co^{2+}, Cu^0, and Pc^{4-}. Additionally, evidence point VIII. states there is an increased current uptake, which heavily implies additional electron transfer occurring alongside the reduction peaks. Considering this, a proposed hypothetical mechanism is as follows:

$$\text{Step 1: } Co^{2+}Pc^{4-} + Cu^0 \longrightarrow Cu^{2+}Pc^{4-} + Co^{2+} + 2e^- \tag{4.4}$$

$$\text{Step 2: } Co^{2+} + 2e^- + 2H_2O \longrightarrow Co(OH)_2 + H_2 \tag{4.5}$$

The formation of the CoCO3 is most likely achieved after the fact by the bicarbonate forming carbonate and water via reaction with the OH^- anion:

$$Co(OH)_2 + H^+ + HCO3^- \longrightarrow CoCO_3 + 2H_2O \tag{4.6}$$

4.4.4 Electrocatalysis

4.4.4.1 CO_2

To test the catalytic activity of Cu/CoPPc/MWNT, four potentials were tested for CO_2 reduction product formation for one hour: -0.85, -0.95, -1.05, and -1.15 V vs RHE. These initial experiments were conducted under the same conditions to CoPPc/MWNT (Section 4.2.4.1), and the Cu/CoPPc/MWNT was found to produce CH_3OH similar to the CoPPc/MWNT. Out of the tested potentials, -1.05 V vs RHE was found to be the optimum potential for CH_3OH production akin to CoPPc/MWNT, so this potential was used going forward for liquid and gas product analysis see (Section II.1.4 for experimental details). Results for the catalytic performance are reported in Figs. 4.27 and 4.28.

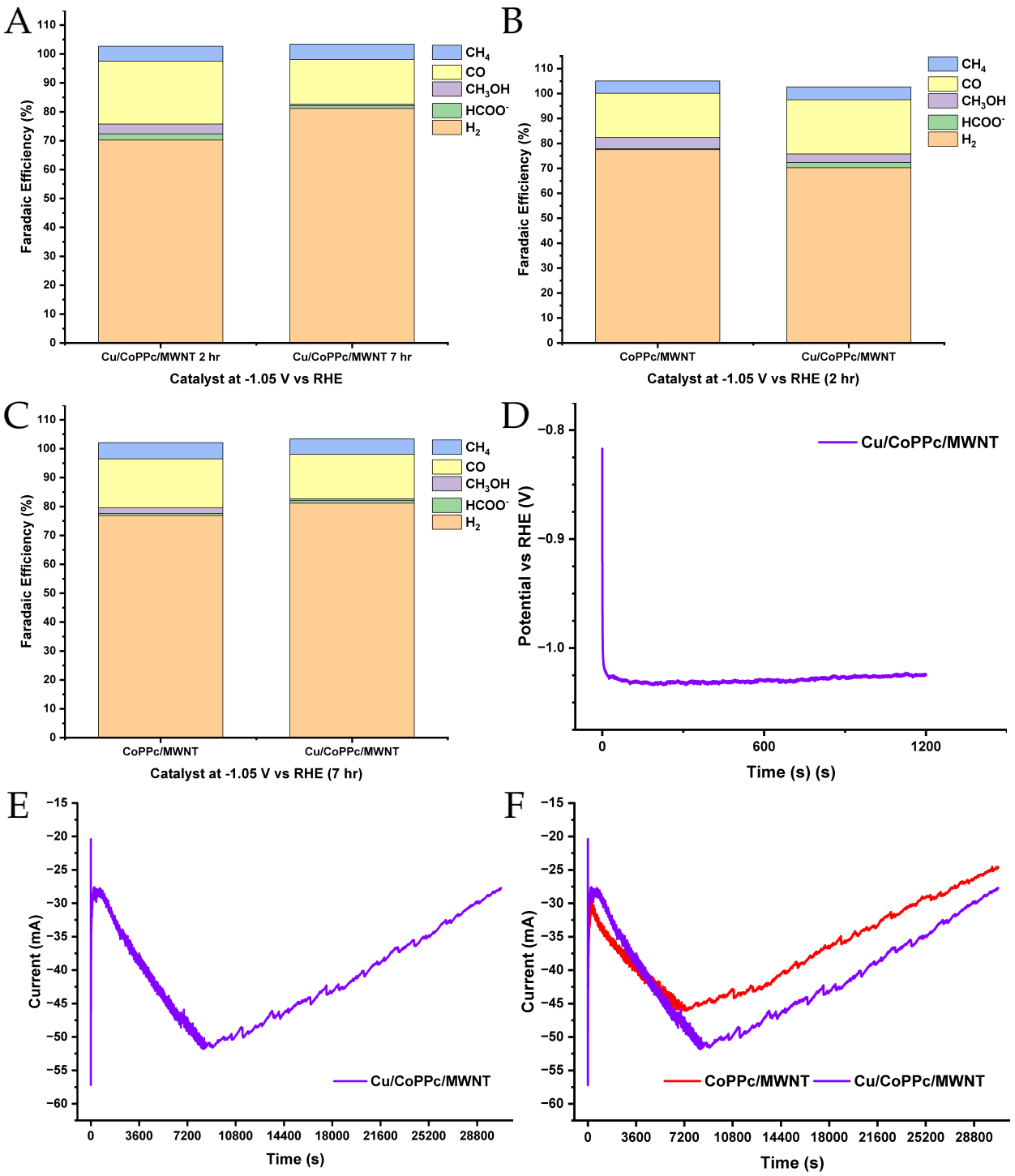


Figure 4.27: (A) Stacked bar chart showing individual product Faradaic efficiencies of Cu/CoPPc/MWNT over 2 hours and 7 hours of electrocatalysis at -1.05 V vs RHE; (B) Moles of gas produced over 2 hours by CoPPc/MWNT and Cu/CoPPc/MWNT during electrocatalysis at -1.05 V vs RHE; (C) Moles of gas produced over 7 hours by CoPPc/MWNT and Cu/CoPPc/MWNT during electrocatalysis at -1.05 V vs RHE; (D) Chronopotentiometry using an RDE of Cu/CoPPc/MWNT at a constant current of 4 mA; (E) Chronoamperometry trace of Cu/CoPPc/MWNT at -1.05 V vs RHE over the 7 hours that product formation was observed. (See Section II); (F) Chronoamperometry trace of CoPPc/MWNT and Cu/CoPPc/MWNT at -1.05 V vs RHE over the 7 hours that product formation was observed (See Section II).

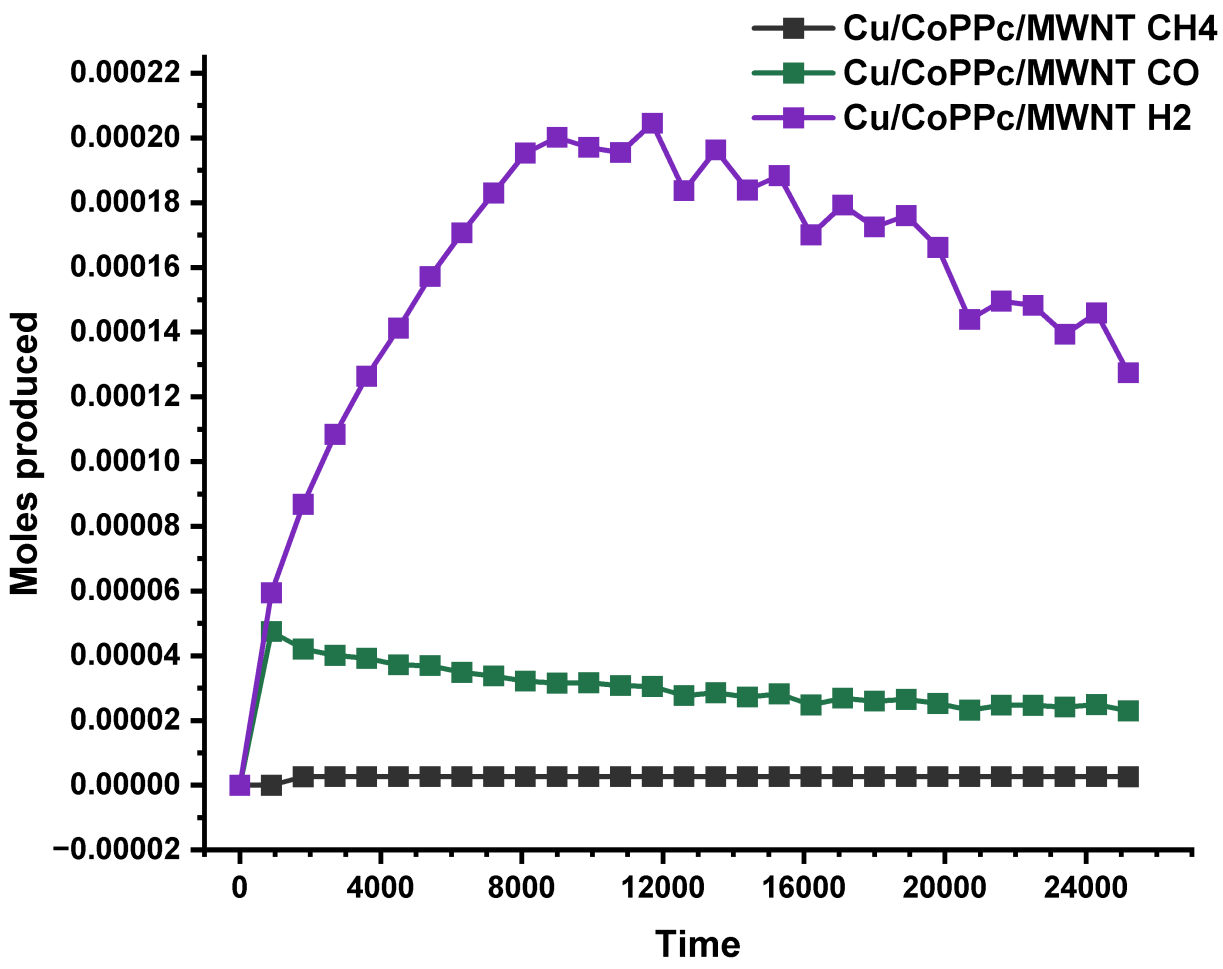


Figure 4.28: Moles of gas produced every 900 seconds over 7 hours by Cu/CoPPc/MWNT during electrocatalysis at −1.05 V vs RHE measured by GC.

From the catalysis results in Figs. 4.27 and 4.28, it can be seen that despite the addition of single atom copper and the observed chemical process (Section 4.4.3) which occurs in Cu/CoPPc/MWNT, the observed FEs are very similar to CoPPc/MWNT, with only the observed current density during the chronoamperometry Fig. 4.27F being greater in Cu/CoPPc/MWNT. Both CoPPc/MWNT and Cu/CoPPc/MWNT produce methanol and methane as products, a trait that remains notable due to being polyphthalocyanine based catalysts, with Cu/CoPPc/MWNT achieving 3.42% FE towards CH_3OH and 5.12% FE towards CH_4 after 2 hours, and 0.57% FE towards CH_3OH and 5.36% FE towards CH_4 after 7 hours. The product selectivity for liquid products seem drop considerably over the course of the 7 hours, however this can be partially explained by the fact that similar to CoPPc/MWNT, the counter electrolyte seems to be fully consumed a little after 2 hours, leading to the gradual decrease of current over the next 5 hours that is observed in Fig. 4.27E. This gradual decrease in current can be associated with cessation of catalytic activity and HER expected dominates at the working electrode, meaning that liquid products which are sampled directly would be observed to essentially cease after the point which counter electrolyte is depleted, but gas products like CO and CH_4 would

continue to be detected due to their dissolution in the electrolyte and slower release into the GC detectors.

Interestingly, when chronoamperometry of Cu/CoPPc/MWNT is performed without connecting the cell to the GC instrument in an open configuration (still with constant CO_2 flowing through the solution), the observed CH_3OH FE over 1 hour is double that of CoPPc/MWNT in the same conditions, with Cu/CoPPc/MWNT reaching a CH_3OH FE of 8.33% compared to CoPPc/MWNTs 4.58%. Additionally, the chronoamperometry traces in this open cell configuration is much more stable, passing a steady current throughout the duration, as opposed to the closed configuration which trends downwards considerably from the start of the experiment. This is likely a result of the closed system experiencing a higher pressure in the headspace of the cell due to the small vent in the GC, as this higher pressure will result in more gaseous products and CO_2 staying dissolved in the electrolyte. This over extended periods likely had a poisoning effect on the catalyst, so the downwards trend in the chronoamperometry can be associated with the increase in H_2 production from the HER and electrolyte degredation.

Despite the lack of improvement of desired catalytic activity, the Cu/CoPPc/MWNT is still shown to be stable towards catalysis, as shown in the flat chronopotentiometry response at currents observed at -1.05 V vs RHE (Fig. 4.27D). This provides evidence to the fact that despite the electrochemical insertion of the Cu into the phthalocyanine ring, the catalyst is stable at negative potentials.

4.4.5 Conclusions

Overall, CoPPc/MWNT presents itself to be a stable, highly active electrocatalyst for CO_2RR, with the ability to produce further reduced products than other unmodified cobalt phthalocyanine based catalysts in literature (as of writing). However, the key drawback to this catalyst is its poor selectivity towards one specific product, especially as its major product is H_2.

It is evident that the CoPPc/MWNT catalyst investigated has catalytic activity that is starkly different to previous syntheses of the catalyst,[7,16] as there is a large change in product selectivity from CO at high FEs, to much further reduced products like CH_3OH and CH_4 at low FEs, but still featuring a relatively large CO FE in line with prior works.[7,16] It is speculated the ability for $> 2\,e^-$ CO_2RR products results from the much thinner polymeric layer on the surface on the MWNT compared to previous syntheses[7,16] which results in the reduction route towards further reduction following CO becoming energetically accessible due to lack of aggregation.[12] This explanation would also explain the still present CO, as the further reduction is highly dependant on areas with a low degree of aggregation. The thin polymer layer is most likely due to the larger MWNT diameter than prior literature, which also explains the incomplete coverage due to the precursor amounts being adapted from Han *et al*[16] who make use of smaller diameter

MWNTs and report complete coverage.

Upon modification with with Cu, the Cu/CoPPc/MWNT catalyst synthesised in this work shares the stability towards negative potentials observed in CoPPc/MWNT, and whilst the addition of Cu does improve the FE towards methanol by nearly a factor of 2, the selectivity still does not achieve desirable enough results compared to the results seen by Boutin and Wu *et al*[2,5] to merit further study as a CO_2 electrocatalyst. Despite this finding, the Cu/CoPPc/MWNT was found that on the application of potentials more negative then -1.05 V, in which a electrochemically driven metal displacement was observed, producing a vibrant purple colour from the electrode that was not observed in the CoPPc/MWNT catalyst at the same potentials. This behaviour was rationalised with electrochemical analysis and is consistent with the findings of Cheng *et al*[59] who observed this electrochemically induced metal displacement in metal phthalocyanines, however this work is distinct from Cheng *et al*'s[59] due to the fact that the Co centre that undergoes the displacement by Cu has higher binding affinity to the Pc ring than Cu in almost all levels of ionisation.[60] It is the findings of this work that this displacement proceeds due to two factors, the first being the fact that the metal centre in CoPc undergoes significant structural distortion out of the Pc plane at negative potentials,[61] and the second being that the Cu atoms in Cu/CoPPc/MWNT exist almost entirely in single atom form stabilised by the N atoms of the Pc ring that, putting them in close proximity to the Co centre, which has been evidenced by AC-STEM and novel EELS-SI with single atom resolution conducted on the Cu/CoPPc/MWNT.

Future work looking to improve the electrocatalytic activity of the CoPPc/MWNT and Cu/CoPPc/MWNT towards methanol should focus on obtaining uniform, and thin polymer coverage on the MWNT. To achieve this, defect engineering or surface modifcation of the nanotube could allow more favourable CoPPc interactions with the MWNT surface, rather than already bound polymer. Additionally, Brunauer-Emmett-Teller surface area analysis (BET) could be employed to obtain an average MWNT surface area, and then using the surface area to calculate more exact reagent quantities for closer to monolayer coverage. Unfortunately, perfect monolayer coverage of the polymer to the MWNT is improbable with the phthalonitrile synthesis, due the unavoidable formation external nanotube pores, which will always present incredibly favourable aggregation sites. It may prove more worthwhile to take insights and possibly adapt the synthesis of monolayer CoPc achieved by Song *et al*[64] of ultrathin CoPc covalent organic frameworks to achieve a more controlled polymeric growth.

Chapter 4 Bibliography

(1) C. M. Lieber and N. S. Lewis, "Catalytic Reduction of CO2 at Carbon Electrodes Modified with Cobalt Phthalocyanine", *Journal of the American Chemical Society*, 1984, **106**, 5033–5034.

(2) Y. Wu, Z. Jiang, X. Lu, Y. Liang and H. Wang, "Domino electroreduction of CO2 to methanol on a molecular catalyst", *Nature*, 2019, **575**, 639–642.

(3) X. Liu, B. Q. Li, B. Ni, L. Wang and H. J. Peng, "A perspective on the electrocatalytic conversion of carbon dioxide to methanol with metallomacrocyclic catalysts", *Journal of Energy Chemistry*, 2021, **64**, 263–275.

(4) S. Kapusta and N. Hackerman, "Carbon Dioxide Reduction at a Metal Phthalocyanine Catalyzed Carbon Electrode", *Journal of The Electrochemical Society*, 1984, **131**, 1511–1514.

(5) E. Boutin, M. Wang, J. C. Lin, M. Mesnage, D. Mendoza, B. Lassalle-Kaiser, C. Hahn, T. F. Jaramillo and M. Robert, "Aqueous Electrochemical Reduction of Carbon Dioxide and Carbon Monoxide into Methanol with Cobalt Phthalocyanine", *Angewandte Chemie - International Edition*, 2019, **58**, 16172–16176.

(6) T. V. Magdesieva, T. Yamamoto, D. A. Tryk and A. Fujishima, "Electrochemical Reduction of CO[sub 2] with Transition Metal Phthalocyanine and Porphyrin Complexes Supported on Activated Carbon Fibers", *Journal of The Electrochemical Society*, 2002, **149**, D89.

(7) J. Chen, J. Li, W. Liu, X. Ma, J. Xu, M. Zhu and Y. F. Han, "Facile synthesis of polymerized cobalt phthalocyanines for highly efficient CO2 reduction", *Green Chemistry*, 2019, **21**, 6056–6061.

(8) S. Lin, C. S. Diercks, Y. B. Zhang, N. Kornienko, E. M. Nichols, Y. Zhao, A. R. Paris, D. Kim, P. Yang, O. M. Yaghi and C. J. Chang, "Covalent organic frameworks comprising cobalt porphyrins for catalytic CO2 reduction in water", *Science*, 2015, **349**, 1208–1213.

(9) Z. Zhang, J. Xiao, X. J. Chen, S. Yu, L. Yu, R. Si, Y. Wang, S. Wang, X. Meng, Y. Wang, Z. Q. Tian and D. Deng, "Reaction Mechanisms of Well-Defined Metal–N4 Sites in Electrocatalytic CO2 Reduction", *Angewandte Chemie - International Edition*, 2018, **57**, 16339–16342.

(10) M. Wang, L. Chen, T. C. Lau and M. Robert, "A Hybrid Co Quaterpyridine Complex/Carbon Nanotube Catalytic Material for CO2 Reduction in Water", *Angewandte Chemie - International Edition*, 2018, **57**, 7769–7773.
(11) M. Wang, K. Torbensen, D. Salvatore, S. Ren, D. Joulié, F. Dumoulin, D. Mendoza, B. Lassalle-Kaiser, U. Işci, C. P. Berlinguette and M. Robert, "CO2 electrochemical catalytic reduction with a highly active cobalt phthalocyanine", *Nature Communications*, 2019, **10**, DOI: 10.1038/s41467-019-11542-w.
(12) X. Chen, D. Wei and M. S. Ahlquist, "Aggregation and Significant Difference in Reactivity Therein: Blocking the CO2-to-CH3OH Reaction", *Organometallics*, 2021, **40**, 3087–3093.
(13) J. F. Walker, R. P. Corporation, C. (Londyn). and Hall, in *American Chemical Society Monograph Series*, ed. Reinhold Publishing Corporation, C. (Londyn). and Hall, Reinhold Publishing Corporation, WASHINGTON, 3rd edn., 1964, ch. 159, pp. 206–226.
(14) Y. Y. Birdja and M. T. Koper, "The importance of cannizzaro-type reactions during electrocatalytic reduction of carbon dioxide", *Journal of the American Chemical Society*, 2017, **139**, 2030–2034.
(15) F. Gund, "New Developments in the Application of Phthalocyanines in Textile Printing", *Journal of the Society of Dyers and Colourists*, 1953, **69**, 671–682.
(16) N. Han, Y. Wang, L. Ma, J. Wen, J. Li, H. Zheng, K. Nie, X. Wang, F. Zhao, Y. Li, J. Fan, J. Zhong, T. Wu, D. J. Miller, J. Lu, S. T. Lee and Y. Li, "Supported Cobalt Polyphthalocyanine for High-Performance Electrocatalytic CO2 Reduction", *Chem*, 2017, **3**, 652–664.
(17) D. Karapinar, A. Zitolo, T. N. Huan, S. Zanna, D. Taverna, L. H. Galvão Tizei, D. Giaume, P. Marcus, V. Mougel and M. Fontecave, "Carbon-Nanotube-Supported Copper Polyphthalocyanine for Efficient and Selective Electrocatalytic CO2 Reduction to CO", *ChemSusChem*, 2020, **13**, 173–179.
(18) Y. Lu, J. Zhang, W. Wei, D. D. Ma, X. T. Wu and Q. L. Zhu, "Efficient Carbon Dioxide Electroreduction over Ultrathin Covalent Organic Framework Nanolayers with Isolated Cobalt Porphyrin Units", *ACS Applied Materials and Interfaces*, 2020, **12**, 37986–37992.
(19) C. S. Diercks, S. Lin, N. Kornienko, E. A. Kapustin, E. M. Nichols, C. Zhu, Y. Zhao, C. J. Chang and O. M. Yaghi, "Reticular Electronic Tuning of Porphyrin Active Sites in Covalent Organic Frameworks for Electrocatalytic Carbon Dioxide Reduction", *Journal of the American Chemical Society*, 2018, **140**, 1116–1122.
(20) T. He, C. Yang, Y. Chen, N. Huang, S. Duan, Z. Zhang, W. Hu and D. Jiang, "Bottom-Up Interfacial Design of Covalent Organic Frameworks for Highly Efficient and Selective Electrocatalysis of CO2", *Advanced Materials*, 2022, **34**, 2205186.
(21) Z. Chen, N. Li and Q. Zhang, "Covalent Organic Frameworks as Promising Platforms for Efficient Electrochemical Reduction of Carbon Dioxide: A Review", *Small Structures*, 2024, **5**, 2300495.

(22) Y. Hori, A. Murata and R. Takahashi, "Formation of hydrocarbons in the electrochemical reduction of carbon dioxide at a copper electrode in aqueous solution", *Journal of the Chemical Society, Faraday Transactions 1: Physical Chemistry in Condensed Phases*, 1989, **85**, 2309–2326.

(23) K. P. Kuhl, E. R. Cave, D. N. Abram and T. F. Jaramillo, "New insights into the electrochemical reduction of carbon dioxide on metallic copper surfaces", *Energy and Environmental Science*, 2012, **5**, 7050–7059.

(24) S. Nitopi, E. Bertheussen, S. B. Scott, X. Liu, A. K. Engstfeld, S. Horch, B. Seger, I. E. Stephens, K. Chan, C. Hahn, J. K. Nørskov, T. F. Jaramillo and I. Chorkendorff, "Progress and Perspectives of Electrochemical CO2 Reduction on Copper in Aqueous Electrolyte", *Chemical Reviews*, 2019, **119**, 7610–7672.

(25) T. Burwell, M. Thangamuthu, G. N. Aliev, S. Ghaderzadeh, E. C. Kohlrausch, Y. Chen, W. Theis, L. T. Norman, J. A. Fernandes, E. Besley, P. Licence and A. N. Khlobystov, "Direct formation of copper nanoparticles from atoms at graphitic step edges lowers overpotential and improves selectivity of electrocatalytic CO2 reduction", *Communications Chemistry*, 2024, **7**, 140.

(26) J. Gao, H. Zhang, X. Guo, J. Luo, S. M. Zakeeruddin, D. Ren and M. Grätzel, "Selective C-C Coupling in Carbon Dioxide Electroreduction via Efficient Spillover of Intermediates As Supported by Operando Raman Spectroscopy", *Journal of the American Chemical Society*, 2019, **141**, 18704–18714.

(27) S. A. Chala, R. Liu, E. O. Oseghe, S. T. Clausing, C. Kampf, J. Bansmann, A. H. Clark, Y. Zhou, I. Lieberwirth, J. Biskupek, U. Kaiser and C. Streb, "Selective Electroreduction of CO ¡sub¿2¡/sub¿ to Ethanol via Cobalt–Copper Tandem Catalysts", *ACS Catalysis*, 2024, **14**, 15553–15564.

(28) J. Zhang, T. H. My Pham, Z. Gao, M. Li, Y. Ko, L. Lombardo, W. Zhao, W. Luo and A. Züttel, "Electrochemical CO2 Reduction over Copper Phthalocyanine Derived Catalysts with Enhanced Selectivity for Multicarbon Products", *ACS Catalysis*, 2023, **13**, 9326–9335.

(29) J. Zeng, M. Mignosa, N. B. Monti, A. Sacco and C. F. Pirri, "Engineering copper nanoparticle electrodes for tunable electrochemical reduction of carbon dioxide", *Electrochimica Acta*, 2023, **464**, 142862.

(30) N. Rawat, Z. Pan, C. J. Lamarche, A. Wetherby, R. Waterman, T. Tokumoto, J. G. Cherian, R. L. Headrick, S. A. McGill and M. I. Furis, "Spin Exchange Interaction in Substituted Copper Phthalocyanine Crystalline Thin Films", *Scientific Reports*, 2015, **5**, 16536.

(31) G. Antczak, W. Kamiński and K. Morgenstern, "Apparent Height of the Metal Atom in Phthalocyanine: Co vs Cu", *Journal of Physical Chemistry C*, 2024, **128**, 14056–14064.

(32) S. W. Oliver and T. D. Smith, "Oligomeric cyclization of dinitriles in the synthesis of phthalocyanines and related compounds: The role of the alkoxide anion", *Journal of the Chemical Society, Perkin Transactions 2*, 1987, 1579–1582.

(33) S. Yamamoto, S. V. Dudkin, M. Kimura and N. Kobayashi, in *Handbook of Porphyrin Science: With Applications to Chemistry, Physics, Materials Science, Engineering, Biology and Medicine - Volume 45: Phthalocyanine Synthesis and Computational Design of Functional Tetrapyrroles*, WORLD SCIENTIFIC, 2019, vol. Volume 45, pp. 1–168.
(34) D. A. Britz and A. N. Khlobystov, "Noncovalent interactions of molecules with single walled carbon nanotubes", *Chemical Society Reviews*, 2006, **35**, 637–659.
(35) Z. Jiang, Y. Wang, X. Zhang, H. Zheng, X. Wang and Y. Liang, "Revealing the hidden performance of metal phthalocyanines for CO2 reduction electrocatalysis by hybridization with carbon nanotubes", *Nano Research*, 2019, **12**, 2330–2334.
(36) G. Zanotti, P. Imperatori, A. M. Paoletti and G. Pennesi, "Sustainable approaches to the synthesis of metallophthalocyanines in solution", *Molecules*, 2021, **26**, 1760.
(37) B. H. Lipshutz, S. Ghorai and M. Cortes-Clerget, "The Hydrophobic Effect Applied to Organic Synthesis: Recent Synthetic Chemistry "in Water"", *Chemistry - A European Journal*, 2018, **24**, 6672–6695.
(38) F. Doraghi, M. H. Morshedsolouk, N. A. Zahedi, B. Larijani and M. Mahdavi, "Phthalimides: developments in synthesis and functionalization", *RSC Advances*, 2024, **14**, 22809–22827.
(39) K. Mitra and M. C. Hartman, "Silicon phthalocyanines: synthesis and resurgent applications", *Organic and Biomolecular Chemistry*, 2021, **19**, 1168–1190.
(40) G. Zanotti, F. Palmeri and V. Raglione, "Phthalocyanines Synthesis: A State-of-The-Art Review of Sustainable Approaches Through Green Chemistry Metrics", *Chemistry – A European Journal*, 2024, **n/a**, e202400908.
(41) C. Heidelberger, A. Guggisberg, E. Stephanon and M. Hesse, "Amidine als Zwischenprodukte bei Umamidierungsreaktionen. 9. Mitteilung über Umamidierungsreaktionen", *Helvetica Chimica Acta*, 1981, **64**, 399–406.
(42) A. M. Hyde, R. Calabria, R. Arvary, X. Wang and A. Klapars, "Investigating the Underappreciated Hydrolytic Instability of 1,8-Diazabicyclo[5.4.0]undec-7-ene and Related Unsaturated Nitrogenous Bases", *Organic Process Research and Development*, 2019, **23**, 1860–1871.
(43) N. Kobayashi, R. Kondo, S. ichiro Nakajima and T. Osa, "New Route to Unsymmetrical Phthalocyanine Analogues by the Use of Structurally Distorted Subphthalocyanines", *Journal of the American Chemical Society*, 1990, **112**, 9640–9641.
(44) J. Obirai, N. P. Rodrigues, F. Bedioui and T. Nyokong, "Synthesis, spectral and electrochemical properties of a new family of pyrrole substituted cobalt, iron, manganese, nickel and zinc phthalocyanine complexes", *Journal of Porphyrins and Phthalocyanines*, 2003, **7**, 508–520.
(45) S. Li, Y. Liu, D. Xu and H.-g. Wang, "Conjugated polycopper phthalocyanine as the anode-active material with high specific capacity for lithium-organic batteries", *Materials Letters*, 2023, **333**, 133682.
(46) J. P. Tessonnier, O. Ersen, G. Weinberg, C. Pham-Huu, D. S. Su and R. Schlögl, "Selective deposition of metal nanoparticles inside or outside multiwalled carbon nanotubes", *ACS Nano*, 2009, **3**, 2081–2089.

(47) S. J. Pennycook and P. D. Nellist, in *Impact of Electron and Scanning Probe Microscopy on Materials Research*, ed. D. G. Rickerby, G. Valdrè and U. Valdrè, Springer Netherlands, Dordrecht, 1999, pp. 161–207.
(48) A. Kumar Jagadeesan, K. Thangavelu and V. Dhananjeyan, in *21st Century Surface Science - a Handbook*, ed. P. Pham, P. Goel, S. Kumar and K. Yadav, IntechOpen, Rijeka, 2020, Ch. 2.
(49) M. L'her and A. Pondaven, in *The Porphyrin Handbook: Phthalocyanines: Spectroscopic and Electrochemical Characterization*, ed. K. M. Kadish, K. M. Smith and R. B. T. .-. T. P. H. Guilard, Academic Press, Amsterdam, 2003, vol. 16, pp. 117–169.
(50) K. Sakamoto, in *Voltammetry*, ed. N. W. Maxakato, S. S. Gwebu and G. H. Mhlongo, IntechOpen, Rijeka, 2019, ch. 3.
(51) R. Frydendal, E. A. Paoli, B. P. Knudsen, B. Wickman, P. Malacrida, I. E. Stephens and I. Chorkendorff, "Benchmarking the Stability of Oxygen Evolution Reaction Catalysts: The Importance of Monitoring Mass Losses", *ChemElectroChem*, 2014, **1**, 2075–2081.
(52) A. Koca, H. A. Dinçer, M. B. Koçak and A. Gül, "Electrochemical characterization of Co(II) and Pd(II) phthalocyanines carrying diethoxymalonyl and carboxymethyl substituents", *Russian Journal of Electrochemistry*, 2006, **42**, 31–37.
(53) F. Pertlik, "Structures of hydrothermally synthesized cobalt (II) carbonate and nickel (II) carbonate.", *Acta Crystallographica*, 1986, **C42**, 4–5.
(54) D. E. Newton, *Chemical Elements*, ed. K. J. Edgar and Gale (Firm), Detroit: UXL, Detroit, 2nd ed., 2010, p. 1003.
(55) R. H. Petrucci, F. G. Herring, J. D. Madura and C. Bissonnette, *General Chemistry : principles and modern applications*, Toronto : Pearson, Toronto, 11th ed., 2017, p. 1325.
(56) F. Ghani, J. Kristen and H. Riegler, "Solubility properties of unsubstituted metal phthalocyanines in different types of solvents", *Journal of Chemical and Engineering Data*, 2012, **57**, 439–449.
(57) N. Sagawa and T. Shikata, "Are all polar molecules hydrophilic? Hydration numbers of nitro compounds and nitriles in aqueous solution", *Physical Chemistry Chemical Physics*, 2014, **16**, 13262–13270.
(58) G. Gümrükçü Köse, G. Keser Karaoğlan, S. Neccaroğlu Işık, D. Akyüz and A. Koca, "The Synthesis, Characterization, Electrochemical and Spectroelectrochemical Properties of Novel Unsymmetrical Phthalocyanines Containing Naphthoic Acid and Di-tert-butylphenoxy Groups", *Synthetic Metals*, 2020, **264**, 116386.
(59) Y. Cheng, J. P. Veder, L. Thomsen, S. Zhao, M. Saunders, R. Demichelis, C. Liu, R. De Marco and S. P. Jiang, "Electrochemically substituted metal phthalocyanines, e-MPc (M = Co, Ni), as highly active and selective catalysts for CO2 reduction", *Journal of Materials Chemistry A*, 2018, **6**, 1370–1375.
(60) M. S. Liao and S. Scheiner, "Electronic structure and bonding in metal phthalocyanines, metal=Fe, Co, Ni, Cu, Zn, Mg", *Journal of Chemical Physics*, 2001, **114**, 9780–9791.

(61) H. Yang, N. Guo, S. Xi, Y. Wu, B. Yao, Q. He, C. Zhang and L. Wang, "Potential-driven structural distortion in cobalt phthalocyanine for electrocatalytic CO2/CO reduction towards methanol", *Nature Communications*, 2024, **15**, 7703.
(62) H. Baş, N. Kahriman and Z. Biyiklioğlu, "Synthesis and electrochemical properties of copper(II), manganese(III) phthalocyanines bearing chalcone groups at peripheral or nonperipheral positions", *Turkish Journal of Chemistry*, 2020, **44**, 1549–1555.
(63) S. D. Giri and A. Sarkar, "Electrochemical Study of Bulk and Monolayer Copper in Alkaline Solution", *Journal of The Electrochemical Society*, 2016, **163**, H252–H259.
(64) Y. Song, J. J. Zhang, Z. Zhu, X. Chen, L. Huang, J. Su, Z. Xu, T. H. Ly, C. S. Lee, B. I. Yakobson, B. Z. Tang and R. Ye, "Zwitterionic ultrathin covalent organic polymers for high-performance electrocatalytic carbon dioxide reduction", *Applied Catalysis B: Environmental*, 2021, **284**, 119750.

Chapter 5

P-Block Metals on MWNTs for the electrochemical CO_2 reduction reaction

5.1 Background

5.1.1 Lead for the CO_2RR

Pb has been known to selectively produce $HCOO^-$ in the electrochemical CO_2RR since 1985,[1] however it has seen far less research attention compared to other p-block metals owing to its well known toxicity.[2,3] Despite this, there are definite benefits in investigating the use of Pb as a CO_2RR catalyst, such as its high $HCOO^-$ selectivity,[1,3–5] relative low cost to other metal catalysts such as Cu,[6] and use in conjunction with CNTs presents significant promise due to CNTs recent use as in lead wastewater decontamination.[7]

The high selectivity of Pb towards $HCOO^-$ stems from a strong O affinity and low C and H affinities, which theoretically would result in selective formation of the $\cdot$OCHO species producing solely $HCOO^-$ and preventing H_2 formation.[8] However, computational work by Zhao *et al*[9] predict that for Pb (111) direct carbon bonding to form the $\cdot$COOH species is the dominant catalytic pathway, and actively suppresses the $\cdot$OCHO pathway when solvated in a cation containing solution, i.e an electrolyte.[9] Whilst $HCOO^-$ is still favoured, the $\cdot$COOH intermediate pathway opens the possibility of the formation of further reduced products such as CO, a fact which is validated by numerous experimental works observing both CO and CH_4 as a product.[1,5,10–12] Additionally unfortunate is the fact that K^+ cations in particular were predicted to increase production of CO as its greater hydrophobicity (relative to smaller group 1 metal cations) destabilises Pb adsorbed HCOO.[9] due to the seminal works by Hori *et al*,[13] Ringe *et al*,[14] and König *et al*[15] who generally find that larger cations result in higher CO_2RR activity by increasing the favourability of CO_2 adsorption,[13–15] It has become commonplace to use $KHCO_3$ as the electrolyte for co_2rr research, with this work included.

The selectivity of Pb for the CO_2RR has been demonstrated to be highly dependant on morphology, as was demonstrated by Pander *et al*[16] who prepared Pb catalysts from the electroreduction of PbS and PbO, with the PbS derived material featuring a wafer-like nanostructure with a much higher surface area than that of the PbO counterpart which featured rounded rough contiguous surface.[16] Normalisation of the j_{HCOO^-} between the wafer and rounded catalysts by Electrochemical Surface Area (ECSA) and roughness factor, the wafer-like nanostructure achieved greater j_{HCOO^-} and co$_2$rr onset potential despite the area normalisation and chemical indistinguishability.[16] In addition, the X-ray Diffraction Spectroscopy (XRD) of the PbS sample reveals a polycrystalline structure, with evidence of both the (111) and (020) planes in the catalyst, with the (111) being the most prevalent in Pb^0.[16] For further evidence on the effect of morphology, the work by Fan *et al*[17] also demonstrates a morphological effect on the catalytic activity of Pb for the CO_2RR. The work by Fan *et al*[17] investigates a Pb honeycomb structure with dendritic Pb with the catalytically active surface being predominantly Pb(100). Fan *et al*'s[17] catalyst resulted in 97% FE_{HCOO^-},[17] a result greater than the expected $\sim$ 90% range for previous Pb catalysts.[3] Importantly, in Fan *et al*'s[17] work no CO was observed as a side product, this is notable as Zhao *et al* performed their computational study assuming a Pb (111) plane, so it can be assumed that the lack of CO observed can be attributed to the nanostructure; specifically the Pb crystal plane, which directly impacts the adsorbed CO_2 intermediate being $\cdot$COOH in the case of the (111) plane and $\cdot$OCHO in the case of the (100) plane. Additionally, both of the works by Fan and Pander *et al*[16,17] make use of a $KHCO_3$ electrolyte, so it can be concluded that the cationic and solvation effects observed by Zhao *et al*[9] does not impose great enough effect on $\cdot$OCHO binding to the (100) plane. Overall, using these works it can be determined that morphology greatly impacts the catalytic performance of Pb, demonstrated by the large differences in FE observed for $HCOO^-$ in research, ranging from $\sim$ 72% in the early work by Hori *et al*[1] which utilises an unmodified Pb surface, to 97% in Fan *et al*'s work.[17]

Alongside fitting the theme of this thesis, MWNTs have been shown in a recent review by Pyrzynska[7] to have applications for use in Pb ion contaminated wastewater treatment due to their exceptionally high surface area and porosity.[7] From these insights, there is potential for a dual-use catalysts, in which MWNTs can be first used for Pb decontamination, and then further used as an electrocatalyst for the CO_2RR as the decontamination process results in physically absorbed Pb^{2+} ions which are facile to reduce electrochemically.

With this potential use in mind, and having determined a framework for factors which effect the catalytic activity of Pb, the use of Pb/MWNT can be evaluated. Due to the aforementioned toxicity of Pb[2] resulting in low research interest, as of the time of writing there is only one work on a Pb/MWNT system, that being the work by Xing *et al*.[5] In the work by Xing *et al*,[5] a Pb/MWNT system was produced by forming Pb nanoparticles derived from $Pb(CH_3COO)_2$ capped with chitosan, physically mixed, and then thermally decomposed.[5] This produced a Pb/MWNT catalyst with surface adsorbed Pb particles

with a diameter of $\sim 400 - 500$ nm and crystalline with a (220) plane.[5] This catalyst achieved a FE_{HCOO^-} of 84.6% and produced CO, CH_4, and H_2 as side products,[5] confirming that this catalyst follows the mechanism involving the $\cdot$COOH intermediate.[9] Comparing to the work by Fan and Pander *et al*,[17] these results imply that the $\cdot$OCHO pathway is unique to the (100) Pb dendritic morphology investigated by Fan *et al*.[17]

A commonality between works investigating Pb electrocatalytic CO_2RR is the existence of crystalline PbO regardless of the major and minor products produced.[1,3,9,13,16–19] This implies that for Pb to active towards the CO_2RR, crystallinity is required, and consequently this requirement necessitates Pb sites large enough to be crystalline, a requirement that is further evidenced by this work in the fact that the single atom/nanoparticle Pb did not achieve any appreciable $HCOO^-$ production above trace amounts, likely resulting resulting from uncommon aggregates observed in the TEM (Section 5.2.3).

5.1.2 Bismuth for the CO_2RR

The high selectivity of Bi towards $HCOO^-$ was first observed in 1995 by Komatsu *et al*[20] in which near 100% FE_{KHCO_3} was observed for a Bi plated electrode. Despite the demonstration of promising catalytic activity and low cost of Bi,[6] the work by Komatsu *et al*[20] received no research attention and zero works were published on Bi for the CO_2RR until 18 years later in 2013 by DiMeglio *et al*,[21] with the most likely explanation for this gap being greater research attention at the time being directed into Sn CO_2RR catalysts.[19]

The work by DiMeglio *et al*[21] made use of electrodeposition of Bi on GC and observed 95% FE_{CO} with no formate observed, the reason for the production of CO rather than $HCOO^-$ works before and after[3,19,20] would observe is due DiMeglio *et al*'s[21] use of an ionic liquid as an electrolyte. The ionic liquid cations utilised: $[EMIM]^+$ and $[BMIM]^+$, are capable of providing $2\,H^+ + 2\,e^-$ via deprotonation of the central imidazolium carbon,[21] meaning that to observe CO formation the adsorbed intermediate must be direct carbon bonded $\cdot$COOH,[8] and that the ionic liquid electrolyte must influence the favourability of CO desorption as almost all studies in aqueous electrolyte since observe $HCOO^-$.[3,19]

Since the work by DiMeglio *et al*,[21] Bi catalysts received more research attention and drew attention to the original work by Komatsu *et al*,[20] with the focus of future works in evaluating the capability to produce $HCOO^-$.[3,19] The first notable work to come from this renewed research interest is that of Zhong *et al*,[22] who achieved 96.4% FE_{HCOO^-} and a j_{HCOO^-} of 15.2 mA cm^{-2} with electrodeposited Bi on carbon paper at ~ -1.1 V vs RHE in 0.5 M $NaHCO_3$.[22] Another work by Liu *et al*[23] utilised Bi_2O_3 nanosheets on a carbon matrix to achieve a FE_{HCOO^-} of 93.8% and a j_{HCOO^-} of 17 mA cm^2 at ~ -1.23 V vs RHE in 0.1 M $KHCO_3$.[23] These two works[22,23] highlight the issue of Bi requiring high overpotentials (≥ 1 V vs RHE), meaning that despite Bi's incredible selectivity, avoiding the competitive HER is difficult, and introduces the possibility of reductive deactivation of catalysts over longer timescales.[3,19]

An additional problem Bi catalysts face is an issue of uncertainty regarding the catalytic mechanism, specifically the role of BiO_x species and if there is a role at all. Work by Pander *et al*[24] investigated Bi during the electrochemical CO_2RR with *in situ* Attenuated Total Reflectance Infra-red Spectroscopy (ATR-IR) and found the Bi oxide layer remains unchanged after the reaction and no metal carbonate intermediates were detected during the reaction, and thus stated that Bi is an oxide independent CO_2RR catalyst. However, more recent computational and experimental work state the contrary, one such work being the computational study by Oh *et al*,[25] who found that the Bi(111) surface is inert to the adsorption of most species barring O_2 as Bi−O bonds are much more stable than Bi−C due to better hybridization of Bi's 6s and 6p orbitals with the O 2p.[25] This more favourable Bi−O interaction results in the stabilisation of the $\cdot$OCHO intermediate as opposed to the $\cdot$COOH intermediate, resulting in selective formation of formate as opposed to other carbon products.[25] Due to the detection of CO as a minor product in Pander and Liu *et al*'s work[23,24] and the major product in Zhong *et al*'s[22] work, it is unlikely that $\cdot$OCHO is the intermediate in all cases, but it is also unlikely that the mechanism is BiO independent, with the works by Walker *et al*[26] and Nolan[27] somewhat reconciling these conflicting findings by suggesting the $\cdot$COOH pathway is used with the Bi^{3+} lone pair electrons found in Bi_2O_3 catalysts facilitating CO_2 adsorption and interaction.[26,27]

Like Pb, Bi's selectivity and activity has been shown to highly dependant on morphology. Comparing the aforementioned work by Liu *et al*[23] who utilised Bi nanosheets on a carbon matrix to the work by Koh *et al*[28] who utilised electrodeposition to form Bi hierarchical dendrites. The work by Koh *et al*[28] achieved 89% FE_{HCOO^-} at -0.74 V vs RHE with a j_{HCOO^-} of $\sim$ 3 mA cm^2 and at -1.13 V vs RHE achieved a FE_{HCOO^-} of $\sim$ 27% with a j_{HCOO^-} of $\sim$ 15 mA cm^2,[28] whilst Pander *et al*'s[24] achieved FE_{HCOO^-} of 93.8% at -1.23 V vs RHE and a j_{HCOO^-} of 17 mA cm^2, but only $\sim$ 40% FE_{HCOO^-} with a j_{HCOO^-} of 3 mA cm^2 at at -0.80 V vs RHE.[24] These two differently structured Bi catalysts demonstrate vastly different selectivities dependant on overpotential, with the dendritic Bi shows a much higher selectivity at lower overpotentials and the carbon matrix nanosheets showing much higher selectivity and activity at higher overpotentials.[24,28] These two results imply a mechanistic difference between the two catalysts, as at higher overpotentials ($\sim$ -1.1 V vs RHE) Koh *et al*'s[28] work found the major product to have shifted to H_2 in dendritic Bi, but in Bi foil and in Pander *et al*'s work[24] the major product was $HCOO^-$ at similar potentials.[24,28] This difference is possible attributed to crystal structure, with the dendritic Bi preferentially forming high index (012), (110), and (104) planes, with the foil predominantly the (003) plane, with the (003) plane expected to favour the $\cdot$OCHO intermediate and (012), (110), and (104) planes favouring the $\cdot$COOH intermediate,[28] however this is hard to compare to the Bi carbon matrix nanosheets due to it's composition of Bi_2O_3 as no post mortem crystallinity information is given..[24]

The highest selectivity achieved at the lowest overpotential for Bi was demonstrated by[29] with Bi nanoflakes on Cu, reaching $\sim$ 100% FE_{HCOO^-} at -0.6 V vs RHE with a j_{HCOO^-} of

$\sim$ 3.5 mA cm^2, however this drops to $\sim$ 80% FE_{HCOO^-} at -1.0 V vs RHE with a j_{HCOO^-} of $\sim$ 9 mA cm^2.[29] The Bi nanoflakes are reported to be predominantly crystalline with the (012) plane, supporting the findings by Koh *et al*,[28] however the improvement shown in the nanoflakes compared to the dendrites is attributed to increased surface area with a majority of sites being edge or corner sites.[29]

Kim, Koh, and Pander *et al*'s work[24,28,29] illustrate the the effect of morphology on Bi, specifically the Bi (012) plane allowing low overpotential selectivity, and beyond these works this appears to be a trend in almost all of the existing work in CO_2RR electrocatalysis using Bi, with low overpotential (≤ -0.8 V vs RHE) selectivity ($\geq$ 80% FE_{HCOO^-}) only seen in catalysts in which the Bi^0(012) is the most prevalent crystal plane after the electrochemical reduction from Bi^{x+}.[20,22,24,28–37]

With this conclusion in mind, interesting to note is the work of Gong *et al*[31] who achieved $\sim$ 90% FE_{HCOO^-} at -0.8 V vs RHE with a j_{HCOO^-} of $\sim$ 30 mA cm^2 with Bi_2O_3 Double-Walled Carbon Nanotubes (DWNTs). This nanotube catalyst is highly active at ≤ -0.8 V vs RHE , and initially is composed of Bi^{3+} then during electrocatalysis is reduced to Bi^0 forming a defective Bi nanotube.[31] The XRD data in Gong *et al*'s work shows that after reduction, the Bi nanotube catalyst becomes predominantly Bi (012), further supporting the above conclusion.

Lastly, as of the time of writing, only one work exists utilising a Bi/MWNT system, that being the work by Zhang *et al*[38] published in 2024 after the experimental work for this thesis on Bi/MWNT concluded.[38] The work by Zhang *et al* is highly similar to the work contained within this thesis, as Bi and Bi_2O_3 nanoparticles were deposited on MWNTs, as well as Bi2S3, and Bi_2Se_3.[38] The nanoparticles were first prepared separate to the MWNTs from an initial $Bi(NO_3)_3$ precursor followed by addition bismuth citrate and $NaBH_4$ to produce Bi nanoparticles, similar to the classic Turkevich method for nanoparticle synthesis,[39] the Bi nanoparticles were then mixed with the MWNTs via sonication at various weight %s to produce Bi/MWNT.[38] This differs from this work in two ways, firstly this work prepared the nanoparticles from nitrate already adhered to the MWNT in solution, and also no cappping agents to stabilise the nanoparticles were used since they were pre stabilised by the MWNT surface.[40] Zhang *et al*'s work finds that the various Bi nanoparticles on MWNTs achieved $>$ 90% FE_{HCOO^-} at -0.9 $--1.15$ V vs RHE , notable however is the j_{HCOO^-} between the different systems was roughly similar at $\sim$ 10 mA cm^2; this similarity is due to the fact that similar to Gong *et al*'s[31] work, after applied negative potentials for CO_2RR all of the catalysts are found to be Bi^0 with the (012) plane as it's most prevalent structure and explains the nearly identical post mortem XPS results.[38]

In conclusion, from reviewing the use Bi for the electrochemical CO_2RR, the most important insight found is that the Bi (012) allows for low overpotential selectivity. This key insight explains the middling performance of the Bi/MWNT catalyst in this work, as the Bi was largely amorphous, and the low activity towards formate that was observed was

likely due to observed crystalline deposits which then could potentially form the Bi (012) plane (Section 5.3.2.1).

5.1.3 Indium for the CO_2RR

Formate selectivity using In based electrocatalysts was first demonstrated by Hori *et al*.[41] Despite demonstrating a higher FE_{HCOO^-} than Sn; similar to Bi (Section 5.1.2), In did receive not a large amount of experimental attention compared to Sn based catalysts.[19] This lack of experimental attention was likely due to the much higher cost of In when compared to other p-block metals in which CO_2RR activity had been observed, such as Sn. Pb, and Bi.[6,19] However, significant research attention has been devoted to In since, frequently demonstrates FE_{HCOO^-}'s of $\sim 100\%$ in engineered electrocatalysts.[3,19]

The reason for Ins selectivity towards $HCOO^-$ stems from the formation of $In(OH)_3$ active sites which react with CO_2 to form active $In-CO_3$ species.[42] This was first demonstrated by Detweiler *et al*[42] in a work which conducted *in-operando* ATR-IR on the In electrode during CO_2RR and found that the redox active In_2O_3 species is key for formate selectivity, due to their reaction with water to form the catalytically active $In(OH)_3$ species.[42] This was supported further in the work by comparing a reduced In^0 electrode to an anodized In_2O_3 electrode, which resulted in the anodized electrode achieving FE_{HCOO^-} of $> 80\%$ at ~ -0.95 V vs RHE whilst the reduced electrode achieving $< 70\%$ under the same conditions.[42] Interestingly, a key finding of Detweiler *et al*'s is that $In(OH)_3$ nanoparticles lack any redox peaks in voltammetry using K_2SO_4 electrolyte, only having presenting a catalytic reduction onset in CO_2 at -0.85 V vs RHE , and nothing in Ar.[42]

Further work by White *et al*[43] begins to elucidate the electrochemical behaviour of $In(OH)_3$ by comparing unsupported In, In_2O_3, and $In(OH)_3$ nanoparticles which were then physically mixed with carbon black and found that between the three, selectivity was highest in the order of $In > In_2O_3 > In(OH)_3$.[43] These results from White *et al*[43] are rationalised by the lower conductivities of In_2O_3 and $In(OH)_3$, which increased the required overpotential for catalytic activity, with $> 80\%$ FE_{HCOO^-} being only observed in In_2O_3 at -0.95 V vs RHE compared to In showing near 100% at potentials as low as -0.65 V vs RHE.[43] The activity in In results from the incomplete oxidation in air resulting in a In^0 and In^{3+} mixed system, forming an active $In(OH)_3$ surface.[43] Interestingly, White *et al*[43] report redox activity in their Ar voltammetry of $In(OH)_3$ nanoparticles in K_2SO_4.[43] This finding is unusual as the $In(OH)_3$ nanoparticles were synthesised using an identical method to Detweiler *et al*[42] in the exact same electrolyte system and electrode for voltammetry.[42,43] This can be rationalised by looking at the redox peak observed in Ar saturated $In(OH)_3$, as it is nearly identical in position and separation to the Ar saturated In_2O_3 redox couple, albeit with less current, and also both CO_2 traces are practically identical, with identical onset potentials and current densities with no redox couple observed.[43] The reason for lack of redox couple in CO_2 saturated electrolyte is explained

by both works that the In in the $In-CO_3^-$ does not accept electrons and instead passes the electron directly to the bound CO_2.[42,43]

The difference between the Ar saturated $In(OH)_3$ voltammetry in White *et al*'s[43] work can be found by comparing the conditions in the electrochemical cell to Detweiler *et al*'s[42] work, as the Ar saturated CVs performed by Detweiler *et al* was pH adjusted to 7.5 whilst White *et al*[43] adjusted to 5.3. Therefore, the disparity in observed redox activity in $In(OH)_3$ is explained by looking at the Pourbaix diagram of In (Fig. 5.1):

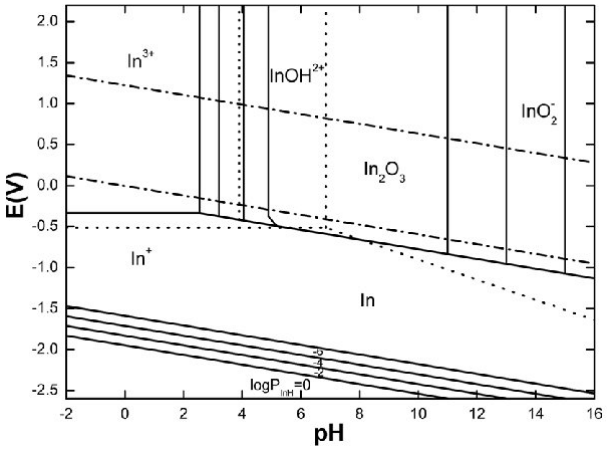


Figure 5.1: Potential-pH equillibrium diagram for In in water at 25°C, adapted from.[44]

The redox couple reported by Detweiler and White *et al* occurs at *ca* -0.5 V vs RHE,[42,43] and Fig. 5.1 shows that at a pH of 5.3 the $In(OH)_3$ can proceed to a reduction towards In^+ or In^0, whilst at a pH of 7.5 it cannot remain as $In(OH)_3$.[44]

Important to note is the work by Huang *et al*,[45] which reveals that for In_2O_3 catalysts, smaller size is not necessarily associated with improved catalytic activity, as the energetic favourability of the three catalytic pathways available; these pathways being $\cdot OCHO$ and $\cdot COOH$ for CO_2RR, and $H\cdot$ for HER, increases with decreasing size, with the binding of H approaching thermoneutrality as the catalyst size decreases.[45] Notably, this size effect is only applicable to In_2O_3 catalysts, as Detweiler and White *et al*'s[42,43] work do not encounter this size effect, despite an average particle size of ~ 6 nm. This suggests that for formate production, In and $In_2O_3/In(OH)_3$ have distinct catalytic mechanisms, with the oxide/hydroxide route proceeding via a singly bound oxygen in CO_2 toIn, whilst In proceeds by both the oxygen atoms in CO_2 binding to the In surface, with these two mechanisms shown by Fig. 5.2.[46,47]

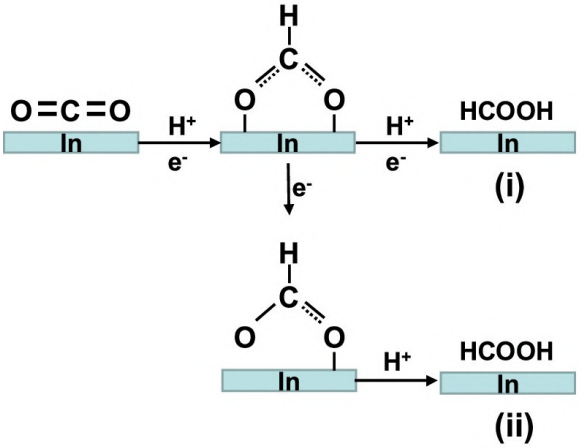


Figure 5.2: Catalytic pathways for In (i) and $In(OH)_3$ (ii). Adapted from.[47]

Both of these mechanisms result in exclusively $HCOO^-$ formation,[46] and alongside the size dependency observed by Huang *et al*,[45] reconcile the high activity observed by In and In_2O_3 nanoparticles[42,43,48] with only the latter showing appreciable H_2 generation, and neither finding CO_2RR products other than $HCOO^-$. Interestingly, CO is an available product via a direct carbon bonding mechanism and has been observed in non-nanoparticulate In_2O_3/C catalysts.[49,50]

The works by Detweiler and White *et al*[42,43] shed light on the activity for In nanoparticles, however it has demonstrated that there is a difference between physically mixed In catalysts to supports and In with strong chemical interactions to the support. Demonstrating this is the work by Mou *et al*[48] who prepared an In_2O_3/C via coprecipitation of $In(NO_3)_3$ and carbon black followed by pyrolysis which achieved a FE_{HCOO^-} of 87.6% with a j_{HCOO^-} of $\sim 15\,mA\,cm^2$ at -1.2 V vs RHE.[48] Mou *et al*'s[48] work demonstrates that chemically binding In_2O_3 to the support rather than the physical mixing demonstrated by Detweiler and White *et al*[42,43] allows for greater selectivity in In_2O_3 catalysts, which is likely due to the greater ability for electron delivery stemming from the chemical interaction to the conductive support that allows the In_2O_3 to be electrochemically active despite it's lower conductivity.[43] The downside of the In catalyst employed by Mou *et al*[48] was the HER activity observed in the catalyst, with near $\sim$ 13% of the charge consumed going towards the competitive HER, which is attributed to both the carbon black support promoting HER,[48] but also the small particle size of In_2O_3.[45]

5.2 Pb/MWNTs

5.2.1 Synthesis

The synthesis of p-block metals on MWNTs (Pb/MWNT, Bi/MWNT, In/MWNT) was achieved via the thermal decomposition of p-block metal nitrates (MNO_3) on MWNTs

into metal and metal oxide nanoparticles on the surface of the nanotube. This method of nanoparticle deposition on MWNTs was first described by Capobianchi *et al*,[51] with further refinement on solvent selection from Tessonnier *et al*,[40] the latter of which was used as the basis for experimental method development. The initial synthesis of Pb/MWNT was as follows: first, to MWNTs (250 mg) was added a solution of $PbNO_3$ (1 wt% Pb w.r.t MWNT) in H_2O (6 mL). This mixture was subsequently stirred with a glass rod until the resulting "paste" was homogeneous without any large lumps, and then was dried for 24 hrs at 60 °C to produce $PbNO_3$/MWNT in a powder form. This powder was then transferred to a furnace and decomposed at 350 °C for 2 hrs with a 10 °C min^{-1} ramp time, this decomposition time and temperature was chosen based off data on the thermal decomposition of $PbNO_3$/MWNT from Vratny *et al*.[52] After decomposition, a powder of Pb/MWNT is produced with a hypothetical weight loading of Pb on MWNTs of 1 wt%.

This initial synthesis was adapted to match the outer-wall deposition method outlined by Tessonnier *et al*,[40] however as will be further explored in Sections 5.2.3.1 and 5.2.4, this synthesis required further modification due to the incredibly low coverage of Pb nanoparticles (Section 5.2.2.1). The low nanoparticle coverage resulted from the high atomic weight of Pb meaning 1 wt% results in a low amount of actual Pb atoms in the sample. This in practice meant that all future syntheses required a much greater weight loading of Pb, and 25 wt% resulted being the lowest weight loading synthesised for most samples, and 10 wt% being the lowest analysed out of all catalysts in future.

Alongside the low coverage, Insights from TEM of Pb/MWNT Section 5.2.2.1 highlighted concerns regarding the decomposition temperature used due to the observed degradation of the MWNT support resulting from thermal decomposition of the nanotube. The decomposition temperature and time would prove challenging to standardise between p-block metal catalysts, due to the requirement of full metal nitrate decomposition and the fact that the metal nitrate will inherently catalyse earlier thermal decomposition of the MWNTs than otherwise would be seen in pristine MWNTs (see Section 5.2.2.2 for TGA plots).

As Pb/MWNT was the first p-block metal on MWNT catalyst synthesised and tested, various combinations of decomposition temperature and time were tested as listed in Table 5.1.

Pb/MWNT			
Catalyst Name	Target Pb wt%	Decomposition temp. (°C)	Decomposition time (hrs)
(a)	1	350	2
(b)	10	300	2
(c)	35.31	350	3
(d)	25	290	12
Pb-25	25	350	1
Pb-35	35	350	1
Pb-50	50	350	1

Table 5.1: Table of decomposition conditions used for the syntheses of Pb/MWNT

Catalysts (a)-(d) (Table 5.1) were the initial catalysts tested before the decomposition conditions were standardised to 350 °C and 1 hrwith target weight loadings of 25 wt%, 35 wt%, and 50 wt%. These standardised samples are named Pb-25, Pb-35, and Pb-50 corresponding to their target weight loadings of 25 wt%, 35 wt%, 50 wt% of Pb metal respectively (Table 5.1). These conditions were chosen due to these standard synthesis conditions being used for the testing of Bi/MWNT and In/MWNT which were completed after the testing of (a)-(d) due to these catalysts poor electrocatalytic performance. Therefore for accurate comparison, Pb/MWNT was revisited and resynthesised using these standard conditions.

Therefore, the synthesis for Pb-25, Pb-35, and Pb-50 is as follows: To MWNTs (250 mg) was added a solution of $PbNO_3$ (25 , 35, and 50 wt% of Pb w.r.t MWNT) in H_2O (6 mL). This mixture was subsequently stirred with a glass rod until the resulting "paste" was homogeneous without any large lumps, and then was dried for 24 hrs at 60 °C to produce $PbNO_3$/MWNT in a powder form. This powder was then transferred to a furnace and decomposed at 350 °C for 1 hrwith a 10 °C min^{-1} ramp time. After decomposition, a powder of Pb/MWNT is produced with a hypothetical weight loading of Pb on MWNTs of 25 wt%, 35 wt%, and 50 wt%.

5.2.2 Characterisation

5.2.2.1 Electron Microscopy

To gain information on the structure of the Pb on the MWNT, TEM was utilised to image each of the Pb/MWNT samples. Important to note is the use of out of focus images throughout the TEM images, as due to the small size of the Pb nanoparticles throughout the catalysts, the point of focus is very small for the nanoparticles. These nanoparticles will appear invisible to the beam as a result of this, due to TEM images typically being focussed with respect to the MWNT graphitic wall.

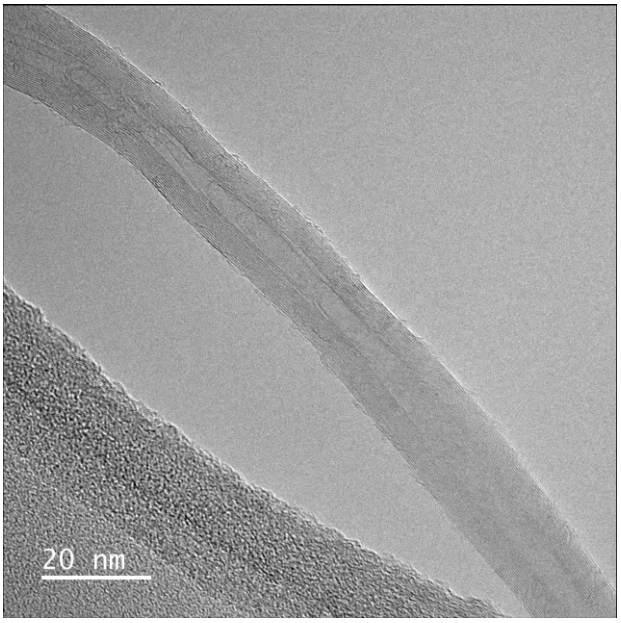


Figure 5.3: HR-TEM image of catalyst (a).

Catalyst (a) was imaged first via TEM (Fig. 5.3), and it is immediately evident from microscopy that 1 wt% loading of Pb is not high enough for adequate loading, as the catalyst appears almost identical to bare MWNT with no visible metal nanoparticles on the surface of the MWNT.

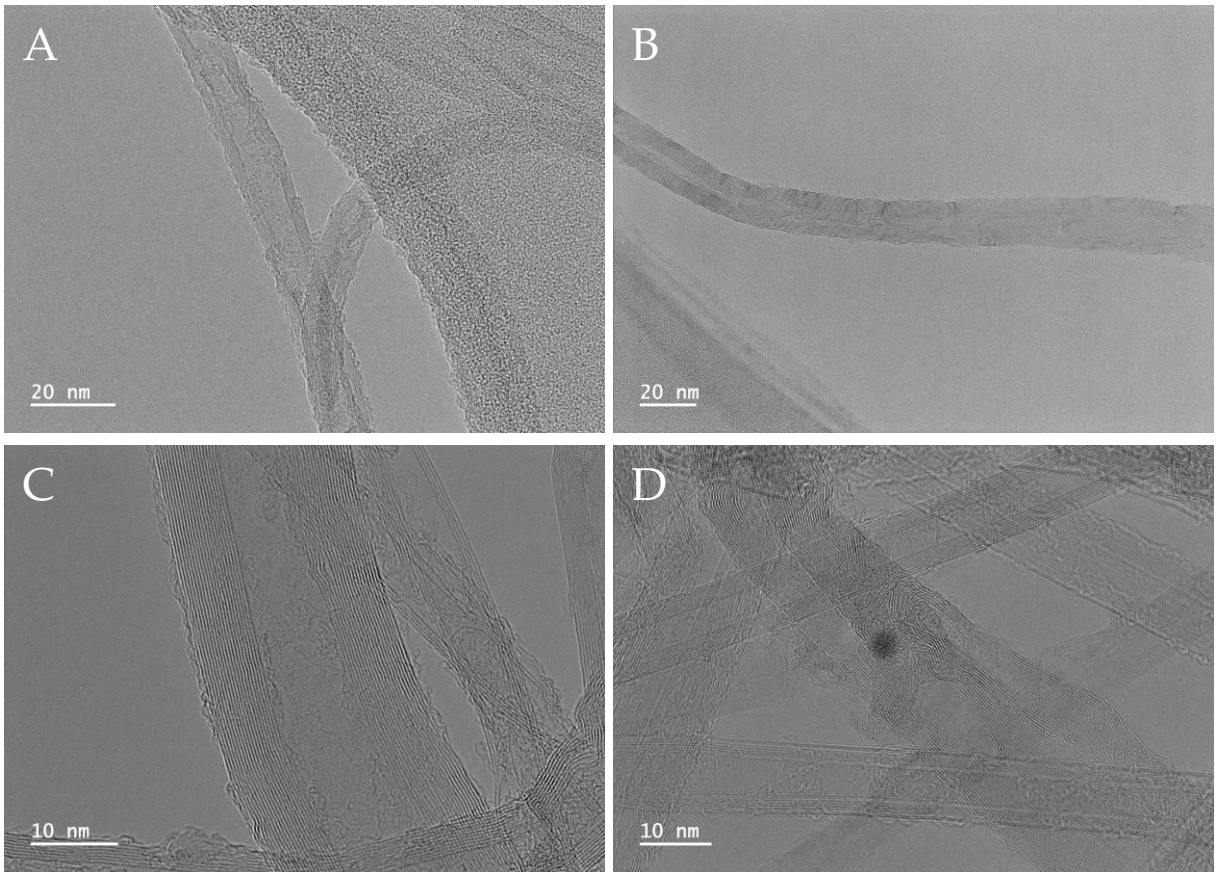


Figure 5.4: (A) TEM image of catalyst (b) out of focus with respect to the MWNT to highlight Pb nanoparticles on the MWNT; (B) TEM of (b) showing dark spots of Pb on the surface and internal deformation on the inner cavity of the MWNT; (C) zoomed TEM image of (b); (D) TEM image of (b) with a Pb metal nanocluster causing nanotube deformation

When increasing the Pb weight loading to 10 wt% in (b), TEM images begin showing small dark spots on the MWNT surface (Figs. 5.4A to 5.4C). It can also be observed that the thermal decomposition of $PbNO_3$ begins to also catalyse nanotube deformation/destruction, especially around larger Pb nanoclusters (Figs. 5.4B and 5.4D). This nanotube deformation continues to be present in the Pb/MWNT catalysts, and occurs at all decomposition temperatures used (Table 5.1).

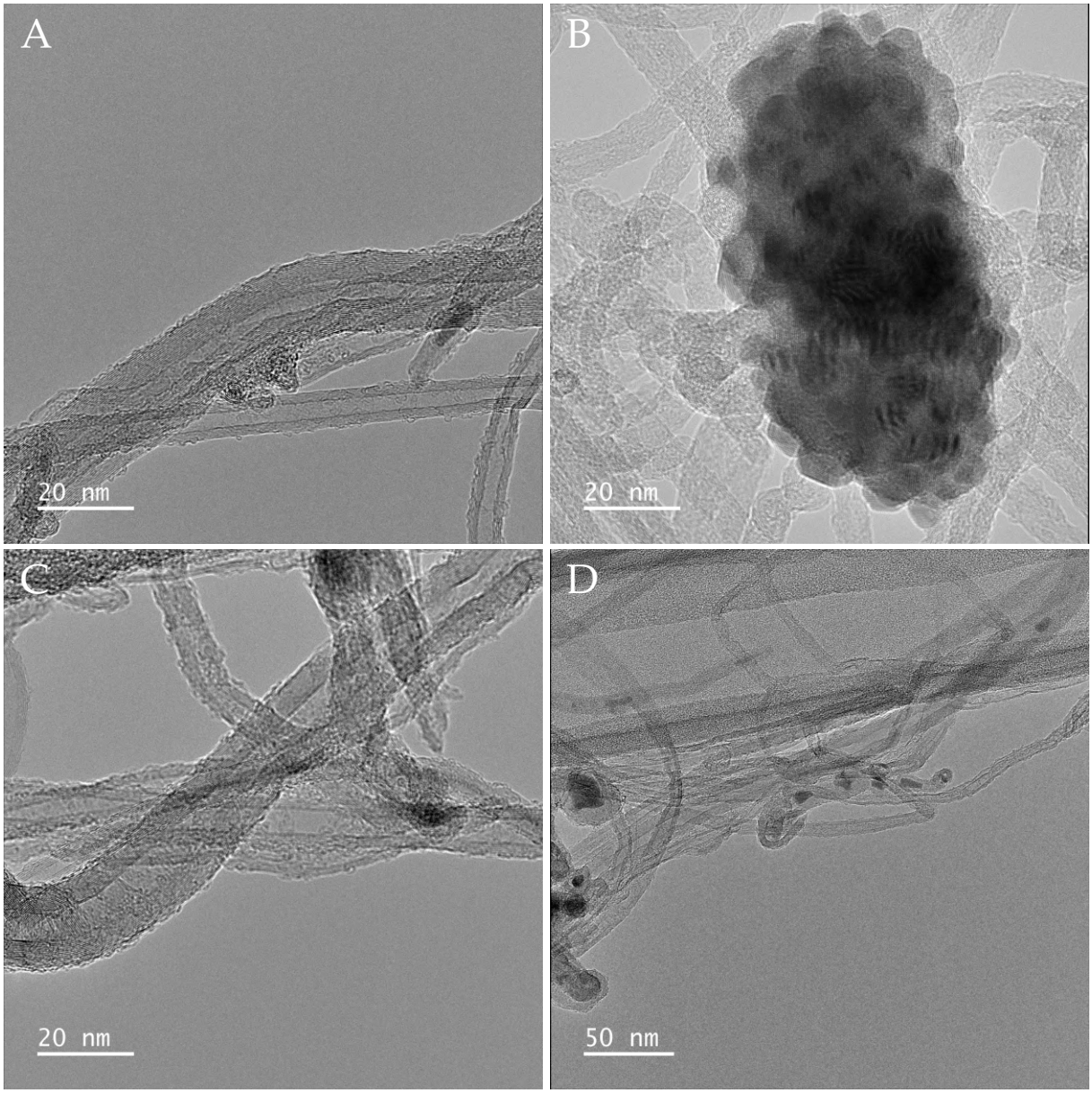


Figure 5.5: (A) TEM image of catalyst (c) showing Pb nanoparticles on the MWNT surface as dark spots in the tube; (B) TEM of (c) showing a large Pb aggregation at a large nanotube crossing site; (C) zoomed TEM image of (c) out of focus with respect to the MWNT to better illustrate Pb nanoparticles; (D) TEM image of (c) zoomed out to show Pb nanoparticle coverage and Pb aggregation sites.

Catalyst (c) has a Pb metal weight much higher than (a) or (b) at 35.31 wt% (Table 5.1), and is the first catalyst that begins to show clear Pb nanoparticle formation on the surface of the MWNT, as seen in Fig. 5.5 as small dark spots on the MWNT wall edge, or observed inside the wall in the images. Nanoparticles observed inbetween graphitic wall layers in TEM are not inserted into the lattice, rather this appearance is a result of the projection of a three dimensional structure on a two dimensional plane, meaning these nanoparticles are above or below where they are seen. The size of the Pb nanoparticles measured in

Fig. 5.5C range from 0.404 nm to 0.77 nm, strongly suggesting single or dual atom Pb sites, given the Pb van der Waal's radius of 0.202 nm.[53] The size of the nanoparticles additionally suggest that the Pb nanoparticle sites would be in the form of Pb^0 or Pb^{2+}.

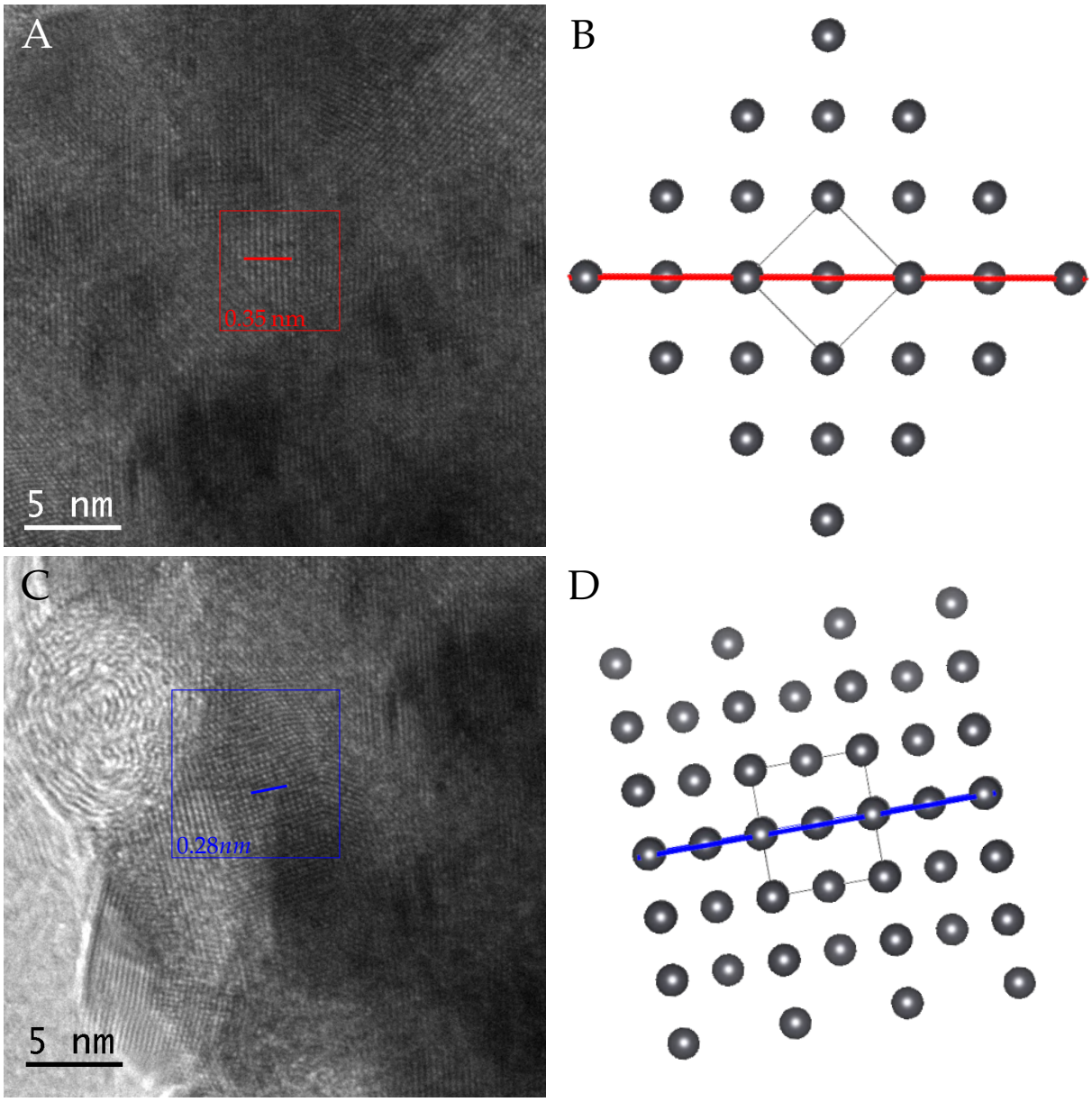


Figure 5.6: (A) Zoomed TEM image of catalyst (c) from figure Fig. 5.5B with crystal domain area outlined in a red box, the area measured for PbO_2 (1 1 0) d-spacing given by a red line, and the measured d-spacing value annotated on the bottom left of the domain area; (B) Simulated crystal structure of PbO_2 with the (1 1 0) plane given in red. Crystal structure has been rotated to match the domain measured in Fig. 5.6A, oxygen atoms have been omitted for clarity; (C) Zoomed TEM image of catalyst (c) from figure Fig. 5.5B with crystal domain area outlined in a blue box, the area measured for PbO_2 (1 0 1) d-spacing given by a blue line, and the measured d-spacing value annotated on the bottom left of the domain area; (D) Simulated crystal structure of PbO_2 with the (1 0 1) plane given in blue. Crystal structure has been rotated to match the domain measured in Fig. 5.6C, oxygen atoms have been omitted for clarity

Notably in Fig. 5.5, large PbO_2 aggregations with multiple crystal domains were observed with diameters of $\sim$ 100 nm. These aggregations, whilst technically nanoparticles by

IUPAC definition,[54] will be referred to as aggregations for clarity when comparing to the much smaller single/dual atom nanoparticles present. The aggregation was confirmed as PbO_2 via the observed d-spacing values in TEM of multiple crystal domains near perfectly matching literature for PbO_2 crystal structures. Within the Pb aggregation, d-spacings of of 0.35 nm and 0.28 nm were measured from two distinct crystal domains within the aggregate, and these values show an almost perfect match to the (1 1 0) and (1 0 1) PbO_2 planes.[55] Additionally in the (1 0 1) plane in TEM (Fig. 5.6C) distinct Pb atoms within the crystal structure can be resolved, and observed is the same face-centered cubic crystal structure as seen in the simulated (1 0 1) PbO_2 crystal plane, which makes it evident that the aggregate is composed of PbO_2.

As seen in TGA analysis Section 5.2.2.2, the thermal decomposition window of the MWNT in presence of $PbNO_3$ is lowered to be coincident with the $PbNO_3$ precursor. This results in some nanotube decomposition being unavoidable during thermal decomposition, with this being the most evident in the case of catalyst (d) (Fig. 5.7).

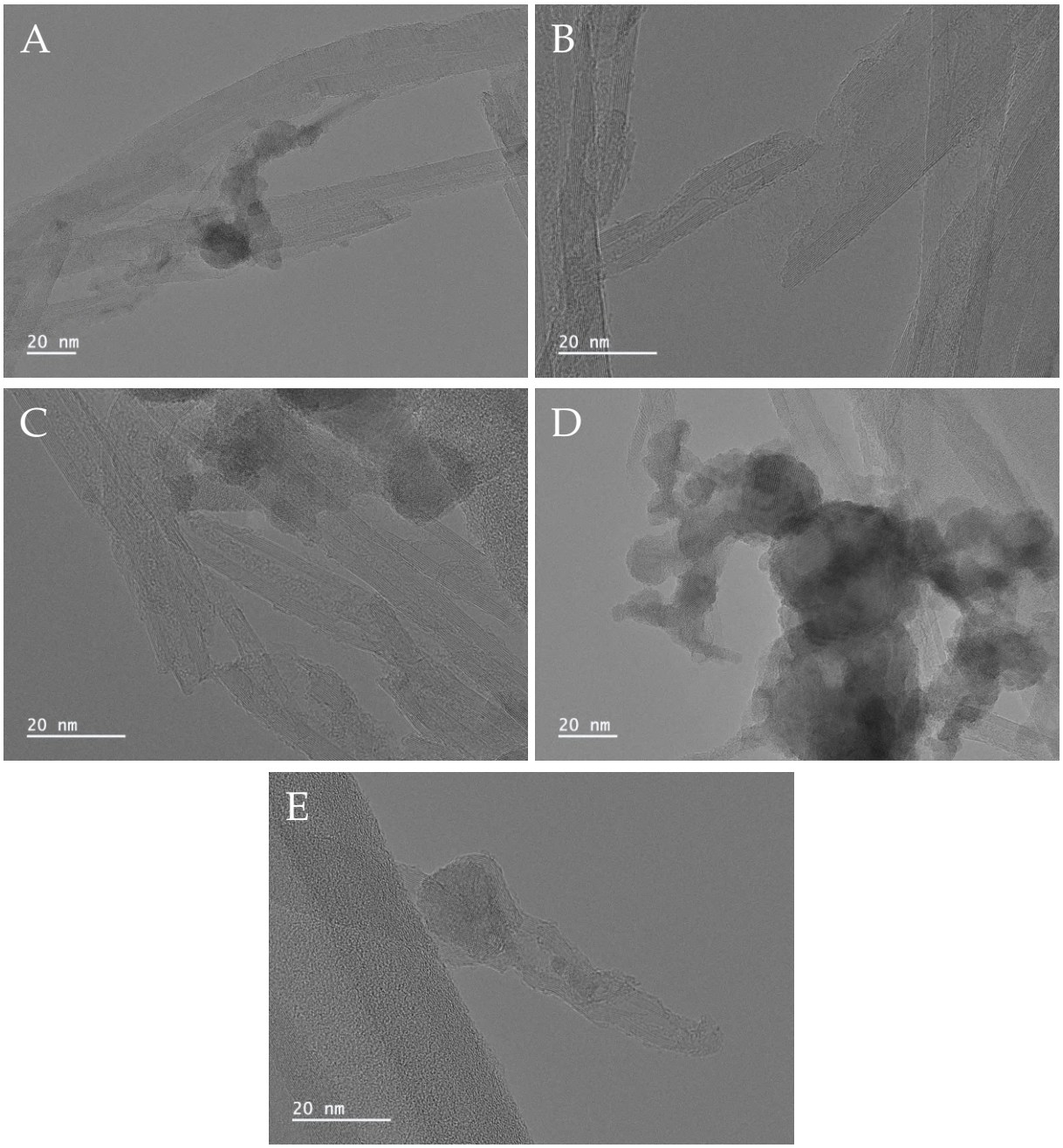


Figure 5.7: (A) TEM image of catalyst (d) showing large Pb aggregations and Pb nanoparticles on the MWNT surface as dark spots on the tube; (B) TEM of (c) showing MWNT degradation from $PbNO_3$ catalysed thermal decomposition with some Pb embedded into the MWNT tip; (C) Further TEM image MWNT degradation from $PbNO_3$ catalysed thermal decomposition with large Pb aggregation visible at the top of the image and Pb nanoparticles visible on the MWNT edge; (D) Large PbO_2 aggregate with degraded MWNT feeding into the aggregate; (E) MWNT tip with Pb nanoparticles visible at the tip and a large PbO_2 aggregate that has embedded into the tube structure. Also visible is another small MWNT section that is seen broken off and merged into the MWNT tip.

The TEM images of (d) (Fig. 5.7) highlight the impact the length of thermal decomposition

on the nanostructure of the Pb/MWNT. In the images, the MWNTs in catalyst (d) are seen to be clearly decomposed and broken, with large tears and broken ends being visible Figs. 5.7B and 5.7C. Additionally, the longer decomposition time appears to promote the growth of large PbO_2 aggregates, which can also be seen to have "chewed" through MWNT sections, as is the case for Figs. 5.7D and 5.7E, where small nanotube segments are seen to be close proximity/incorporated into the aggregates, and in the case of Fig. 5.7E, have eaten their way into the nanotube internal cavity, gaining a carbon shell from the MWNT wall.

From the TEM images of catalysts (a)-(d), consistent synthesis conditions were chosen that would ensure the highest amount of Pb single atom/dual atom sites, and also would minimise destruction of the MWNTs. Catalyst (c) had the highest visible coverage of Pb nanoparticles, so 350 °C was taken forward, and as decomposition time was shown to have the greatest impact on aggregation formation, the decomposition time was set to 1 hr to ensure complete decomposition whilst minimising nanotube degradation. With the synthesis conditions set to be constant, catalysts Pb-25, Pb-35, and Pb-50 were synthesised with varying weight loadings of Pb, at 25 wt%, 35 wt%, and 50 wt% of Pb metal to MWNT respectively.

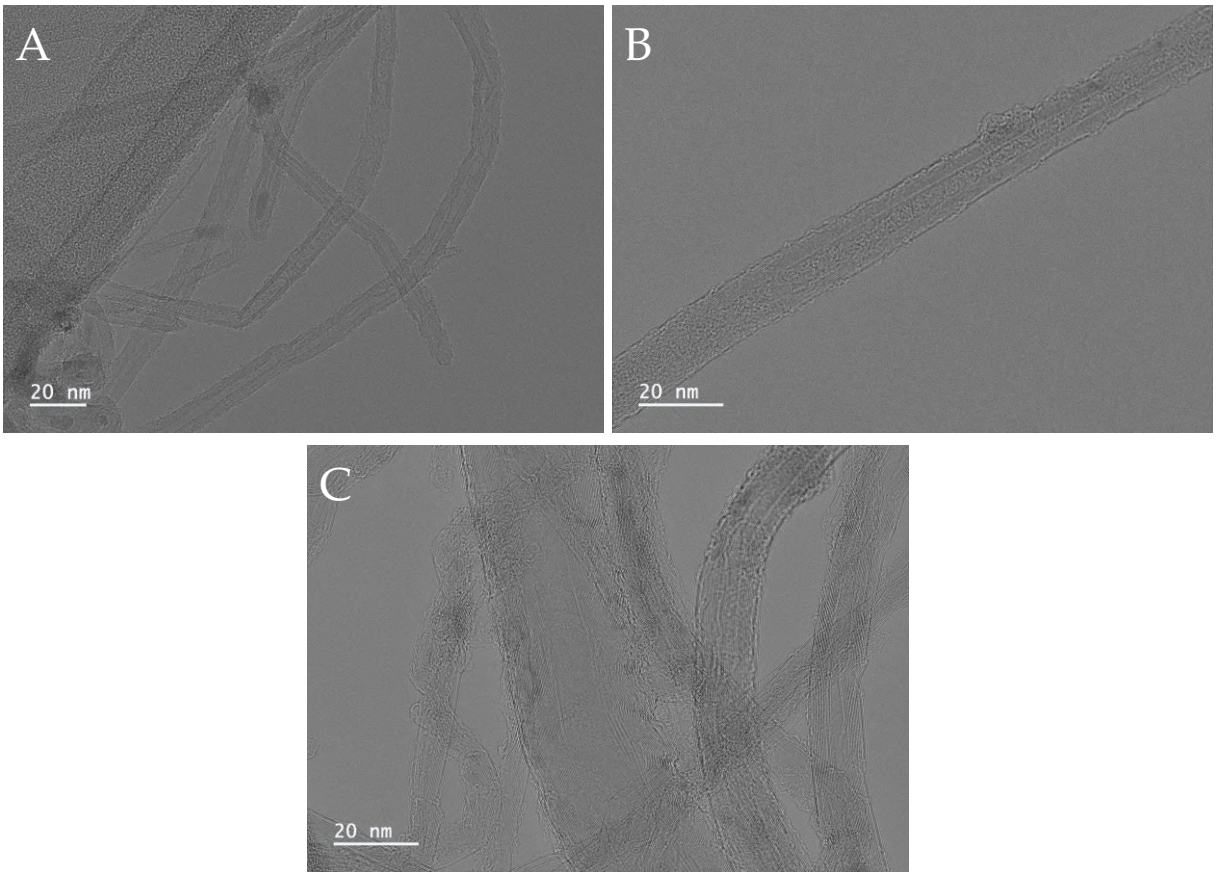


Figure 5.8: (A) TEM image of Pb-25 showing Pb nanoparticles on the MWNT surface as dark spots in the tube; (B) TEM image taken out of focus of a MWNT in Pb-25 showing Pb nanoparticles on the MWNT surface as dark spots in the tube; (C) TEM image taken out of focus of multiple MWNTs in Pb-25 showing Pb nanoparticles on the MWNT surface as dark spots in the tube.

The TEM images of Pb-25 (Fig. 5.8) show an increase of Pb nanoparticles, with much smaller and less prevalent aggregates, showing the efficacy of the modified synthesis for specifically targeting nanoparticle formation.

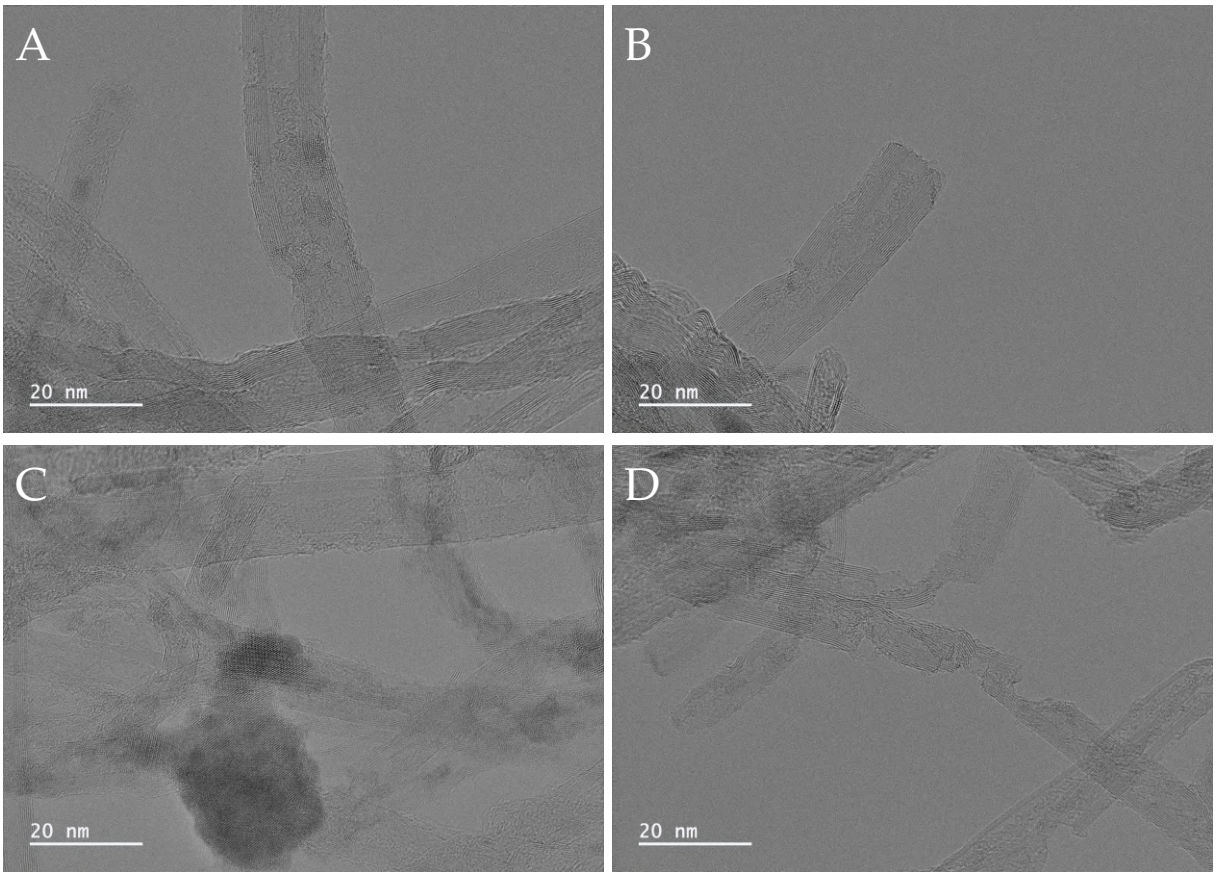


Figure 5.9: (A) TEM image of Pb-35 showing Pb crystalline features embedded into the surface of a damaged MWNT; (B) TEM image of Pb-35 showing Pb nanoparticles on the MWNT surface as dark spots on the tube. Additionally it is seen that the typical rounded end of the tube has been decomposed into a flat opening; (C) TEM image of Pb-35 showing Pb aggregates on the surface MWNT. Additionally the tube at the top of the image can be seen with wall damage; (D) Damaged MWNT with small nanoclusters of Pb embedded into the nanotube and also on the outside of the nanotube wall.

Increasing the Pb loading to 35 wt% in Pb-35 seems to dramatically increase the MWNT damage compared to Pb-25, despite the shorter decomposition time (Fig. 5.9). From the TEM images of Pb-35, it is evident that $PbNO_3$ is too strong an oxidiser to be compatible with the thermal decomposition synthesis used for the p-block metal catalysts (Section 5.2.1). It can be seen in Figs. 5.9A and 5.9D that Pb nanoparticles seem to be co-located with areas of MWNT damage, with the Pb nanoparticles in the case of Fig. 5.9A seemingly eating away the MWNT wall, embedding themselves in the created wall defects.

The formation of defects in the MWNT were not observed under the electron beam when imaging, however it is possible that it is not the $PbNO_3$ oxidising the nanotube, but instead resulting Pb metal when heated causing defect formation, similar to the defect formation observed in Ni and Os encapsulated in MWNTs by Skowrown *et al*.[56]

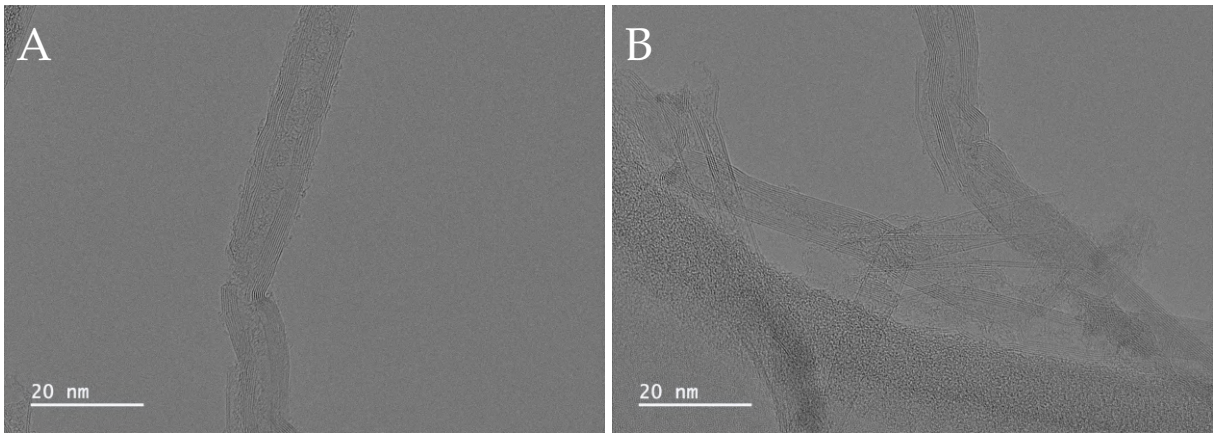


Figure 5.10: (A) TEM image of Pb-50 showing scattered Pb nanoparticles on the MWNT, a prominent wall defect can be observed in the image; (B) Multiple MWNTs with large defects on the nanotube ends which has formed a large crossing of short nanotubes with clusters of Pb nanoparticles at the crossing point

Further increasing the Pb weight loading to 50 wt% in Pb-50 (Fig. 5.10) expectedly increases defect formation, with multiple nanotubes being observed to have been "chewed" up from the ends by Pb nanoparticles and clusters. Additionally, single/dual atom Pb sites seem to be largely absent, with only multi-atom clusters present at defect sites.

Lastly, it is pertinent to image Pb/MWNT pre-decomposition in the form of Lead Nitrate on Multi-Walled Carbon Nanotubes ($PbNO_3$/MWNT), to help provide insight on how the observed Pb structures (single atoms/nanoclusters/aggregates) arise, and whether the Pb are restructuring under temperature or are largely forming structures based on their initial deposition on the wall.

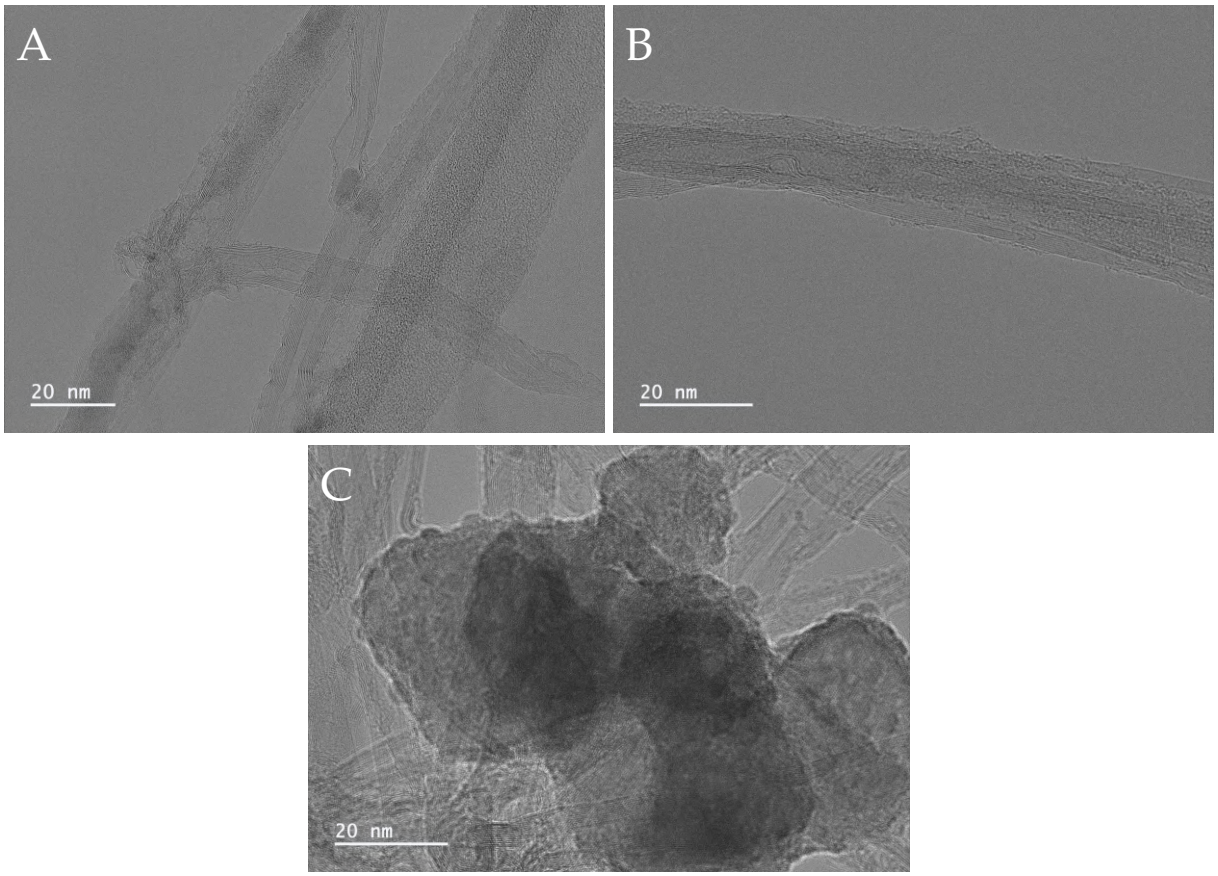


Figure 5.11: (A)TEM image of Pb nanoclusters along the MWNT wall; (B) TEM image of Pb single/dual atom nanoparticles along MWNT wall ; (C) TEM image of a large $PbNO_3$ aggregation.

As seen in Fig. 5.11, $PbNO_3$ forms both single/dual atoms and aggregations on the MWNT surface prior to thermal decomposition, but the multi-atom nanoclusters appear largely absent. Single atoms can be seen in Fig. 5.11B in similar fashion to prior catalysts, whilst aggregations of $PbNO_3$ can be observed in Figs. 5.11A and 5.11C, in the former case forming a long aggregate along the length of the nanotube, whilst in the latter, forming a large aggregate spanning multiple nanotubes. This implies the large aggregation and single/dual atom sites are largely present prior to the thermal decomposition, but the multi-atom nanoclusters and MWNT defects appear to be a result of the thermal decomposition, likely from the single atom sites forming defects, migrating, and aggregating into multi-atom clusters.

Overall, it appears that Pb does not produce catalytically desirable nanostructures (single atom sites) via the metal nitrate synthesis method over catalytically undesireable structures (aggregates), likely resulting from the high reactivity of Pb metal and $PbNO_3$ with carbon.[57]

5.2.2.2 Other characterisation

For weight loading determination, TGA of Pb-25, Pb-35, and Pb-50 was conducted to calculate the actual metal loading and to observe changes in the decomposition temperature depending on metal loading (Fig. 5.12).

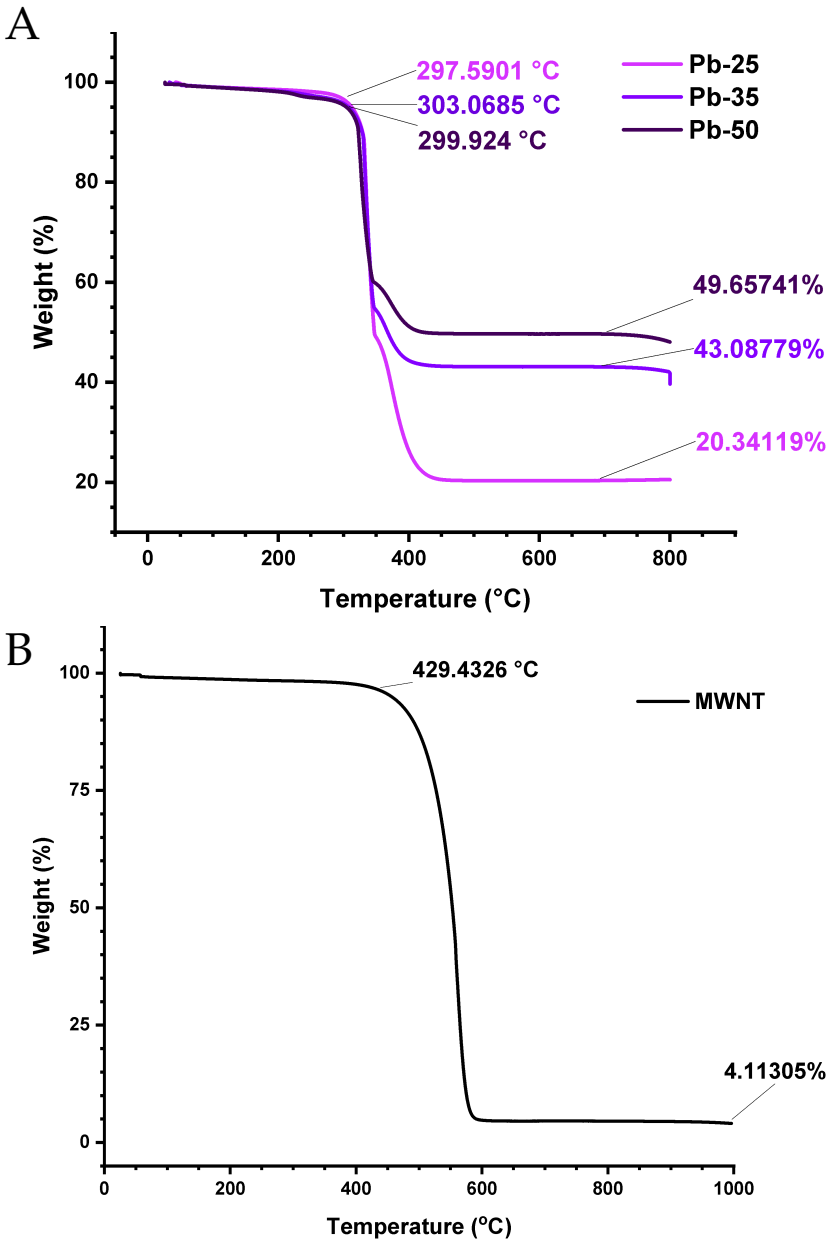


Figure 5.12: (A) TGA plot of Pb-25, Pb-35, and Pb-50 in air with initial decomposition temperature and final weight % labelled; (B) TGA plot of MWNT in air with initial decomposition temperature and final weight % labelled.

As seen in Fig. 5.12, the decomposition temperature of Pb/MWNT is $\sim$ 100°C earlier than in bare MWNT, which is to be expected due to the catalytic effect of metal oxides on thermal decomposition.[58]

The residual weight in the bare MWNTs of 4.11% (Fig. 5.12B) results from the nanotube internal catalyst from the nanotube synthesis,[59] so taking the difference between the weight %s of each Pb/MWNT catalyst and the MWNT the weight loading of PbO on the surface of the MWNT can be attained, and assuming the oxide is PbO, the ratio of atomic mass of Pb to O can be used to determine the real weight loading of Pb as illustrated by Section 5.2.2.2.

$$\text{PbO Wt\%} = \text{Wt\%}_{\text{Pb/MWNT}} - \text{Wt\%}_{\text{MWNT}} \tag{5.1}$$

$$\tag{5.2}$$

$$\text{Pb Wt\%} \quad = \text{PbO}_{\text{Wt\%}} \times \frac{x \cdot M_{r\text{Pb}}}{M_{r\text{Pb}_x\text{O}}} \tag{5.3}$$

Thus, the PbO weight loadings of Pb-25, Pb-35, and Pb-50 to 2 d.p. are calculated to be 16.23%, 38.97%, and 45.54% respectively, and the Pb weight loadings are 15.07%, 36.18%, and 42.27% respectively.

The weight loading of Pb being lower than initially predicted is likely due to a combination of transfer losses from drying to the crucible and additional mass error from hydration of the $PbNO3_2$

5.2.3 Electrochemistry

5.2.3.1 Voltammetry

To evaluate the electrochemical characteristics and catalytic performance of the three Pb/MWNT catalysts: Pb-25, Pb-35, and Pb-50, LSV Fig. 5.13 and CV were were utilised.

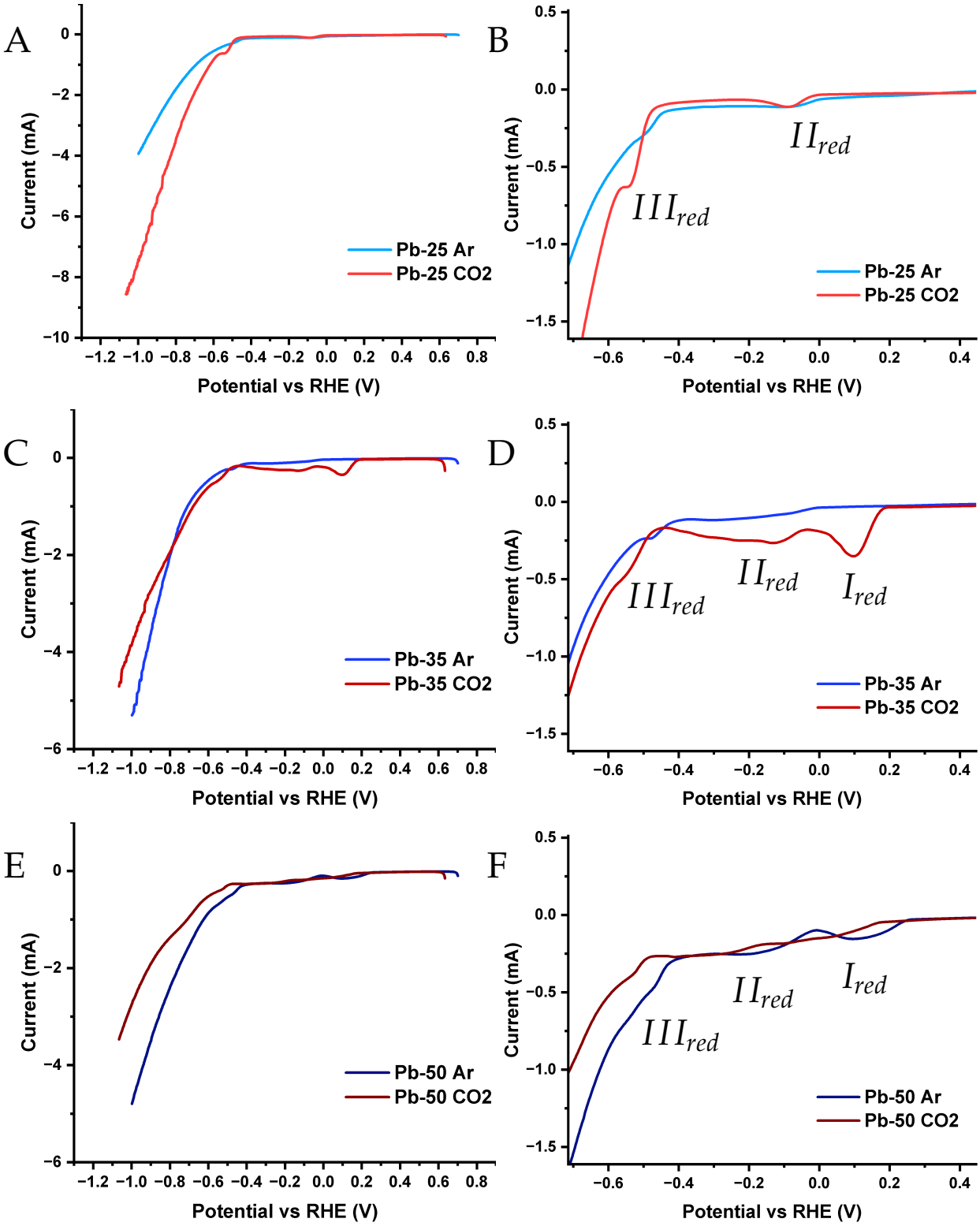


Figure 5.13: (A) LSV of Pb-25 using an RDE in Argon and CO_2 saturated 0.5 M $KHCO_3$ at 0.005 V s^{-1} at a rotation rate of 1600 rpm; (B) LSV from Fig. 5.13A with reduction peaks labelled, voltammogram has been zoomed into the non CO_2RR region for clarity; (C) LSV of Pb-35 using an RDE in Argon and CO_2 saturated 0.5 M $KHCO_3$ at 0.005 V s^{-1} at a rotation rate of 1600 rpm; (D) LSV from Fig. 5.13C with reduction peaks labelled, voltammogram has been zoomed into the non CO_2RR region for clarity; (E) LSV of Pb-50 using an RDE in Argon and CO_2 saturated 0.5 M $KHCO_3$ at 0.005 V s^{-1} at a rotation rate of 1600 rpm; (F) LSV from Fig. 5.13E with reduction peaks labelled, voltammogram has been zoomed into the non CO_2RR region for clarity

From the LSV experiments in Fig. 5.13, it is immediately evident that the weight loading directly impacts the electrochemical characteristics of the catalyst, with Pb-25 showing two reduction peaks: II_{red} and III_{red} (Figs. 5.13A and 5.13B), however Pb-35 and Pb-50 show three reduction peaks: I_{red}, II_{red} and III_{red}. This can be rationalised by the structural differences seen in the TEM images of Pb-25, Pb-35, and Pb-50 (Figs. 5.8 to 5.10), with Pb-25 having mostly single/dual atom sites, whilst Pb-35 and Pb-50 have a much larger proportion of aggregates and nanoclusters. It is possible that the absence of I_{red} in the LSV of Pb-25 is related to the primarily single atom sites that comprise Pb-25, which can further be related to the fact that single atom sites will be comprised of either Pb^{2+} or Pb^{+}, without the possibility of Pb_3O_4 structures due to the single atom nature of the sites. This implies that the I_{red} peak at $\sim$ 0.15 V vs RHE can be attributed to the presence of Pb_3O_4, a fact supported by El Aal *et al*.[60] Peak I_{red} is reported to be a composite peak, comprised of firstly the $3\,Pb^{4+}/[Pb^{2+}]_2[Pb^{4+}]$ couple, followed by the Pb^{4+}/Pb^{2+} redox couple, leaving primarily PbO.[61]

The II_{red} peak in the LSVs of Pb-35 and Pb-50 (Figs. 5.13D and 5.13F) is much broader than in Pb-25, which can be explained by the fact that the reduction of Pb^{4+}/Pb^{2+} requires OH^{-}, limiting the reducible Pb species to those on the surface of aggregates that are in contact with the aqueous electrolyte. The multi-peaked II_{red} in Pb-35 (Fig. 5.13D) and the broad, continuous II_{red} peak in Pb-50 (Fig. 5.13F) is explained by the fact that a the peak shape in voltammetry arises from the increasing and decreasing rates of a redox reaction on the electrode, so this continual reduction occurring in the catalysts with aggregates is explained by Pb_3O_4 being reduced from the outside in at a steady rate as more Pb_3O_4 sites come in contact with the electrolyte throughout the II_{red} peak.

In regards to the III_{red} peak at ~ -0.55 V vs RHE, it is pertinent to note that in argon saturated electrolyte the peak is much less prominent than in CO_2 for all Pb/MWNT loadings (Fig. 5.13), directly implying that this reduction peak is related to the reduction of a $PbCO_3$ species. This is directly supported by both El Aal *et al*[60] and Xing *et al*,[5] The former evidencing the formation of $PbCO_3$ on the electrode surface in carbonate electrolyte,[60] and the latter evidencing a similar III_{red} peak only in CO_2 saturated electrolyte positioned at catalytic onset potential, albeit shifted by $\sim$ 0.2 V.[5]

With the insights from literature, TEM images of the Pb catalysts, and the previously discussed LSVs it is possible to plausibly assign the reduction peaks in Fig. 5.13. These peak assignments are given in Eqs. (5.4) to (5.7).

$$I_{red}^{Step\,1} : 3\,PbO_2 + 2H_2O + 4e^- \longrightarrow Pb_3O_4 + 4OH^- \qquad V = 0.15\,\text{vs RHE} \quad (5.4)$$

$$I_{red}^{Step\,2} : 5Pb_3O_4 + 9\,H_2O + 10\,e^- \longrightarrow 15PbO + 10\,OH^- \qquad V = 0.15\,\text{vs RHE} \quad (5.5)$$

$$II_{red} : PbO + 2e^- + 2H^+ \longrightarrow Pb + H2O \qquad V = -0.05\,\text{vs RHE} \quad (5.6)$$

$$III_{red} : PbCO_3 + 2\,e^- \longrightarrow Pb + {CO_3}^{2-} \qquad V = -0.80\,\text{vs RHE} \quad (5.7)$$

With the reduction peaks identified from the LSV experiments, looking at the CV experiments conducted after the LSV for comparison (Fig. 5.14).

The CV in Fig. 5.14 reveal that peak I_{red} and any potential corresponding oxidation peak are completely absent in all catalyst weight loading and electrolyte saturations. This indicates that the reduction towards PbO is complete and fully irreversible. This peak loss is to be expected due to the I_{red} being multi-step, and likely involving a change in the Pb structure making the formation of Pb_3O_4 disfavoured.

Additionally, the CVs show that in CO_2 saturated electrolyte, there is a single oxidation peak in II_{ox} centered at 0.2 V vs RHE, whilst in Ar saturated electrolyte for all cases, the III_{ox} peak splits into two peaks, II_{ox} and III_{ox}. Peak III_{ox} is likely associated with formation of $PbCO_3$ from Pb, which is then further oxidised to PbO in II_{ox}, as evidenced by El Aal *et al*.[60] This also explains the presence of III_{red} in both CO_2 and Ar saturated electrolyte, due to the oxidative potential sweep forcing its formation in both electrolytes rather than just surface bound Pb^{2+} reacting with the bicarbonate electrolyte. Additionally, the formation of $PbCO_3$ explains the single III_{ox} peak in CO_2 saturated electrolyte and the much smaller II_{ox} peak by comparison in Ar, as the increase in CO_2 concentration is dramatically increasing the carbonate formed in the oxidative sweep, in the case of CO_2 saturation completely overtaking the oxidation with little to no PbO formation, whilst in Ar some PbO formation can still occur. The oxidation to PbO therefore is rate limited and very slow, explaining why the primarily single atom dominated Pb-25 presents a much larger II_{ox} peak compared to the other catalysts where aggregates dominate.

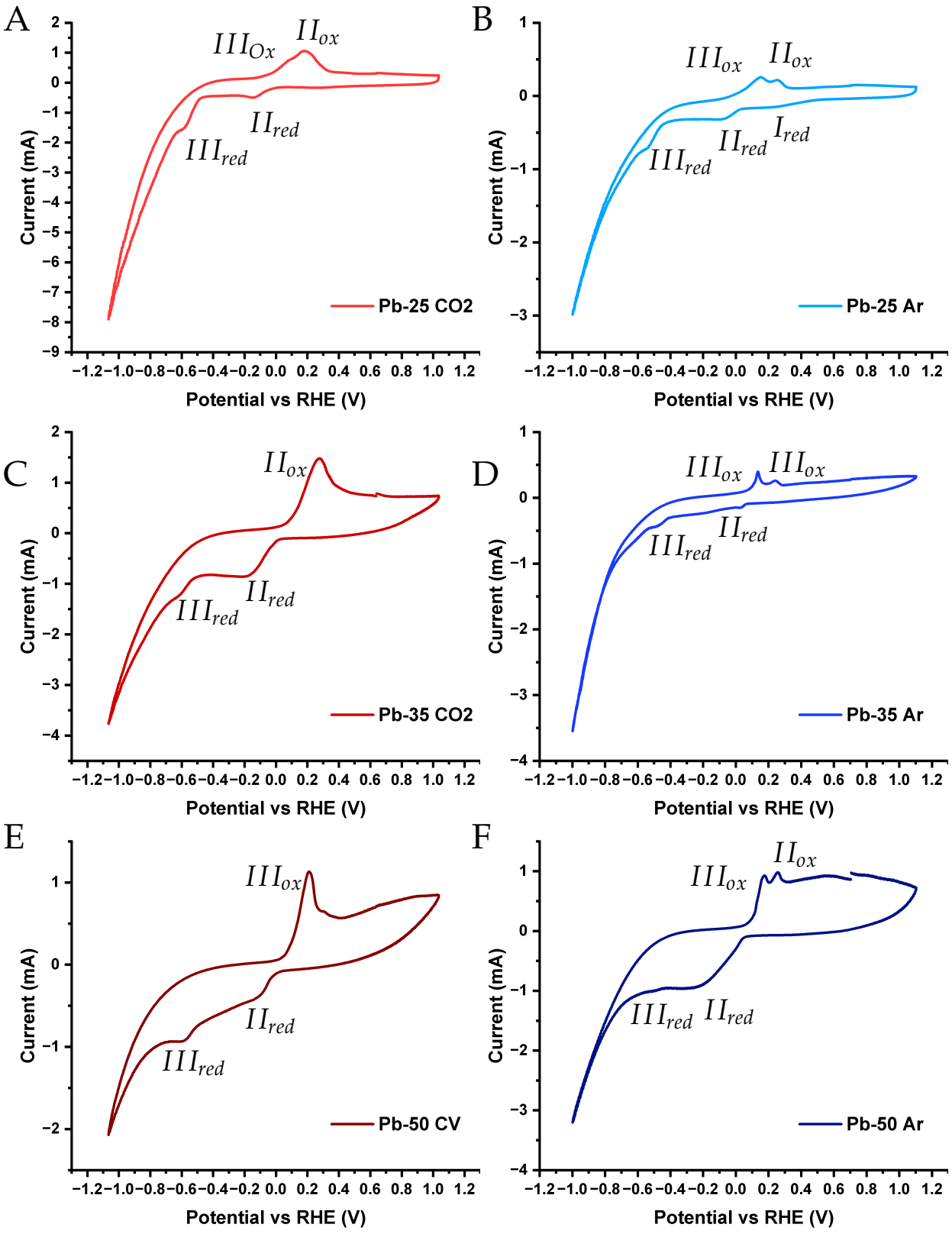


Figure 5.14: (A) CV of Pb-25 using a RDE in CO_2 saturated 0.5 M $KHCO_3$ at 0.05 V s^{-1} at a rotation rate of 1600 rpm with redox peaks labelled; (B) CV of Pb-25 using a RDE in Ar saturated 0.5 M $KHCO_3$ at 0.05 V s^{-1} at a rotation rate of 1600 rpm with redox peaks labelled; (C) CV of Pb-35 using a RDE in CO_2 saturated 0.5 M $KHCO_3$ at 0.05 V s^{-1} at a rotation rate of 1600 rpm with redox peaks labelled; (D) CV of Pb-35 using a RDE in Ar saturated 0.5 M $KHCO_3$ at 0.05 V s^{-1} at a rotation rate of 1600 rpm with redox peaks labelled; (E) CV of Pb-50 using a RDE in CO_2 saturated 0.5 M $KHCO_3$ at 0.05 V s^{-1} at a rotation rate of 1600 rpm with redox peaks labelled; (F) CV of Pb-50 using a RDE in Ar saturated 0.5 M $KHCO_3$ at 0.05 V s^{-1} at a rotation rate of 1600 rpm with redox peaks labelled.

5.2.4 Electrocatalysis

To test the catalytic activity of Pb/MWNT, a range of potentials were tested for CO_2 reduction to produce formate for one hour: -0.85, -0.95, -1.05, -1.15, and -1.35 V vs RHE. Out of these potentials, -1.05 V vs RHE showed the highest FE towards formate, and this potential was used as the potential that all Pb/MWNT catalysts were tested at. Despite the high current densities observed in chronoamperometry for the Pb/MWNT catalysts, particularly in the case of Pb-35 (Fig. 5.15), very little formate production was observed, with the formate FEs for Pb-25, Pb-35, Pb-50 being 0.67%, 0.25%, and 0.51% respectively with no other liquid products observed. From GC results, the remaining FE is attributed to H_2, as no other gas products were observed for any of the Pb/MWNT catalysts.

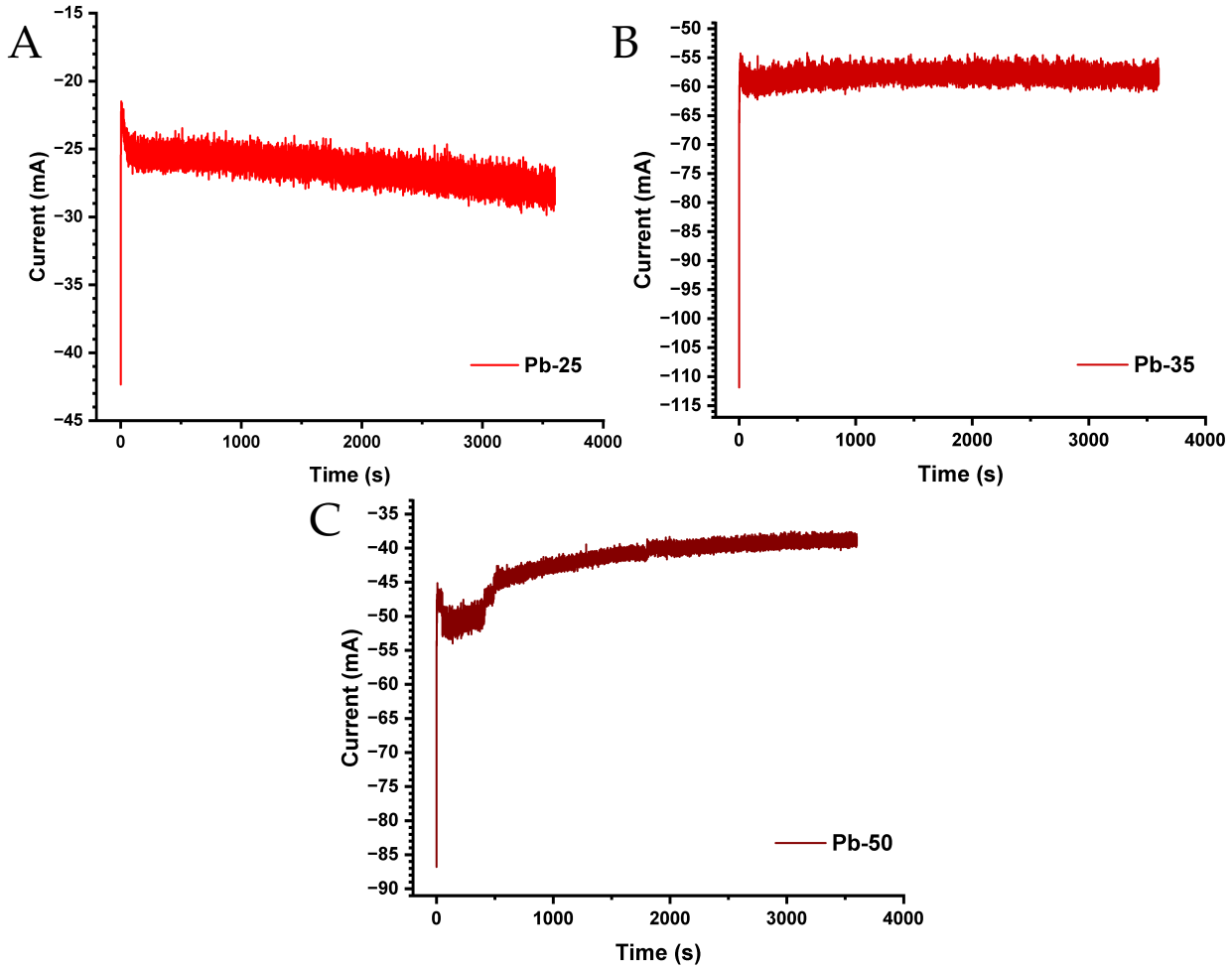


Figure 5.15: (A) Chronoamperometry of Pb-25 dropcasted on 5% PTFE carbon paper in a $1x1\ cm^2$ area at -1.7 V vs RHE in 0.5 M $KHCO_3$ with constant CO_2 gas flow into the electrolyte; (B) Chronoamperometry of Pb-35 dropcasted on 5% PTFE carbon paper in a $1x1\ cm^2$ area at -1.7 V vs RHE in 0.5 M $KHCO_3$ with constant CO_2 gas flow into the electrolyte; (C) Chronoamperometry of Pb-50 dropcasted on 5% PTFE carbon paper in a $1x1\ cm^2$ area at -1.7 V vs RHE in 0.5 M $KHCO_3$ with constant CO_2 gas flow into the electrolyte.

The electrocatalysis results for the Pb/MWNT catalysts was anomalous given Pb in literature showing to be a highly selective catalyst towards formate,[5] and the reason for this is unclear. It can be speculated that the Pb catalyst is not in the active form during electrocatalysis, and it is likely that this deactivated form is $KHCO_3$, due to the nanoscale nature of the single atom sites and aggregates when compared to literature[5,12] likely causing leaching of the Pb from the MWNT, causing catalytic inactivity.

5.3 Bi/MWNTs

5.3.1 Synthesis

The Bi/MWNT catalyst was prepared in similar fashion to Pb/MWNT, however as the conditions as of the synthesis of Bi/MWNT were standardised at this time, only three catalysts were synthesised: Bi-25, Bi-35, and Bi-50 with 25%, 35%, and 50% weight relative to the MWNT support. The synthesis of Bi/MWNT is as follows: To MWNTs (250 mg) was added a solution of $Bi(NO_3)_3 \cdot 5\,H_2O$ (25, 35, and 50 wt% Bi w.r.t MWNT) in H_2O (6 mL). This mixture was subsequently stirred with a glass rod until the resulting "paste" was homogeneous without any large lumps, and then was dried for 24 hrs at 60 °C to produce $Bi(NO_3)_3 \cdot 5\,H_2O$/MWNT in a powder form. This powder was then transferred to a furnace and decomposed at 350 °C for 1 hrwith a 10 °C min^{-1} ramp time. After decomposition, a powder of Bi/MWNT is produced with a hypothetical weight loading of Bi on MWNTs of 25 wt%, 35 wt%, and 50 wt%.

5.3.2 Characterisation

5.3.2.1 Electron Microscopy

To evaluate the nanostructure of the Bi/MWNT catalysts the three catalysts, Bi-25, Bi-35, and Bi-50 were imaged via TEM.

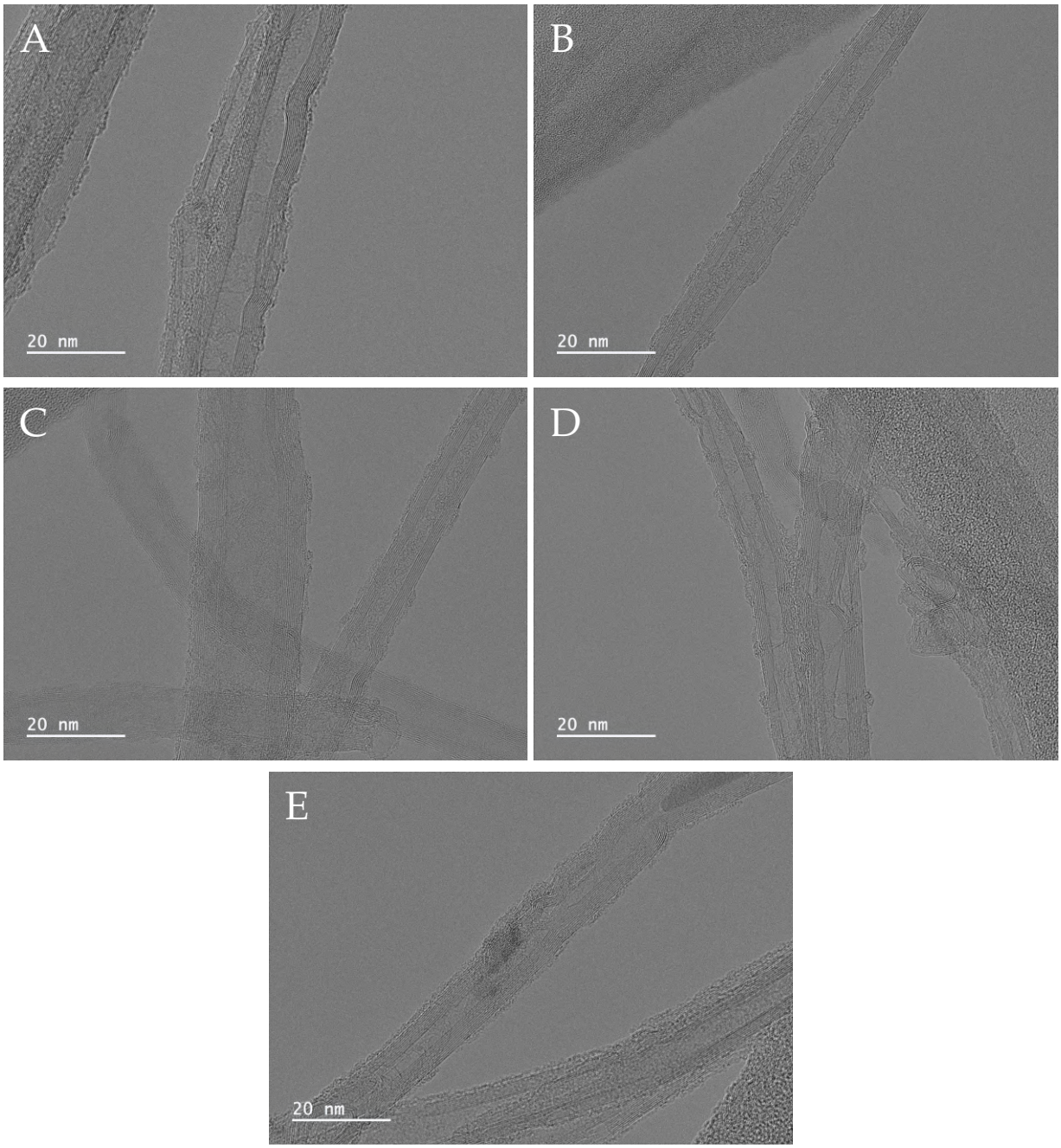


Figure 5.16: (A) TEM image of catalyst Bi-25 showing Bi nanoparticles on the MWNT surface as dark spots in the tube; (B) TEM of Bi-25 showing Bi nanoparticles on the MWNT surface as dark spots in the tube, the MWNT can also be seen to have a large amount of amorphous carbon on the surface; (C) Bi nanoparticles on the MWNT surface as dark spots in the tube; (D) TEM image of Bi-25 in which Bi nanoparticles can be observed in the effective pore from two MWNTs crossing; (E) TEM image of Bi-25 win which a large Bi aggregation can be seen as a dark area on a MWNT.

As can be seen in the TEM images of Bi-25 (Fig. 5.16), small single/dual atom Bi nanoparticles can be observed on the MWNT wall (Figs. 5.16A and 5.16B) as small dark spots in the image. Additionally, Bi aggregations could be observed on the MWNT wall (Fig. 5.16E), however these were not as common in the imaged sample. Another key facet observed from the images of Bi-25 is the high amount amorphous carbon on the walls of nanotube. Whilst also present in the Pb catalysts, it appears particularly prominent in Bi-25, which may indicate that the thermal decomposition of $Bi(NO_3)_3$ may be more destructive to the MWNT support than $Pb(NO)_3$.

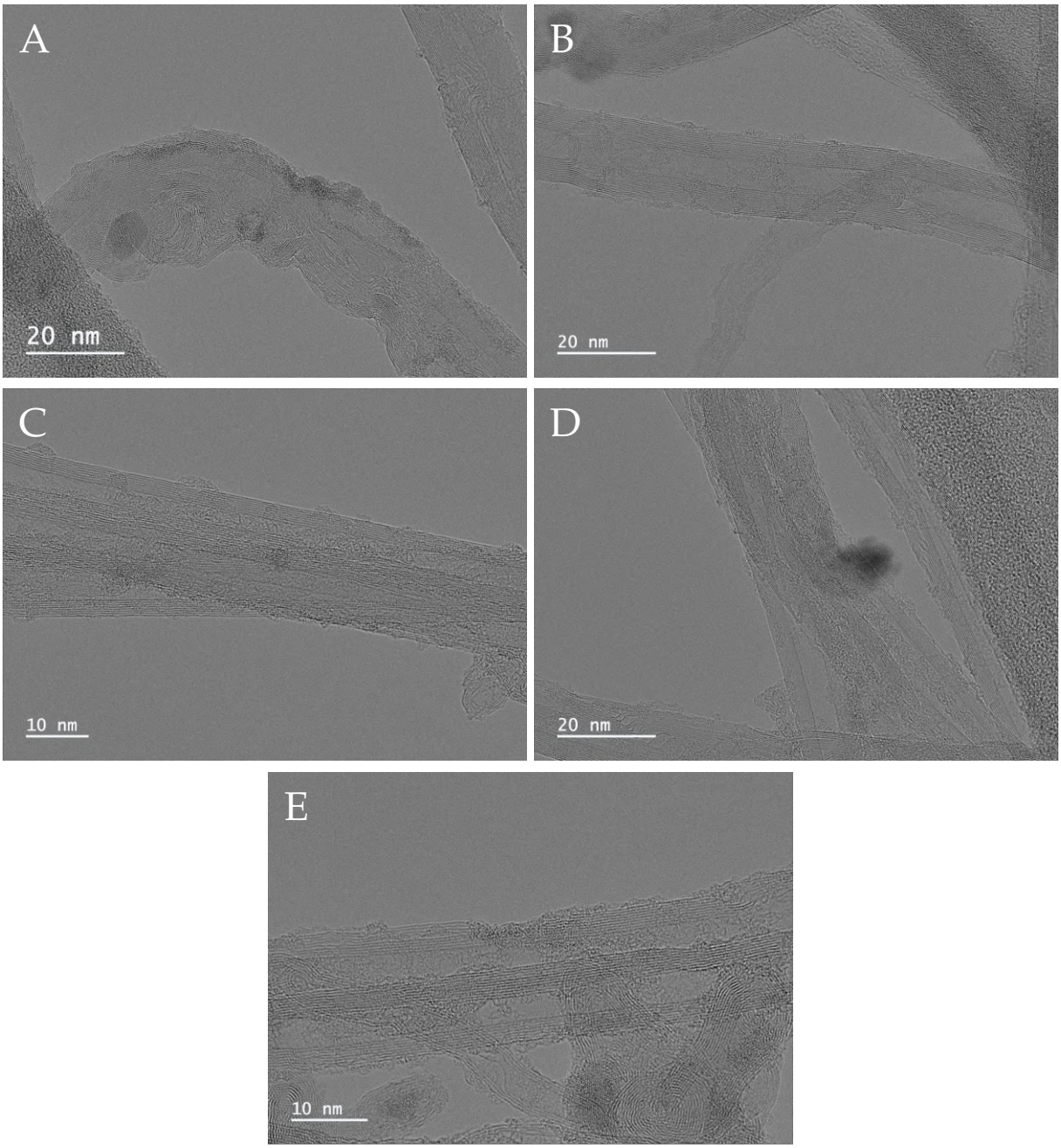


Figure 5.17: (A) TEM image of catalyst Bi-35 showing a Bi aggregation on the MWNT outer wall; (B) TEM of Bi-35 showing Bi nanoparticles on the amorphous carbon found on the MWNT surface as dark spots; (C) High density of Bi nanoparticles on the MWNT surface and MWNT crossing site as dark spots; (D) TEM image of Bi-35 showing a large Bi aggregate at the end of a tube with a high density of Bi nanoparticles on the surface shown as dark spots; (E) Zoomed TEM image of Bi-35 in which damage in the MWNT can be observed with Bi metal observed at the area of damage.

Increasing the weight % to 35 for the Bi-35 catalyst appears to shift the nanostructure to the formation of Bi aggregates as opposed to nanoparticles, as can be seen in Fig. 5.17. The aggregates can be seen to eating away into the nanotubes outer wall, forming an

embedded aggregate in the MWNT structure (Figs. 5.17A and 5.17E). Nanoparticles are still present in the structure (Figs. 5.17B and 5.17C), however it is apparent in the images of Bi-35 that the nanoparticles are predominantly found encased in the amorphous carbon on the MWNT surface, which presents potential issues for surface site availability for electrocatalysis.

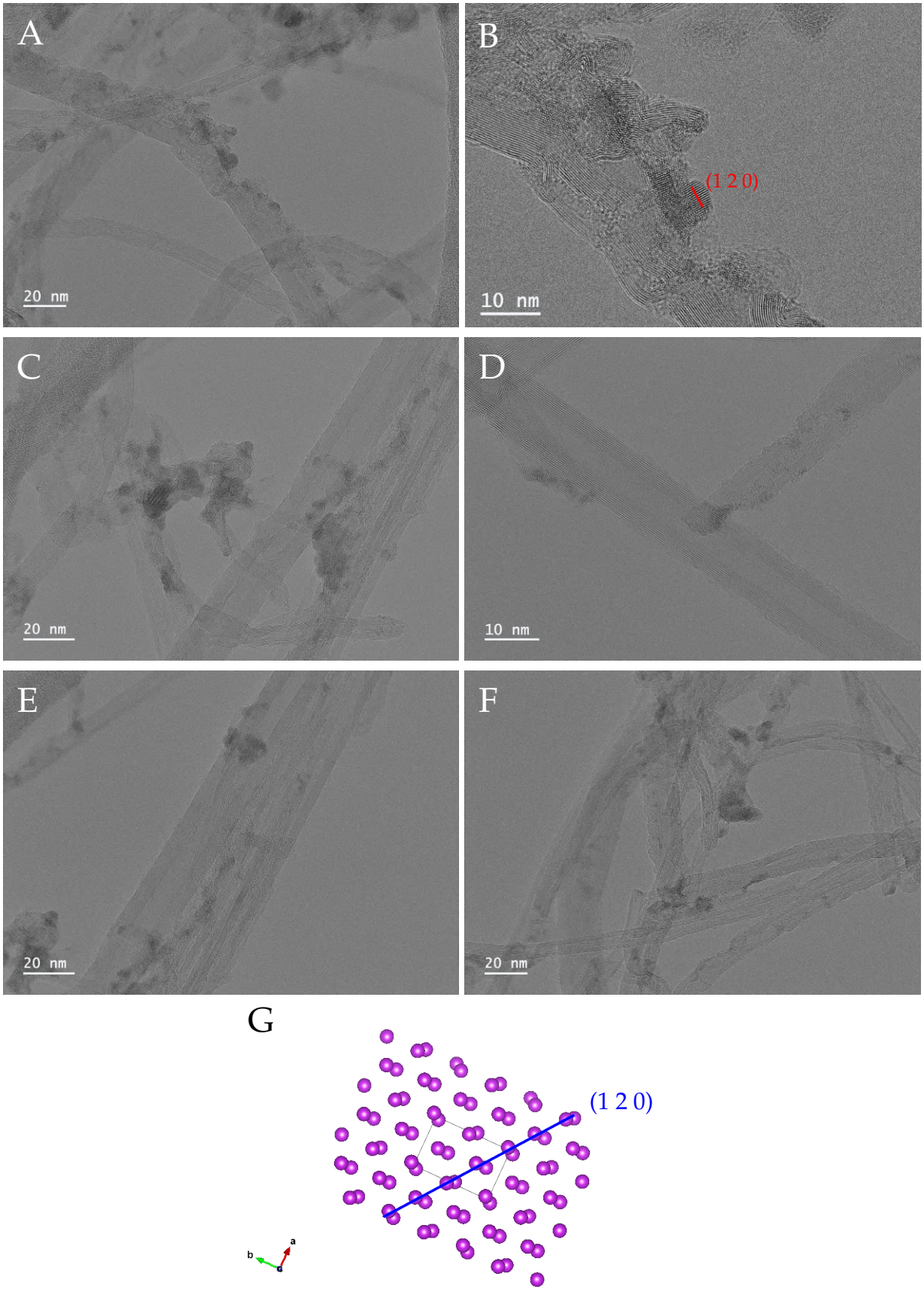


Figure 5.18: (A) TEM of Bi-35 showing Bi nanoparticles on the amorphous carbon found on the MWNT surface as dark spots; (B) zoomed area of Fig. 5.18A with measured d-spacing labelled; (C) TEM image of catalyst Bi-35 showing a large Bi aggregation binding together multiple MWNT ends; (C) High density of Bi nanoparticles on the MWNT surface and MWNT crossing site as dark spots; (D) TEM image of Bi-35 showing a large Bi aggregate at the end of a tube with a high density of Bi nanoparticles on the surface shown as dark spots; (E) Zoomed TEM image of Bi-35 in which damage in the MWNT can be observed with Bi metal observed at the area of damage; (G) Simulated crystal structure of α Bi_2O_3 predicted from Fig. 5.18B with (1 2 0) plane labelled as a blue line.

Increasing the weight % further in Bi-50 (Fig. 5.18) continues the trend observed in Bi-35, with Bi aggregations dominating as the most common Bi nanostructure, with nanoparticles only present in areas of MWNT defects or amorphous surface carbon. This trend for nanoparticle formation on surface sites that appear to prevent surface migration can be clearly observed by comparing Fig. 5.18D and Fig. 5.18F, with the former having little to no amorphous carbon or defects on the surface, and the latter having a large amount of defect sites and nanotube pores resulting from crossing on the nanotubes. As a consequence, it can be seen in Fig. 5.18D has no nanoparticles on the surface and a large aggregation at the tip of the tube which has eaten into the nanotube wall, whilst in Fig. 5.18F nanoparticles can be observed in the crossing sites and amorphous carbon with open areas containing the aggregates.

5.3.2.2 Other characterisation

For weight loading determination, TGA of Bi-25, Bi-35, and Bi-50 was conducted to calculate the actual metal loading and to observe changes in the decomposition temperature depending on metal loading (Fig. 5.12).

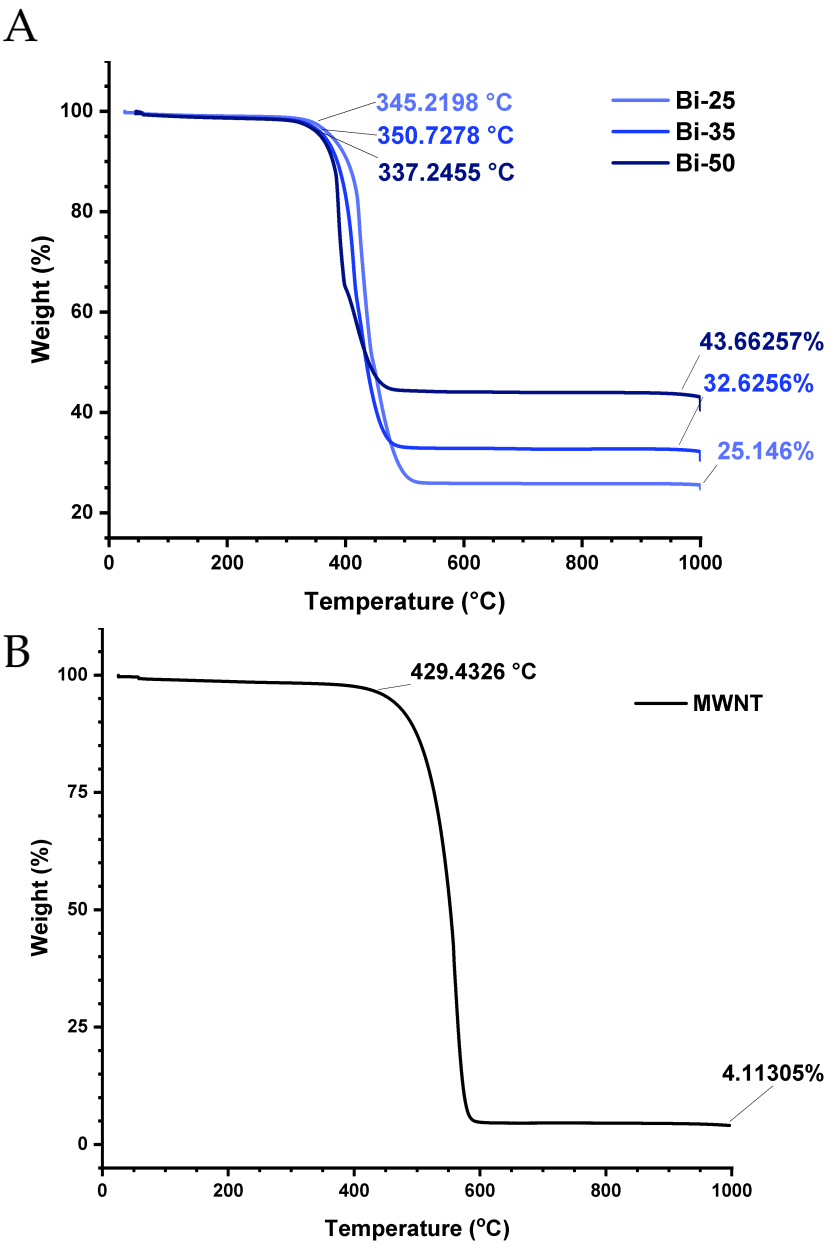


Figure 5.19: (A) TGA plot of Bi-25, Bi-35, and Bi-50 in air with initial decomposition temperature and final weight % labelled; (B) TGA plot of MWNT in air with initial decomposition temperature and final weight % labelled.

As seen in Fig. 5.19, the decomposition temperature of Pb/MWNT is $\sim 80 - 90$°C earlier than in bare MWNT, which is to be expected due to the catalytic effect of metal oxides on thermal decomposition.[58]

By utilising the same method as Section 5.2.2.2, an accurate Bi_2O_3 and Bi weight loading can be calculated for Bi-25, Bi-35, and Bi-50 via Section 5.2.2.2. To 2 d.p. the Bi_2O_3 weight loading of Bi-25, Bi-35, and Bi-50 are calculated to be 21.03%, 28.51%, and 39.55% respectively, and the Bi weight loadings therefore are 18.81%, 25.49%, and 35.37% respectively. Compared to Pb/MWNT (Section 5.2.2.2), there is a much larger disparity between the

theoretical and observed weight loadings of Bi, and the exact reason is unclear, but is likely to do with transfer losses, variable hydration of the crystal structure, and an assumed lower adsorption affinity of $Bi(NO_3)_3$ to the MWNT resulting in metal loss in the crucible.

5.3.3 Electrochemistry

5.3.3.1 Voltammetry

To evaluate the electrochemical performance and electrocatalytic activity of the three Bi/MWNT catalysts: Bi-25, Bi-35, and Bi-50, LSV using a RDE at 1600 rpm at a scan rate of 0.005 V s^{-1} was utilised (Fig. 5.20)

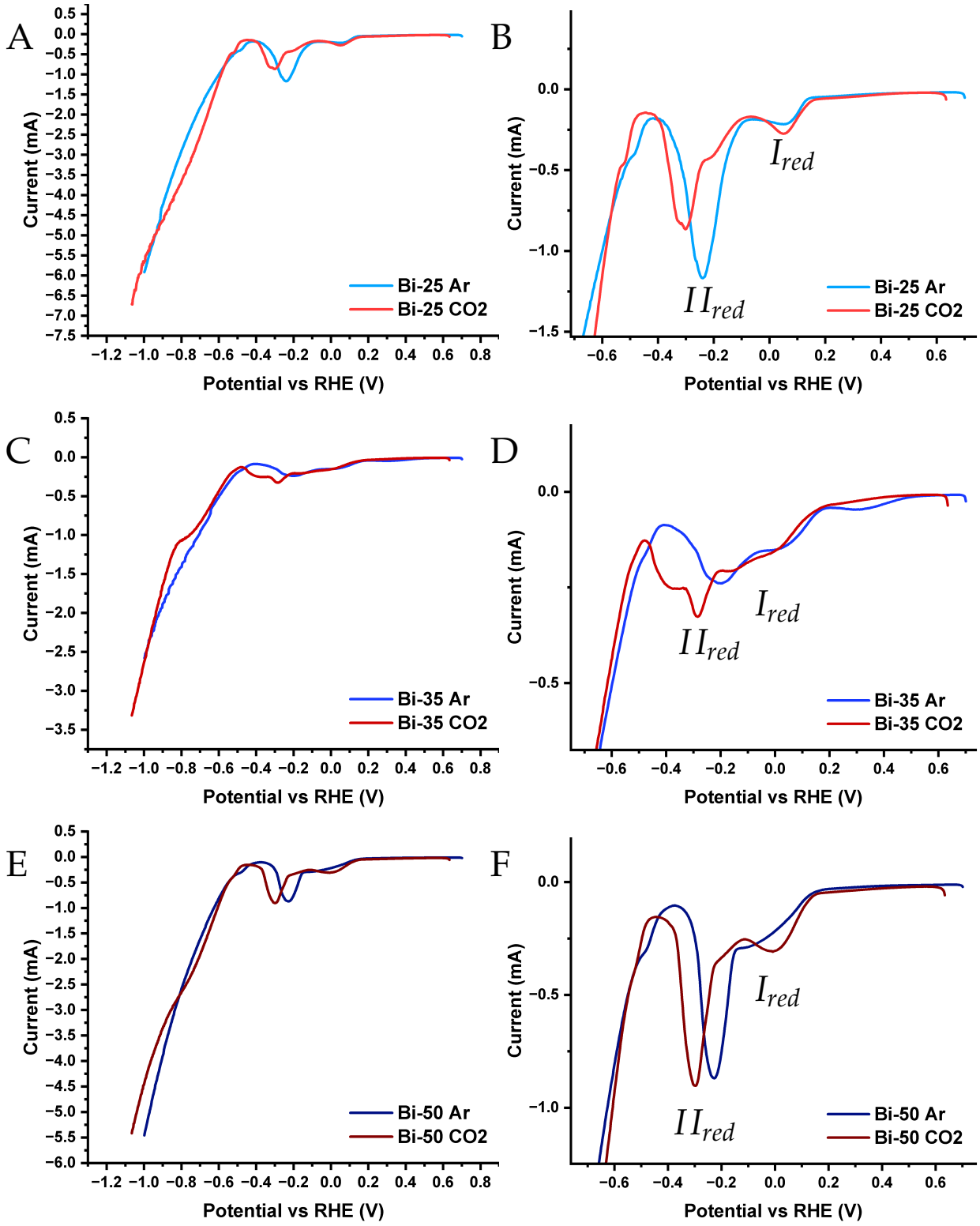


Figure 5.20: (A) LSV of Bi-25 using an RDE in Argon and CO_2 saturated 0.5 M $KHCO_3$ at 0.005 V s^{-1} at a rotation rate of 1600 rpm; (B) LSV from Fig. 5.20A with reduction peaks labelled, voltammogram has been zoomed into the non CO_2RR region for clarity; (C) LSV of Bi-35 using an RDE in Argon and CO_2 saturated 0.5 M $KHCO_3$ at 0.005 V s^{-1} at a rotation rate of 1600 rpm; (D) LSV from Fig. 5.20C with reduction peaks labelled, with reduction peaks labelled, voltammogram has been zoomed into the non CO_2RR region for clarity; (E) LSV of Bi-50 using an RDE in Argon and CO_2 saturated 0.5 M $KHCO_3$ at 0.005 V s^{-1} at a rotation rate of 1600 rpm; (F) LSV from Fig. 5.20E with reduction peaks labelled, voltammogram has been zoomed into the non CO_2RR region for clarity

The LSVs of the Bi catalysts presents two prominent reduction peaks: I_{red} and II_{red} at 0.1, and $-0.25/-0.3$ V vs RHE respectively with peak II_{red} being a shouldered peak. Peak I_{red} corresponds to the Bi^{3+}/Bi^{2+} redox couple from the partial reduction of Bi_2O_3 via Eq. (5.8)[62–64]:

$$Bi_2O_3 + 2\,OH^- \longrightarrow 2\,BiO_2^- + 2\,H_2O \tag{5.8}$$

Peak II_{red} is a shouldered peak, with the main, larger, peak corresponding to the Bi^{2+}/Bi^0 redox couple resulting from the two step reduction of $BiO_2{}^-$ via Eqs. (5.9) and (5.10)[62–64]:

$$BiO_2^- + e^- \longrightarrow BiO_2^{2-} \tag{5.9}$$

$$3\,BiO_2^{2-} + 2\,H_2O \xrightleftharpoons{\text{Disproportionation}} 2\,BiO_2^{2-} + 4\,OH^- + Bi^0 \tag{5.10}$$

The smaller peak is likely associated with the reduction of $Bi_2O_2CO_3$ formed from surface active Bi_2O_3 reaction with the $KHCO_3$ to $BiOH_3$ via Eq. (5.11)[63]:

$$Bi_2O_2CO_3 + 2\,OH^- + 2\,H_2O \longrightarrow 2BiOH_3 + CO_3^{2-} \tag{5.11}$$

The prior attributions of peak II_{red} and it's shoulder match the observed result that the shoulder is only present in CO_2 saturatred electrolyte and are in agreement with the voltammetry study performed by Vivier *et al.*[63,64] Additionally, the LSVs of the Bi/MWNT catalysts present an onset potential of -0.5 V vs RHE for both CO_2 and Ar saturated electrolyte at all weight loadings of Bi. Notably, both Bi-25 and Bi-50 have an increased current in CO_2 saturated electrolyte over Ar up to around -0.9 V vs RHE, whilst in Bi-35, the Ar saturated current is greater throughout the CO_2RR region. This is likely due to the difficulty experienced with the creation of a homogenous ink for Bi-35 in particular, which was of particular issue with the CO_2 saturated electrolyte voltammogram, and can help in explaining it's different voltammogram profile compared to Bi-35 in Ar, and Bi-25 and Bi-50 in both electrolyte saturations.

To further characterise the Bi catalysts, CV analysis was subsequently performed on the Bi/MWNT catalysts following the LSV experiments (Fig. 5.21).

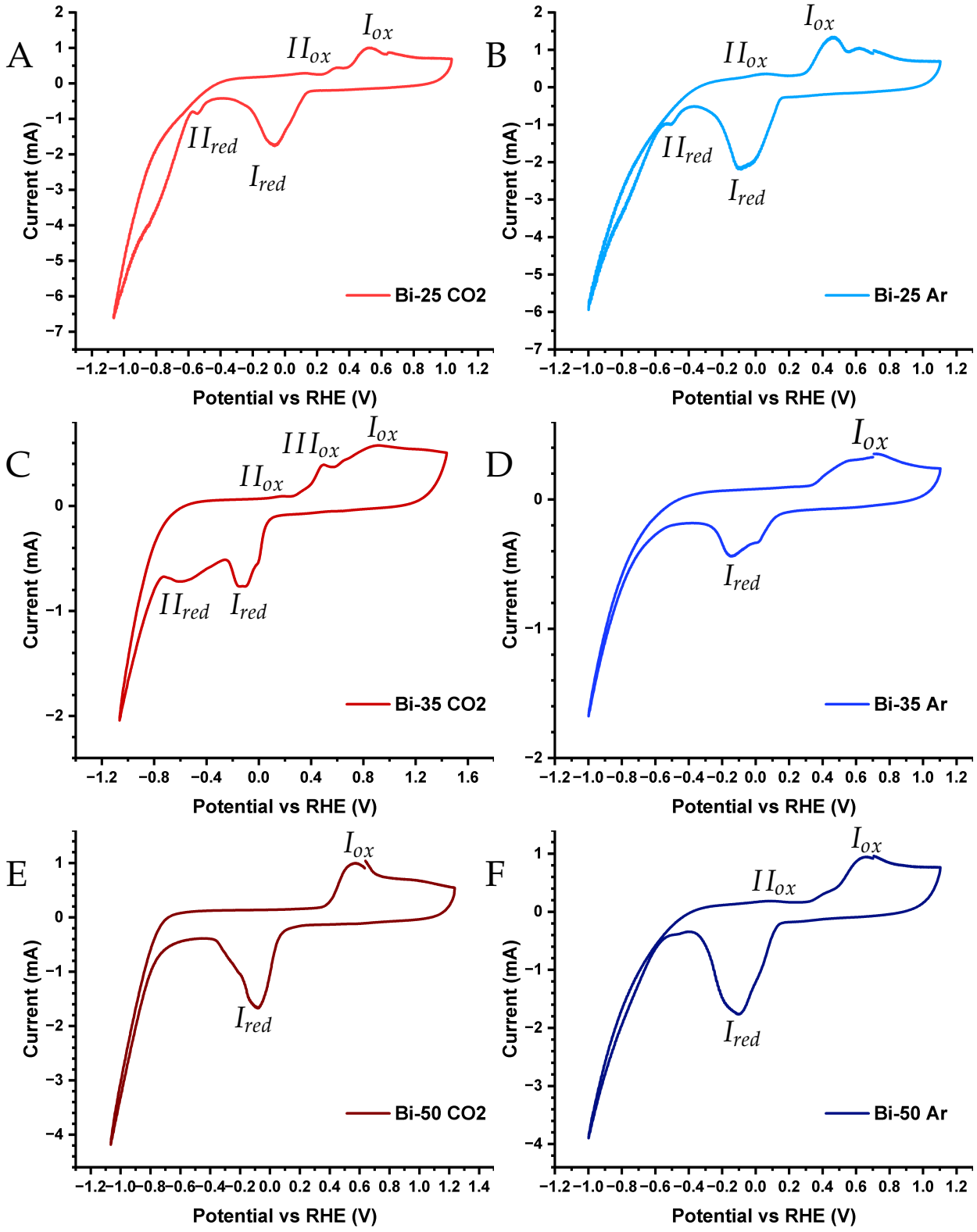


Figure 5.21: (A) CV of Bi-25 using a RDE in CO_2 saturated 0.5 M $KHCO_3$ at 0.05 V s^{-1} at a rotation rate of 1600 rpm with reduction and oxidation peaks labelled; (B) CV of Bi-25 using a RDE in Ar saturated 0.5 M $KHCO_3$ at 0.05 V s^{-1} at a rotation rate of 1600 rpm with reduction and oxidation peaks labelled; (C) CV of Bi-35 using a RDE in CO_2 saturated 0.5 M $KHCO_3$ at 0.05 V s^{-1} at a rotation rate of 1600 rpm with reduction and oxidation peaks labelled; (D) CV of Bi-35 using a RDE in Ar saturated 0.5 M $KHCO_3$ at 0.05 V s^{-1} at a rotation rate of 1600 rpm with reduction and oxidation peaks labelled; (E) CV of Bi-50 using a RDE in CO_2 saturated 0.5 M $KHCO_3$ at 0.05 V s^{-1} at a rotation rate of 1600 rpm with reduction and oxidation peaks labelled; (F) CV of Bi-50 using a RDE in Ar saturated 0.5 M $KHCO_3$ at 0.05 V s^{-1} at a rotation rate of 1600 rpm with reduction and oxidation peaks labelled

The CVs of the Bi/MWNT catalysts reveal that the peak at 0.1 V vs RHE in the LSV (Fig. 5.20) has now been incorporated into a shoulder at the large peak at $\sim -0.1 - -0.2$ V vs RHE (Fig. 5.21). Additionally, in Bi-25, a new peak labelled II_{red} is observed at ~ -0.55 V vs RHE (Figs. 5.21A and 5.21B). The onset potential in the CV is later than in the LSV experiments, now at -0.6 V vs RHE in both electrolyte saturations of Bi-25, and Ar saturated Bi-35 and Bi-50, whilst it is lower at -0.8 V vs RHE in CO_2 saturated Bi-35 and Bi-50 (Fig. 5.21). It is likely that the later potential of -0.8 is the CO_2RR more accurate onset potential for the catalyst, as the sharp increase in current seen at -0.5 V vs RHE in the LSV (Fig. 5.20) is associated with the formation of the active form of the catalyst, explaining the shape of the tail feature which incorporates an elongated peak-like shape in the LSVs when first reaching -0.5 V vs RHE (Fig. 5.20) and in the Bi-25 CVs in which this feature within the tail is centred roughly around -0.8 V vs RHE (Figs. 5.21A and 5.21B).

The I_{ox} peaks in Figs. 5.21A, 5.21B, 5.21D and 5.21F are split into two, with one at -0.4 and one at -0.6 V vs RHE, whilst notably in Fig. 5.21E it a single peak at -0.6 V vs RHE. This splitting is to do with the formation of $BiOH_3$ during the positive sweep, with the peak at -0.4 corresponding to oxidation of $BiOH_3$ to BiO_2^{2-}. Lastly, peak II_{ox} is associated with discharge of the electrochemical double layer during the positive sweep due to the high ionic capacity on the porous CNT support.[62]

Thus, the electrochemical processes of Bi/MWNT can be attributed as follows:

$$I_{red}^{1^{st}} : \mathrm{Bi_2O_3 + 2\,OH \longrightarrow 2\,BiO_2^- + 2\,H_2O} \qquad \mathrm{V = 0.10\,vs\ RHE} \tag{5.12}$$

$$II_{red}^{1^{st}\,Step\,1} : \mathrm{BiO_2^- + e^- \longrightarrow BiO_2^{2-}}$$

$$II_{red}^{1^{st}\,Step\,2} : \mathrm{3\,BiO_2^{2-} + 2\,H_2O \longrightarrow 2\,BiO_2^{2-} + 4\,OH^- + Bi^0} \qquad \mathrm{V = -0.3\,vs\ RHE} \tag{5.13}$$

$$II_{red}^{1^{st}\,Shoulder} : \mathrm{Bi_2O_2CO_3 + 2OH^- + 2\,H_2O \longrightarrow 2BiOH_3 + CO_3^{2-}} \qquad \mathrm{V = -0.20\,vs\ RHE} \tag{5.14}$$

$$I_{Ox}^{Step1} : \mathrm{Bi^0 \longrightarrow Bi^+ + e^-} \qquad \mathrm{V = 0.4\,vs\ RHE} \tag{5.15}$$

$$I_{Ox}^{Step2} : \mathrm{3\,Bi^+ \overset{\text{Disproportionation}}{\longleftrightarrow} Bi^{3+} + 2\,Bi^0}$$

$$\mathrm{Bi^{3+} + 3OH^- \longrightarrow BiOH_3} \qquad \mathrm{V = 0.6\,vs\ RHE} \tag{5.16}$$

$$I_{red}^{2^{nd}} : \mathrm{BiOH_3 + H_2O + 3\,e^- \longrightarrow Bi^0 + 3\,OH^-} \qquad \mathrm{V = -0.10\,vs\ RHE} \tag{5.17}$$

This assignment accounts for the differences seen in the CVs from the LSVs, and postulates that initial reduction from the lsv results in the formation of $BiOH_3$ and Bi from Bi_2O_3, which then undergoes an alternate reduction route, explaining the more shift in peak I_{red} after the first scan Figs. 5.20 and 5.21.

5.3.4 Electrocatalysis

To test the catalytic activity of Bi/MWNT, a range of potentials were tested for CO_2 reduction to produce formate for one hour: -0.85, -0.95, -1.05, -1.15, and -1.35 V vs RHE. Out of these potentials, -1.05 V vs RHE showed the highest FE towards formate, and this potential was used as the potential that all Bi/MWNT catalysts were tested at. After the electrocatalysis runs at -1.05 V vs RHE for 1 hour Fig. 5.22, the Bi/MWNT catalysts: achieved a FE towards formate of 1.8% for Bi-25, 4.6% for Bi-35, and 11.0% for Bi-50. These FE values correspond to j_{HCOO^-} values of 0.72 mA cm^2 for Bi-25, 2.99 mA cm^2 for Bi-35, and 5.5 mA cm^2 for Bi-50.

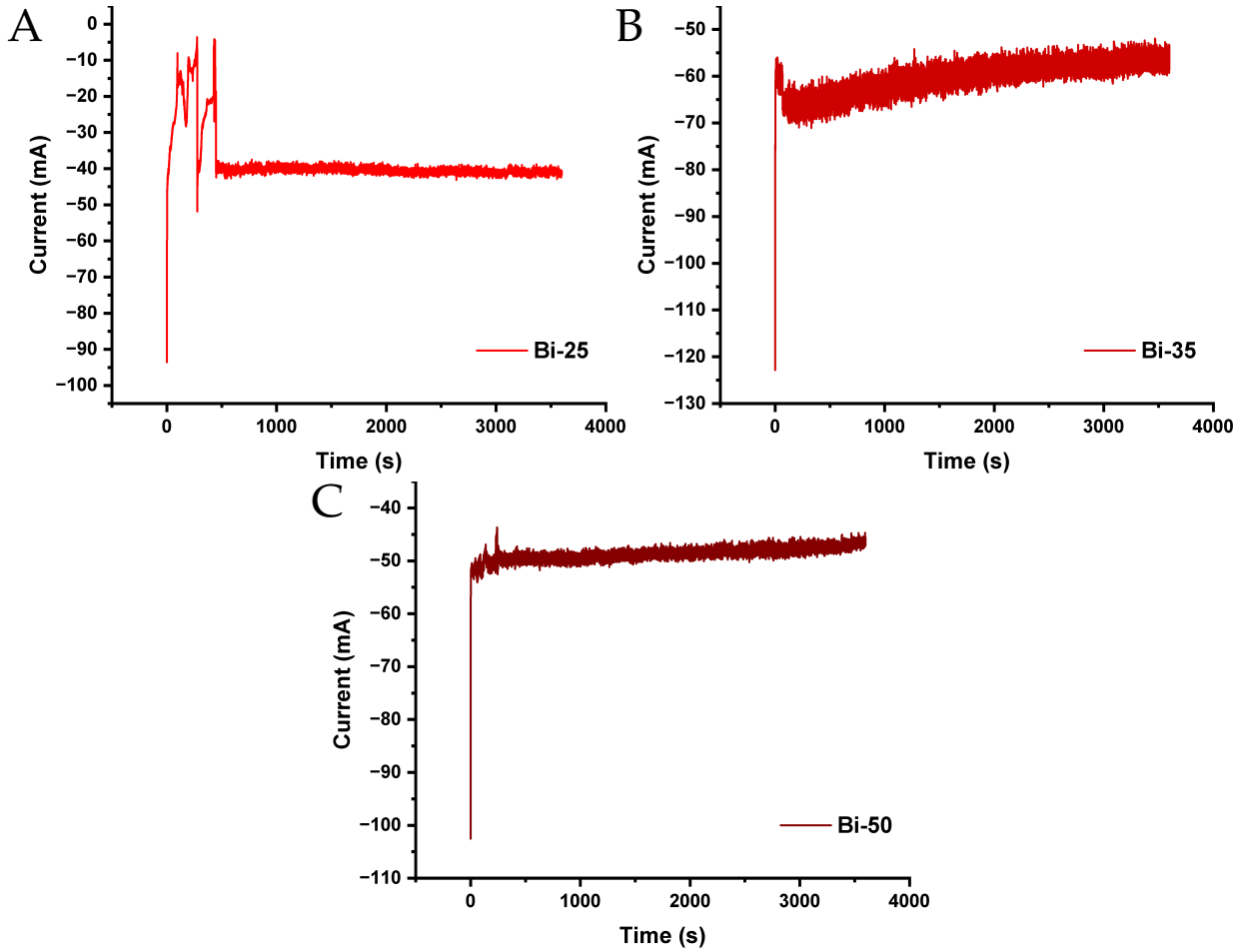


Figure 5.22: (A) Chronoamperometry of Bi-25 dropcasted on 5% PTFE carbon paper in a $1x1\ cm^2$ area at -1.7 V vs RHE in 0.5 M $KHCO_3$ with constant CO_2 gas flow into the electrolyte; (B) Chronoamperometry of Bi-35 dropcasted on 5% PTFE carbon paper in a $1x1\ cm^2$ area at -1.7 V vs RHE in 0.5 M $KHCO_3$ with constant CO_2 gas flow into the electrolyte; (C) Chronoamperometry of Bi-50 dropcasted on 5% PTFE carbon paper in a $1x1\ cm^2$ area at -1.7 V vs RHE in 0.5 M $KHCO_3$ with constant CO_2 gas flow into the electrolyte.

As opposed to Pb/MWNT (Section 5.2.4), Bi/MWNT achieved an appreciable amount of formate production, more in line with what would be expected of Bi electrocatalysts for theCO_2RR for formate according to literature.[3] However, it can be noted that the highest formate FE achieved by these catalysts, 11.0% by Bi-50, is still much lower than the reported high formate selectivities $>$ 90% in literature,[3] pointing towards a large contribution from the MWNTs towards the overall charge passed during the electrocatalysis experiments. This large MWNT catalytic contribution towards gaseous products such as H_2 in the case of the p-block catalysts can likely be attributed to the both catalyst metal encapsulation, and the amorphous carbon present on the MWNT sidewall (Section 5.3.2.1). As for why particularly Bi-50 achieved the highest formate FE, the structural differences between the catalysts observed in the TEM images (Fig. 5.18) can be used to infer that it is possible that the presence of aggregates positively impacts

the catalytic performance. This is supported by the fact that the active site for CO_2RR for Bi requires either Bi_2O_3 or two oxygen binding sites on the bismuth metal,,[65] meaning the likely single atom features observed in the TEM were not able to contribute to the CO_2 catalysis, and most likely acted as HER catalysts instead.

5.4 In/MWNTs

5.4.1 Synthesis

The In/MWNT catalyst was prepared in similar fashion to Pb/MWNT and Bi/MWNT, using the standardised conditions outlined for the synthesis of Bi/MWNT (Section 5.3.1) to make three catalysts: In-25, In-35, and In-50 with 25%, 35%, and 50% weight relative to the MWNT support. Additionally, two more catalysts were synthesised using a lower decomposition temperature of 290 °C: In-25R and In-25 Opt. For the 290 °C decomposition temperature catalysts, In-25R and In-25 Opt were synthesised following the same procedure used for In-25, however in the case of In-25 Opt, the MWNTs were first pretreated by refluxing in conc HNO_3 for 12 hrs, and then prior to the addition of the $In(NO_3)_3 \cdot H_2O$, the MWNTs were first filled with ethylene glycol (*ca.* 4 mL) to the point of incipient wetness to prevent $In(NO_3)_3$ encapsulation by the MWNTs. Therefore, the syntheses of In/MWNT are as follows:

In-25, In-35, and In-50: To MWNTs (250 mg) was added a solution of $In(NO_3)_3 \cdot H_2O$ (25, 35, and 50 wt% In w.r.t MWNT) in H_2O (6 mL). This mixture was subsequently stirred with a glass rod until the resulting ”paste” was homogeneous without any large lumps, and then was dried for 24 hrs at 60 °C to produce $In(NO_3)_3 \cdot H_2O$/MWNT in a powder form. This powder was then transferred to a furnace and decomposed at 350 °C for 1 hrwith a 10 °C min^{-1} ramp time. After decomposition, a powder of In/MWNT is produced with a hypothetical weight loading of In on MWNTs of 25 wt%, 35 wt%, and 50 wt%.

In-25R: To MWNTs (250 mg) was added a solution of $In(NO_3)_3 \cdot H_2O$ (25 wt% In w.r.t MWNT) in H_2O (6 mL). This mixture was subsequently stirred with a glass rod until the resulting ”paste” was homogeneous without any large lumps, and then was dried for 24 hrs at 60 °C to produce $In(NO_3)_3 \cdot H_2O$/MWNT in a powder form. This powder was then transferred to a furnace and decomposed at 290 °C for 1 hrwith a 10 °C min^{-1} ramp time. After decomposition, a powder of In/MWNT is produced with a hypothetical weight loading of In on MWNTs of 25 wt%.

In-25 Opt: MWNTs (1 g) were added to a round bottom flask to which conc. HNO_3 (68%, 100 mL) was added and then refluxed for 12 hrs with continuous stirring. The purified MWNTs were then collected via vacuum filtration and washed with copious water until the filtrate was pH neutral. To the purified MWNTs (250 mg), ethylene glycol was added dropwise (*ca.* 4 mL) until incipient wetness had been reached. $In(NO_3)_3 \cdot H_2O$ (25 wt%

In w.r.t MWNT) in H_2O (6 mL) was then added to the ethylene glycol impregnated MWNTs and then was subsequently stirred with a glass rod until the resulting "paste" was homogeneous, and then was transferred to an oven and dried for 24 hrs at 60 °C to produce $In(NO_3)_3 \cdot H_2O$/MWNT in powder form. This powder was then transferred to a furnace and decomposed at 290 °C for 1 hr with a 10 °C min^{-1} ramp time. After decomposition, a powder of In/MWNT is produced with a hypothetical weight loading of In on MWNTs of 25 wt% with selective In deposition on the outer MWNT wall.

5.4.2 Characterisation

5.4.2.1 Electron Microscopy

To evaluate the nanostructure of the In/MWNT catalysts the catalysts: In-25, In-35, In-50, In-25R, and In-25 Opt were imaged via TEM.

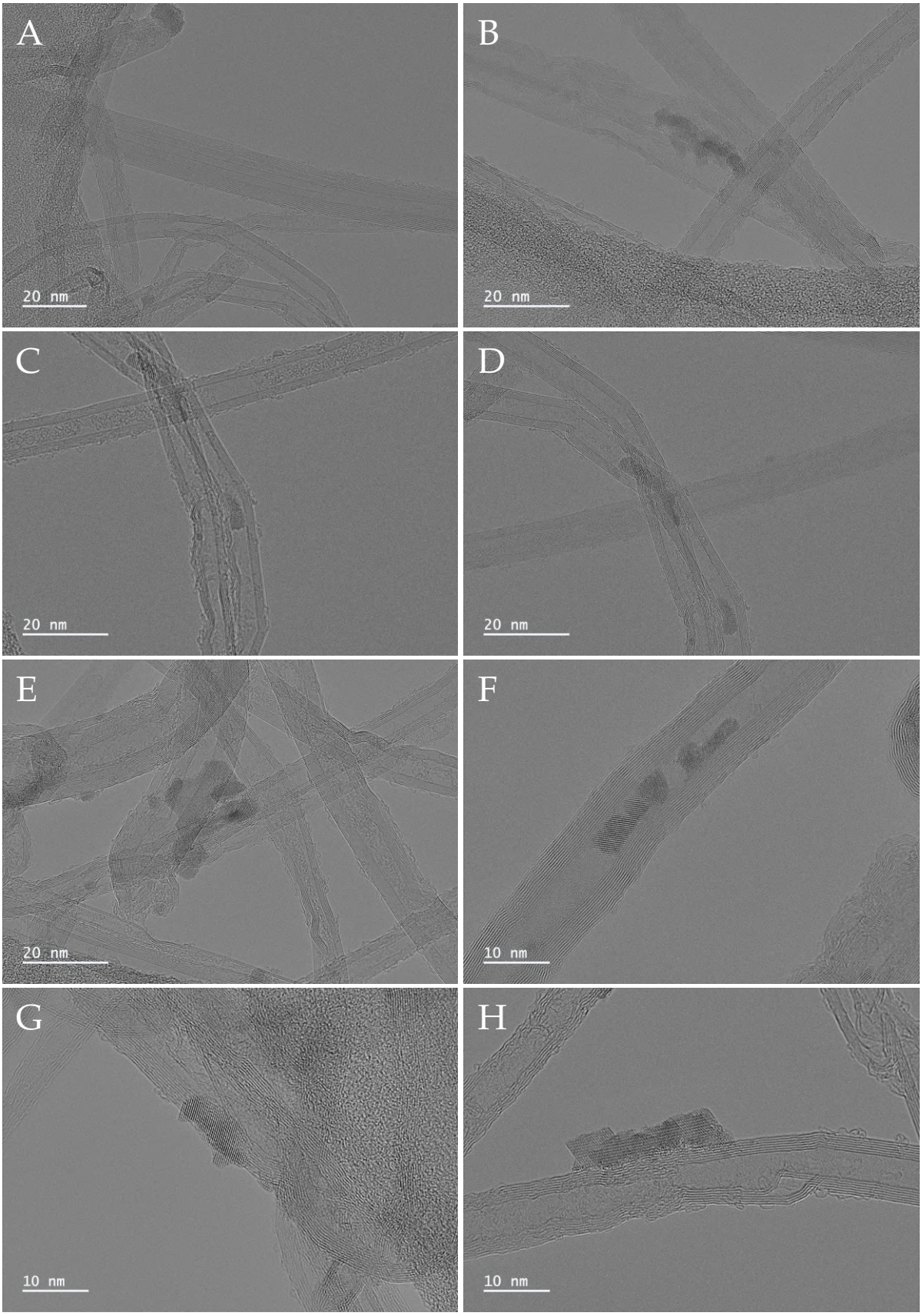


Figure 5.23: (A) TEM image of catalyst In-25 showing the absence of In nanoparticles on various MWNT sizes; (B) TEM of In-25 showing an In aggregation inbetween two MWNTs outer walls; (C) TEM image of In-25 in which In aggregations are encapsulated inside the MWNT with a crystalline structure, the aggregation at the top of the image is elongated along a kink in the MWNT; (D) TEM image of In-25 showing a similar In encapsulation found at a kink in the MWNT structure to that observed in Fig. 5.23C; (E) TEM image of In-25 in which a large crystalline In aggregation can be seen on top of a crossing site for multiple MWNTs. Additionally, small nanoclusters of In can be observed on the outer walls of the MWNT situated to the left of the large aggregate; (F) TEM image of In-25 in which small In aggregations can be observed encapsulated inside the MWNT; (G) TEM image of In-25 in which an In aggregation can be observed over the graphitic outer wall of a MWNT, notably the MWNT wall underneath does not appear to show any signs of damage based on both sides of the aggregation showing no signs of deformity; (H) TEM image of In-25 in which an In aggregation is observed attached directly to the side of a MWNT, Notably, where the aggregation and MWNT meet, the MWNT wall appears to have In atoms incorporated into the graphitic structure.

As can be seen in the TEM images of In-25 (Fig. 5.23), large aggregations are prevalent throughout the catalyst structure, with no observable instances of nanoparticles/single atoms. This is in contrast to Bi-25 and Pb-25 (Figs. 5.8 and 5.16) in which the 25 wt% catalysts presented the most nanoparticles/single atoms out of all of the synthesised catalysts for the respective metal. This is most likely due to the lower atomic mass of indium resulting in higher amount of In atoms on the MWNT at 25 wt% when compared to both Bi and Pb, with near double the amount at 2.18×10^{-6} moles of In in In-25, compared 1.20×10^{-6} and 1.21×10^{-6} moles for Bi and Pb respectively.

Notably, it can also be observed in Fig. 5.23 that In is more susceptible to encapsulation within the MWNT compared to the Pb and Bi catalysts, despite the nanotubes not being opened prior to synthesis. The reason for this is unclear, however it may be likely due to the smaller atomic size of In and the fact that as purchased MWNTs still contain defects and commonly have missing end caps. Additionally, the encapsulated In aggregations appear to induce defects in the form of kinks in the MWNT structure, as can be seen in Figs. 5.23C and 5.23D.

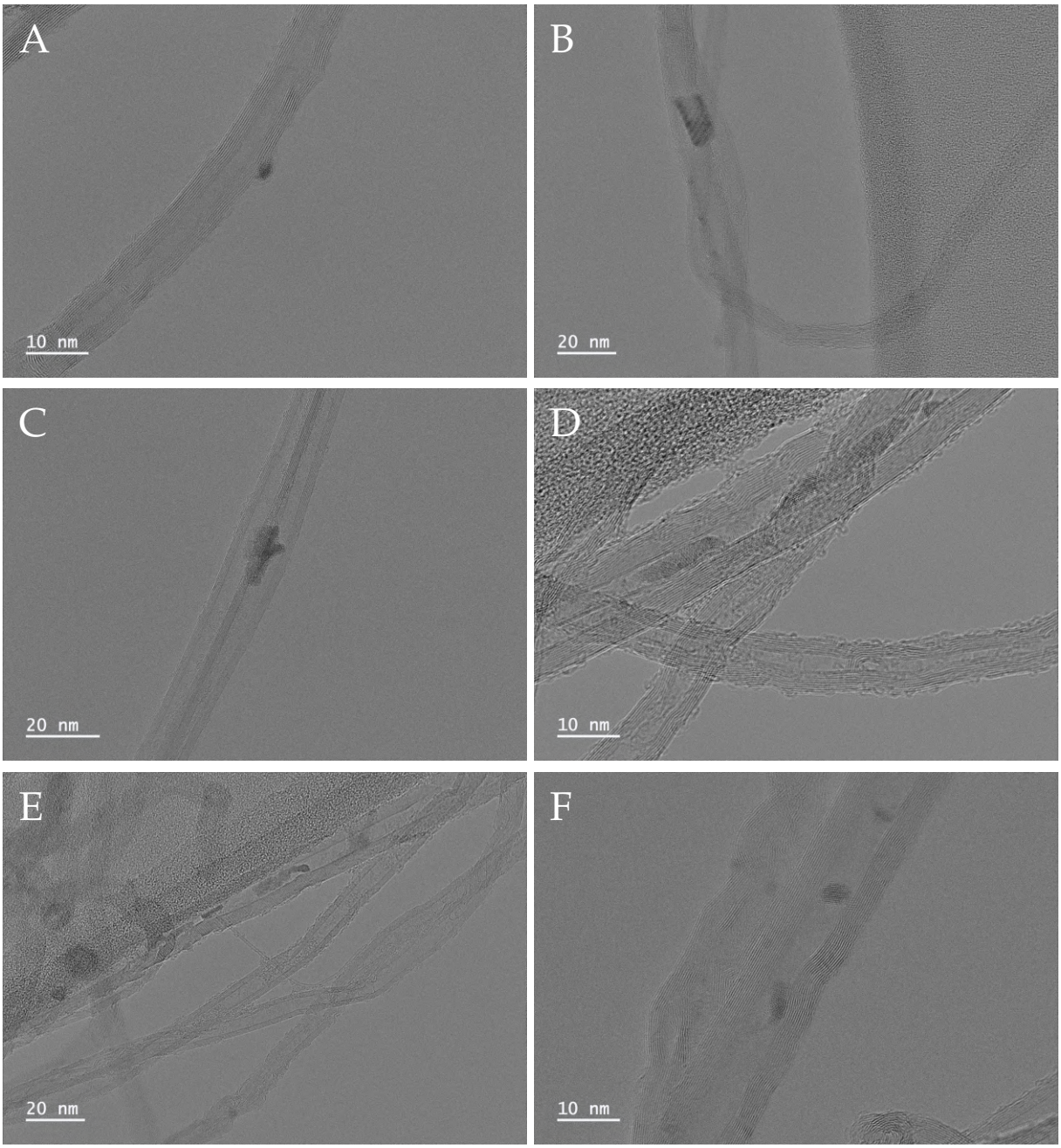


Figure 5.24: (A) TEM image of catalyst In-35 showing a single In nanocluster on the outer surface of the MWNT in similar fashion to Fig. 5.26E; (B) TEM image of In-35 showing a large crystalline In aggregation on MWNTs, notably the rest of the MWNTs imaged lack any In nanoparticles; (C) TEM image of In-35 showing a single In nanocluster between two MWNTs; (D) TEM image of In-35 taken out of focus illustrating that there are little to no In single atoms on the MWNTs surface, with the only metal observed being encapsulated In; (E) TEM image of In-35 illustrating highly deformed MWNTs from the decomposition process, with In aggregations encapsulated in the MWNT and very few In single atoms visible; (F) TEM image of In-35 showing encapsulated crystalline In nanoclusters

As seen in Fig. 5.24, Increasing the In loading to 35 wt%, it is immediately evident that

single atoms on the MWNT are almost completely absent, likely due to the much higher amount of In atoms present. All In on the MWNTs are seen either in the form of surface aggregates, as is the case for Figs. 5.24A to 5.24C, or encapsulated nanoparticles/aggregates, as is the case for Figs. 5.24D to 5.24F.

Interestingly, the outer aggregations observed in Fig. 5.24 appear to be isolated on the MWNT, with outer wall aggregates appearing to be the only In metal visible on any particular MWNT when present. Additionally, unlike Pb and Bi, the surface aggregations exist without any significant damage to the wall of the MWNT, with Figs. 5.24B and 5.24C exemplifying this as visible in the crystal structure of In is an intact MWNT outer wall, with the outer walls above and below the aggregates containing no signs of deformation from wall damage underneath the aggregate. These observations combined with the prevalence of encapsulated In, indicates that unlike Pb and Bi in which were located only in nanotube defects and external pores, In has much greater affinity towards the MWNT surface, thus allowing much greater lability on the surface of the MWNT resulting in more facile aggregation and also much higher likelihood of encapsulation.

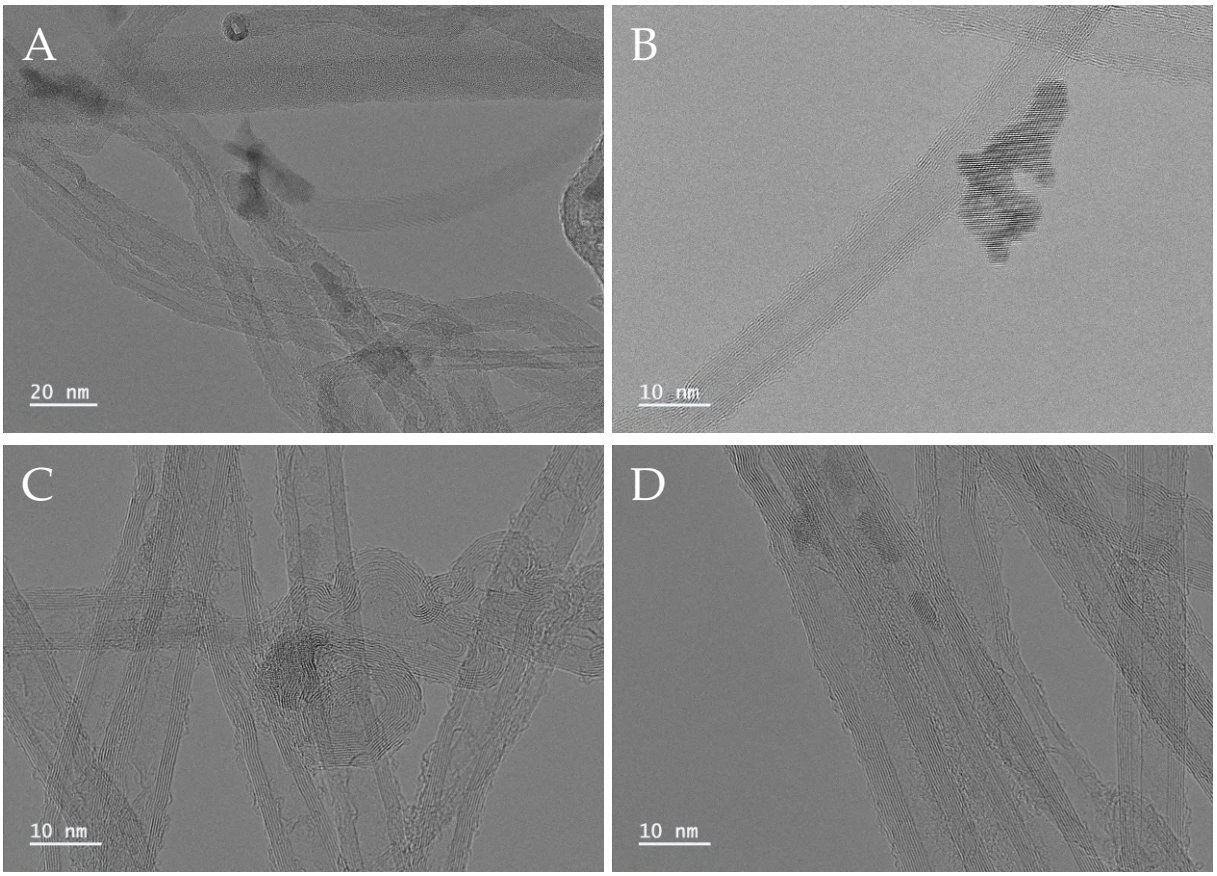


Figure 5.25: (A) TEM image of catalyst In-50 showing a large crystalline In aggregation on the tip of a MWNT; (B) TEM image of In-50 showing a large crystalline In aggregation on MWNTs, notably the rest of the MWNTs imaged lack any In nanoparticles; (C) TEM image of In-50 showing an In aggregation situated in the crossing between multiple MWNTs, notably, the MWNTs in the vicinity of the aggregation showns signs of damage from decomposition; (D) TEM image of In-50 showing two distinct crystalline In aggregations encapsulated inside a MWNT internal cavity. Situated to the left of the encapsulated In is an aggregation of In which appears both on the outer wall of the tube on the right and disrupting the wall structure of the tube on the left. This particular aggregation does not appear encapsulated in the MWNT on the left due to the lack of crystallinity observed

As for In-50 (Fig. 5.25), the further increase in weight% increases the size of the metal aggregations compared to In-35, additionally as was the case with In-35 (Fig. 5.24), no single atoms/nanoparticles are observed. Comparing the aggregations which are specifically isolated (with no other In aggregates present for that particular MWNT), the aggregate length along the wall increases with increasing metal loading, as can be seen in Fig. 5.23G, Fig. 5.24C, and Fig. 5.25B with the aggregations in In-25, In-35, and In-50 having lengths of 13.3 nm, 17.8 nm, 24.3 nm respectively when measured parallel to the MWNT. Additionally, these aggregations share the fact that the MWNT structure is not disrupted beneath, as evidenced by the lack of deformations or changes in nanotube shape at each end of the aggregation.

With the In-25R catalyst being synthesised at a lower decomposition temperature of 290 °C compared to In-25, In-35, and In-50, the TEM images of In-25R can provide insight into the effect on the decomposition temperature used for the synthesis on the In/MWNT nanostructure.

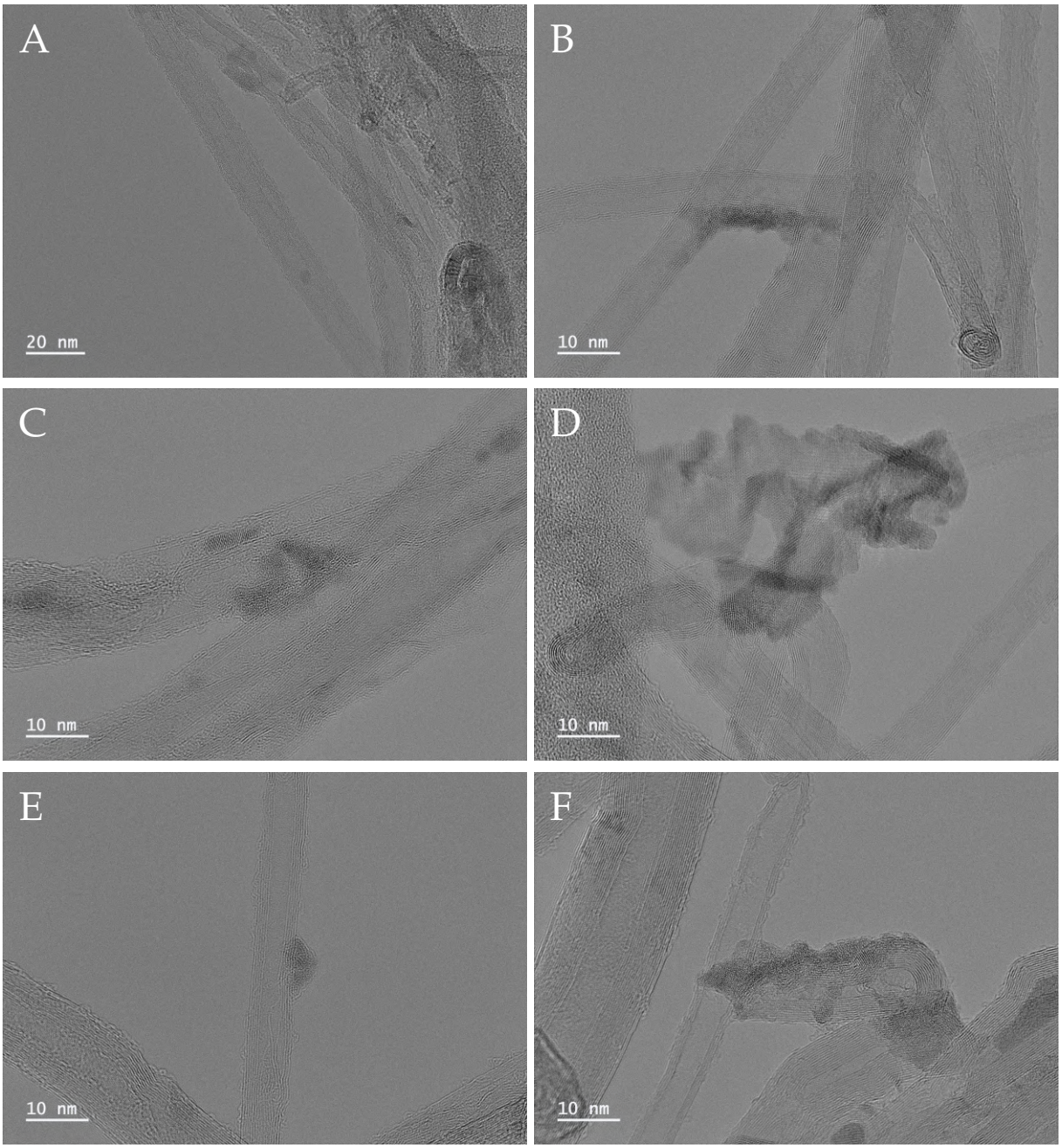


Figure 5.26: (A) TEM image of catalyst In-25R showing sparse In nanoparticles on the MWNT surface as dark spots in the tube; (B) TEM of In-25R showing an In aggregation on the outer walls of a MWNTs; (C) TEM image of In-25R in which In aggregations on both the outer MWNT wall and encapsulated inside the MWNT with a crystalline structure; (D) TEM image of In-25R in which a large crystalline In aggregation can be seen on top of and extruding off of the MWNT; (E) TEM image of In-25R in which an In nanocluster can be observed on the outer wall of the MWNT. Notably with this In aggregate, the outside edge of the has a layer of lower contrast, possibly indicating a carbon shell; (F) TEM image of In-25R in which a large amorphous In aggregation can be observed spanning the edge of a MWNT which has been shortened/damaged so that the tube is comprised of just the tip. Notably, the MWNT wall has been damaged by the In aggregation

In the TEM images of In-25R (Fig. 5.26), it can be seen that the reduction of decomposition temperature to 290°C allows for the formation of some sparse single atoms, as seen in Fig. 5.26A. Additionally, the outer wall aggregations seen In-25R are noticeably appear more amorphous and less structured than those seen in the 350°C decomposition catalysts. This is most noticeable when comparing Figs. 5.26B and 5.26F to Figs. 5.23G and 5.23H, as out of the two 25 wt% catalysts, In-25 surface aggregates are crystalline with clear d-spacing present, whilst In-25R outer wall aggregates are amorphous and less defined, and appear "melted" along the nanotube outer edge. Only one observed outer wall aggregate, Fig. 5.26D, presented crystallinity, however unlike the higher temperature counterparts, this large aggregate is comprise of multiple different orientations of crystal planes, rather than one single orientation, as seen in Fig. 5.23H and Fig. 5.25B. This lack of aggregate crystallinity does not hold true for encapsulated In in In-25R however, as like the previous catalysts there is a clear crystal structure with d-spacing visible with a singular orientation. The difference in crystallinity between In-25 and In-25R could be attributed to the higher temperature inducing nanoscale annealing to In aggregates resulting in single In domains, with higher temperatures producing larger grain sizes as is the case for both In and Indium Tin Oxide (ITO).[66,67]

It can also be concluded that due to In more favourably attaching to MWNTs, the reason some single atoms are observed in In-25R and not in In-25 is due to temperature induced migration along the surface of the MWNT, resulting in aggregation of the indium into larger structures.

Lastly, a feature of note is found in Fig. 5.23E, being that the outside edge of the In aggregate is surrounded by a thin layer of low contrast, which may possibly indicate a carbon shell resulting from the amorphous surface carbon on the MWNT, however it is not possible to discern whether or not this is a diffraction artifact from this image.

As seen in prior TEM images of the In/MWNT catalysts (Figs. 5.23 to 5.26), encapsulated In is present throughout these samples. This encapsulated In posing an issue to catalytic activity towards CO_2 is what informed the modified synthesis of In-25 Opt (Section 5.4.1) to try and decrease loss of catalytic active sites to the MWNT internal cavity.

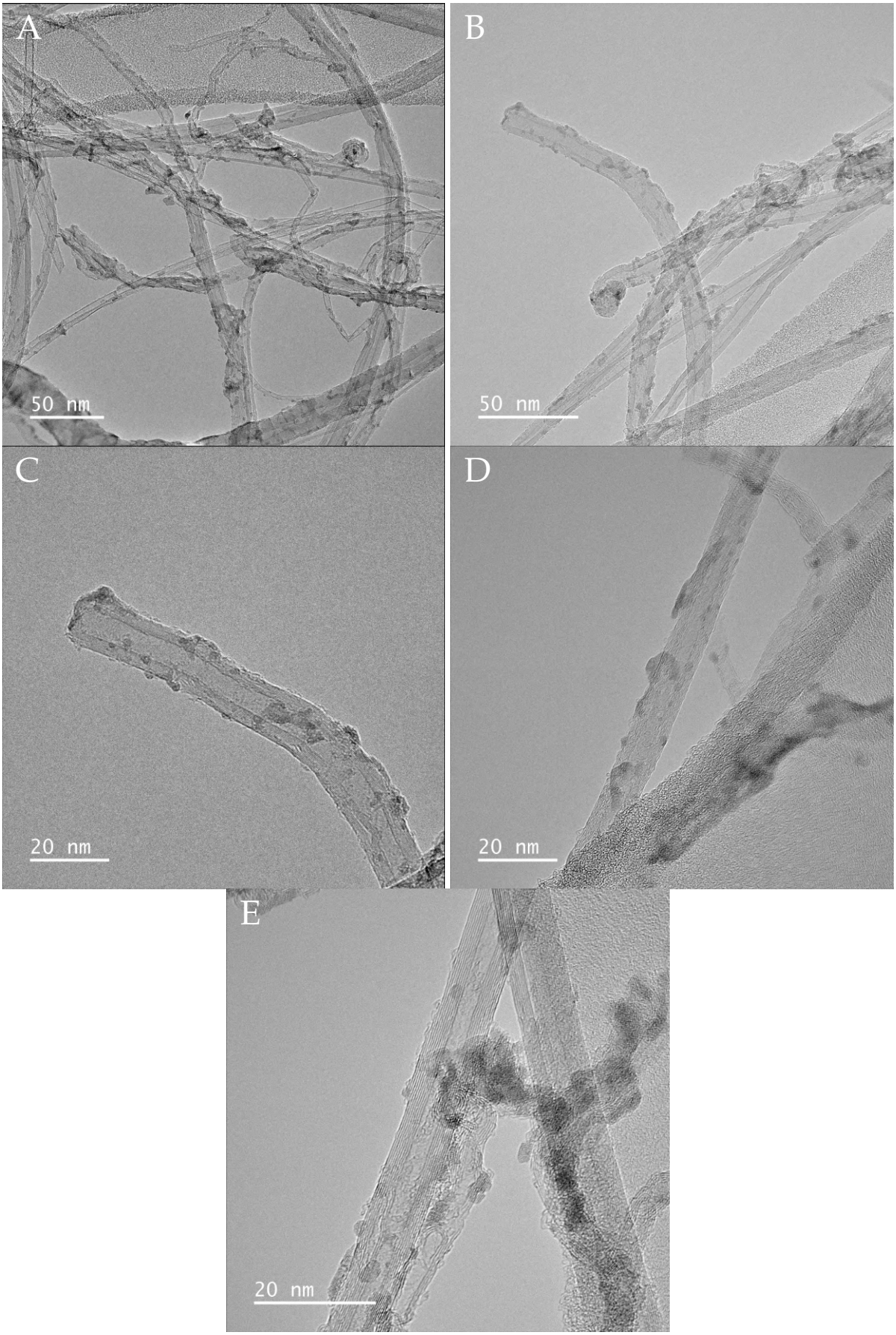


Figure 5.27: (A) TEM image of catalyst In-25 Opt showing an overview of multiple MWNTs highlighting the ubiquity of In on the surface of the MWNTs; (B) TEM image of In-25 Opt showing a bundle of MWNTs with In on the surface of the MWNTs; (C) Zoomed image of Fig. 5.27B highling the MWNT tip seen in the image. Notably, there are multiple small In clusters on close proximity to each other and the MWNT has an open tip. Additionally, an In cluster on the internal cavity is not encapsulated but rather resting on top of the tube due to some of the cluster overlapping with the MWNT sidewall; (D) TEM image of In-25 Opt in which a MWNT can be observed with multiple In aggregations on the surface of a MWNT; (E) TEM image of In-25 of a MWNT in which multiple small In aggregates can be observed and also a large semi-crystalline In aggregation can be observed in a MWNT interstitial site. Notably, no encapsulated In is present.

As seen in Fig. 5.27, there is a observable increase in the amount of In aggregates present on the surface of the MWNT when compared to prior catalysts Figs. 5.23 to 5.26). From Fig. 5.27A it is immediately apparent that each MWNT has multiple In aggregations of small size on the surface rather than the previously seen singular crystalline aggregates seen in Figs. 5.24C and 5.25B for example. Additionally, the surface aggregates are not all crystalline, appearing in a mix of shapes along the surface, with various amorphous In seen in Fig. 5.27D and crystalline and circular nanoclusters of In visible in Fig. 5.27E.

The intended consequences of the modified synthesis (Section 5.4.1) appear to have been achieved, with the MWNT cleaning resulting in a much larger amount of surface In sites, and the MWNT pre-filling with ethylene glycol appears to have almost entirely prevented In encapsulation, with only single encapsulated metal site visible in the overview image (Fig. 5.27A), and even that observed encapsulated metal cannot be differentiated from the MWNT internal growth catalyst.

Interestingly, in comparison to the catalyst with the same metal loading and decomposition temperature conditions, In-25R, it can be seen that the removing amorphous carbon on the surface of the MWNT decreased the aggregate size rather than increasing it, which was expected due to amorphous surface sites aiding in the prevention of surface migration, as was seen in the case of Cu/CoPPc/MWNT (, where the amorphous CoPPc polymer layer prevented Cu nanoparticle migration and aggregation which is to be expected on similar graphitic supports.[68] The reason for this lowered degree of aggregation is unclear, however there are two possible explanations for this observed difference, The first being that if the thin low contrast layer on the In aggregate seen Fig. 5.23E is assumed to be a carbon shell, then it is possible that the amorphous carbon both promotes carbon shell growth on In, and this carbon shell stabilises larger In aggregate formation. The second, more likely explanation would be that the amorphous carbon makes surface adsorption of In less favourable, so that only In only binds to graphitic regions and thus making lowered degree of aggregation due to the fact that less In is present on the surface of In-25R, meaning that the observed In aggregates are stochastically larger.

5.4.2.2 Other characterisation

For weight loading determination, TGA of In-25, In-35, In-50, In-25R, and In-25 Opt was conducted to calculate the actual metal loading and to observe changes in the decomposition temperature depending on metal loading (Fig. 5.28).

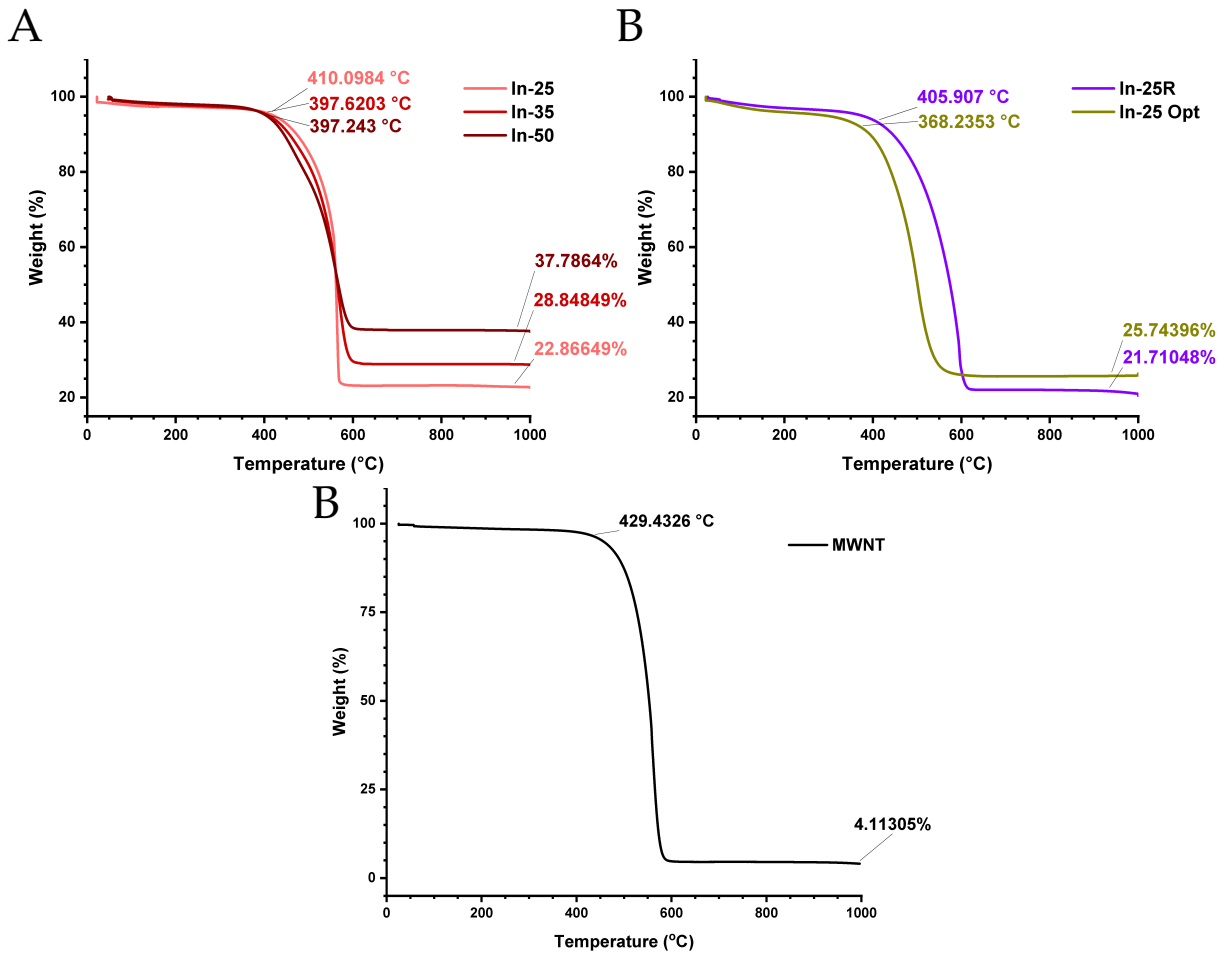


Figure 5.28: (A) TGA plot of In-25, In-35, and In-50 in air with initial decomposition temperature and final weight % labelled; (B) TGA plot of In-25R and In-25 Opt in air with initial decomposition temperature and final weight % labelled; (C) TGA plot of MWNT in air with initial decomposition temperature and final weight % labelled.

As seen in Fig. 5.28, the decomposition temperature of In-25, In-35, In-50, and In-25R is around $30 - 40$°C compared to bare MWNTs with the value increasing when the weight loading is increased above 25%. Interestingly, In-25 Opt however has a much larger decrease in decomposition temperature, with a difference of 61°C between In-25 Opt and the bare MWNTs, which indicates the synthesis was successful in increasing the amount of $In_2(NO_3)$ on the surface of the MWNT, giving it a greater catalytic effect towards thermal decomposition.[58]

By utilising the same method as Section 5.2.2.2, an accurate In_2O_3 and In weight loading can be calculated for In-25, In-35, In-50, In-25R, and In-25 Opt via Section 5.2.2.2. To 2 d.p. the In_2O_3 weight loading of In-25, In-35, In-50, In-25R, and In-25 Opt are calculated to be 18.75%, 24.73%, 33.67%, 17.60%, and 21.63% respectively, and the In weight loadings therefore are 15.51%, 20.46%, 27.85%, 14.55%, and 17.90% respectively. Similarly to both Pb/MWNT and Bi/MWNT (Sections 5.2.2.2 and 5.3.2.2), there is a disparity between the theoretically targeted weight loading and the real weight loadings of each of the

catalysts, and compared to the prior catalysts, the weight loadings are closer in value to Bi/MWNT, meaning the reason for this discrepancy is most likely due to the same factors that impacted Bi/MWNT, those being variable hydration of the crystal, transfer losses, and lower In_2O_3 adsorption affinity to MWNT. Interestingly, In-25 Opt has a higher In weight loading than In-25 and In-25R, being $\sim 3-4\%$ higher, and is also associated with the synthesis which restricted access to the nanotube inner channel, implying more In on the surface resulted in promoted In adsorption and therefore higher loading.

5.4.3 Electrochemistry

5.4.3.1 Voltammetry

To evaluate the electrochemical performance and electrocatalytic activity of the three In/MWNT catalysts decomposed at 350°C: In-25, In-35, and In-50 (Fig. 5.29); and the two In/MWNT catalysts decomposed at 290°C: In-25R and In-25 Opt, LSV using a RDE at 1600 rpm at a scan rate of 0.005 V s^{-1} was utilised.

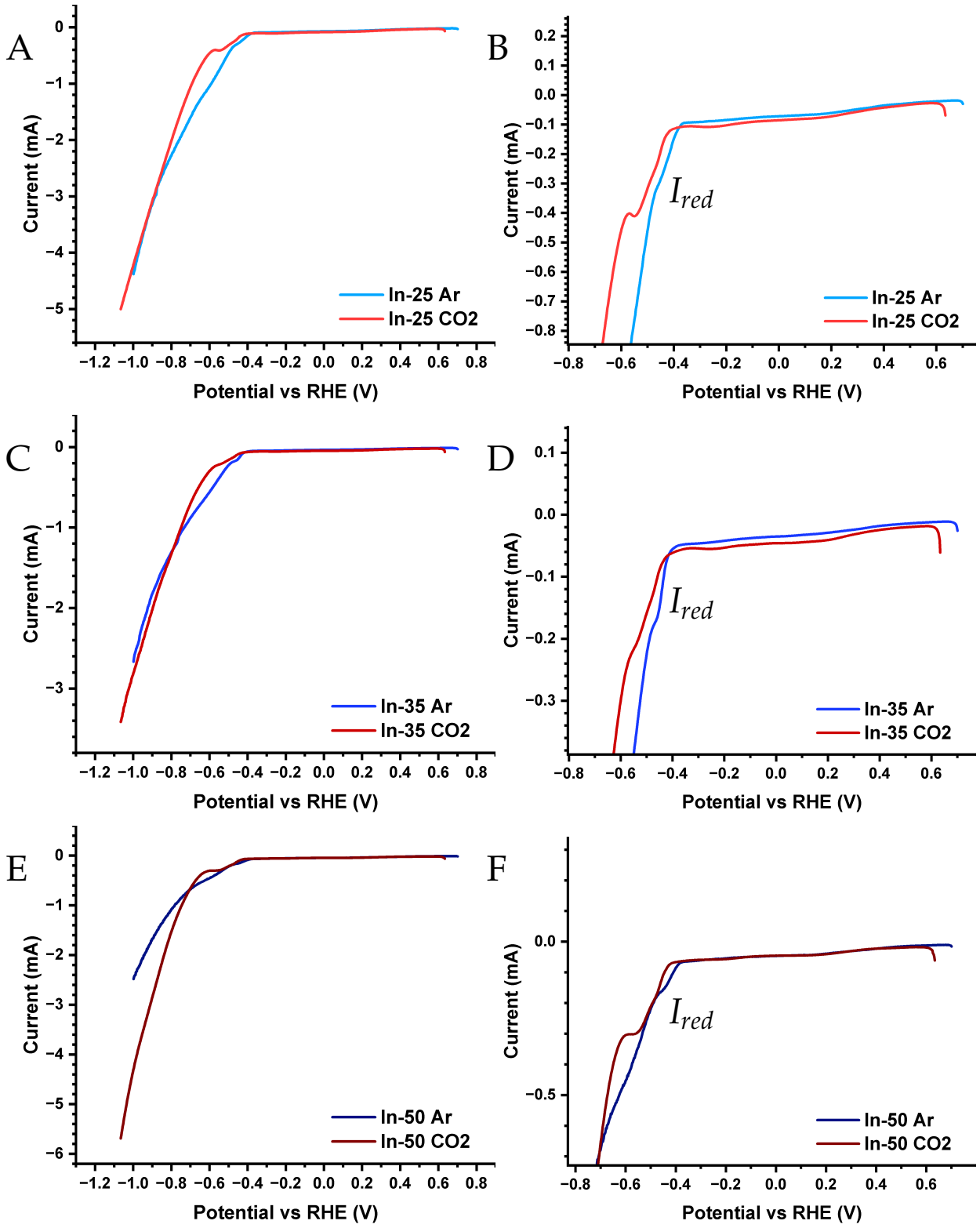


Figure 5.29: (A) LSV of In-25 using an RDE in Argon and CO_2 saturated 0.5 M $KHCO_3$ at 0.005 V s^{-1} at a rotation rate of 1600 rpm; (B) LSV from Fig. 5.29A with reduction peaks labelled, voltammogram has been zoomed into the non CO_2RR region for clarity; (C) LSV of In-35 using an RDE in Argon and CO_2 saturated 0.5 M $KHCO_3$ at 0.005 V s^{-1} at a rotation rate of 1600 rpm; (D) LSV from Fig. 5.29C with reduction peaks labelled, voltammogram has been zoomed into the non CO_2RR region for clarity; (E) LSV of In-50 using an RDE in Argon and CO_2 saturated 0.5 M $KHCO_3$ at 0.005 V s^{-1} at a rotation rate of 1600 rpm; (F) LSV from Fig. 5.29E with reduction peaks labelled, voltammogram has been zoomed into the non CO_2RR region for clarity.

From the LSVs of In-25, In-35, and In-50, one reduction peak: I_{red} can be seen at ~ -0.54 V vs RHE in CO_2 saturated electrolyte and ~ -0.41 V vs RHE in Ar saturated electrolyte, which corresponds to the In^0/In^{3+} reduction.[42] At all wt%s and electrolyte gas saturations this reduction occurs at a similar potential, with the difference between CO_2 and Ar resulting from the RHE conversion, as the original Ag/AgCl scale puts these reduction peak at a near idential potential. The only differences observed between the catalysts being the CO_2RR onset potential and current density j. The onset potentials of In-25, In-35, and In-50 in CO_2 saturated electrolyte being relatively constant at around ~ -0.6 V vs RHE and in Ar saturated electrolyte being less clear, due to two separate onset gradients in the CO_2RR region, with the first beginning at ~ 0.48 V vs RHE and the second at ~ -0.66 — -0.8 V vs RHE. This is most clear in the LSVs of In-50 (Figs. 5.29E and 5.29F), in which the gradient (G_1) post peak I_{red} at ~ 0.48 V vs RHE continues at a consistent rate until -0.6 V vs RHE where there is a shift to a steeper gradient (G_2) and then slowly the gradient increases as the catalytic tail continues as is for the rest of the LSV (Fig. 5.30).

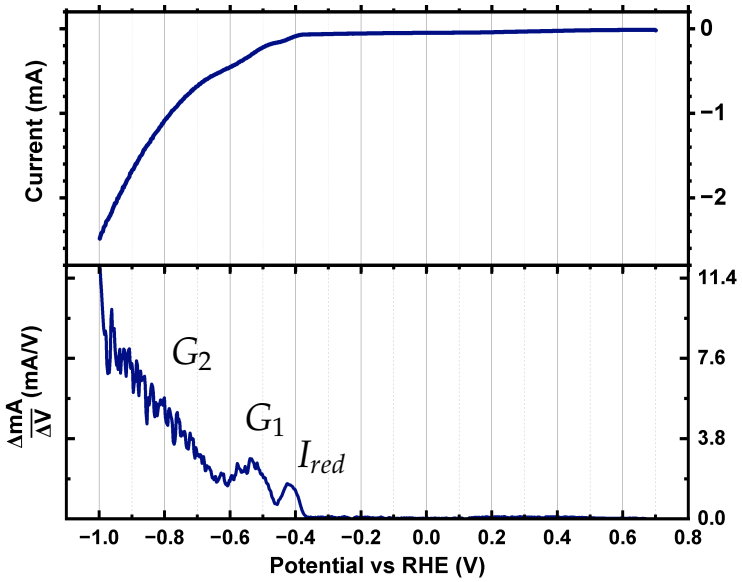


Figure 5.30: LSV of In-50 in Ar saturated electrolyte (top) and Derivative plot of the LSV of In-50 in Ar saturated electrolyte (bottom) with points of gradient change in the CO_2RR region and gradient change associated with the the reduction peak labelled as G_1 and G_2, and I_{red} respectively. (Derivative plot has been smoothed via application of a Savitzky-Golay filter with a window size of 10 to reduce noise in the derivative plot resulting from small instrument fluctuations.)

The reason for this multi-stepped catalytic region in Ar saturated electrolyte is not immediately clear, however it may possibly be attributed to $In(OH)_3$ formation and it's formation of CO_2 intermediates.

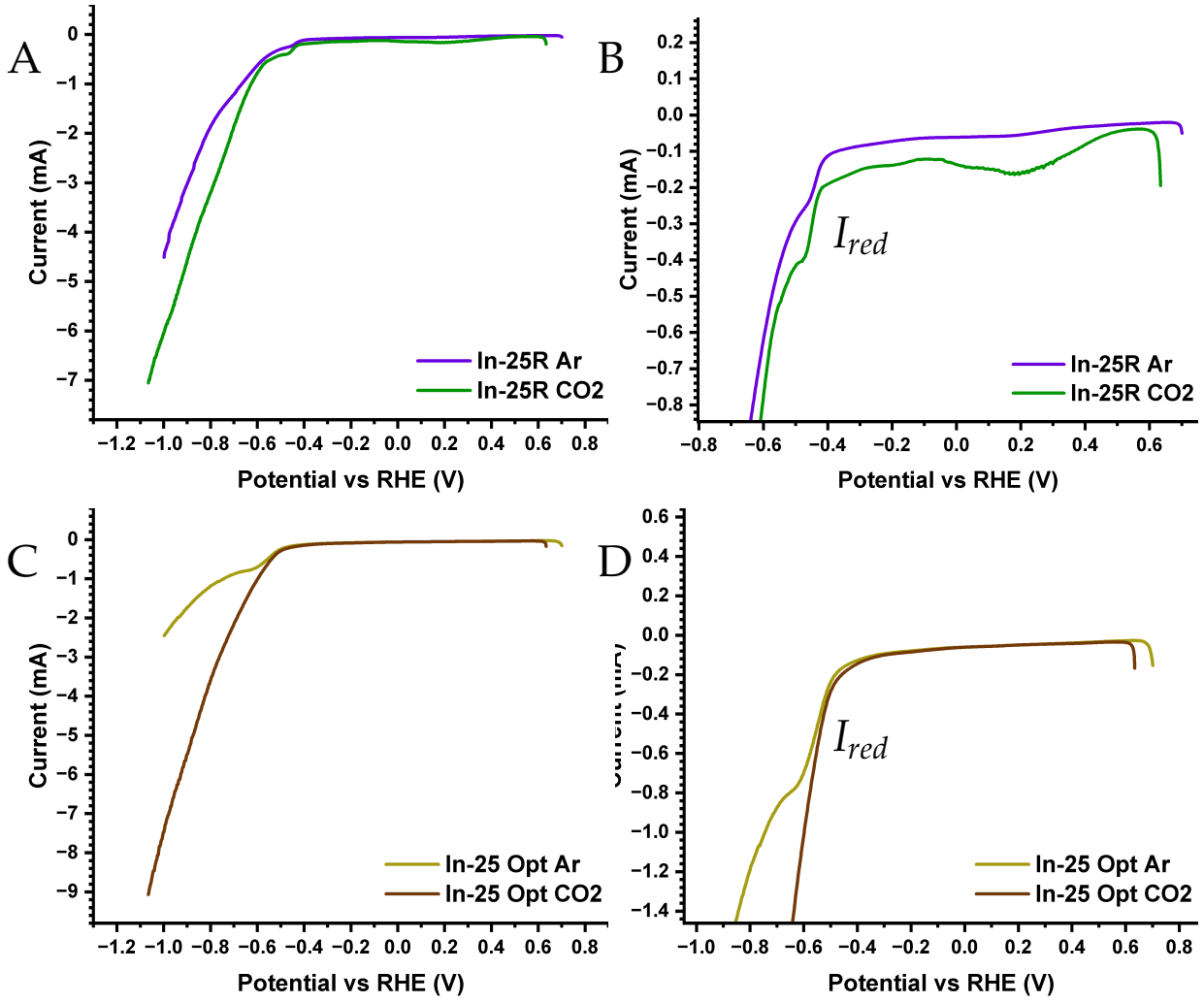


Figure 5.31: (A) LSV of In-25R using an RDE in Argon and CO_2 saturated 0.5 M $KHCO_3$ at 0.005 V s^{-1} at a rotation rate of 1600 rpm; (B) LSV from Fig. 5.31A with reduction peaks labelled, voltammogram has been zoomed into the non CO_2RR region for clarity; (C) LSV of In-25 Opt using an RDE in Argon and CO_2 saturated 0.5 M $KHCO_3$ at 0.005 V s^{-1} at a rotation rate of 1600 rpm; (D) LSV from Fig. 5.31C with reduction peaks labelled, voltammogram has been zoomed into the non CO_2RR region for clarity

Comparing the LSVs of the two 290°C decomposition catalysts: In-25R and In-25 Opt (Fig. 5.31) to the 350°C decomposition catalysts (Fig. 5.29) it can be observed that the redox behaviour and onset potential remains generally the same, with peak I_{red} present and an onset potential of ~ -0.6 observed for both In-25R and In-25 Opt. In the In-25R CO_2 LSV, A reduction peak centred at ~ -0.2 V vs RHE is present, and is unique to this catalyst and LSV, as it is not present in the CV. The most likely attribution for this reduction is the In^+/In transition which occurs at a potential of 0.42 V vs RHE[69] due to the peak beginning around 0.4 V vs RHE. If the In^+/In assignment is presumed correct, due to the fact that peak shape in voltammetry resulting from the oxidation/reduction rate of the surface confined species,[70] it can be implied that the In^+/In reduction is a

slow process, as the breadth of the peak spans 0.4 V vs RHE. It is unlikely that the In^+/In assignment is the case however, as due to the presented LSV in Fig. 5.31A making use of a fresh electrode, it would require the presence of In_3O, which typically only forms at decomposition temperatures of $\sim$ 700oc.[71] A more likely explanation can be found in the LSV of bare MWNT in Ar saturated solution (CREF), which presents a very similar peak centred around the same potential of -0.2 V vs RHE, but with a current density around $\times 100$ weaker. This potential would suggest this peak is attributed the reduction of the Fe internal catalyst of the MWNT, with the redox couple of Fe^{3+}/Fe,[69] however this also cannot be confidently assigned due to the TEM of In-25R Fig. 5.26 not showing evidence of significant structure damage to allow a sufficiently large amount of the internal catalyst to be reduced. Additionally, this reduction was only prominent in the CO_2 saturated LSV, presenting additional complications when trying to assign this reduction as it must be either pH dependant or involve CO_2 in some form. Therefore, due to the multiple possibilities and lack of literature exploring the voltammetry of In at positive enough potentials, the assignment of this peak remains inconclusive.

Looking further on at the LSV results of In-25 Opt, the LSV results present potential for the most promising electrocatalyst explored in this body of work Figs. 5.31C and 5.31D, due to the immediately evident difference between the CO_2 and Ar traces. The current at -1.05 V vs RHE is the largest observed out of all of the In catalysts, at 9 mA with a difference between the CO_2 and Ar currents being 6.5 mA. The most interesting facet of these LSVs is the fact there is a difference in onset potential found between the CO_2 and Ar saturations, unlike other In catalysts previously explored in which the onset potential was the same at $\sim$ -0.6 V vs RHE, the CO_2 saturated LSV presents a catalytic onset potential of -0.48 V vs RHE, whilst the Ar saturated LSV has an onset potential of -0.65 V vs RHE. Additionally, there is a stark difference in the gradient of the catalytic region found past the onset potentials for each LSV, with the CO_2 saturated LSV being markedly steeper than the Ar LSV, indicating different product selectivities between the two catalysts, further indicating that In-25 Opt does not favourably conduct the HER.

To further evaluate and analyse the electrochemical behaviour of the three In/MWNT catalysts decomposed at 350°C: In-25, In-35, and In-50 (Fig. 5.29); and the two In/MWNT catalysts decomposed at 290°C: In-25R and In-25 Opt, CV using a RDE at 1600 rpm at a scan rate of 0.005 V s^{-1} was utilised.

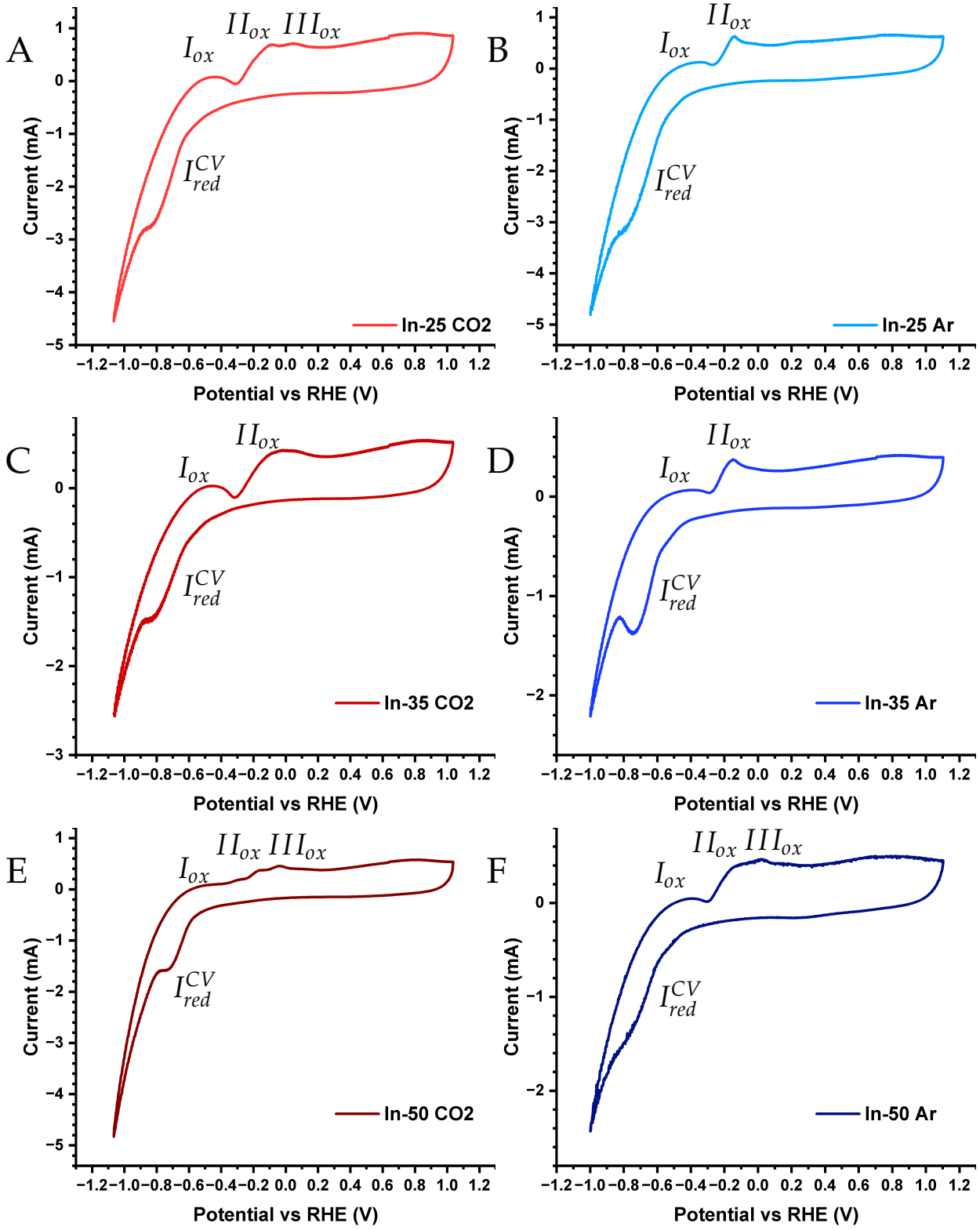


Figure 5.32: (A) CV of In-25 using a RDE in CO_2 saturated 0.5 M $KHCO_3$ at 0.05 V s^{-1} at a rotation rate of 1600 rpm with reduction and oxidation peaks labelled; (B) CV of In-25 using a RDE in Ar saturated 0.5 M $KHCO_3$ at 0.05 V s^{-1} at a rotation rate of 1600 rpm with reduction and oxidation peaks labelled; (C) CV of In-35 using a RDE in CO_2 saturated 0.5 M $KHCO_3$ at 0.05 V s^{-1} at a rotation rate of 1600 rpm with reduction and oxidation peaks labelled; (D) CV of In-35 using a RDE in Ar saturated 0.5 M $KHCO_3$ at 0.005 V s^{-1} at a rotation rate of 1600 rpm with reduction and oxidation peaks labelled; (E) CV of In-35 using a RDE in CO_2 saturated 0.5 M $KHCO_3$ at 0.05 V s^{-1} at a rotation rate of 1600 rpm with reduction and oxidation peaks labelled; (F) CV of In-35 using a RDE in Ar saturated 0.5 M $KHCO_3$ at 0.005 V s^{-1} at a rotation rate of 1600 rpm with reduction and oxidation peaks labelled.

As the CVs were conducted with the same electrodes used for the LSVs, differing electrochemical behaviour will be observed due to the formation of $In(OH)_3$ from In after returning to Open Circuit Potential (OCP) as opposed to the $In_2O_3/In(OH)_3$ interconversion. This is relevant due to the hydroxide being catalytically active towards CO_2 (Fig. 5.33), but electrochemically silent.[42] Additionally, the transformation of In_2O_3 to $In(OH)_3$ is a slow process, on the timescale of $100\,s$,[42] meaning the CVs will reflect a combined $In_2O_3 + In(OH)_3$ system, to reflect this, peak I_{red} has been relabelled to I_{red}^{CV}.

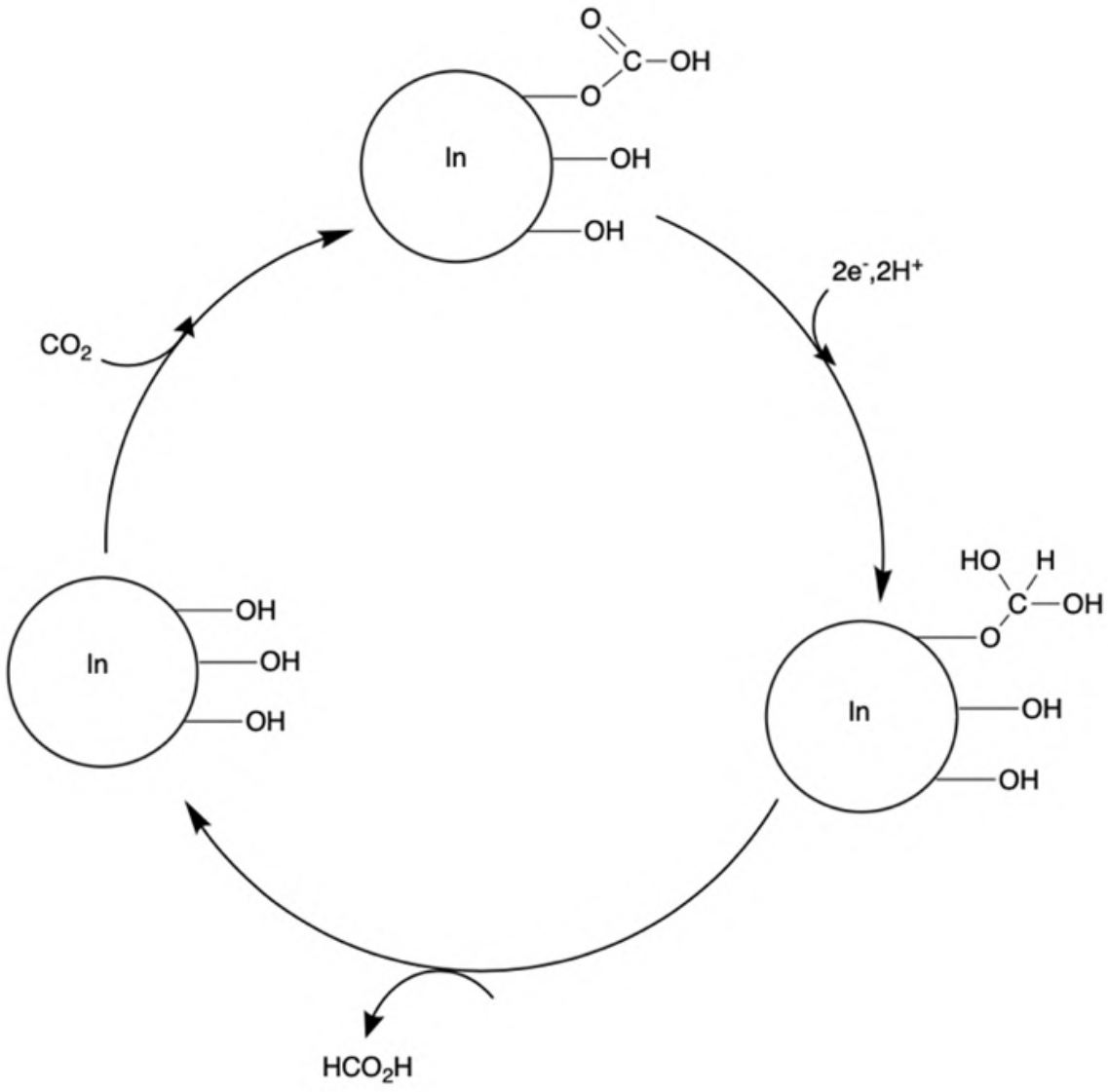


Figure 5.33: Catalytic cycle of for $In(OH)_3$ HCOOH production from CO_2. Figure reproduced based on the cycle outlined by Detweiler *et al*.[42]

Comparing the CVs of the 350°C decomposition temperature catalysts (Fig. 5.32) to the LSVs (Fig. 5.29), it can be seen that peak $I^{CV}{}_{red}$ has shifted in the CV to be centred at -0.75

— -0.8 V vs RHE from -0.6 V vs RHE in the LSV, coinciding with the reduction of the interfacial species of $In-CO_3^-$.[42] It is important to note that $In-CO_3^-$ is stated to be redox inactive,[42] therefore no corresponding oxidation peak is assignable. This assignment is further supported by the fact that peak $I^{CV_{red}}$ now coincides with the catalytic region, as the onset potential for the catalysts has shifted more positively from the LSVs to -0.45 V vs RHEs in the CV.

The oxidation peaks present in the CV (Figs. 5.32 and 5.34) are more challenging to assign due to only two of the three observed peaks resulting from well defined In redox pairs, these peaks being the $In \longrightarrow In_2O_3$ and the $In_2O_3 \longrightarrow In(OH)_3$ processes outlined by Detweiler *et al*.[42] The $In \longrightarrow In_2O_3$ process corresponds to peak II_{ox} and the $In_2O_3 \longrightarrow In(OH)_3$ process corresponds to peak III_{ox},[42,43] leaving the I_{ox} peak as the remaining peak to be assigned. Peak I_{ox} appears unique to this work as there is no equivalent present in electrochemical studies of In,[42,43,72] and due to the fact that $In-CO_3^-$ has equivalent oxidation, assignment of this peak remains challenging, especially due to the unorthodox "dip" in the current despite being on the oxidation wave. Due to the placement of this peak being situated after the forward sweep out of the catalytic tail, it would logically indicate that this peak is associated with the oxidation of a CO_2RR related species, thus the only logical assignment that can be given for this peak would be the corresponding oxidation of the 2 electron PCET reduction to $In-OC(OH)_2H$ intermediate in the catalytic cycle towards formate (Fig. 5.33).

The maximum current densities reached in the CV of In-25 in CO_2 saturated electrolyte (Fig. 5.32A)is unexpectedly lower than its Ar saturated counterpart Fig. 5.32B, the reason for this is is unclear, however given the TEM images showing most In sites being encapsulated or in large aggregates, and also the poor electrocatalytic results, it can be assumed that the encapsulation greatly hindered the $In_2O_3 \longrightarrow In(OH)_3$ process, so the In-25 catalyst does not possess the same selectivity towards CO_2 as the higher wt% catalysts.

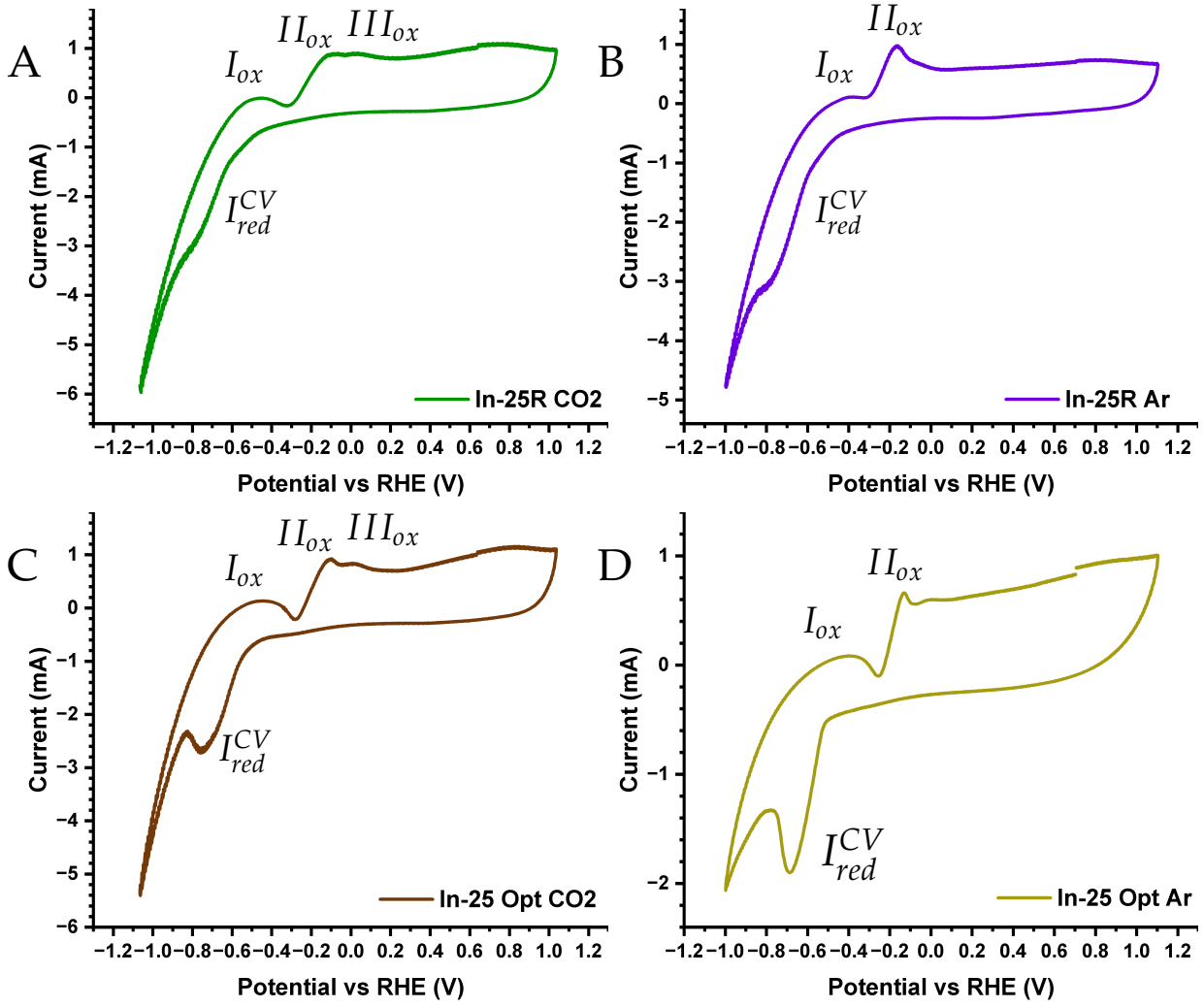


Figure 5.34: (A) CV of In-25R using a RDE in CO_2 saturated 0.5 M $KHCO_3$ at 0.05 V s^{-1} at a rotation rate of 1600 rpm with reduction and oxidation peaks labelled; (B) CV of In-25R using a RDE in Ar saturated 0.5 M $KHCO_3$ at 0.05 V s^{-1} at a rotation rate of 1600 rpm with reduction and oxidation peaks labelled; (C) CV of In-25 Opt using a RDE in CO_2 saturated 0.5 M $KHCO_3$ at 0.05 V s^{-1} at a rotation rate of 1600 rpm with reduction and oxidation peaks labelled; (D) CV of In-25 Opt using a RDE in Ar saturated 0.5 M $KHCO_3$ at 0.005 V s^{-1} at a rotation rate of 1600 rpm with reduction and oxidation peaks labelled.

From the CVs of the 290oc decomposition temperature catalysts: In-25R and In-25 Opt, similar behaviour to the 350 °C catalysts is observed. Notably, the reduction in In encapsulation in In-25 Opt increases peak I^{CV}_{red}s definition, having a more clearly defined peak shape Figs. 5.34C and 5.34D. This is expected due to the much higher catalytic activity of In-25 Opt when compared to the other In catalysts. This much higher catalytic activity is further evidenced by the same large difference between CO_2 and Ar current densities achieved, with the CO_2 saturated electrolyte achieving $\sim$ 3.5 mA greater current than the Ar saturated electrolyte.

5.4.3.2 Electrochemical Impedance Spectroscopy

EIS* discussion

5.4.4 Electrocatalysis

To test the catalytic activity of In/MWNT, initially a range of potentials were tested for CO_2 reduction to produce formate for one hour with the In-25R catalyst due to it being the first catalyst synthesised: -0.85, -0.95, -1.05, and -1.15 V vs RHE (Fig. 5.35). Out of these potentials, -1.05 V vs RHE showed the highest FE towards formate at 59.5%. With -1.05 -1.05 V vs RHE determined as the optimal potential for formate production, this potential was used for electrocatalytically testing all In/MWNT catalysts.

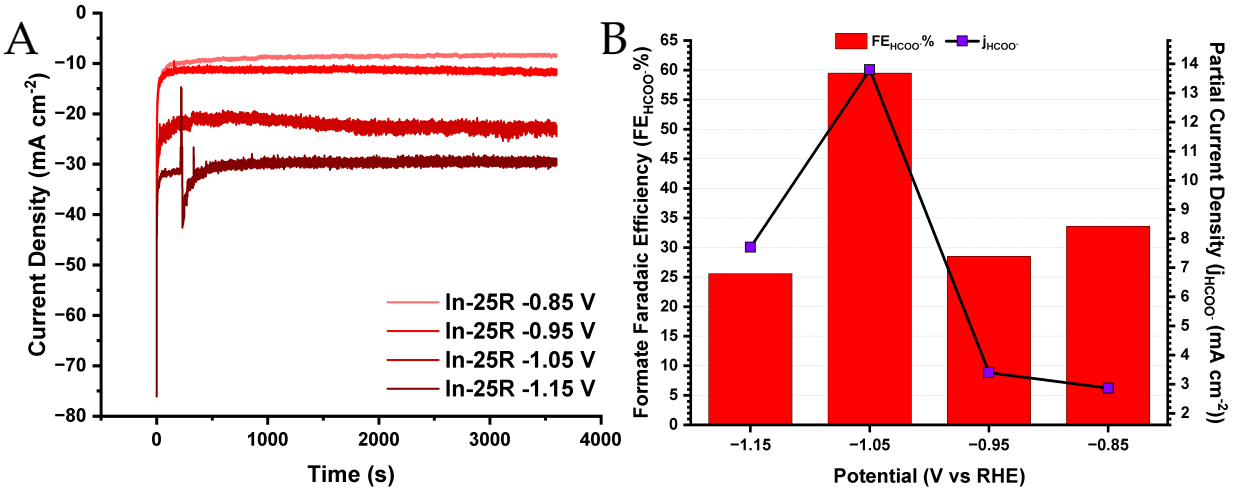


Figure 5.35: (A) Comparison of chronoamperometry traces of In-25R at potentials ranging from −0.95 to −1.15 V vs RHE; (B) Comparison of formate FEs of In-25R at potentials ranging from −0.95 to −1.15 V vs RHE.

As seen in Fig. 5.35A, all current densities were stable over the course of 1 hour, apart from the -1.15 V vs RHE chronoamperometry, which encountered an initial disruption to the current due to an issue resulting from improper connection to the working electrode terminal which was resolved during the experiment and can be seen as spikes in the chronoamperometry trace.

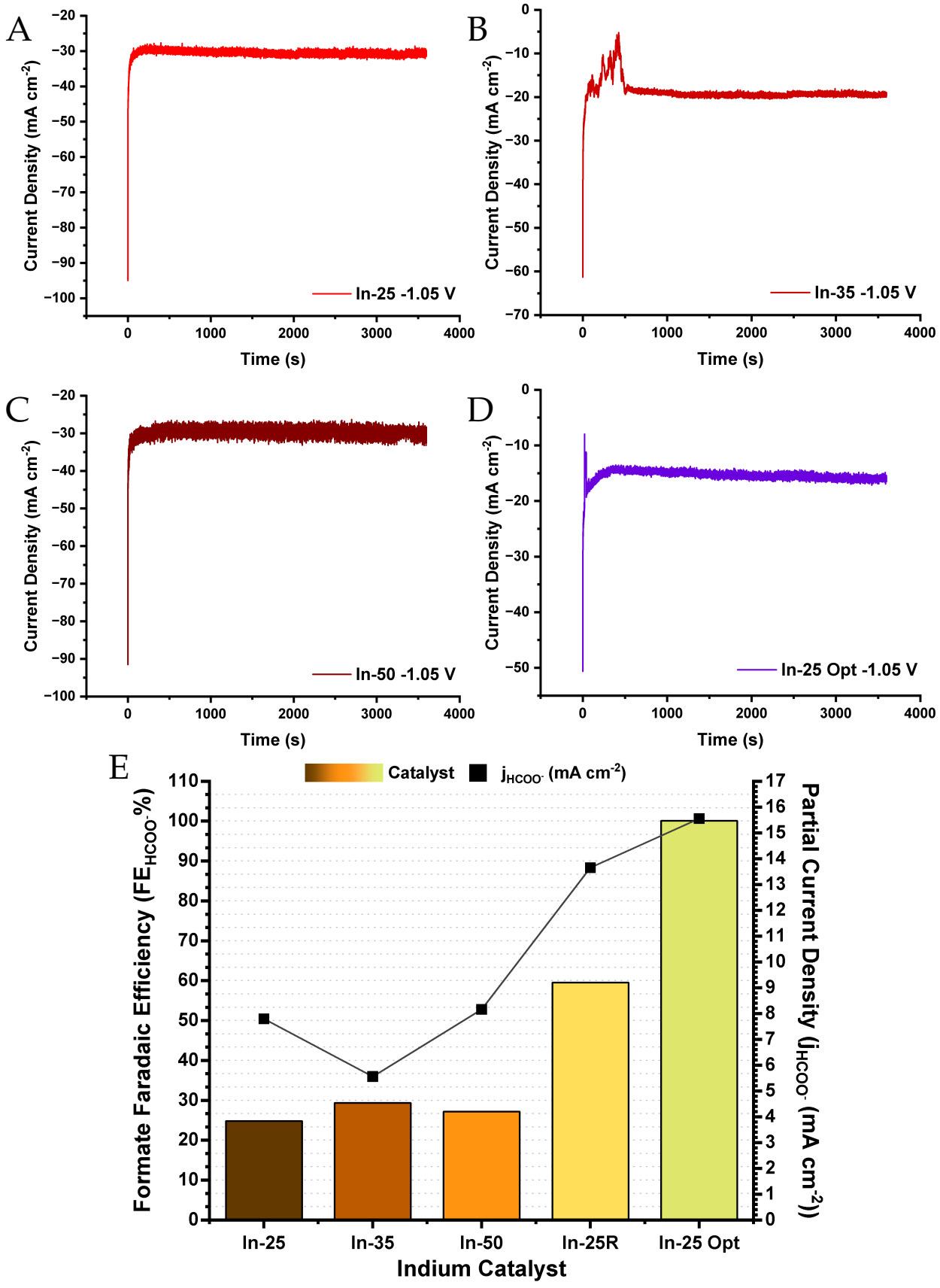


Figure 5.36: (A) Chronoamperometry trace of In-25 at -1.05 V vs RHE; (B) Chronoamperometry trace of In-25 at -1.05 V vs RHE; (C) Chronoamperometry trace of In-25 at -1.05 V vs RHE; (D) Chronoamperometry trace of In-25 at -1.05 V vs RHE; (E) All tested In catalysts Faradaic efficiency and partial current densities towards formate at -1.05 V vs RHE.

Conducting electrocatalysis experiments at -1.05 V vs RHE for the rest of the In catalysts (Fig. 5.36), it can be seen that as predicted, In-25 Opt is by far the best catalysts towards formate, with near 100% Faradaic efficiency towards formate achieved with a partial current density for formate of 15.5 mA cm^{-2}, which is as the time of writing, the highest performing In CO_2RR catalyst in literature. Additionally, the high performance of In-25 Opt is bolstered by the fact it was achieved with the lowest metal weight loading that was tested in this work, meaning this catalyst is much more cost effective than many In catalysts in literature, as it requires a fraction of the metal to be active and selective.

5.5 Conclusions

Overall, In was the highest performing p-block metal CO_2RR catalyst tested in this work, with the lowest performing In catalyst: In-25, over doubling the Faradaic efficiency of the next best p-block metal tested: Bi-50, from 11.15% with Bi-50 to 24.8% with In-25 (Fig. 5.37).

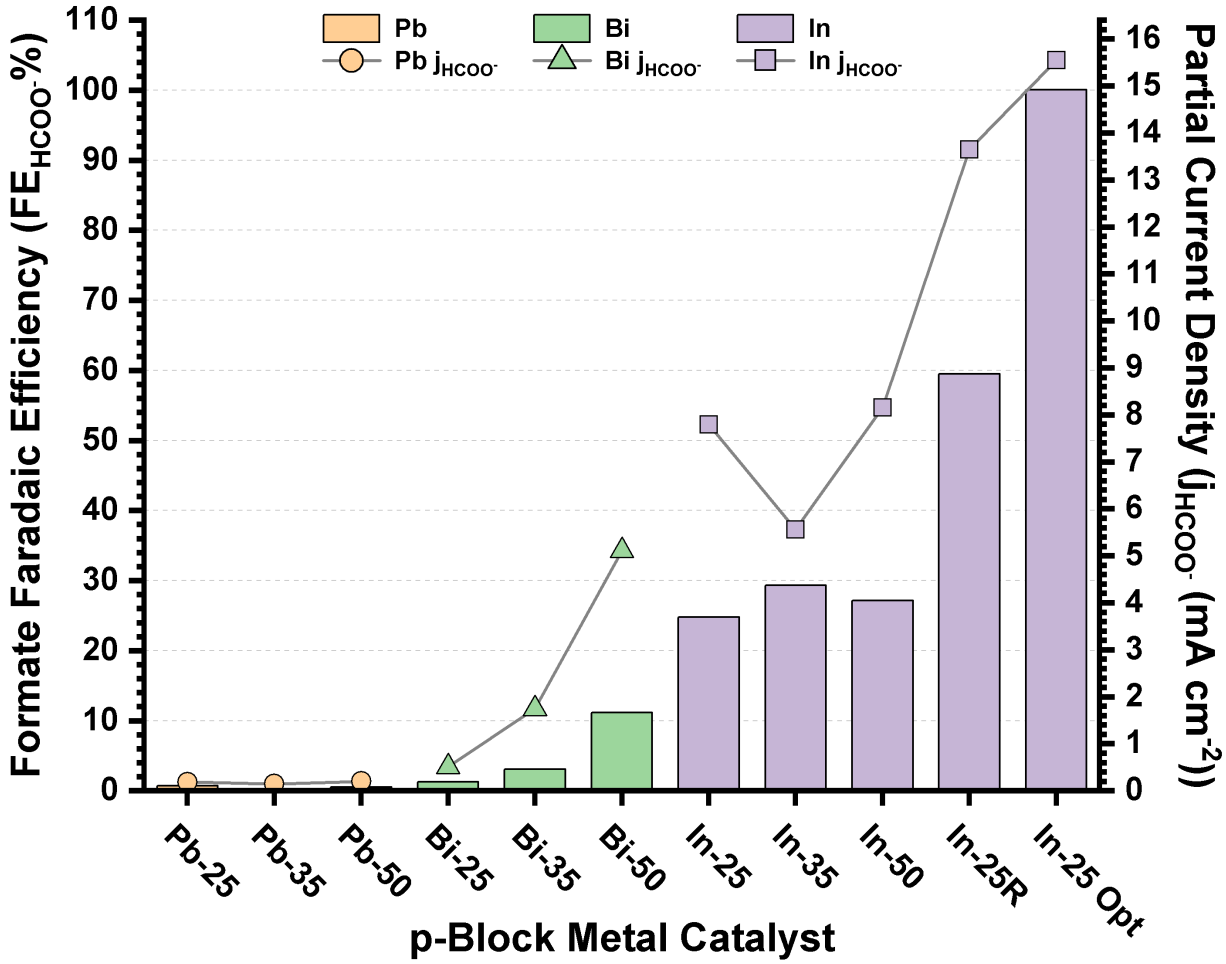


Figure 5.37: Faradaic efficiencies and partial current densities towards formate for all p-block metal catalysts tested throughout Chapter 5.

From Fig. 5.37, a general trend can be observed, that with increasing metal wt%, there is an increase in both FE and also *j*, except in the case of In-35, in which the FE was higher than the trend would predict, but the partial current density towards formate was much lower, resulting from the low current density achieved with the In-35 (Fig. 5.36B).

More importantly however, it can be seen that in the case of In, the factors influencing the nanostructure of the catalyst, such as: decomposition temperature and nature of the MWNT surface; have a much higher impact on the catalytic performance than metal weight loading, as the two lower 290°C decomposition temperature catalysts: In-25R and In-25 Opt, show a dramatic increase in formate selectivity from the higher temperature and higher weight loading 350°C decomposition temperature catalysts. The reason for the catalyst nanostructure having a much more dominant effect on the catalyst performance than the metal weight loading is evident from the TEM images of the In catalysts Section 5.4.2.1 and Figs. 5.24 to 5.27, as the both lower temperature catalysts: In-25R and In-25 Opt, showed less crystalline In structures than the higher temperature catalysts, and between the lower temperature catalysts, the dramatic increase in surface loading of In and decrease of encapsulated In appear to be the largest contributing factors towards higher formate selectivity.

The poor CO_2RR activity observed for Pb/MWNT is disappointing, as even accounting for the lower actual amounts of metal resulting from the higher atomic weight not being reflected in planning the syntheses with weight% in mind, it still dramatically underperformed when compared to Bi/MWNT which has a similar atomic weight, and also performance predicted by literature. With the insights gained from the production of In-25 Opt, the reason for this poor performance may be attributed to incredibly poor surface adsorption of the metal to the MWNT resulting from the amorphous carbon on the MWNT surface.

Chapter 5 Bibliography

(1) Y. Hori, K. Kikuchi and S. Suzuki, "Production of Co and Ch4 in Electrochemical Reduction of Co2 At Metal Electrodes in Aqueous Hydrogencarbonate Solution", *Chemistry Letters*, 1985, **14**, 1695–1698.

(2) A. L. Wani, A. Ara and J. A. Usmani, "Lead toxicity: A review", *Interdisciplinary Toxicology*, 2015, **8**, 55–64.

(3) S. Li, Y. Liu, D. Xu and H.-g. Wang, "Conjugated polycopper phthalocyanine as the anode-active material with high specific capacity for lithium-organic batteries", *Materials Letters*, 2023, **333**, 133682.

(4) C. H. Lee and M. W. Kanan, "Controlling H+ vs CO2 Reduction Selectivity on Pb Electrodes", *ACS Catalysis*, 2015, **5**, 465–469.

(5) Y. Xing, M. Cui, P. Fan, J. Ren, C. Zhang, N. Li, X. Wen and X. Ji, "Efficient and selective electrochemical reduction of CO2 to formate on 3D porous structured multi-walled carbon nanotubes supported Pb nanoparticles", *Materials Chemistry and Physics*, 2019, **237**, 121826.

(6) Federal Institute for Geosciences and Natural Resources, *Preismonitor (Report)*, tech. rep., Federal Institute for Geosciences and Natural Resources, 2020, p. 3.

(7) K. Pyrzynska, *Recent Applications of Carbon Nanotubes for Separation and Enrichment of Lead Ions*, 2023.

(8) J. S. Yoo, R. Christensen, T. Vegge, J. K. Nørskov and F. Studt, "Theoretical Insight into the Trends that Guide the Electrochemical Reduction of Carbon Dioxide to Formic Acid", *ChemSusChem*, 2016, **9**, 358–363.

(9) C. X. Zhao, Y. F. Bu, W. Gao and Q. Jiang, "CO2 Reduction Mechanism on the Pb(111) Surface: Effect of Solvent and Cations", *Journal of Physical Chemistry C*, 2017, **121**, 19767–19773.

(10) S. Ikeda, T. Takagi and K. Ito, "Selective formation of formic acid, oxalic acid, and carbon monoxide by electrochemical reduction of carbon dioxide", *Bulletin of the Chemical Society of Japan*, 1987, **60**, 2517–2522.

(11) M. Azuma, K. Hashimoto, M. Hiramoto, M. Watanabe and T. Sakata, "Electrochemical Reduction of Carbon Dioxide on Various Metal Electrodes in Low-Temperature Aqueous KHCO 3 Media", *Journal of The Electrochemical Society*, 1990, **137**, 1772–1778.

(12) H. Ji Jang, J. Hyun Yang, J. Young Maeng, Y. Jun Kim, C. Kyun Rhee and Y. Sohn, "Electrochemical CO2 reduction over Pb electrodes modified with group 10, 11, and 14 elements", *Applied Surface Science*, 2022, **604**, 154438.
(13) A. Murata and Y. Hori, "Product selectivity affected by cationic species in electrochemical reduction of CO2 and CO at a Cu electrode", *Bulletin of the Chemical Society of Japan*, 1991, **64**, 123–127.
(14) S. Ringe, E. L. Clark, J. Resasco, A. Walton, B. Seger, A. T. Bell and K. Chan, "Understanding cation effects in electrochemical CO2 reduction", *Energy and Environmental Science*, 2019, **12**, 3001–3014.
(15) M. König, J. Vaes, E. Klemm and D. Pant, "Solvents and Supporting Electrolytes in the Electrocatalytic Reduction of CO2", *iScience*, 2019, **19**, 135–160.
(16) J. E. Pander, J. W. J. Lum and B. S. Yeo, "The importance of morphology on the activity of lead cathodes for the reduction of carbon dioxide to formate", *Journal of Materials Chemistry A*, 2019, **7**, 4093–4101.
(17) M. Fan, S. Garbarino, G. A. Botton, A. C. Tavares and D. Guay, "Selective electroreduction of CO2 to formate on 3D [100] Pb dendrites with nanometer-sized needle-like tips", *Journal of Materials Chemistry A*, 2017, **5**, 20747–20756.
(18) Y. Hori, A. Murata and R. Takahashi, "Formation of hydrocarbons in the electrochemical reduction of carbon dioxide at a copper electrode in aqueous solution", *Journal of the Chemical Society, Faraday Transactions 1: Physical Chemistry in Condensed Phases*, 1989, **85**, 2309–2326.
(19) Z. Yang, F. E. Oropeza and K. H. Zhang, "P-block metal-based (Sn, In, Bi, Pb) electrocatalysts for selective reduction of CO2to formate", *APL Materials*, 2020, **8**, 60901.
(20) S. Komatsu, T. Yanagihara, Y. Hiraga, M. Tanaka and A. Kunugi, "Electrochemical Reduction of CO2 at Sb and Bi Electrodes in KHCO3 Solution", *Denki Kagaku oyobi Kogyo Butsuri Kagaku*, 1995, **63**, 217–224.
(21) J. L. Dimeglio and J. Rosenthal, "Selective conversion of CO2 to CO with high efficiency using an inexpensive bismuth-based electrocatalyst", *Journal of the American Chemical Society*, 2013, **135**, 8798–8801.
(22) H. Zhong, Y. Qiu, T. Zhang, X. Li, H. Zhang and X. Chen, "Bismuth nanodendrites as a high performance electrocatalyst for selective conversion of CO2 to formate", *Journal of Materials Chemistry A*, 2016, **4**, 13746–13753.
(23) S. Liu, X. F. Lu, J. Xiao, X. Wang and X. W. Lou, "Bi2O3 Nanosheets Grown on Multi-Channel Carbon Matrix to Catalyze Efficient CO2 Electroreduction to HCOOH", *Angewandte Chemie - International Edition*, 2019, **58**, 13828–13833.
(24) J. E. Pander, M. F. Baruch and A. B. Bocarsly, "Probing the Mechanism of Aqueous CO2 Reduction on Post-Transition-Metal Electrodes using ATR-IR Spectroelectrochemistry", *ACS Catalysis*, 2016, **6**, 7824–7833.
(25) W. Oh, C. K. Rhee, J. W. Han and B. Shong, "Atomic and Molecular Adsorption on the Bi(111) Surface: Insights into Catalytic CO2 Reduction", *Journal of Physical Chemistry C*, 2018, **122**, 23084–23090.

(26) R. J. Walker, A. Pougin, F. E. Oropeza, I. J. Villar-Garcia, M. P. Ryan, J. Strunk and D. J. Payne, "Surface Termination and CO2 Adsorption onto Bismuth Pyrochlore Oxides", *Chemistry of Materials*, 2016, **28**, 90–96.

(27) M. Nolan, "Adsorption of CO2 on Heterostructures of Bi2O3 Nanocluster-Modified TiO2 and the Role of Reduction in Promoting CO2 Activation", *ACS Omega*, 2018, **3**, 13117–13128.

(28) J. H. Koh, D. H. Won, T. Eom, N. K. Kim, K. D. Jung, H. Kim, Y. J. Hwang and B. K. Min, "Facile CO2 Electro-Reduction to Formate via Oxygen Bidentate Intermediate Stabilized by High-Index Planes of Bi Dendrite Catalyst", *ACS Catalysis*, 2017, **7**, 5071–5077.

(29) S. Kim, W. J. Dong, S. Gim, W. Sohn, J. Y. Park, C. J. Yoo, H. W. Jang and J. L. Lee, "Shape-controlled bismuth nanoflakes as highly selective catalysts for electrochemical carbon dioxide reduction to formate", *Nano Energy*, 2017, **39**, 44–52.

(30) Z. Chen, K. Mou, X. Wang and L. Liu, "Nitrogen-Doped Graphene Quantum Dots Enhance the Activity of Bi2O3 Nanosheets for Electrochemical Reduction of CO2 in a Wide Negative Potential Region", *Angewandte Chemie - International Edition*, 2018, **57**, 12790–12794.

(31) Q. Gong, P. Ding, M. Xu, X. Zhu, M. Wang, J. Deng, Q. Ma, N. Han, Y. Zhu, J. Lu, Z. Feng, Y. Li, W. Zhou and Y. Li, "Structural defects on converted bismuth oxide nanotubes enable highly active electrocatalysis of carbon dioxide reduction", *Nature Communications*, 2019, **10**, 2807.

(32) P. Lu, D. Gao, H. He, Q. Wang, Z. Liu, S. Dipazir, M. Yuan, W. Zu and G. Zhang, "Facile synthesis of a bismuth nanostructure with enhanced selectivity for electrochemical conversion of CO2 to formate", *Nanoscale*, 2019, **11**, 7805–7812.

(33) X. Zhang, X. Sun, S. X. Guo, A. M. Bond and J. Zhang, "Formation of lattice-dislocated bismuth nanowires on copper foam for enhanced electrocatalytic CO2 reduction at low overpotential", *Energy and Environmental Science*, 2019, **12**, 1334–1340.

(34) X. Zhang, Y. Zhang, Q. Li, X. Zhou, Q. Li, J. Yi, Y. Liu and J. Zhang, "Highly efficient and durable aqueous electrocatalytic reduction of CO2to HCOOH with a novel bismuth-MOF: experimental and DFT studies", *Journal of Materials Chemistry A*, 2020, **8**, 9776–9787.

(35) H. Yang, N. Han, J. Deng, J. Wu, Y. Wang, Y. Hu, P. Ding, Y. Li, Y. Li and J. Lu, "Selective CO2 Reduction on 2D Mesoporous Bi Nanosheets", *Advanced Energy Materials*, 2018, **8**, 1801536.

(36) D. Wu, J. Liu, Y. Liang, K. Xiang, X. Z. Fu and J. L. Luo, "Electrochemical Transformation of Facet-Controlled BiOI into Mesoporous Bismuth Nanosheets for Selective Electrocatalytic Reduction of CO2 to Formic Acid", *ChemSusChem*, 2019, **12**, 4700–4707.

(37) N. Li, P. Yan, Y. Tang, J. Wang, X. Y. Yu and H. B. Wu, "In-situ formation of ligand-stabilized bismuth nanosheets for efficient CO2 conversion", *Applied Catalysis B: Environmental*, 2021, **297**, 120481.

(38) B. Zhang, G. Yang, Q. Chai, H. Wang, Q. Zhang, Z. Liu and F. Peng, "Bismuth nanoparticles supported on carbon nanotubes for highly efficient production of formate for CO2 electroreduction", *Sustainable Materials and Technologies*, 2024, **41**, e01042.

(39) J. Dong, P. L. Carpinone, G. Pyrgiotakis, P. Demokritou and B. M. Moudgil, "Synthesis of precision gold nanoparticles using Turkevich method", *KONA Powder and Particle Journal*, 2020, **37**, 224–232.

(40) J. P. Tessonnier, O. Ersen, G. Weinberg, C. Pham-Huu, D. S. Su and R. Schlögl, "Selective deposition of metal nanoparticles inside or outside multiwalled carbon nanotubes", *ACS Nano*, 2009, **3**, 2081–2089.

(41) Y. Hori, H. Wakebe, T. Tsukamoto and O. Koga, "Electrocatalytic process of CO selectivity in electrochemical reduction of CO2 at metal electrodes in aqueous media", *Electrochimica Acta*, 1994, **39**, 1833–1839.

(42) Z. M. Detweiler, J. L. White, S. L. Bernasek and A. B. Bocarsly, "Anodized indium metal electrodes for enhanced carbon dioxide reduction in aqueous electrolyte", *Langmuir*, 2014, **30**, 7593–7600.

(43) J. L. White and A. B. Bocarsly, "Enhanced Carbon Dioxide Reduction Activity on Indium-Based Nanoparticles", *Journal of The Electrochemical Society*, 2016, **163**, H410–H416.

(44) M. Pourbaix, *Atlas of electrochemical equilibria in aqueous solutions*, National Association of Corrosion Engineers, Houston, TX, 1974, vol. 13, p. 72436.

(45) Y. Huang, X. Mao, G. Yuan, D. Zhang, B. Pan, J. Deng, Y. Shi, N. Han, C. Li, L. Zhang, L. Wang, L. He, Y. Li and Y. Li, "Size-Dependent Selectivity of Electrochemical CO2 Reduction on Converted In2O3 Nanocrystals", *Angewandte Chemie - International Edition*, 2021, **60**, 15844–15848.

(46) R. Kortlever, J. Shen, K. J. P. Schouten, F. Calle-Vallejo and M. T. Koper, "Catalysts and Reaction Pathways for the Electrochemical Reduction of Carbon Dioxide", *Journal of Physical Chemistry Letters*, 2015, **6**, 4073–4082.

(47) Q. Cheng, M. Huang, Q. Ye, B. Deng and F. Dong, "Indium-based electrocatalysts for CO2 reduction to C1 products", *Chinese Chemical Letters*, 2024, **35**, 109112.

(48) K. Mou, Z. Chen, S. Yao and L. Liu, "Enhanced electrochemical reduction of carbon dioxide to formate with in-situ grown indium-based catalysts in an aqueous electrolyte", *Electrochimica Acta*, 2018, **289**, 65–71.

(49) Z. Zhang, F. Ahmad, W. Zhao, W. Yan, W. Zhang, H. Huang, C. Ma and J. Zeng, "Enhanced Electrocatalytic Reduction of CO2 via Chemical Coupling between Indium Oxide and Reduced Graphene Oxide", *Nano Letters*, 2019, **19**, 4029–4034.

(50) H. Wu, Z. Li, Y. Liu, X. Zou, L. Yin and S. Lin, "A cost-effective indium/carbon catalyst for highly efficient electrocatalytic reduction of CO2to HCOOH", *Sustainable Energy and Fuels*, 2021, **5**, 5798–5803.

(51) A. Capobianchi, S. Foglia, P. Imperatori, A. Notargiacomo, M. Giammatteo, T. D. Buono and E. Palange, "Controlled filling and external cleaning of multi-wall carbon nanotubes using a wet chemical method", *Carbon*, 2007, **45**, 2205–2208.

(52) F. Vratny and F. Gugliotta, "The thermal decomposition of lead nitrate", *Journal of Inorganic and Nuclear Chemistry*, 1963, **25**, 1129–1132.
(53) M. Mantina, A. C. Chamberlin, R. Valero, C. J. Cramer and D. G. Truhlar, "Consistent van der Waals radii for the whole main group", *Journal of Physical Chemistry A*, 2009, **113**, 5806–5812.
(54) M. Vert, Y. Doi, K. H. Hellwich, M. Hess, P. Hodge, P. Kubisa, M. Rinaudo and F. Schué, "Terminology for biorelated polymers and applications (IUPAC recommendations 2012)", *Pure and Applied Chemistry*, 2012, **84**, 377–410.
(55) C. Paulsen, C. Benndorf, J. Kösters, V. Galéa-Clolus, P. Clolus, R. D. Hoffmann and R. Pöttgen, "Tetravalent lead in nature - Plattnerite crystals from Mine du Pradet (France) and Mount Trevasco (Italy)", *Zeitschrift fur Naturforschung - Section B Journal of Chemical Sciences*, 2019, **74**, 427–432.
(56) S. T. Skowron, T. W. Chamberlain, J. Biskupek, U. Kaiser, E. Besley and A. N. Khlobystov, "Chemical Reactions of Molecules Promoted and Simultaneously Imaged by the Electron Beam in Transmission Electron Microscopy", *Accounts of Chemical Research*, 2017, **50**, 1797–1807.
(57) T. Yamada, T. Homma, A. Tomita and Y. Tamai, "Contact between catalyst and carbon in the tin- and lead- catalyzed gasification of carbon with carbon dioxide", *Carbon*, 1984, **22**, 135–140.
(58) W. K. Rudloff and E. S. Freeman, "The catalytic effect of metal oxides on thermal decomposition reactions. II. The catalytic effect of metal oxides on the thermal decomposition of potassium chlorate and potassium perchlorate as detected by thermal analysis methods", *Journal of Physical Chemistry*, 1970, **74**, 3317–3324.
(59) D. C. Lee, F. V. Mikulec and B. A. Korgel, "Carbon Nanotube Synthesis in Supercritical Toluene", *Journal of the American Chemical Society*, 2004, **126**, 4951–4957.
(60) E. E. Abd El Aal, S. Abd El Wanees and A. Abd El Aal, "Anodic behaviour and passivation of a lead electrode in sodium carbonate solutions", *Journal of Materials Science*, 1993, **28**, 2607–2614.
(61) H. J. Terpstra, R. A. De Groot and C. Haas, "The electronic structure of the mixed valence compound Pb3O4", *Journal of Physics and Chemistry of Solids*, 1997, **58**, 561–566.
(62) H. D. Tran, A. H. Le and U. P. Tran, "Preparation of Electrode Material Based to Bismuth Oxide-Attached Multiwalled Carbon Nanotubes for Lead (II) Ion Determination", *Journal of Nanomaterials*, 2021, **2021**, 4702995.
(63) V. Vivier, C. Cachet-Vivier, S. Mezaille, B. L. Wu, C. S. Cha, J.-Y. Nedelec, M. Fedoroff, D. Michel and L. T. Yu, "Electrochemical Study of Bi[sub 2]O[sub 3] and Bi[sub 2]O[sub 2]CO[sub 3] by Means of a Cavity Microelectrode. I. Observed Phenomena and Direct Analysis of Results", *Journal of The Electrochemical Society*, 2000, **147**, 4252.
(64) V. Vivier, A. Régis, G. Sagon, J. Y. Nedelec, L. T. Yu and C. Cachet-Vivier, "Cyclic voltammetry study of bismuth oxide Bi2O3 powder by means of a cavity micro-

electrode coupled with Raman microspectrometry", *Electrochimica Acta*, 2001, **46**, 907–914.

(65) X. D. Liang, N. Tian, S. N. Hu, Z. Y. Zhou and S. G. Sun, "Recent advances of bismuth-based electrocatalysts for CO2 reduction: Strategies, mechanism and applications", *Materials Reports: Energy*, 2023, **3**, 100191.

(66) A. Sudha, S. L. Sharma and T. K. Maity, "Effects of annealing temperature on structural and electrical properties of indium oxide thin films prepared by thermal evaporation", *Materials Letters*, 2015, **157**, 19–22.

(67) N. M. Ahmed, F. A. Sabah, H. I. Abdulgafour, A. Alsadig, A. Sulieman and M. Alkhoaryef, "The effect of post annealing temperature on grain size of indium-tin-oxide for optical and electrical properties improvement", *Results in Physics*, 2019, **13**, 102159.

(68) T. Burwell, M. Thangamuthu, G. N. Aliev, S. Ghaderzadeh, E. C. Kohlrausch, Y. Chen, W. Theis, L. T. Norman, J. A. Fernandes, E. Besley, P. Licence and A. N. Khlobystov, "Direct formation of copper nanoparticles from atoms at graphitic step edges lowers overpotential and improves selectivity of electrocatalytic CO2 reduction", *Communications Chemistry*, 2024, **7**, 140.

(69) P. W. Atkins, *Shriver & Atkins' inorganic chemistry*, Oxford University Press, Oxford SE - xxiv, 824 pages : color illustrations ; 28 cm, 5th ed, 2010.

(70) M. López-Tenés, J. González, E. Laborda and A. Molina, "Insights into the cyclic voltammetry of surface-confined molecules undergoing two-electron transfers of any reversibility and any ordering of the formal potentials: Unravelling the apparent governing factors", *Electrochimica Acta*, 2023, **462**, 142694.

(71) A. J. ((Downs, *Chemistry of Aluminium, Gallium, Indium and Thallium*, London : Blackie academic and professional, 1st ed., 1993.

(72) A. J. Bard and J. A. A. Ketelaar, "Encyclopedia of Electrochemistry of the Elements", *Journal of The Electrochemical Society*, 1976, **6**, DOI: 10.1149/1.2132649.

Chapter 6

Conclusions and Future Work

6.1 Polyphthalocyanines on Multi-Walled Carbon Nanotubes

The work conducted in Chapter 4 investigated the monometallic CoPPc/MWNT, and novel bimetallic Cu/CoPPc/MWNT with the aim of improving the stability and FE towards methanol production demonstrated in CoPc/MWNT previous to the investigations onset. Whilst the aim of achieving a high methanol FEs was not achieved in this work, the process revealed a unique electrochemical metal displacement reaction between Cu and Co in the synthesised Cu/CoPPc/MWNT whilst showing an improvement in CO_2RR activity compared to the monometallic CoPPc/MWNT.

It is evident that the main findings of interest encapsulated in Chapter 4 is the metal displacement reaction of the bimetallic catalyst, and the single atom microscopy performed. Improving the CO_2RR performance of Cu/CoPPc/MWNT would likely not be worthwhile, due to the large amount of improvement required. Instead, future work on bimetallic polyphthalocyanines supported by MWNTs should focus on further exploring the unique electrochemical metal displacement that occurs, as the more promising electrocatalytic system in this work can be found with the indium based catalysts in Chapter 5.

Specifically. future work regarding the polyphthalocyanines on MWNTs in this thesis would encompass the following:

- Further exploration of the electrochemically induced metal displacement observed in Cu/CoPPc/MWNT and the electrochemically displaced product via techniques such as in-situ Raman, XPS, and identical location TEM and AC-STEM.
- Investigation of whether this metal displacement can be observed using other metals in place of Cu, and if it can be conducted with similar macrocylic systems such as porphyrin based polymers or phthalocyanine based covalent organic frameworks

6.2 P-Block Metals on Multi-Walled Carbon Nanotubes

The work conducted in Chapter 5 investigated three p-block metals on MWNTs: Pb/MWNT, Bi/MWNT, and In/MWNT for the electrochemical CO_2RR for the production of formate in aims to create a high selectivity and activity catalyst whilst adhering to a relatively facile synthesis. Out of the three catalysts investigated, In/MWNT emerged as the highest performing by a large margin, inspiring further optimisation towards the best performing catalyst: In-25R. In-25R features near uniform selectivity towards formate with good current density. Both Pb and Bi significantly underperformed compared to what was expected from past works, however with the insights gained from In-25 Opt, it may be that far better performance from these metals may be achieved with a similar optimisation process of the MWNT and synthesis. In particular, using higher metal loadings to be equivalent in molarity to In-25 Opt, rather than mass, and also utilising the same MWNT internal cavity blocking procedure.

Overall, the main findings of interest encapsulated in Chapter 5 are the In-25 Opt catalyst and its synthesis. The ease of synthesis compared to literature, along with the low amount of In used give motivation for utilising the In-25 Opt catalyst in a flow cell set-up which can then prove viability for further scale-up, given its stability and activity remain good enough for longer term use.

Specifically future work regarding the p-block metals on MWNTs work in this thesis would encompass the following:

- Testing both Pb and Bi with treated MWNTs in a similar fashion to In-25 Opt, and it is expected that with optimisation based on the results of this work, both pb/mwnt and Bi/MWNT could be found to be high performing CO_2RR catalysts with little new work needing to be conducted.
- Further testing of the In-25 Opt catalyst for stability over longer periods, optimising for even lower amounts of metal loading, and scaling up the system to see if appreciable amounts of formate can be achieved for use outside of a research setting.

Appendices

I Kapusta and Hackerman[1]

To comment on the catalytic system utilised by Kapusta and Hackerman,[1] the catalyst system is akin to that of modern methanol producing CoPc systems, being CoPc immobilised on a conductive carbon support, however the work does not utilise a negative enough potential demonstrated by modern works such as Boutin *et al* and Wang *et al*[2,3] to be capable of methanol production utilising a CoPc based electrocatalyst (< -0.54 V vs RHE). Additionally as stated in text.[1] the inconsistent thickness of the electrode would additionally contribute to poor methanol activity as predicted by Chen *et al*.[4] Kapusta and Hackerman[1] additionally formate production is observed in neutral pH, and when pH < 4 then was methanol observed, which is attributed to the fact that HCOOH above this pH is largely dissociated into $HCOO^-$ (pKa $= 4.9$), however these findings are inconsistent with the current predicted mechanistic pathway of methanol production with CoPc outlined by Chen *et al*[5] which predicts CO or CH_3OH are the only possible end products for both monomeric and dimeric CoPc electrocatalysts.

Due to these factors it proved incredibly difficult to incorporate the work by Kapusta and Hackerman[1] into the main text discussion in Chapter 4 on the overall development of CoPc based catalysts, however it would be worthwhile to pursue replicating this work to improve the current understanding of the CoPc CO_2RR mechansm.

II Experimental

II.1 Chapter 4 Experimental

II.1.1 Ink preparation

40 mg of Polyphthalocyanine catalyst (CoPPc/MWNT, CuPPc/MWNT, Cu/CoPPc/MWNT with 10 ml ethanol and 800 μL of Nafion 5% perfluorinated resin solution were sonicated for 30 minutes to create an ink solution which was used for voltammetry and chronoamperometry.

II.1.2 Voltammetry cell setup

For CV, LSV, and chronopotentiometry measurements, the working electrode was an Autolab RDE from Metrohm with a 3 mm diameter glassy carbon electrode tip. The electrode was prepared via dropcasting of 50 μL of the polyphthalocyanine catalyst ink Section II.1.1 a few drops at a time and allowed to dry in air to allow an uniform coating to form.

The reference electrode used was a 3 M NaCl Ag/AgCl electrode. The counter electrode was a 25 $mm \times 25\,mm$ 99% purity Pt gauze woven from 0.1 mm diameter wire (Sigma-Aldrich). Electrodes were used in a 3 electrode one compartment air-tight electrochemical

cell filled with 30 ml of 0.5 M $KHCO_3$ solution. Experiments were performed using a PGSTAT204 potentiostat purchased from Metrohm. CO_2 or Ar gas was saturated into solution via bubbling of gas at a constant rate of 50 sccm before measurements began, and during electrochemical measurements the gas was removed from the electrolyte and flowed over the electrolyte. All electrolytes were made up with Milli-Q ultrapure deionised water.

II.1.3 Electrocatalysis cell setup

For chronoamperometry measurements, the working electrode was Toray Carbon Paper 060 5% PTFE (FuelCellStore) which was cut into a $2 \times 1\, cm^2$ electrode. Using Kapton tape, the electrode was covered to expose only $1 \times 1\, cm^2$ area and placed on a petri dish. The covered carbon paper was then dropcasted with 250 μL of polyphthalocyanine catalyst ink (Section II.1.1) so that the weight loading of the electrode is $1\, mg\, cm^{-2}$. During dropcasting the electrode was mildly heated at 50oc using a hotplate to aid ink drying and also to help form a uniform coating by prevent uneven aggregations forming on the surface of the electrode as it dries.

The reference electrode used was a 3 M NaCl Ag/AgCl electrode. The counter electrode was a $25\, mm \times 25\, mm$ 99% purity Pt gauze woven from 0.1 mm diameter wire (Sigma-Aldrich).

Electrodes were used in an air-tight 3 electrode two compartment H-Cell electrochemical cell, and each compartment was filled with 35 ml of 0.5 M $KHCO_3$ solution, with both compartments saturated with CO_2 via bubbling of gas at a constant rate of 50 sccm using a mass-flow controller before for 30 minutes and during chronoamperometry measurements.

II.1.4 Product Quantification

For liquid product quantification, electrolyte samples were taken via 1 mL syringe before, during, and after the chronoamperometry measurements. 0.4 mL of the electrolyte samples were added to an NMR tube and mixed with 40 μL of 4 mM DMSO and 44 μL of D_2O and then run on a ^1H NMR program with single solvent suppression of water at 4.70 ppm, 30 second delay time, and 256 scans. From the NMR data, liquid product amounts were calculated from the known amount of DMSO via the quantitative NMR equation Eq. (1)[6]

$$C_{\text{Product}} = C_{\text{DMSO}} \frac{\frac{I_{\text{Product}}}{H_{\text{Product}}}}{\frac{I_{\text{DMSO}}}{H_{\text{DMSO}}}} \tag{1}$$

where C is the concentration in the NMR tube, I is the integral area of the peak, and H is

the amount of protons associated with the peak ($H = 3$ for CH_3OH due to deuterium exchange with the alcohol group[6]). After the concentration is obtained, cross multiplication with the volumes of the cell and tube can be used to obtain the volume and hence the moles of products produced in the electrochemical cell.

For gas product quantification, during electrocatalysis the gas outlet of the H-Cell was connected to an Agilent 8890 GC and the CO_2 gas bubbling through the solution at would be constantly carrying gas products out of the cell and into the GC 200 μL sample loop where a sample would be taken every 15 minutes. The gas flow into the GC was measured in *sccm* by an AliCat mass-flow controller so that the gas products could be converted into $mol\ s^{-1}$ via Eq. (2):

$$1\ sccm = 7.45 \times 10^{-7}\ mol\ s^{-1} \tag{2}$$

To obtain the amount of gas in $mol\ s^{-1}$, the GC was calibrated using a calibration gas from Air Products, and was composed of a mix of 30% H_2, 20% N_2, and 10% CH_4, C_2H_6, C_3H_8, CO_2, and CO. By varying the flow rate of the calibration gas, calibration curves were produced that correlated the peak area of a specific gas to the flow rate in $mol\ s^{-1}$. The mass flow controller used did not allow flow rate calculations in sccm for the gas mixture, so the flow rate measured was given for that of 100% CO_2 and then corrected using a mass-flow gas correction factor calculated using the partial pressures of the gas calibration mixture. The calibration curves used are shown below in Fig. 1:

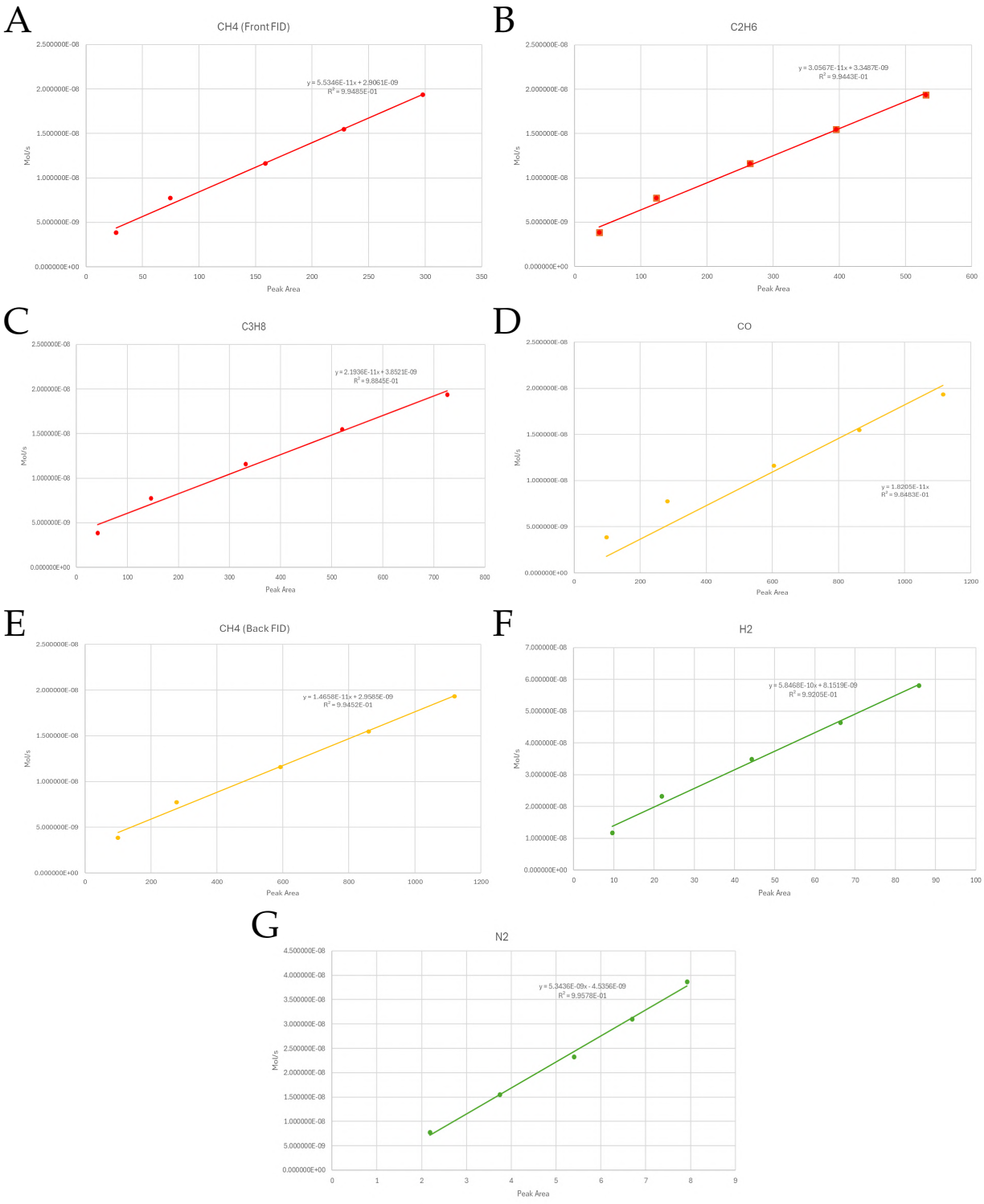


Figure 1: Calibration curves and associated line of best fit equations and R^2 values for (A) CH_4 in the front FID detector; (B) C_2H_6; (C) C_3H_8; (D) CO; (E) CH_4 in the back FID detector; (F) H_2; and (G) N_2.

The resulting value was multiplied by the experiment duration at time of injection to give the moles of gas produced since the last measurement. Due to practical limitations,

changes to the rate of gas production by the electrocatalyst could only be measured at a time interval corresponding to the time between injections. Measurements were taken every 8 minutes and the amount of gas produced was calculated for every 8 minutes and summed to give the final value.

II.2 Chapter 5 Experimental

II.2.1 Ink preparation

2 mg of p-block metal catalyst (Pb/MWNT, Bi/MWNT, In/MWNT with 1 ml ethanol and 50 μL of Nafion 5% perfluorinated resin solution were sonicated for 30 - 60 minutes to create an ink solution which was used for voltammetry and chronoamperometry. Due to the differences between the p-block metal catalysts affecting the ability of the ink to homogenise, various sonication lengths were used and the inks were prepared in smaller quantities compared to Section II.1.1

II.2.2 Voltammetry cell setup

For CV, LSV, and chronopotentiometry measurements, the working electrode was an Autolab RDE from Metrohm with a 3 mm diameter glassy carbon electrode tip. The electrode was prepared via dropcasting of 50 μL of the p-block catalyst ink Section II.2.1 a few drops at a time and allowed to dry in air to allow an uniform coating to form.

The reference electrode used was a 3 M NaCl Ag/AgCl electrode. The counter electrode was a 25 $mm \times 25\,mm$ 99% purity Pt gauze woven from 0.1 mm diameter wire (Sigma-Aldrich). Electrodes were used in a 3 electrode one compartment air-tight electrochemical cell filled with 30 ml of 0.5 M $KHCO_3$ solution. Experiments were performed using a PGSTAT204 potentiostat purchased from Metrohm. CO_2 or Ar gas was saturated into solution via bubbling of gas at a constant rate of 50 sccm before measurements began, and during electrochemical measurements the gas was removed from the electrolyte and flowed over the electrolyte. All electrolytes were made up with Milli-Q ultrapure deionised water.

II.2.3 Electrocatalysis cell setup

For chronoamperometry measurements, the working electrode was Toray Carbon Paper 060 5% PTFE (FuelCellStore) which was cut into a $2 \times 1\ cm^2$ electrode. Using Kapton tape, the electrode was covered to expose only $1 \times 1\ cm^2$ area and placed on a petri dish. The covered carbon paper was then dropcasted with 500 μL of p-block catalyst ink (Section II.2.1) so that the weight loading of the electrode is $1\ mg\ cm^{-2}$. During dropcasting the electrode was mildly heated at 50oc using a hotplate to aid ink drying and also to help form a uniform coating by prevent uneven aggregations forming on the surface of the electrode as it dries.

The reference electrode used was a 3 M NaCl Ag/AgCl electrode. The counter electrode was a 25 $mm \times 25\,mm$ 99% purity Pt gauze woven from 0.1 mm diameter wire (Sigma-Aldrich).

Electrodes were used in an air-tight 3 electrode two compartment H-Cell electrochemical cell, and each compartment was filled with 35 ml of 0.5 M $KHCO_3$ solution, with both compartments saturated with CO_2 via bubbling of gas at a constant rate of 50 sccm using a mass-flow controller before for 30 minutes and during chronoamperometry measurements. .

II.2.4 Product Quantification

Liquid product quantification was performed identically as outlined in Section II.1.4.

Gas product quantification was not performed and only were analysed quantitatively due to the sole product of interest being $HCOO^-$ which was measured quantitatively by NMR. Qualitative measurements were performed on catalysts Pb-50 and In-25 Opt (Sections 5.2 and 5.4) in which no products above the detection limit were observed.

Appendices Bibliography

(1) S. Kapusta and N. Hackerman, "Carbon Dioxide Reduction at a Metal Phthalocyanine Catalyzed Carbon Electrode", *Journal of The Electrochemical Society*, 1984, **131**, 1511–1514.

(2) E. Boutin, M. Wang, J. C. Lin, M. Mesnage, D. Mendoza, B. Lassalle-Kaiser, C. Hahn, T. F. Jaramillo and M. Robert, "Aqueous Electrochemical Reduction of Carbon Dioxide and Carbon Monoxide into Methanol with Cobalt Phthalocyanine", *Angewandte Chemie - International Edition*, 2019, **58**, 16172–16176.

(3) M. Wang, K. Torbensen, D. Salvatore, S. Ren, D. Joulié, F. Dumoulin, D. Mendoza, B. Lassalle-Kaiser, U. Işci, C. P. Berlinguette and M. Robert, "CO2 electrochemical catalytic reduction with a highly active cobalt phthalocyanine", *Nature Communications*, 2019, **10**, DOI: 10.1038/s41467-019-11542-w.

(4) X. Chen, D. Wei and M. S. Ahlquist, "Aggregation and Significant Difference in Reactivity Therein: Blocking the CO2-to-CH3OH Reaction", *Organometallics*, 2021, **40**, 3087–3093.

(5) J. Chen, J. Li, W. Liu, X. Ma, J. Xu, M. Zhu and Y. F. Han, "Facile synthesis of polymerized cobalt phthalocyanines for highly efficient CO2 reduction", *Green Chemistry*, 2019, **21**, 6056–6061.

(6) T. Chatterjee, E. Boutin and M. Robert, "Manifesto for the routine use of NMR for the liquid product analysis of aqueous CO2 reduction: From comprehensive chemical shift data to formaldehyde quantification in water", *Dalton Transactions*, 2020, **49**, 4257–4265.